

Modeling and remote sensing of airglow emissions in the mesopause region: algorithm development and science applications

I n a u g u r a l d i s s e r t a t i o n

zur

Erlangung des akademischen Grades eines
Doktors der Naturwissenschaften (Dr. rer. nat.)

der

Mathematisch-Naturwissenschaftlichen Fakultät

der

Universität Greifswald

vorgelegt von

Olexandr Lednyts'kyy

Greifswald, November 2019

Dekan: Prof. Dr. Werner Weitschies

1. Gutachter: Prof. Dr. Christian von Savigny

2. Gutachter: Prof. Dr. Jörg Gumbel

Tag der Promotion: 4. Februar 2020

“Zwei Dinge erfüllen das Gemüt mit immer neuer und zunehmender Bewunderung und Ehrfurcht, je öfter und anhaltender sich das Nachdenken damit beschäftigt:
Der bestirnte Himmel über mir, und das moralische Gesetz in mir.”
Immanuel Kant (1724 - 1804), Kritik der praktischen Vernunft, 1788.

Contents

1. Introduction	1
2. Employed <i>in situ</i> and remote sensing measurements	7
3. Methodological approaches in the $[O(^3P)]$ retrievals	11
3.1. Models with not identified excited O_2 states employed to retrieve $[O(^3P)]$ time series – Article II	11
3.2. Identified excited O_2 states in the models worked out to retrieve $[O(^3P)]$ profiles – Articles V and VI	15
4. Results and discussion	25
4.1. Retrievals of Volume Emission Rate (VER) time series – Article II	25
4.2. Verification of the retrieved $[O(^3P)]$ time series on the basis of input atmospheric parameters from different sources – Articles I and II	27
4.3. Validation of the $[O(^3P)]$ retrievals carried out using models with not identified excited O_2 states – Articles V and VI	30
4.4. Sensitivity of $O(^3P)$ to the solar activity forcing – Article IV	31
4.5. Sensitivity of $O(^3P)$ to the lunar gravitational forcing – Article III	38
4.6. Validation of the $[O(^3P)]$ retrievals carried out using the proposed Multiple Airglow Chemistry model – Articles V and VI	39
5. Summary and outlook	47
 Appendix	 67
A. Articles of the cumulative doctoral thesis	69
B. Declaration of Originality (Eigenständigkeitserklärung)	175
C. Curriculum Vitae	177
D. Publications and contributions to conferences	179
E. Acknowledgements	183

1. Introduction

The origin of global airglow emissions has been misinterpreted to be the same as of aurora emissions for decades since the first nightglow observations of the green line at 557.7 nm were carried out in 1868 by Ångström [1869]. The origin of the 557.7 nm green line emission was associated with atomic oxygen (O) in 1923 [McLennan and Shrum, 1925]. The oxygen green line emission is a layer phenomenon occurring both in the airglow and the aurora and is represented by the following transition:

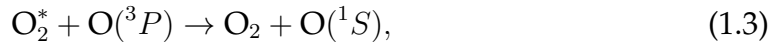
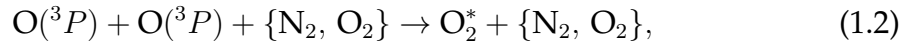
$$\text{O}(^1S) \rightarrow \text{O}(^1D) + h\nu (\lambda = 557.7 \text{ nm}), \quad (1.1)$$

where 1S and 1D denote the second and first electronically excited states of O, respectively. The discussion about the origin of airglow emissions related to O and molecular oxygen (O_2) is still open because the corresponding excitation mechanisms are not well known, see section 3 regarding precursors, e.g., of $\text{O}(^1S)$.

Airglow is a globally occurring faint luminescence caused directly or indirectly by selective absorption of solar radiation in the atmosphere [von Savigny, 2017]. Dayglow, twilightglow and nightglow can be observed at conditions of day time, dusk or night time, respectively, at altitudes ~ 50 . . 300 km in the atmosphere of the Earth [Khomich et al., 2008, Nagy et al., 2008]. Airglow can be also observed in atmospheres of other planets, e.g., Mars and Venus [Krasnopolsky, 2011]. Dayglow is generally stronger than nightglow, but on the Earth's sunlit side it is difficult to distinguish dayglow emissions from scattered solar radiation.

The Earth's atmosphere is considered to be stratified in air layers [Brasseur and Solomon, 2005, Khomich et al., 2008, McDade, 1998, Nagy et al., 2008]. Between the lower atmosphere (troposphere and tropopause) and the turbopause at ~ 100 km is the middle atmosphere (stratosphere, stratopause, mesosphere and mesopause) [Brasseur and Solomon, 2005]. Diatomic molecules are most abundant in the atmosphere below the turbopause [Mlynczak et al., 2013b]. The terms "weather" and "climate" refer to meteorology, i.e., investigation of the atmosphere below the turbopause. Sydney Chapman investigated the atmosphere and introduced the term "aeronomy" referring to the altitude range of "the upper region of atmosphere, where dissociation and ionization are important" [Nagy et al., 2008]. The Earth's outer space is the part of the atmosphere above the Kármán line at 100 km. Right above the middle atmosphere is thermosphere, and the strongest airglow emissions are detected in the upper Mesosphere and Lower Thermosphere (MLT).

Studying the MLT region on the basis of airglow phenomena enables scientific understanding of different atmospheric layers, which are coupled with each other [Brasseur and Solomon, 2005]. Emitting species (e.g., $O(^1S)$) and their precursors are studied in the field of atmospheric chemistry to retrieve their abundance using airglow observations. The excitation of $O(^1S)$ responsible for the green line emission, see Eq. (1.1), was proposed to be explained using the Chapman and Barth excitation schemes introduced in 1931 and 1962, respectively, see section 3.1 and Bates [1979] for details. Other suggestions related to the $O(^1S)$ production discussed by Bates [1981] are considered to be of the minor conceptual and historical importance in the range of pressure values in the MLT. The Chapman excitation scheme consists of one reaction involving O in the ground state denoted $O(^3P)$. Specifically, three neutral $O(^3P)$ atoms collide with each other resulting in one O_2 molecule in the ground state and one $O(^1S)$ atom [Chapman, 1931, 1937]. Note that it was very difficult to estimate the rate coefficient of this reaction theoretically and experimentally according to Bates [1978] and Greer et al. [1987], who suggested that this collision does not have enough energy to generate an $O(^1S)$ atom. The Barth transfer scheme consists of the three-body recombination reaction followed by the energy transfer through collision:



where $\{N_2, O_2\}$ is a third body represented by a heavy molecule in the ground electronic state (molecular nitrogen, N_2 , or O_2) abundant in the MLT, and O_2^* (referred to as the $O(^1S)$ precursor) is an electronically excited O_2 molecule in a not identified state or a group of O_2 molecules in not identified states.

Because $O(^3P)$ atoms are involved in the three-body recombination reaction, their abundance can be retrieved on the basis of observed airglow emissions, e.g., the oxygen green line emission. In order to retrieve $O(^3P)$ concentrations denoted $[O(^3P)]$, principles of photochemical modeling of O_2 and O in electronically excited and ground states were worked out and innovative algorithms were proposed and implemented in this doctoral thesis, see chapter 3 for the methodological approaches and chapter 4 for the discussion of the obtained results.

Photosynthesis is the main source of atmospheric O_2 and $O(^3P)$, whereas dissociation of water vapor (H_2O) also plays an important role [Yung and DeMore, 1998]. $O(^3P)$ is the major component of the neutral bath gas being more abundant than O_2 at altitudes higher than about 120 km [Colegrove et al., 1965], where the maximum of the O_2 photodissociation rate for the overhead Sun is [Solomon and Qian, 2005]. Above the middle atmosphere $O(^3P)$ is mostly ionized and can escape to space [Brasseur and Solomon, 2005, Shematovich et al., 2011, Wei et al., 2014].

Interaction between radiation, composition and atmospheric dynamics results in the energy balance and in the thermal structure of the Earth's atmosphere.

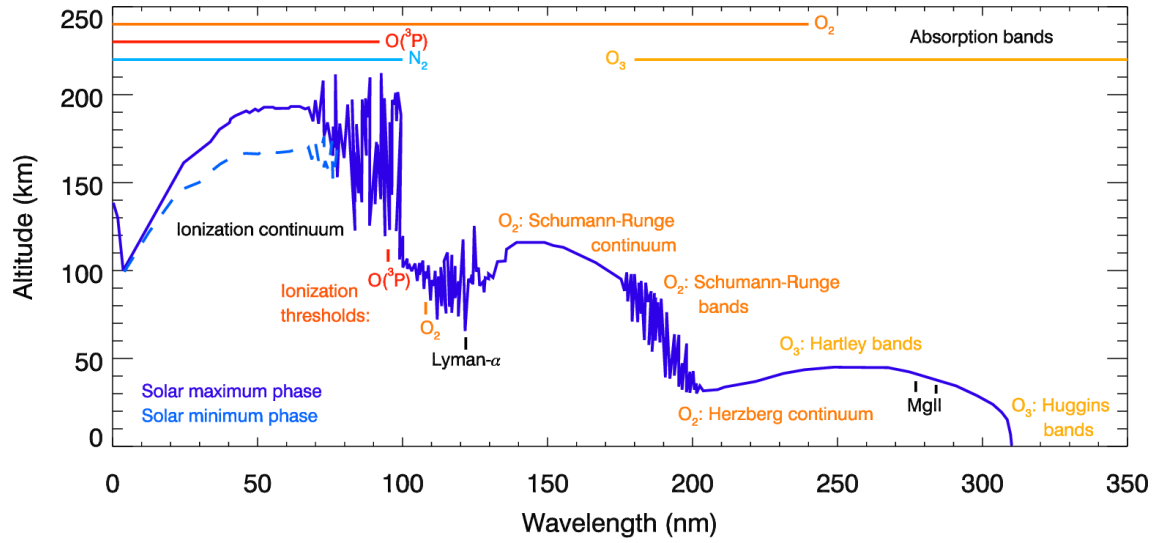


Figure 1.1.: Spectral dependence of the simulated altitude at which the transmission of the vertically incident solar radiation has reached $1/e$ of its original value, i.e., altitude of unit optical depth, [Andrews, 2010, Meier, 1991]. Values of the atmospheric opacity function are indicated by solid violet and dashed blue lines for the maximum and minimum phases of the quasi-11-year cycle of solar activity, respectively, see legend in the left lower corner. Horizontal solid colored lines at the top in the figure illustrate spectral regions of significant extinction by atmospheric species indicated by the colored text. $O(^1D)$ is generated mainly through the photodissociation of O_2 at wavelengths (λ) less than 175 nm. Indicators of solar activity represented by MgII index and Lyman- α are characteristic for different λ values indicated by the black text [Brasseur and Solomon, 2005, Snow et al., 2014]. Ionization thresholds are indicated for $O(^3P)$ and O_2 [Brasseur and Solomon, 2005, Meier, 1991]. Absorption of sunlight in the Extreme UltraViolet range (EUV, 30. . .121 nm) in the ionization continuum produces particles in the ionosphere and heats the thermosphere. Solar radiation in the Far-UltraViolet range (FUV, 122. . .200 nm) is strongly absorbed by O_2 in the MLT, and that in the Middle-UltraViolet range (MUV, 200. . .300 nm) by O_3 in the stratosphere [Dudok de Wit et al., 2009]. Solar radiation in the Near UltraViolet range (NUV, 300. . .400 nm) is absorbed by O_3 in the middle and lower atmosphere as well as on the Earth's surface. Ionization caused by absorption of solar radiation in the EUV range occurs at different altitudes during changing phases of solar activity. For the maximum and minimum phases, as indicated in the figure, the same values of the atmospheric opacity are expected at altitudes, which differ from each other by more than 20 km at λ values of about 50 nm. This figure was reproduced by using Fig. 2 in Meier [1991].

Absorption of solar radiation by ozone (O_3) prevails that by O_2 in the MLT [Brasseur and Solomon, 2005]. Molecular diffusion and ionization of $O(^3P)$, O_2 , atomic nitrogen (N) and N_2 dominate in the thermosphere, where absorption of solar radiation is the dominant heating source, see Fig. 1.1. $O(^3P)$ is a chemically active trace gas being a critical component of the energy budget of the MLT. For instance, $O(^3P)$ was taken into account by García-Comas et al. [2008], Remsberg et al. [2008] and Rezac et al. [2015] to retrieve profiles of carbon dioxide (CO_2) concentrations, kinetic temperature and pressure.

The energy budget in the MLT is dominated by thermal effects produced by solar radiation, chemical, radiative and dynamical processes [Brasseur and Offermann, 1986, Brasseur and Solomon, 2005, Crutzen, 1971]. An appreciable part of the released chemical energy is converted into the vibrational energy of O_2 , N_2 and hydroxyl radicals (OH^*) [Crutzen, 1971]. Energy loss due to airglow emission (e.g., by O_2 at $1.27\ \mu m$ and $762\ nm$, $CO_2(\nu_3)$ at $4.3\ \mu m$ as well as $OH(\nu = 1 - 9)$, where ν denotes a vibrational level of excitation) does not reduce the kinetic temperature of the atmospheric gases [Beig et al., 2008]. Estimates of chemical heating rates due to the seven most important exothermic reactions [Smith et al., 2003] involving odd oxygen ($O(^3P)$, O_3 and $O(^1D)$) and odd hydrogen (H, OH^* and HO_2) vary between $\sim 10 \dots 20\ K\ day^{-1}$ [Mlynczak and Solomon, 1991, 1993] and $\sim 1 \dots 15\ K\ day^{-1}$ [Brasseur and Solomon, 2005]. The author of this doctoral thesis calculated heating rates for seven exothermic reactions considered by Smith et al. [2003] for the WAVE2004 campaign and discussed it during the Talk VII, see chapter D for details.

Reaction rates measured under laboratory conditions can be compared with reaction rates derived using photochemical models. The Stern-Volmer method is often applied to measure quenching reaction rates under laboratory conditions using the following concept: fluorescence competes with non-radiative transitions. Because of simplifications during a particular laboratory measurement, the number of reactions considered in laboratory studies and photochemical models is usually limited. The Stern-Volmer method can be applied to analyze kinetics adding a quencher to a homogeneous system on the basis of the measured change in (1) concentration or (2) lifetime of fluorescent molecules [Lakowicz, 2006]. Measuring concentrations, a rate coefficient of the obtained true pseudo-first order decay is determined. Measuring lifetimes, characteristics of the decay curve decreasing with fluorescence decay time and representing emission intensity are calculated. This might limit the applicability of the analyzed kinetic systems because of the speed and complexity of quenching phenomena. Note that it is difficult to distinguish between static quenching and dynamic quenching according to Carraway et al. [1991] who quantified their contribution for a simple kinetic system.

Conditions established during a laboratory experiment limit the applicability of measured reaction rates, which are valid in limited temperature and pressure ranges [Brasseur and Solomon, 2005], making reaction rates derived using atmospheric models valuable. Particularly, there are three points to argue: (1) labora-

tory conditions when inelastic collisions are rare – compare Fig. 6 in [Kharchenko et al., 2002] and Figs. 6 and 7 in Balakrishnan et al. [1998] – might increase the probability of dynamic quenching comparing to that of other quenching types. These conditions are typical for the MLT during low solar activity when energetic particles are rare and the abundance of ionized particles is low, see section 4.4 for details, (2) the number of known reaction rates considered in a model describing airglow might be lower than it is required, and (3) the number of reactions considered in a model describing airglow might be higher than that considered under laboratory conditions. These points might be appropriately treated by representing unknown or poorly constrained reaction rates as some ratios, which are derived resulting in the so-called empirical coefficients, see, e.g., McDade et al. [1986]. Note that both (1) derived values of reactions rates treated explicitly and (2) empirical coefficients introduced to treat reactions rates implicitly can be compared with reaction rates determined under laboratory conditions.

The following investigation topics were worked out as part of this doctoral thesis. The retrieval of Volume Emission Rate (VER) profiles on the basis of the 557.7 nm green line emission spectrally measured remotely and near-globally from space was optimized with regard to the *a priori* data and uncertainties of the treated data, see section 4.1 in this doctoral thesis and Lednyts'kyy et al. [2015]. The Barth excitation transfer scheme was implemented using the well-known cubic equation of McDade et al. [1986] and the extended cubic equation of Gobbi et al. [1992] modified by Lednyts'kyy et al. [2015]. Both cubic equations can be represented as $d[\text{O}(^3P)]^3 + e[\text{O}(^3P)]^2 + f[\text{O}(^3P)] + g = 0$, where the coefficient d is the same for both the well-known and extended cubic equations, f and g for the well-known cubic equation differ from those for the extended cubic equation, and e is equal to zero for the well-known cubic equation. The coefficients f and g include the VER term as a multiplier for the well-known cubic equation, whereas e , f and g include the VER term for the extended cubic equation. Both equations are solved for $[\text{O}(^3P)]$ values based on known values of VER and other terms, which depend on temperature, $[\text{N}_2]$ or $[\text{O}_2]$. Note that atmospheric density is represented by the sum of $[\text{N}_2]$ and $[\text{O}_2]$.

Values of empirical coefficients implemented in both cubic equations were modified to apply them for different phases of solar activity, see section 3.1 and Lednyts'kyy et al. [2015]. Both cubic equations representing the cases of the minimal and enhanced $\text{O}(^1S)$ quenching were applied to retrieve $[\text{O}(^3P)]$ profiles on the basis of near-global VER time series, see section 3.1. The $[\text{O}(^3P)]$ response to the solar and lunar gravitational forcing was quantified, see sections 4.4 and 4.5 in this doctoral thesis as well as Lednyts'kyy et al. [2017] and von Savigny et al. [2015], respectively. Multiple nightglow emissions were implemented for the case of the moderate $\text{O}(^1S)$ quenching in the proposed Multiple Airglow Chemistry (MAC) model, see section 3.2 as well as Lednyts'kyy and von Savigny [2019] and Lednyts'kyy et al. [2019]. Finally, the MAC model was applied to retrieve $[\text{O}(^3P)]$ profiles at several steps on the basis of the corresponding *in situ* VER profiles obtained using sounding rockets, see section 4.6 in this doctoral thesis as well as Lednyts'kyy and von Savigny [2019] and Lednyts'kyy et al. [2019].

2. Employed *in situ* and remote sensing measurements

In this work data sets simulated with different models – e.g., MSIS (Mass Spectrometer Incoherent Scatter) or WACCM (Whole Atmosphere Community Climate Model) – and measured data sets were employed as follows: (1) *in situ* measurements carried out during the WADIS (WAVE propagation and DISSIPATION) experiment, (2) remote and *in situ* measurements carried out during the WAVE2004 (WAVes in airglow structures Experiment, year 2004) campaign, (3) simulated data sets as well as remote and *in situ* measurements carried out during the WAVE2000 campaign, (4) simulated data sets and *in situ* measurements carried out during the ETON (Energy Transfer in the Oxygen Nightglow) campaign, and (5) simulated data sets and remote measurements carried out using the instruments SABER (Sounding of the Atmosphere using Broadband Emission Radiometry) and SCIAMACHY (SCanning Imaging Absorption spectroMeter for Atmospheric CHartographY).

In this chapter, the employed *in situ* and remote data sets are described in chronological order, i.e., ETON, WAVE2000, WAVE2004, SABER, SCIAMACHY and WADIS-2 (WADIS, the second rocket launch). This description is followed by a brief overview as to how the data sets were employed. Finally, sensor techniques of the employed measurements are described.

The ETON rocket campaign was carried out on 23 March 1982 from ~21:27 until ~23:55 UT (Universal Time, i.e., the mean solar time at 0° N longitude) during nighttime [Greer et al., 1986, McDade et al., 1986] to measure multiple O and O₂ nightglow emissions *in situ*, see also sections 3.2 and 4.6. The ETON rockets P227H and P229H launched during one night at ~22:11 and ~22:58 UT, respectively, were chosen from seven ETON rockets because all nightglow emissions were measured using devices aboard these two rockets in a relatively short period of time. Additionally, these measurements cover all nightglow emissions obtained during the ETON campaign. The respective temperature, [N₂] and [O₂] profiles were simulated with the semi-empirical atmospheric model NRLMSISE-00 (Naval Research Laboratory MSIS Extended, version year 2000 [Picone et al., 2002]).

The WAVE2000 campaign was carried out during several days in January of 2000, and the S-310-29 rocket was launched on January 9 at ~20:50 UT during nighttime [Iwagami et al., 2003, 2002] to measure multiple O and O₂ nightglow emissions *in situ*, see also sections 3.2 and 4.6. The *in situ* measurement site of the rocket was

collocated with that of the MU (Middle and Upper atmosphere) RADAR (RADio Detection And Ranging). Based on this coincidence (collocation of the respective measurement sites characterized by the geographical positions of the obtained profiles), this enabled to combine temperature data sets measured remotely using the MU RADAR with emissions measured *in situ* using the S-310-29 rocket, whereas $[N_2]$ and $[O_2]$ were modeled with the NRLMSISE-00 model.

The WAVE2004 campaign was carried out during several days in January of 2004, and the S-310-33 rocket was launched on January 17 at $\sim 15:30$ UT during nighttime [Iwagami et al., 2005, Kubota et al., 2006] to measure multiple O and O_2 nightglow emissions *in situ*, see also sections 3.2 and 4.6. The coincidence of measurements obtained *in situ* using the rocket and remotely using the SABER instrument was employed to avoid modeled data sets. Specifically, emissions measured *in situ* using the S-310-33 rocket were combined with emissions in the Infrared Atmospheric band, temperature and atmospheric density measured remotely using the SABER instrument.

The TIMED (Thermosphere Ionosphere Mesosphere Energetics and Dynamics) satellite carrying the SABER instrument was launched on 7 December 2001 by the NASA (National Aeronautics and Space Administration) to perform ~ 15 orbits per day [Russell III et al., 1999]. The inclination of the orbit plane of the TIMED satellite is 74.1° , and the satellite changes its orientation every 60-day yaw cycle to avoid direct illumination by the Sun during SABER measurements. This limits the latitudinal coverage to the ranges of either from 87° S to 54° N or from 54° S to 87° N [Mertens et al., 2003]. The SABER instrument observes emissions in ten infrared channels, providing simultaneous and contiguous spectral measurements in the 1.27 to $16.9 \mu\text{m}$ wavelength range [Russell III et al., 1999]. SABER data sets provided by NASA are continuously updated at http://saber.gats-inc.com/browse_data.php. For the employed SABER nighttime limb emission measurements (see sections 3.1 and 4.3), the typical spatial resolution is as follows: vertically ~ 2.2 km being sampled every ~ 0.4 km and horizontally ~ 28 km across-track [Esplin et al., 1995] and ~ 100 km along-track [Mlynckzak et al., 2010] being extended in viewing direction mainly because of limb scanning duration.

Temperature and atmospheric density measured remotely using the SABER instrument in the time range of SCIAMACHY routine operations were also employed to retrieve $[O(^3P)]$ on the basis of emissions measured remotely using the spectrometer SCIAMACHY aboard the Envisat satellite. For this, the well-known cubic equation of McDade et al. [1986] was modified by Lednyts'ky et al. [2015], see sections 3.1 and 4.3 in this doctoral thesis.

The Envisat satellite carrying the SCIAMACHY instrument was launched on 1 March 2002 by the European Space Agency (ESA). The SCIAMACHY routine operations described by Burrows et al. [1995] and Gottwald and Bovensmann [2011] were started on 2 August 2002 and ended on 8 April 2012 because the communication link to Envisat was interrupted. Observations of long emission time series were carried out with the SCIAMACHY instrument, providing simultaneous and contiguous spectral measurements in the 240 to 1750 nm wavelength range

[Bovensmann et al., 1999]. The Envisat satellite was launched into a near-circular polar sun-synchronous orbit to perform about 14.3 orbits per day with the inclination of its orbit plane of 98.55° . Continuous coverage of the SCIAMACHY nighttime limb measurements throughout the year was only possible for latitudes between the equator and about 25° N. For the employed SCIAMACHY nighttime limb emission measurements (see sections 3.1 and 4.3), the typical spatial resolution is as follows: vertically ~ 3.3 km and horizontally ~ 1000 km across-track and ~ 400 km along-track [Gottwald and Bovensmann, 2011]. SCIAMACHY data sets provided by ESA at `ftp://scia-ftp-ds.eo.esa.int` were preprocessed by Dr. K.-U. Eichmann applying all calibration flags [Gottwald and Bovensmann, 2011], and the resulting SCIAMACHY spectral measurements were provided for the work described in this doctoral thesis, see Lednyts'kyi et al. [2015] as well as sections 3.1 and 4.3 for details. The nominal difference between two adjacent tangent heights of the employed SCIAMACHY limb measurements was ~ 3.3 km representing a good estimate of the SCIAMACHY vertical resolution. The Volume Emission Rate (VER) time series of the 557.7 nm green line emission ($\text{VER}\{\text{O}(^1S - ^1D)\}$) available at a fixed time of $\sim 22:00$ LT (solar Local Time) were employed to retrieve and analyze $[\text{O}(^3P)]$ time series, see section 3.1 in this doctoral thesis as well as von Savigny and Lednyts'kyi [2013], Lednyts'kyi et al. [2015], von Savigny et al. [2015] and Lednyts'kyi et al. [2017].

More than 30 years after the ETON campaign, emissions, temperature and atmospheric density were measured *in situ* simultaneously for the first time during the second WADIS campaign carried out during several days in March of 2015 [Gritzner and Strelnikov, 2013, Strelnikov et al., 2017]. The WADIS-2 rocket was launched on March 5 at $\sim 01:44$ UT during nighttime.

This motivated to propose the Multiple Airglow Chemistry (MAC) model (see section 3.2) on the basis of multiple emissions measured *in situ* during the ETON campaign [Lednyts'kyi and von Savigny, 2019] and to apply the MAC model using the same reaction rates on the basis of data sets measured during three other rocket campaigns (WADIS-2, WAVE2000 and WAVE2004) [Lednyts'kyi et al., 2019]. Note that satellite-borne and ground-based instruments enable measuring long time series of emissions, but the main drawback of the mentioned photochemical modeling applied to retrieve $[\text{O}(^3P)]$ was that temperature and atmospheric density were simulated using models, whereas emissions were measured.

During the ETON, WAVE2000 and WAVE2004 campaigns, the employed $[\text{O}(^3P)]$ profiles were measured *in situ* using the ultraviolet resonance lamp and a photomultiplier representing the optical atomic oxygen sensor technique [Dickinson et al., 1980, Gumbel et al., 1998]. During the WADIS-2 campaign, the $[\text{O}(^3P)]$ profiles were measured *in situ* using the non-optical atomic oxygen sensor technique [Eberhart et al., 2015]. Specifically, the employed $[\text{O}(^3P)]$ values were measured during the WADIS-2 campaign using the solid electrolyte sensors in a refined version of FIPEX (Flux ϕ (pH) Probe EXperiment) with improved selectivity towards $\text{O}(^3P)$. *In situ* measurements carried out using both techniques are charac-

terized by the respective measurement uncertainties and require further validation. Eberhart et al. [2015] introduced a second sensor system of the non-optical atomic oxygen sensor technique employed to measure the $O(^3P)$ abundance during the rocket project WADIS: PHLUX (Pyrometric Heat Flux Experiment) based on catalytic effects. Because interpretation of the PHLUX results requires – according to Eberhart et al. [2015] – a thorough analysis, further investigation is required to argue about the most suitable sensor system applied to measure the $O(^3P)$ abundance *in situ*. The author of this doctoral thesis read out all *in situ* data sets required for calculations using the MAC model from the available tables and figures in the corresponding open access articles published in journals with high ranking, see Lednyts'kyy and von Savigny [2019] and Lednyts'kyy et al. [2019] for details.

Additionally to the analysis of the data sets mentioned above, hands-on work was carried out with infrared instruments (spectrometer and imager) in the work group laboratory of the University of Greifswald that resulted in ground-based spectral measurements carried out automatically.

3. Methodological approaches in the $[O(^3P)]$ retrievals

Approaches applied in the $[O(^3P)]$ retrievals are described in this chapter focusing on photochemical models. Section 3.1 is about models considering not identified excited O_2 states, and section 3.2 deals with models considering identified excited O_2 states.

3.1. Models with not identified excited O_2 states employed to retrieve $[O(^3P)]$ time series – Article II

The photochemical models described below were basically developed to retrieve $[O(^3P)]$ on the basis of measurements carried out under atmospheric conditions. In case of unknown or poorly constrained reaction rates, these rates were determined by tuning the photochemical models, whereas rates of known reactions were updated with those measured under laboratory conditions.

The coupling of O_2 and O states with each other was implemented in a number of the photochemical models presented in earlier studies, see Table 3.1 for studies presenting the most important models. Each row in this table represents one particular publication about one or several models. Scientific ideas faced limits because a number of reaction rates were not measured due to lack in appropriate measurement techniques employed during the time of work described in these publications. It was assumed that the starting point (to investigate how O_2 states are coupled with each other) can be sufficiently represented by reactions involving O_2^* . Specifically, O_2^* was understood as a not identified excited O_2 state or a group of them in order to avoid modeling of complex processes coupling identified excited O_2 states. The idea of this simplification was based on considering excitation energy of O_2 states as follows: O_2 states are de-excited from the highest electronic O_2 state to the lower excited ones. This idea was formulated as the integrity of the O_2 electronic states' identity in the hypothesis of Huestis [2002], see Slanger et al. [2004a] for details.

The Stern-Volmer method mentioned in chapter 1 was widely employed to measure reaction rates under laboratory conditions [Steadman and Thrush, 1994,

Table 3.1.: States of O_2 and O considered in various photochemical models are marked by plus signs in the table separated in three panels representing (1) the three-body recombinations reactions, see Eq. (1.2), producing O_2 species shown in the head of columns of the upper panel, (2) O_2 in not identified electronically excited states coupled with each other as shown in the head of columns of the middle panel, and (3) O_2 and O in identified electronically excited states coupled with each other as shown in the head of columns of the lower panel. The used references (see column Ref.) are denoted as follows: So79 is for [Solheim and Llewellyn, 1979], Gr91 – [Greer et al., 1981], To85 – [Torr et al., 1985], Mc86 – [McDade et al., 1986], Mu86 – [Murtagh et al., 1986], Go92 – [Gobbi et al., 1992], Se97 – [Semenov, 1997], Mc87 – [McDade et al., 1987], Lo92 – [López-González et al., 1992], Sh14 – [Sharp et al., 2014], Hi93 – [Hickey et al., 1993], Hi97 – [Hickey et al., 1997], Vl05 – [Vlasov et al., 2005], Hu14 – [Huang and George, 2014], Gr19 – [Grygalashvily et al., 2019], Ml93 – [Mlynczak et al., 1993].

Ref.	$O_2(A)$	$O_2(A')$	$O_2(c)$	O_2^*	O_2^{**}	$O_2(b)$	$O_2(a)$	$O_2(X)$
So79			+					
Gr91			+					+
To85	+	+	+			+		+
Mc86				+	+	+		
Mu86				+				
Go92				+				
Se97				+				
Mc87							+	
Lo92	+	+		+				
Sh14							+	
Hi93			+			+		+
Hi97			+			+		+
Vl05				+		+	+	+
Hu14			+			+		+
Gr19					+	+		+
Ref.	$O_2^*-O_2(c)$	$O_2^*-O_2(b)$	$O_2^*-O_2(X)$	$O_2^*-O(^1S)$	$O_2^*-O(^1D)$	$O_2^{**}-O_2(b)$	$O_2^{**}-O_2(a)$	$O_2^{**}-O_2(X)$
Mc86			+	+		+		+
Go92			+	+				
Se97			+	+				
Gr19						+		+
Ref.	$O_2(c-b)$	$O_2(c-X)$	$O_2(c)-O(^1S)$	$O_2(b-a)$	$O_2(b-X)$	$O_2(a-X)$	$O(^1S-^1D)$	$O(^1S-^3P)$
So79		+	+				+	+
Gr91	+	+			+			
To85		+			+	+		+
Mc86					+		+	+
Mc87						+		
Ml93				+	+	+		
Hi93	+	+			+			
Hi97	+	+	+				+	+
Vl05				+	+	+		
Hu14	+	+	+		+		+	+

Stott and Thrush, 1989]. Because the measured reaction rates are usually compared with derived ones, the number of reactions considered in a model is kept low in order to effectively interpret the obtained results using the Stern-Volmer method. For instance, McDade et al. [1986] simplified the developed three models employing the Stern-Volmer method on the basis of the ETON *in situ* nightglow intensity measurements. This enabled McDade et al. [1986] to consider a limited number of reaction rate values and to replace ratios of unknown reaction rates

by empirical coefficients. Additionally, this inspired McDade et al. [1986] to assume that the involvement of identified excited O_2 states can be omitted, and the $O(^1S)$ precursor can be simply represented by O_2^* . Note that López-González et al. [1992] and Krasnopolsky [2011] also employed the ETON measurements, they derived other values of the empirical coefficients, whereas Stegman and Murtagh [1991] adopted those derived by McDade et al. [1986].

McDade et al. [1986] developed two photochemical models applied to retrieve $[O(^3P)]$ on the basis of emissions in the Atmospheric band: transitions from the ground vibrational state of $O_2(b)$ to that of $O_2(X)$. The first model was developed using the one-step excitation scheme implementing $O_2(b)$ produced in the three-body recombination reaction shown by Eq. (1.2). McDade et al. [1986] applied the first model and observed non-linearities because reaction rates of the collisional relaxation depend on temperature and pressure values as well as atmospheric dynamics. The second model was developed using the two-step excitation scheme implementing the $O_2(b)$ precursor (O_2^{**}) and $O_2(b)$ being both produced in the three-body recombination reactions. Developing the second model, the well-known quadratic equation of McDade et al. [1986] was implemented using derived rate values of reactions involving O_2^{**} and other reactions that resulted in retrievals where the mentioned non-linearities were not observed. In other words, this favored implementing O_2^{**} and $O_2(b)$ in the second model with the use of the two-step excitation scheme. Consequently, implementing O_2^* and $O(^1S)$ in the third photochemical model, McDade et al. [1986] favoured the two-step (referred to as Barth) excitation scheme, see Eqs. (1.2) and (1.3), whereas the one-step (referred to as Chapman) excitation scheme was implemented neither in this work nor in McDade et al. [1986] to retrieve $[O(^3P)]$, see also chapter 1. Developing the third model, the steady-state continuity equation referred to as the well-known cubic equation of McDade et al. [1986] was implemented. The $O(^1S)$ quenching with O_2 only was considered in the well-known cubic equation and referred to as the case of the minimal $O(^1S)$ quenching, see also chapter 1. Note that the $O(^1S)$ quenching reactions were reported in Garcia and Solomon [1985] to be not completely established.

Gobbi et al. [1992] modified the well-known cubic equation of McDade et al. [1986] and proposed the extended cubic equation considering the $O(^1S)$ quenching with O_2 , N_2 and $O(^3P)$. The cubic equation of Semenov [1997] applied to retrieve $[O(^3P)]$ on the basis of $VER\{O(^1S - ^1D)\}$ is similar to the extended cubic equation. Semenov [1997] applied the specific relationship among $[O(^3P)]$ and $VER\{O(^1S - ^1D)\}$ profiles to solve it considering a higher rate of the $O(^1S)$ quenching with $O(^3P)$ provided by Johnston and Broadfoot [1993] than that adopted by Gobbi et al. [1992] and discussed by Krauss and Neumann [1975] and Kenner and Ogryzlo [1982].

All mentioned cubic equations were established to explain the origin of the green line emission and to retrieve $[O(^3P)]$. Their further expansion incorporating other excited O_2 species produced through the three-body recombination reactions faced the problem that appropriate equations were of the fourth or higher

degree, and the obtained solutions were difficult to interpret. Specifically, the $O(^1S)$ quenching with $O_2(a)$ was emphasized by Bates [1981] and Kenner and Ogryzlo [1982] to be very effective, which required to incorporate the three-body recombination reactions producing $O_2(a)$. Note that if several three-body recombination reactions producing O_2^* and $O_2(a)$ were considered in models applied to retrieve $[O(^3P)]$ on the basis of a $VER\{O(^1S - ^1D)\}$ or a $VER\{O_2(a - X)\}$ profile, then the corresponding continuity equation would be represented by a polynomial equation of the fourth degree. Therefore, reactions of the $O(^1S)$ quenching with O_2 , N_2 and $O(^3P)$ were explicitly implemented and the $O(^1S)$ quenching with $O_2(a)$ was implicitly implemented in the extended cubic equation because both the relatively high rate of the $O(^1S)$ quenching with $O(^3P)$ and the analytical method of Semenov [1997] were adopted, see Lednyts'kyi et al. [2015] and Lednyts'kyi and von Savigny [2019]. This was referred to as the case of the enhanced $O(^1S)$ quenching, see also chapter 1.

Empirical coefficients employed in the well-known cubic equation were derived by McDade et al. [1986] on the basis of the ETON measurements carried out during several night hours on 23rd March 1982. Additionally, the corresponding profiles of temperature, $[N_2]$ and $[O_2]$ were simulated by McDade et al. [1986] with the semi-empirical model MSIS-83 (MSIS, version year 1983 [Hedin, 1983]). Considering the 11-year cycle of solar activity, several studies applying different values of empirical coefficients for different phases of solar activity were analyzed to adjust the empirical coefficients derived by McDade et al. [1986] in order to increase their applicability, see Lednyts'kyi et al. [2015] and Lednyts'kyi and von Savigny [2019] for details. This was done to reflect differences in optical depths during the solar cycle, see Fig. 1.1, Meier [1991] and Dudok de Wit et al. [2009] for details.

Adjusted empirical coefficients were applied in the well-known and extended cubic equations to retrieve time series of $[O(^3P)]$ on the basis of time series of temperature, $[N_2]$ and $[O_2]$ obtained from three available sources as well as SCIAMACHY $VER\{O(^1S - ^1D)\}$. The three data sources are the semi-empirical atmospheric model NRLMSISE-00 [Picone et al., 2002], the chemical-dynamical model SD-WACCM4 (WACCM, version 4 [Liu et al., 2010], with Specified Dynamics [Lamarque et al., 2012]) and the SABER instrument. The $[O(^3P)]$ time series were tested for consistency by comparing different data sets at several steps to verify calculations carried out using both cubic equations with adjusted empirical coefficients and updated reaction rates, see 4.2 in this doctoral thesis as well as Lednyts'kyi et al. [2015] for details regarding the employed verification procedure. Finally, an error analysis was performed to estimate the maximum error for the retrieved $[O(^3P)]$ time series, see sections 6.2 and 7.1 in Lednyts'kyi et al. [2015] for details.

3.2. Identified excited O₂ states in the models worked out to retrieve [O(³P)] profiles – Articles V and VI

The photochemical models involving identified O and O₂ states described in Table 3.1 were analyzed to investigate the coupling among O and O₂ states. The term diagrams of the low-lying energy levels of the O and O₂ states (also referred to as the Grotrian and Jablonski diagrams, respectively) are shown in the left and right panels in Fig. 3.1 to illustrate optical transitions among these states. Abbreviations of the considered optical transitions are provided in Table 3.2.

Table 3.2.: Abbreviations (Abr.) of the optical transitions and the corresponding Volume Emission Rates (VER) are shown in the same order as indicated in Fig. 3.1. Particular emission lines indicated near the description of the corresponding emission bands were measured using the ETON rockets P227H and P229H [Greer et al., 1986], see also chapter 2.

Abr. of emission and VER	Emission band
BG , VER{O ₂ (A – b)}	Broida-Gaydon band
H_zI , VER{O ₂ (A – X)}	Herzberg I band, note the 320 nm line
Ch_a , VER{O ₂ (A' – a)}	Chamberlain band, note the 370 nm line
H_zIII , VER{O ₂ (A' – X)}	Herzberg III band
cbK , VER{O ₂ (c – b)}	New Keck I/II band [Slanger et al., 2004b]
RJ , VER{O ₂ (c – a)}	Richards-Johnson band
H_zII , VER{O ₂ (c – X)}	Herzberg II band
Abr. of emission and VER	Emission line
GrL , VER{O(¹ S – ¹ D)}	557.7 nm green line
UVL , VER{O(¹ S – ³ P ₁)}	297.2 nm ultraviolet line
UVL* , VER{O(¹ S – ³ P ₂)}	295.8 nm ultraviolet line
ReL , VER{O(¹ D – ³ P ₂ , ³ P ₁)}	630.0 and 636.4 nm red lines
Abr. of emission and VER	Emission band
Nox , VER{O ₂ (b – a)}	Noxon band
Atm , VER{O ₂ (b – X)}	Atmospheric band, note the 761.9 nm line
IRAtm , VER{O ₂ (a – X)}	Infrared Atm band, note the 1270 nm line

McDade et al. [1986] formulated a set of concepts regarding excitation of airglow and proposed algorithms referred to as the McDade *et al.* approach. Firstly, McDade et al. [1986] updated reaction rates and derived values of empirical coefficients considered in the second and third models, see section 3.1 for details, on the basis of the corresponding ETON *in situ* VER profiles. Secondly, the second model of McDade et al. [1986] was applied on the basis of VER{O₂(b – X)}

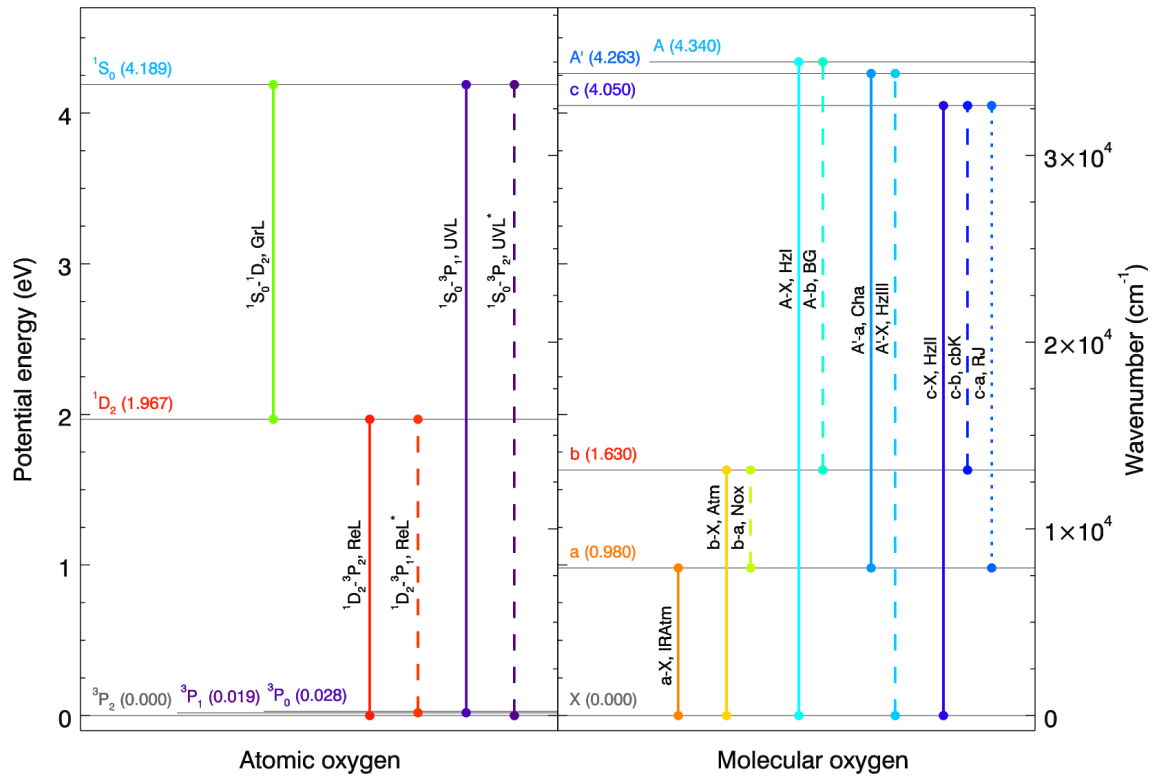


Figure 3.1.: The term diagrams of atomic and molecular oxygen are shown in the left and right panels, respectively. Horizontal solid black lines correspond to the low-lying energy levels given in units of electron-volt (eV) [Capitelli et al., 2012, Jones et al., 2006] and in wavenumber (cm⁻¹) shown near the left and right vertical axes, respectively. O₂ electronic states ($X^3\Sigma_g^-$, $a^1\Delta_g$, $b^1\Sigma_g^+$, $c^1\Sigma_u^-$, $A'^3\Delta_u$ and $A^3\Sigma_u^+$) are shown in short as X, a, b, c, A' and A. The energy of the ground vibrational state of O₂(⁵Π) is about 5.07 eV according to Fig. 1 in Slanger and Copeland [2003] and additional calculations [Bates, 1988a, Minaev et al., 2013]. Transitions involving O₂(⁵Π) are not shown because the lifetime of O₂(⁵Π) is short and the corresponding transitions are difficult to measure, see chapter 1. Optical transitions are illustrated using vertical colored solid lines. Transitions shown by solid lines are stronger than those shown by dashed lines, and transitions shown by dashed lines are stronger than those shown by dotted lines in each of the shown group of transitions according to Khomich et al. [2008], McDade [1998] and Nagy et al. [2008]. The electronic states and the respective abbreviated identification of emission are shown in black in vicinity of lines indicating optical transitions. The O(¹S) precursor denoted as O₂^{*}, see chapter 1 for details, can be represented by the electronic states ⁵Π, $A^3\Sigma_u^+$, $A^3\Delta_u$ and $c^1\Sigma_u^-$ (or the group of these states) with the corresponding vibrational levels being higher than 4.19 eV. The figure was discussed during Talk VI mentioned in the Appendix D and in Lednyts'kyi et al. [2019] by using their Fig. 1.

profiles for retrieving $[O_2(b)]$ used to retrieve the corresponding $[O(^3P)]$ profiles. Additionally, the third model of McDade et al. [1986] was applied on the basis of $VER\{O(^1S - ^1D)\}$ profiles for retrieving $[O(^1S)]$ used to retrieve the corresponding $[O(^3P)]$ profiles. As expected, all retrieved $[O(^3P)]$ profiles were similar to each other and to the reference *in situ* $[O(^3P)]$ profile that enabled validating the calculations carried out using the photochemical models of McDade et al. [1986]. Murtagh et al. [1986] applied the models of McDade et al. [1986] on the basis of *in situ* profiles from different rocket campaigns to retrieve $[O(^3P)]$ profiles employed to evaluate the corresponding VER profiles. Finally, comparing the *in situ* and evaluated VER profiles enabled Murtagh et al. [1986] to verify the models of McDade et al. [1986].

Comparing O and O_2 states shown in Table 3.1 and in Fig. 3.1 with each other, quenching reactions were proposed to be considered in the Multiple Airglow Chemistry (MAC) model implemented to couple the higher excited O and O_2 states with the corresponding lower excited states. The McDade *et al.* approach was adopted to derive rate values of the proposed reactions and to verify and validate the MAC calculations applied in the $[O(^3P)]$ retrievals. The MAC model was discussed in Lednyts'kyy and von Savigny [2016] for the first time. In the following text of this section, other concepts adopted or modified to propose the MAC model are discussed.

Young and Sharpless [1963] assumed that O_2^* and O_2^{**} are coupled with each other by the energy transfer. According to the McDade *et al.* approach, O_2^* and O_2^{**} were implemented as the $O(^1S)$ and $O_2(b)$ precursors, respectively, see section 3.1 for details, which was justified by the hypothesis of Huestis [2002]. Slanger and Copeland [2003] expected energetically nearly resonant intermolecular processes in conversions of higher to lower excited O_2 electronic states. This enabled Slanger et al. [2004a] to refute the hypothesis of Huestis [2002] on the basis of laboratory studies mentioned in Slanger et al. [2004a], see also Pejaković et al. [2007]. Slanger et al. [2004a] proposed that $O_2(A, A', c)$ (the Herzberg states) transform to $O_2(^5\Pi)$ and back through collisions. Finally, states of the $O_2(^5\Pi)$ – $O_2(A, A', c)$ –group are converted to very high vibrational levels of $O_2(b, a)$ (the singlet lower excited states) and $O_2(X)$ (the ground electronic state).

A combination of reactions considered in the three established models developed by (1) Mlynczak et al. [1993] and Sharp et al. [2014], (2) Huang and George [2014] and (3) Gobbi et al. [1992], McDade et al. [1986] and Semenov [1997] was sufficient to represent the first electronically excited singlet states of $O_2(c, b, a)$, the ground triplet state of $O_2(X)$, the first electronically excited singlet states of $O(^1S, ^1D)$ and the ground triplet state of $O(^3P)$ in the MAC model. Additionally, complementary reactions (C-reactions) were proposed to complete the coupling of the $O_2(c, b, a, X)$ and $O(^1S, ^1D, ^3P)$ states considered in the three established models with the O_2 states of the $O_2(^5\Pi)$ – $O_2(A, A')$ –group implemented in the MAC model. Proposing C-reactions required a slight modification of the hypothesis of Slanger et al. [2004a]. Figure 3.2 illustrates reactions considered in the MAC model to couple $O_2(^5\Pi, A, A', c, b, a, X)$ and $O(^1S, ^1D, ^3P)$.

The idea to introduce C-reactions originates from many studies, among which the pioneering works of Torr et al. [1985] and Swenson et al. [1989] are emphasized here. These works are based on several remote measurements of multiple O and O₂ nightglow emissions widely scattered in place during two nights. Multiple nightglow emissions analyzed by Torr et al. [1985] and Swenson et al. [1989] were measured remotely employing an imager by the team of the first international Shuttle mission (including the first ESA astronaut Ulf Merbold) in December 1983.

Torr et al. [1985] considered the O₂(A, A', c, b, a, X) and O(¹S, ³P) states in individual sets of reactions so that not all of these states were coupled with each other. Specifically, both Torr et al. [1985] and Huang and George [2014] considered the coupling of O₂(c) and O₂(b), and Torr et al. [1985] considered (but Huang and George [2014] omitted) the coupling of O(¹S) and O₂(a) implemented as the O(¹S) quenching with O₂(a). This quenching was reported to be very effective according to Bates [1981] and Kenner and Ogryzlo [1982]. Torr et al. [1985] calculated [O₂(a)] in the continuity equation involving O₂(a) on the basis of VER{O₂(a – X)} and then applied [O₂(a)] in the continuity equation involving O(¹S) to retrieve [O(³P)] on the basis of VER{O(¹S – ¹D)}. In summary, the coupling of O₂(a, X) and O(¹S, ³P) was implemented by coupling of the two continuity equations. Considering all reactions implemented by Torr et al. [1985] in a number of similar sets of reactions, Swenson et al. [1989] suggested to combine all of them in one photochemical model. Nevertheless, only a few of the O and O₂ states considered in Swenson et al. [1989] were coupled and the largest number of them remained uncoupled as in the work of Torr et al. [1985]. Torr et al. [1985] and Swenson et al. [1989] operated with emission profiles scattered in place and time and they employed simulated profiles of temperature, [N₂] and [O₂] that resulted in a low level of the data sets' consistency and, therefore, poor matching of the [O(³P)] profiles retrieved on the basis of different emissions. This and the fact that a number of reaction rates were unknown set the airglow investigations back for decades because tuning of reaction rates using models encompassing coupled O and O₂ states and multiple emissions appeared to be difficult.

Considering retrievals of [O(³P)] profiles carried out on the basis of the corresponding emission profiles, the approach of Swenson *et al.* can be interpreted as an extended version of the McDade *et al.* approach. Specifically, the Swenson *et al.* approach enables retrieving concentrations of excited O and O₂ states at five steps considering separate sets of reactions at each step: (1) [O₂(A)] on the basis of VER{O₂(A – X)}, (2) [O₂(A')] on the basis of VER{O₂(A' – a)}, (3) [O₂(b)] on the basis of VER{O₂(b – X)}, (4) [O₂(a)] on the basis of VER{O₂(a – X)}, (5) [O(¹S)] on the basis of VER{O(¹S – ¹D)} and [O₂(a)]. Each retrieval step is carried out using continuity equations of the second or third degree and the obtained solutions can be easily interpreted. The most strong feature of the approach of Swenson et al. [1989] is that at each of these steps an [O(³P)] profile can be retrieved and compared with [O(³P)] profiles retrieved at another steps.

Additionally to the approach of Swenson et al. [1989], the approach of

Yankovsky et al. [2007] was considered to be adopted because it enabled retrieving concentrations of higher excited O and O₂ states, which are considered at next retrieval steps applied to retrieve concentrations of lower excited O and O₂ states. This enabled Yankovsky et al. [2016] to couple the electronic and vibrational states of O₂(*b*, *a*, *X*) and the electronic states of O(¹*D*, ³*P*) with each other. Although multiple vibrational states of O₂ were not considered in the MAC model, the approaches discussed in this section were adopted to carry out calculations using the MAC model to couple the O₂(⁵Π, *A*, *A'*, *c*, *b*, *a*, *X*) and O(¹*S*, ¹*D*, ³*P*) states with each other. The flow chart of the algorithm proposed to solve the system of reactions considered in the MAC model is shown in Fig. 3.3. Specifically, the MAC calculations were carried out applying a number of continuity equations described in appendix in Lednyts'kyi and von Savigny [2019] and implemented to retrieve [O(³*P*)] and concentrations of the particular excited O₂ states on the basis of the corresponding VER profiles at steps 2.1, 2.2, 2.3, 3.1, 3.2 and 4.1. The final retrieval step 5.1 of the MAC calculations was accurately implemented to retrieve [O(³*P*)] when VER profiles were no longer required, i.e., on the basis of concentrations of the O₂(*A*, *A'*, *c*, *b*, *a*) and O(¹*S*, ¹*D*) states retrieved at steps 2.1, 2.2, 2.3, 3.1, 3.2 and 4.1. This was done to avoid *a priori* data, which are required in a time-dependent model to start calculations on the basis of assumed concentration values of the considered O and O₂ states. Note that reactions implemented in the MAC model are considered to be adopted extending the set of reactions considered in the time-dependent box model which is incorporated in the three-dimensional model EMAC/EDITH (MLT extension of ECHAM MESSy [Jöckel et al., 2016, Stevens et al., 2013]) worked out at the Karlsruhe Institute of Technology.

In summary, the whole system of reactions considered in the MAC model was solved analytically step-wise using the corresponding continuity equations of the second or third degree, i.e., providing retrieved concentration values of the particular excited O₂ states from one equation to another. Calculations carried out according to this algorithm appeared to be more stable than calculations carried out according to the algorithm implemented in a typical zero-dimensional box model [Sandu and Sander, 2006].

The MAC calculations were tested for two cases either involving or excluding O₂(*A*) and O₂(*A'*) because the number of reactions involving these states is higher than that excluding them. The triplet states O₂(*A*, *A'*) and O₂(*X*) were expected to be strongly coupled with each other, and the strength of their coupling was employed to study different sets of reactions considered for the two cases. Because limitations on the intensities of transitions are imposed by the Franck-Condon principle [Hollas, 2004] and Franck-Condon factors are calculated using the corresponding internuclear distances (INDs), INDs are discussed identifying the strength of coupling between (1) the excited triplet O₂(*A*, *A'*) and singlet O₂(*c*, *b*, *a*) states as well as (2) the excited triplet O₂(*A*, *A'*) states and the ground triplet O₂(*X*) state. Differences in the INDs between O₂(*A*) and O₂(*X*), between O₂(*A'*) and O₂(*X*) and between O₂(*c*) and O₂(*X*) are approximately equal to each other, and the Franck-Condon factors are expected to be approximately equal

to each other. Additionally, differences in the INDs between $O_2(b)$ and $O_2(X)$ and between $O_2(a)$ and $O_2(X)$ are also approximately equal to each other, and the Franck-Condon factors are also expected to be approximately equal to each other. The Franck-Condon factors rapidly decrease with decreasing $O_2(A)$ state vibrational level according to Slanger and Copeland [2003], and quenching rate coefficients for transitions between higher vibrational levels of $O_2(A)$ and $O_2(X)$ are significantly higher comparing to those between their lower vibrational levels according to Krasnopolsky [1986]. Although the INDs for $O_2(A)$, $O_2(A')$ and $O_2(c)$ are higher than the INDs for $O_2(b)$ and $O_2(a)$ [Slanger and Copeland, 2003], the role of differences in Franck-Condon factors for the transitions from $O_2(A)$ (or $O_2(A')$) to $O_2(X)$ and for transitions from $O_2(b)$ (or $O_2(a)$) to $O_2(X)$ is supposed to be lower than the role of a spin flip because Owens et al. [1993] have shown that the ratio between intensity values in the $O_2(A - X)$ and $O_2(c - X)$ band systems in the 275...300 nm region exceeds 6. A spin flip is required for transitions among the singlet and triplet O_2 states, but it is not required for energetically favorable transitions among the triplet states or for transitions among singlet states. Specifically, the spatial wavefunction is antisymmetric for a triplet state and symmetric for a singlet state due to the spin orientation, so that the corresponding electron-electron repulsion energies lead to the energy difference between the singlet and triplet states [Thorne et al., 1999]. In summary, mainly because of a spin flip required for transitions between the singlet $O_2(b)$ (or $O_2(a)$) state and the triplet $O_2(X)$ state, the probability of these transitions was assumed to be lower than that of transitions between the triplet $O_2(A)$ (or $O_2(A')$) state and the triplet $O_2(X)$ state. This implies that variations in $[O_2(A)]$ and $[O_2(A')]$ cause minor variations in $[O_2(b)]$ and $[O_2(a)]$. This and the fact that variations in $[O_2(X)]$ were not in focus of this study enabled excluding $O_2(A)$ and $O_2(A')$ from the MAC calculations if the corresponding emission profiles – e.g., $VER\{O_2(A - X)\}$ or $VER\{O_2(A' - a)\}$ – were not available.

Employing the concept of the strong coupling among the triplet states $O_2(A, A')$ and $O_2(X)$, the MAC model was implemented modifying the hypothesis of Slanger et al. [2004a] to consider the $O_2(^5\Pi)$ – $O_2(A, A')$ –group in the MAC model instead of the $O_2(^5\Pi)$ – $O_2(A, A', c)$ –group introduced by Slanger et al. [2004a]. Because the $O_2(^5\Pi)$ – $O_2(A, A')$ –group was expected to be removed by conversion to very high vibrational levels of $O_2(b, a, X)$ according to the modified hypothesis of Slanger et al. [2004a], $O_2(^5\Pi)$ was considered in all modifications of the MAC model. In summary, this enabled carrying out the MAC calculations for two cases considering whether $VER\{O_2(A - X)\}$ and $VER\{O_2(A' - a)\}$ were available or they were not available as follows: (1) involving and (2) excluding $O_2(A)$ and $O_2(A')$.

Although Krasnopolsky [1986] emphasized that $O(^5\Pi)$ had been never observed, he considered reactions involving $O_2(^5\Pi)$ in the kinetic model. It is worth noting that the large part of reactions involving $O_2(^5\Pi)$ were omitted in the study of Krasnopolsky [2011] carried out later than the study of Krasnopolsky [1986]. This calls the applicability of the kinetic model of Krasnopolsky [1986] regarding energy transfer reactions involving $O_2(^5\Pi)$ molecules into question. $O_2(^5\Pi)$ was

discovered experimentally not earlier than in 1998 [Huestis, 2002] because $O_2(^5\Pi)$ has a very short lifetime being less than $\sim 0.4 \mu s$ according to Fig. 21 in Slanger and Copeland [2003]. Additionally, studies about reactions involving $O_2(^5\Pi)$ under laboratory conditions are rare, see Huestis [2002] for an overview. This motivated Krasnopolsky [2011] to call the applicability of the Stern-Volmer method under laboratory conditions regarding reactions with $O_2(^5\Pi)$ as a precursor of $O(^1S)$ into question.

Because reactions involving $O_2(^5\Pi)$ were debated, it was reasonable not to consider them in the MAC model explicitly. Instead, they were considered implicitly assuming that $O_2(^5\Pi)$ and the other O_2 states are coupled. This coupling was implemented according to the modified hypothesis of Slanger et al. [2004a], and the contribution of $O_2(^5\Pi)$ in the conversion of the $O_2(^5\Pi)$ – $O_2(A, A')$ –group to very high vibrational levels of $O_2(b, a, X)$ was implemented employing the association rate values derived by Bates [1988a]. According to the MAC approach, the association rate values of $O_2(b, a, X)$ were adjusted by portions of the association rate value of $O_2(^5\Pi)$ because of the conversions among these O_2 states. Association rate values for these O_2 states resulting from three-body recombination reactions are approximately proportional to their statistical weight multiplied by squared INDs. Statistical weights are equal to the multiplicity value for Σ -states, and they are equal to double values of the multiplicity for Π and Δ states due to Λ -doubling [Krasnopolsky, 2011].

Association rates were derived by Bates [1988a] using the hard-sphere concept also applied earlier by Bates [1951], Wraight [1982] and Smith [1984]. Note that the hard-sphere concept was also applied considering the rate value of the three-body recombination reaction, see Eq. (1.2). Specifically, the rate value of the three-body recombination reaction was found by Smith and Robertson [2008] to be lower than that one provided by Campbell and Gray [1973], but it was not provided in the established studies on chemical kinetics, e.g., the Jet Propulsion Laboratory (JPL) databases [Burkholder et al., 2015]. It is remarkable that the rate value of the three-body recombination reaction measured with N_2 as a third body was assumed to be equal to that with O_2 , presumably, because only masses and radii of hard spheres representing N_2 and O_2 molecules were taken into account. Nevertheless, this assumption should be treated with caution, because Bates [1979] suggested that if two $O(^3P)$ atoms collide, then their common surface of potential energy (O_2^\ddagger) reacts with a third body, see also Greer et al. [1987]. Note that the activation barrier of the reaction between N_2 considered as a third body in the three-body recombination reaction with O_2^\ddagger differs from that between O_2 as a third body and O_2^\ddagger because in the last case molecules with similar properties react [Falk et al., 1983, Job and Herrmann, 2006]. This motivated calling the rate value of the three-body recombination reaction with two $O(^3P)$ atoms and one O_2 molecule as a third body into question. As the result, the additional $O(^3P)$ loss processes were implemented in the MAC model, see Lednyts'kyy and von Savigny [2019] for details.

Reaction rates considered in the MAC model were updated with the use of data-

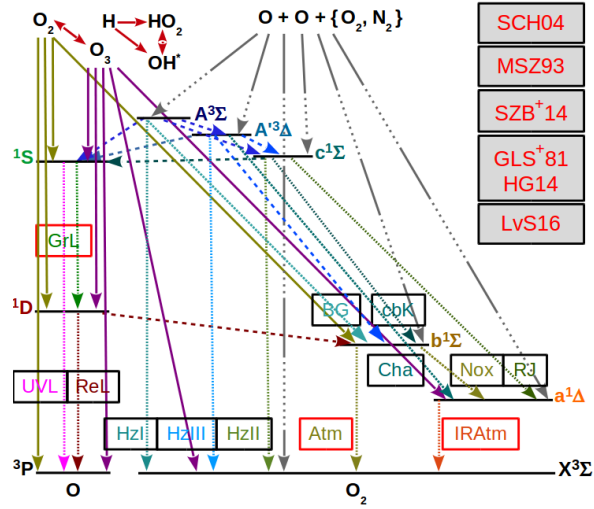


Figure 3.2.: O and O₂ term diagrams illustrating processes of the MAC model. Optical transitions mentioned in Fig. 3.1 and the other processes couple O and O₂ states with each other. The O states are represented by the first two electronically excited states O(¹S) (¹S) and O(¹D) (¹D), and O in the ground state O(³P) (³P). The O₂ states are represented by the first six electronically excited states: O₂(⁵Π) (⁵Π), O₂(A, A') (A³Σ_u⁺ and A³Δ_u), O₂(c) (c¹Σ_u⁻), O₂(b, a) (b¹Σ and a¹Δ) and O₂(X) (the ground state X³Σ_g⁻). The O and O₂ states including those of the O₂(⁵Π)–O₂(A, A')–group [Slanger et al., 2004a] are coupled with each other through emissions and quenching reactions. Three-body recombination reactions resulting in O₂(⁵Π, c, b, a, X) are indicated by “O+O+{O₂, N₂}” and gray lines shown by many dots and one long dash. O₂(⁵Π) is not shown because of its very short lifetime and because reactions involving it are not known well. Transitions are indicated by an abbreviation of the emission provided near lines shown by 2 dots and 3 dashes. Transitions and quenching reactions are indicated by the fine dashed line. Quenching reactions are indicated by the dashed line. Processes involving odd oxygen (O₃, O(¹D), O(³P)) related to the O(³P) loss as well as catalytic O₃ destruction and photolysis are indicated by the solid olive and violet lines. Processes involving odd hydrogen related to OH* and HO₂ species are indicated by the solid red lines. The figure was discussed during Talk IX, see section D, and in Lednyts'kyy et al. [2019] by using their Fig. 5.

bases provided by the JPL [Burkholder et al., 2015], the National Institute of Standards and Technology (available at <https://www.nist.gov/pml/>) and other high ranking sources listed in Huestis [2002] and Jones et al. [2006]. Three modifications of the MAC model were implemented considering the three following sets of reactions: (1) involving or excluding $O_2(A)$ and $O_2(A')$ in the case of excluding O_3 , H , CO_2 , OH^* and HO_2 for the ETON campaign, (2) involving or excluding O_3 , H , CO_2 , OH^* and HO_2 in the case of excluding $O_2(A)$ and $O_2(A')$ for the WAVE2004 campaign, and (3) involving only $O_2(c, b)$ and $O_2(X)$ for the WAVE2000 and WADIS-2 campaigns. These modifications of the MAC model were verified and tested for validity for the four campaigns, see section 4.6 for details.

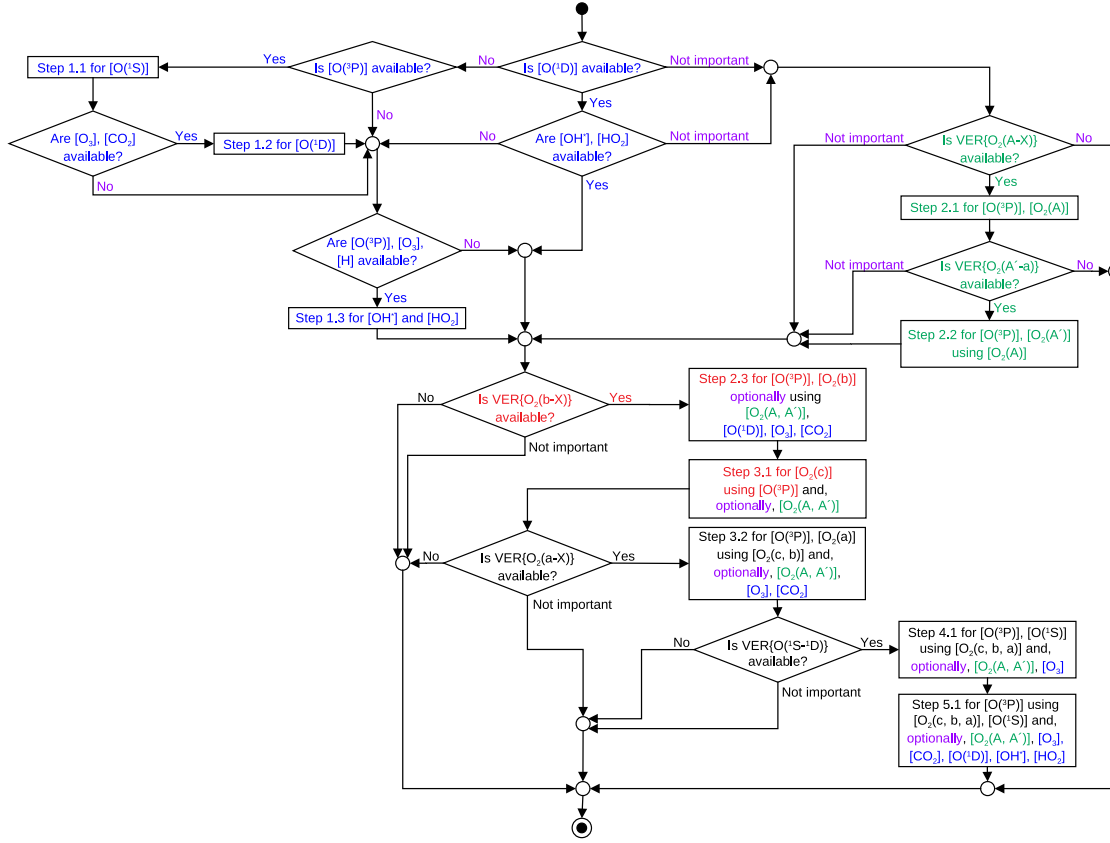


Figure 3.3.: The flow chart shows calculation steps carried out to solve the system of reactions considered in the MAC model. Black circles on the top and bottom of the figure indicate the start and end states, respectively. Rhombs and rectangles indicate decisions and processes, respectively, carried out according to the proposed MAC approach. The calculation steps shown in blue correspond to the prior retrieval procedure. The decision “Not important” shown in violet shown near a rhomb denotes a step considered in the prior retrieval procedure, which can be omitted as it is the case for the ETON campaign. The case when the decision “Not important” has to be taken is represented by the text “optionally” shown in violet in rectangles, i.e., for (1) the prior retrieval procedure (see text shown in blue in rectangles) and (2) retrievals of $[O_2(A)]$ or $[O_2(A')]$ (see text shown in green in rectangles). Because $O_2(A, A')$ states can be excluded from the MAC calculations, the $[O(^3P)]$ retrieval carried out on the basis of available values of $VER\{O_2(b-X)\}$ was found to be the most accurate one that is indicated by the text shown in red. The figure was discussed during Talk VIII, see section D, and in Lednyts'kyy and von Savigny [2019].

4. Results and discussion

4.1. Retrievals of Volume Emission Rate (VER) time series – Article II

Raw spectral emissions measured remotely using the SCIAMACHY instrument were preprocessed, see chapter 2 for details, and the obtained limb spectral measurements of the oxygen green line emission were analyzed to retrieve near-global time series of $\text{VER}\{\text{O}({}^1S - {}^1D)\}$ profiles as described below, see also section 3 in Lednyts'kyy et al. [2015]. Regarding the rocket or SABER nightglow measurements, inversions required to retrieve the employed VER profiles were already carried out by the corresponding science teams. The rocket VER profiles were read out from tables and figures published in earlier studies and the SABER time series were downloaded, see chapter 2 for details.

The obtained SCIAMACHY spectral emissions were analyzed to detect emissions with the focus on the studied green line emission according to the proposed and implemented approach. The quality of green line emission spectra was determined in three steps to exclude particularly bad quality spectra from further processing as follows: (1) the SCIAMACHY quality and data anomaly reports provided by the German Aerospace Center via <http://www.atmos.caf.dlr.de/projects/scops/> were employed to estimate the influence of high energy particles on SCIAMACHY spectra, (2) the data sets of hemispheric power index provided via <http://legacy-www.swpc.noaa.gov/ftpdir/lists/hpi/> were taken into account to reproduce the geographical position of auroral events influencing SCIAMACHY spectra, and (3) a band-pass filter was developed to analyze emissions and noise in three wavelength intervals (555...557 nm, 557...559 nm and 559...561 nm) to exclude spectra with strong contaminating emissions, e.g., in the Q and P branches of the OH(7-1) emission band, from further processing of the 557.7 nm green line emission spectra. A sample SCIAMACHY night spectrum of the green line emission is shown in the left panel of Fig. 4.1.

The SCIAMACHY instrument observed emissions through the entrance slit [Skupin et al., 2005] along the Line Of Sight (LOS) in the limb geometry, and the obtained spectra in units of $\text{photons s}^{-1} \text{m}^{-2} \text{sr}^{-1} \text{nm}^{-1}$ were (1) considered in the central wavelength interval (557...559 nm) as well as in the two adjacent ones, (2) processed using a band-pass filter applied to spectral values in the central and adjacent intervals, (3) multiplied by $(4\pi)^{-1} \cdot 10^{10}$ to obtain data in units of

Rayleigh nm^{-1} [Baker and Romick, 1976], and (4) integrated in the range 557. . . 559 nm to represent the 557.7 nm line emission spectra by a profile of Limb Emission Rate (LER) values in units of Rayleigh at each LER profile altitude. A sample SCIAMACHY LER profile is shown in the middle panel of Fig. 4.1.

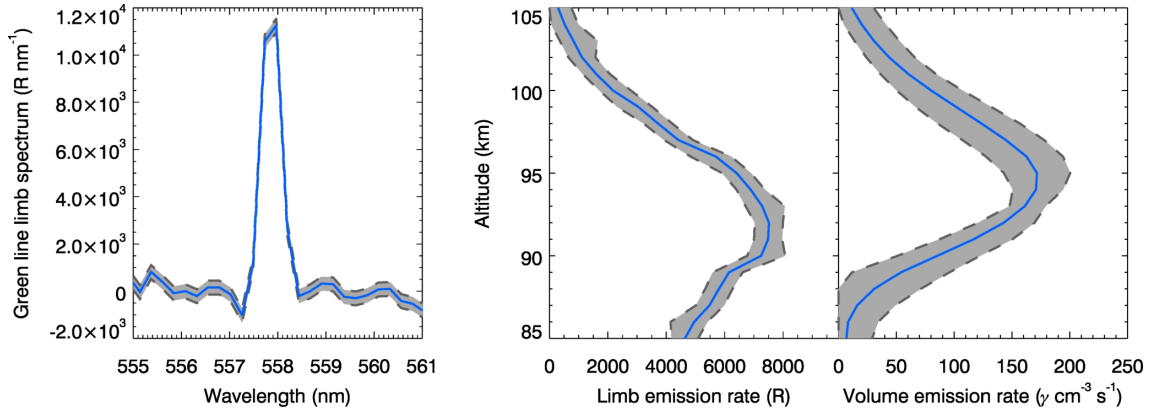


Figure 4.1.: Sample SCIAMACHY data sets of the oxygen green line emission averaged monthly for September 2010 in the latitude range 20°N . . . 25°N . The left panel shows a spectrum calculated by averaging 480 orbital spectral measurements obtained at 95 km altitude, see the blue solid line. The middle and right panels show profiles of Limb Emission Rate (LER) and Volume Emission Rate (VER) by blue solid lines. Additionally, the corresponding errors described in section 6.1 in Lednyts'kyy et al. [2015] are shown by the light gray area. The data sets shown in the figure were discussed during Talks I. . . IV mentioned in the Appendix D and in Lednyts'kyy et al. [2015] by using the right panels of their Figs. 3, 4 and 6.

The oxygen green line nightglow emission in the MLT was represented by homogeneously emitting equidistant layers of 1 km thickness chosen because the SCIAMACHY instrument viewed along LOS through similar layers of the atmosphere. To set air layers around the Earth, the model WGS84 was chosen because this model was also applied by ESA to take into account the varying curvature of the Earth along Envisat orbits [Noël et al., 2002]. Then, intersections of the air layers with the LOS of the SCIAMACHY instrument were calculated. Finally, distances between intersection points were obtained. Because both distances and LER values are characterized by uncertainties in their determination, the Regularized Total Least Squares (RTLS) minimization approach developed by Sima et al. [2004] was applied. The retrieval of each $\text{VER}\{\text{O}({}^1S - {}^1D)\}$ profile on the basis of the corresponding LER profile was carried out using the RTLS approach and the first-order linear Bayesian approach. This Bayesian approach was adopted considering the generalization for independent components of the state vector represented by a VER profile, see Rodgers [2000], page 70. This method was optimized to minimize the dependence of the obtained solution on the *a priori* data. Specifically, an *a priori* covariance matrix \mathbf{S}_a (representing uncertainties of a retrieved VER profile) was obtained on the basis of statistical properties of the correspond-

ing diagonal measurement covariance matrix S_e (representing uncertainties of a derived LER profile) according to the proposed procedure described in section 4 in Lednyts'kyy et al. [2015]. This enabled optimizing the regularized VER retrieval to make it insensitive to the *a priori* information, i.e., S_a , and to carry it out for each LER profile individually and automatically. A sample SCIAMACHY VER profile is shown in the right panel of Fig. 4.1.

The retrieval results were found to be consistent because the compared values of the synthetic LER (calculated using VER) and the original LER (employed to retrieve VER) were in good agreement with each other by sight. The retrieval results were found resembling an ideal observing system [Rodgers, 1990] because the compared shapes of derived averaging kernels and shapes of a simple peak were in good agreement with each other by sight. The described diagnostics and characteristics of the inversion procedure are also discussed in section 4.1 and Fig. 5 in Lednyts'kyy et al. [2015]. Finally, an error analysis was performed to estimate the maximum error for the retrieved VER profiles, see sections 4.3 and 6.1 in Lednyts'kyy et al. [2015] for details.

4.2. Verification of the retrieved $[O(^3P)]$ time series on the basis of input atmospheric parameters from different sources – Articles I and II

The $[O(^3P)]$ retrievals based on SCIAMACHY measurements of the oxygen green line were tested regarding their sensitivity to the input parameters, i.e., SCIAMACHY VER $\{O(^1S - ^1D)\}$, temperature, $[N_2]$ and $[O_2]$. These parameters were employed as input parameters of the well-known and extended cubic equations that resulted in six retrieved $[O(^3P)]$ data sets. The last three input parameters were obtained from three sources: NRLMSISE-00, SD-WACCM4 or SABER, see chapter 2 and section 3.1 for details. The three sources were also employed to extract the reference $[O(^3P)]$ data sets. Specifically, $[O(^3P)]$ profiles retrieved using the well-known (or extended) cubic equation on the basis of the SABER data sets were denoted $[O_{SABER}^{cubic}]$ (or $[O_{SABER}^{quench}]$), those retrieved on the basis of the NRLMSISE-00 data sets $[O_{MSIS00}^{cubic}]$ (or $[O_{MSIS00}^{quench}]$), and those retrieved on the basis of the SD-WACCM4 data sets $[O_{WACCM4}^{cubic}]$ (or $[O_{WACCM4}^{quench}]$). Reference $[O(^3P)]$ profiles extracted using NRLMSISE-00, SD-WACCM4 and SABER were denoted $[O^{MSIS00}]$, $[O^{WACCM4}]$ and $[O^{SABER}]$, respectively, and employed to compare them with the retrieved ones according to the three proposed verification steps. $[O^{MSIS00}]$ and $[O^{WACCM4}]$ were simulated for 22:00 LT, and SABER data sets were averaged in the time interval 21:00. . . 23:00 LT to obtain $[O^{SABER}]$.

Three verification methods were proposed in order to compare the retrieved and reference $[O(^3P)]$ data sets regarding their (1) profile shape, peak magnitude and

altitude values, (2) relative differences, and (3) values of cross-correlation calculated over time, see also sections 7.2, 7.3 and 7.4 in Lednyts'kyy et al. [2015]. The main idea of the proposed verification methods was to consider features of data sets obtained using the mentioned sources of the input parameters. The retrieved and reference $[O(^3P)]$ values obtained using the same data source were compared with each other, and features of the considered data source were identified. Then, the retrieved and reference $[O(^3P)]$ values obtained using the different data sources were compared with each other to identify similar or opposite features. Thus, the identified features were considered for each of the six retrieved $[O(^3P)]$ data sets.

The first verification step was based on the comparison of profiles obtained in the altitude range 85...100 km for sample profiles averaged daily and monthly in the latitude range 20°N...25°N. The left panel of Fig. 4.2 enables drawing the same conclusion as in Lednyts'kyy et al. [2015] using their Figs. 9, 10 and 11: the agreement between the reference $[O^{SABER}]$ and retrieved $[O_{SABER}^{quench}]$ profiles is significantly better than that between other profiles. The left panel of Fig. 4.2 was obtained averaging in the time interval from April 2010 to March 2011, for which SD-WACCM4 data sets were available.

The second verification step was based on the comparison of relative differences analyzed in contour plots with abscissa values in the latitude range from 50°S to 70°N and ordinate values in the altitude range 85...100 km. Absolute values of relative differences were averaged in the whole latitude range, the altitude range 86...100 km and the time interval from April 2010 to March 2011. Note that the oxygen green line emissions are negligible beside of these latitude and altitude ranges. The averaged absolute value of relative differences (AAVRD) calculated using $[O_{SABER}^{quench}]$ and $[O^{SABER}]$ was equal to ~19% – the lowest one comparing with the AAVRD calculated using other data sets. The right panel of Fig. 4.2 corresponds to the bottom right panel of Fig. 12 in Lednyts'kyy et al. [2015] illustrating relative differences between $[O_{SABER}^{quench}]$ and $[O^{SABER}]$. The results of both verification steps enabled preferring the $[O_{SABER}^{quench}]$ data set compared with the other ones. The $[O_{SABER}^{quench}]$ data set was also preferred on the basis of results obtained at the third verification step described below. Because of this, figures illustrating the results of the third verification step described below are omitted here, see Fig. 13 in Lednyts'kyy et al. [2015] for details.

The $[O(^3P)]$ data sets retrieved using the extended cubic equation on the basis of the NRLMSISE-00, SD-WACCM4 and SABER data sets were analyzed at the third verification step, see Lednyts'kyy et al. [2015] for details. Cross-correlation values calculated using $[O^{SABER}]$ and $[O_{SABER}^{quench}]$ over time were found to be higher than the other ones calculated using the $[O(^3P)]$ data sets retrieved on the basis of simulated data sets of input parameters, see Fig. 13 in Lednyts'kyy et al. [2015]. Note that the retrieved $[O_{SABER}^{quench}]$ data set was retrieved on the basis of measured input parameters provided by the SABER instrument. The SD-WACCM4 model basically represents a General Circulation Model based on the Navier-Stokes equa-

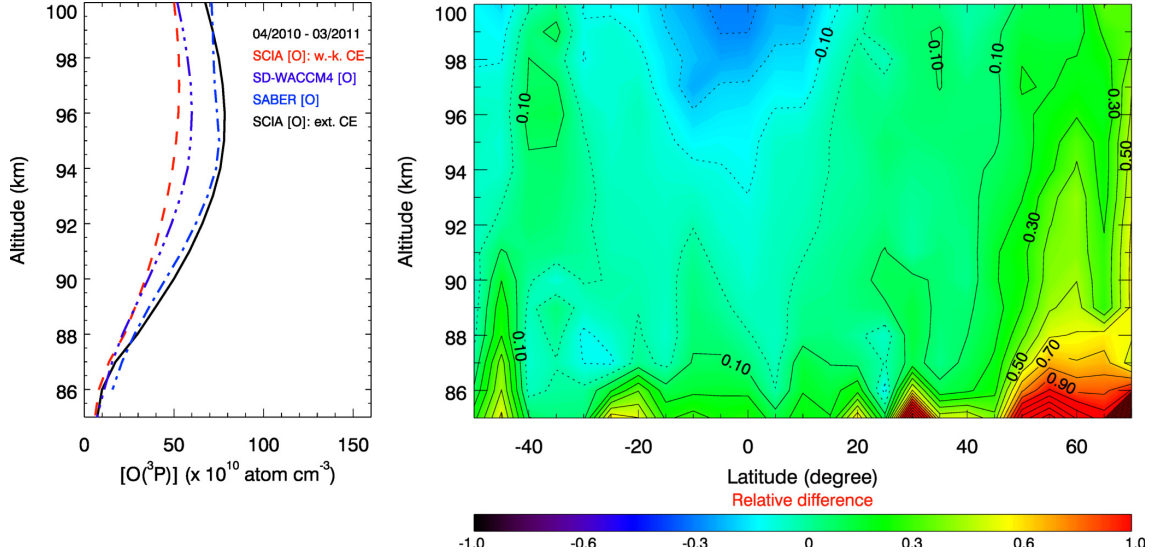


Figure 4.2.: Sample retrieved and reference $[O(^3P)]$ profiles. The left panel of the figure shows sample $[O_{SABER}^{cubic}]$ and $[O_{SABER}^{quench}]$ profiles retrieved using the well-known cubic equation (see the red dash-dotted line and w.-k. CE in the legend) and the extended cubic equation (see the black solid line and ext. CE in the legend), respectively. Additionally, the reference $[O(^3P)]$ profiles are shown being obtained using SD-WACCM4 (see the violet line shown by three dots and one long dash) and SABER (see the blue dash-dotted line). All profiles were averaged in the latitude range $20^\circ N \dots 25^\circ N$. In the right panel, relative differences between $[O_{SABER}^{quench}]$ and $[O_{SABER}^{SABER}]$ are shown. Both panels show data sets averaged in the time interval from April 2010 to March 2011. The shown relative differences were discussed during Talks II. . IV, see section D, and in Lednyts'kyy et al. [2015] by using the bottom right panel of their Fig. 12.

tions applied for conditions of a rotating sphere describing the general atmospheric circulation, whereas the NRLMSISE-00 model is a semi-empirical model based on a measurement database and analytic empirical approximations.

The retrieved $[O_{\text{SABER}}^{\text{quench}}]$ data set was also chosen to study the OH^* quenching with $O(^3P)$ and its influence on vertical shifts between Meinel $OH(\nu)$ emission bands for different vibrational levels ν . This influence was confirmed in von Savigny and Lednyts'kyy [2013] experimentally for the first time. The seasonal variability of $[O(^3P)]$ was concluded in von Savigny and Lednyts'kyy [2013] to be caused by the enhanced downward transport associated with adiabatic heating that is reflected by temperature maxima. von Savigny and Lednyts'kyy [2013] pointed out that solstice conditions and the enhanced downward motion in the MLT region at a local time of $\sim 22:00$ LT, when the SCIAMACHY measurements took place, are related to each other. This is consistent with the evidence of high values of $[O(^3P)]$, emission rates of the green line and OH^* as well as low values in OH^* emission peak altitudes observed under solstice conditions, see von Savigny and Lednyts'kyy [2013] for details.

4.3. Validation of the $[O(^3P)]$ retrievals carried out using models with not identified excited O_2 states – Articles V and VI

The main goals of this doctoral thesis were to develop algorithms and to retrieve $[O(^3P)]$ on the basis of nightglow emissions measured using the SCIAMACHY instrument because it measured multiple airglow emissions simultaneously which increases the level of the data sets' self-consistency.

First $[O(^3P)]$ retrievals were carried out for two cases of the $O(^1S)$ quenching (minimal and enhanced) implemented using the (well-known and extended) cubic equations, see Lednyts'kyy et al. [2015] as well as chapter 1 and section 3.1 in this doctoral thesis. The averaged $[O(^3P)]$ time series were applied by von Savigny and Lednyts'kyy [2013], von Savigny et al. [2015] and Lednyts'kyy et al. [2017].

In order to test calculations carried out using the MAC model, where multiple $O(^1S)$ precursors and the case of the moderate $O(^1S)$ quenching were implemented, suitable data sets were chosen to be *in situ* measurements. For instance, all data sets obtained during the WADIS-2 campaign were measured *in situ* simultaneously using devices aboard the WADIS-2 rocket which qualifies these data sets as self-consistent ones. Because data sets measured remotely are characterized by the spatial resolution represented by the corresponding limb region, see chapter 2 for details, the level of self-consistency of data sets measured remotely and simulated using models is lower than that of data sets measured *in situ* during one rocket campaign. Additionally, data sets measured remotely are usually

averaged climatologically (i.e., for several seasons of a year or several years to reduce the seasonal bias) that decreases the level of self-consistency of the averaged data sets.

As soon as appropriate *in situ* measurements were found, retrievals carried out on the basis of $\text{VER}\{\text{O}(^1S - ^1D)\}$ profiles using the well-known cubic equation of McDade et al. [1986] and the extended cubic equation of Lednyts'kyi et al. [2015], see section 3.1 for details, were tested for their validity. Specifically, the $[\text{O}(^3P)]$ profiles retrieved on the basis of NRLMSISE-00 (or SABER) atmospheric parameters were compared with the *in situ* $[\text{O}(^3P)]$ profiles for the ETON (or WAVE2004) campaign, see the left (or right) panel in Fig. 4.3. Additionally, the well-known quadratic equation of McDade et al. [1986] mentioned in section 3.1 was applied on the basis of $\text{VER}\{\text{O}_2(b - X)\}$ profiles to retrieve $[\text{O}(^3P)]$ profiles also shown in this figure. The comparison carried out for each panel in Fig. 4.3 indicates good overall agreement between realistic concentration values, their profile shapes were well reproduced. Specifically, there are systematic and expected differences between the $[\text{O}(^3P)]$ profiles retrieved using both well-known equations of McDade et al. [1986] and those retrieved using the extended cubic equation of Lednyts'kyi et al. [2015]. Note that the *in situ* $[\text{O}(^3P)]$ profile considered for each rocket campaign is almost equidistant from the extremes represented by two $[\text{O}(^3P)]$ profiles retrieved using both the well-known and extended cubic equations. Because the well-known cubic equation was employed to study the minimal $\text{O}(^1S)$ quenching, and the extended cubic equations was employed to study the enhanced $\text{O}(^1S)$ quenching, both retrieved $[\text{O}(^3P)]$ profiles were used to obtain the arithmetically averaged $[\text{O}(^3P)]$ profile. As the result, the *in situ* $[\text{O}(^3P)]$ profile agreed well with the arithmetically averaged $[\text{O}(^3P)]$ profile considered for each rocket campaign.

Because the empirical coefficients employed in the quadratic and cubic equations were introduced by McDade et al. [1986] phenomenologically (to represent ratios of a limited number of unknown reaction rates, see section 3.1), further investigations were planned to avoid using ratios of unknown reaction rates. These investigations resulted in the MAC model.

4.4. Sensitivity of $\text{O}(^3P)$ to the solar activity forcing – Article IV

Space weather refers to conditions in the Earth's space environment above the Kármán line at 100 km, whereas weather and climate refer to conditions below the Kármán line. The Sun, being a huge thermonuclear reactor, is the principal driver of space weather because it emits electromagnetic waves in the range from X-rays to radio waves, a hot plasma stream (referred to as solar wind) and violent solar flares etc. [Dudok de Wit and Watermann, 2010]. Solar Energetic Particle (SEP) events are associated with sporadic solar wind structures, see the list

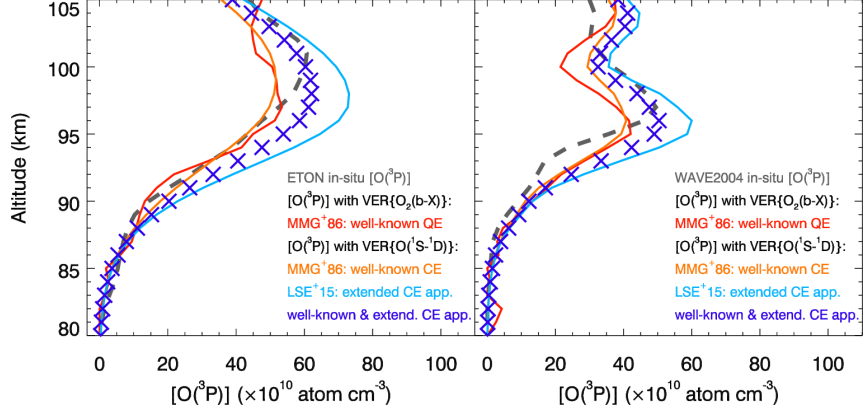


Figure 4.3.: The *in situ* and retrieved $[O(^3P)]$ profiles are compared with each other to test the carried out calculations for their validity. The $[O(^3P)]$ profiles for the ETON campaign are shown in the left panel and those for the WAVE2004 campaign are shown in the right panel. The *in situ* $[O(^3P)]$ profiles are shown by dashed gray lines. The $[O(^3P)]$ profiles retrieved using the well-known quadratic (QE) and cubic (CE) equations of McDade et al. [1986] (MMG⁺86) are shown by the solid red and orange lines, respectively. The well-known QE was applied on the basis of VER profiles representing emissions in the Atmospheric band that is denoted by $VER\{O_2(b-X)\}$. The extended CE was applied using the empirical coefficients adjusted by Lednyts'kyy et al. [2015] (LSE⁺15) and solved using the method of Semenov [1997] to retrieve the $[O(^3P)]$ profiles shown by solid cyan lines. Both CEs were applied on the basis of VER profiles representing the oxygen green line emissions that is denoted by $VER\{O(^1S - ^1D)\}$. The *in situ* $[O(^3P)]$ profile values were found to be equidistant from the retrieved CE $[O(^3P)]$ profile values for both campaigns, and the retrieved profile values were averaged arithmetically (see violet crosses) to compare them with the *in situ* profile values. The profiles shown in the figure were discussed during Talks VIII and IX, see section D, and in Lednyts'kyy and von Savigny [2019] by using their Fig. 4 and in Lednyts'kyy et al. [2019] by using their Fig. 10.

of solar proton events presented on <http://umbra.nascom.nasa.gov/SEP/>. Proton flux events with proton energies of more than 2500 MeV shown in this list correspond to bad quality data found using the SCIAMACHY quality and data anomaly reports, see section 4.1. These bad quality data were excluded from the further processing of the SCIAMACHY green line emission spectra. It follows that the analyzed SCIAMACHY data sets (see chapter 2) employed to retrieve $\text{VER}\{\text{O}(^1S - ^1D)\}$ and $[\text{O}(^3P)]$ time series (see sections 3.1, 4.2 and 4.3 for details) exclude the influence of the proton flux events of more than ~ 2500 MeV.

Solar activity is mainly characterized by major periodic variations of the magnetic field of the Sun. Processes in the Sun's interior and surface result in the periodical nature of the solar activity cycles, coupling effects in the interplanetary space controlled by the Sun, and modulation of the galactic cosmic ray flux by the solar wind structures [Krivolutsky and Repnev, 2012].

Dominant periodicities in solar spectral irradiance are represented by the 11-year and the 27-day solar cycles [Dudok de Wit and Watermann, 2010]. The period of the 11-year solar cycle may range from 9 to 14 years [Kane, 2002]. The sign of the polarity of the Sun's internal magnetic field changes every ~ 11 years [McIntosh et al., 2015, 2014]. The Sun's equator surface rotates faster than near the polar caps, and the value of the Sun's rotational period varies in the time range from ~ 24 to ~ 35 days depending on heliographical latitude. The quasi-27-day and the quasi-13-day solar cycles are characterized by corresponding amplitudes and phases, values of which change with time because evolving and growing active regions of the Sun are superimposed with the Sun's rotational period [Lean, 1987]. Note that two activity band regions on opposite sides of the Sun (with respect to the Sun's rotational axis) may result in the quasi-13-day solar cycle [Lean, 1987].

The response of the retrieved SCIAMACHY $[\text{O}(^3P)]$ time series to solar forcing represented by the 11-year and the 27-day solar activity cycles was quantified applying linear regression analysis techniques and the superposed epoch analysis (SEA [Chree, 1913] also referred to as composite analysis) and published in Lednyts'kyy et al. [2017]. Unfortunately, only a limited number of publications regarding observed data is available on this topic. For instance, Kaufmann et al. [2014], Russell et al. [2004], Zhu et al. [2015] and Lednyts'kyy et al. [2015] described signatures of the 11-year solar cycle identified in $[\text{O}(^3P)]$ time series retrieved on the basis of emissions measured remotely using satellites-borne instruments. The influence of solar activity on $\text{O}(^3P)$ was studied previously using chemistry-climate models simulating the 11-year cycle, see, e.g., Schmidt et al. [2006] and Marsh et al. [2007], and the 27-day cycle, see, e.g., Gruzdev et al. [2009].

The $[\text{O}(^3P)]$ time series retrieved using the well-known and extended cubic equations denoted $[\text{O}_{\text{SABER}}^{\text{cubic}}]$ and $[\text{O}_{\text{SABER}}^{\text{quench}}]$, respectively, see section 4.2 for details, were employed to obtain the corresponding $[\text{O}(^3P)]$ anomaly time series. The anomaly time series were determined in two steps: removing a 35-day running mean

from the original time series, and smoothing the resulting time series with a 7-day running mean. This technique is equivalent to the band-pass filtering with the boxcar lengths equal to 7 and 35 days, chosen to suppress variations at the time scales shorter than 7 days and longer than 35 days, see Lednyts'kyy et al. [2017] for details. The solar forcing was represented by such solar proxies as the Mg II index, the Lyman- α irradiance and the F10.7 cm radio flux. The Lyman- α line of atomic hydrogen at 121.6 nm is the brightest emission line in the wavelength range 30. . . 200 nm [Dudok de Wit et al., 2008]. Lyman- α radiation is absorbed by O₂ in the mesosphere and in the upper atmospheric layers [Brasseur and Solomon, 2005]. The irradiance in the Middle-UltraViolet region (MUV, 200. . . 300 nm) is absorbed by O₂ and O₃, mainly in the Hartley band in the stratosphere [Dudok de Wit et al., 2009]. The Mg II index is determined on the basis of the selected Mg⁺ Fraunhofer lines [Snow et al., 2014] in the MUV region. The decimetric radio flux F10.7 emitted at 10.7 cm or 2800 MHz is a proxy indicator of solar activity used most widely in climate modeling because it has been observed daily since 1947. Although long time series of F10.7 are easy to measure from the Earth surface, this indicator of solar radiation does not have a direct impact on climate [Dudok de Wit and Watermann, 2010].

The sensitivity of the nine year SCIAMACHY [O(³P)] anomaly time series to solar forcing was estimated using anomalies averaged yearly ([O^a]), monthly ([O^m]) and daily ([O^d]), respectively. [O^a] and [O^m] distorted by some gaps in SCIAMACHY data sets (see section 3.2 in Lednyts'kyy et al. [2017] for details) were analyzed in the time range from 1 January 2003 to 31 December 2011 using the linear regression analysis and the multiple-linear regression analysis techniques, see the left and right panels in Fig. 4.4, respectively.

In order to determine the linear long-term trend (*LT*), solar variations, quasi-biennial oscillations (*QBO*) and seasonal (annual, *AO*, and semi-annual, *SAO*) oscillations in the [O^m] time series, a multi-linear regression analysis was carried out. The multiple-linear regression fit equation includes elementary trigonometric functions considered in the time (*t*) dependent model (*FIT(t)*) used to identify and quantify oscillation effects in [O^m] obtained in altitude ranges 88. . . 90, 91. . . 93, 94. . . 96, 97. . . 99 and 100. . . 102 km. The fit equation, also referred to as harmonic fit in the right panel in Fig. 4.4, is as follows:

$$FIT(t) = Offset + LT^{Amp} \cdot t + MgII^{Amp} \cdot MgII(t + MgII^{Pha}) + QBO + ASO, \quad (4.1)$$

where *ASO* is represented by *AO* and *SAO* oscillations, and the solar parameters (either the monthly averaged proxy time series of MgII index or those of Lyman- α) indicate variability of solar activity with respect to a mean value represented by an offset term (*Offset*). The solar parameters describing the [O(³P)] response to solar forcing are characterized by values of amplitude (*MgII^{Amp}*) and phase shift (*MgII^{Pha}*) of the considered proxy time series (MgII index chosen here for brevity) with respect to [O^m]. The quasi-biennial oscillations are represented by two components indicated by lower indices 1 and 2 as follows: *QBO* = *QBO*₁^{*Amp*}.

$\cos\left(\frac{2\pi t}{QBO_1^{Per}} + QBO_1^{Pha}\right) + QBO_2^{Amp} \cdot \cos\left(\frac{2\pi t}{QBO_2^{Per}} + QBO_2^{Pha}\right)$, where QBO^{Per} denote periods and QBO^{Pha} denotes phases shift of cosine functions, and QBO^{Amp} denote amplitudes. The other (AO and SAO) oscillations considered in $[O^m]$ are $ASO = AO^{Amp} \cdot \cos\left(\frac{2\pi t}{AO^{Per}} + AO^{Pha}\right) + SAO^{Amp} \cdot \cos\left(\frac{2\pi t}{SAO^{Per}} + SAO^{Pha}\right)$, where AO (or SAO) are characterized by values of amplitude AO^{Amp} (or SAO^{Amp}), cosine functions with values of period AO^{Per} (or SAO^{Per}) and phase shift AO^{Pha} (or SAO^{Pha}). Amplitudes are given in atom cm^{-3} and those of period and phase – in month.

The multiple-linear regression analysis technique was proposed and accurately applied on the monthly averaged time series within two runs in a sequence of five steps in order to determine optimal values of the fitting parameters at each step. The $FIT(t)$ model was run using the Interactive Data Language (IDL) routine MPFIT found at <http://cow.physics.wisc.edu/~craigm/idl/idl.html> which is based on the Levenberg-Marquardt algorithm [Markwardt, 2009]. The first run was performed in five steps to determine optimal values of the fitting parameters used as initial values in the second run. During the first run, the band-pass filtering technique was applied to the $[O^m]$ time series in a similar way as was done to obtain the $[O(^3P)]$ anomaly time series, see in this section above, but using different boxcar length values. Additionally, the input parameter values were set during the first run to be equal to the *a priori* values according to the description provided in section 4.4 in Lednyts'kyy et al. [2017]. The main purpose of calculations carried out at each step was to determine optimal values of the corresponding fitting parameters. The fit Eq. (4.1) was applied sequentially to limit the number of fitted parameters in order to minimize the degree of freedom in calculations because the fit was found to be instable if all unknown values of the input parameters were fitted simultaneously. The optimal values of the corresponding fitting parameters were chosen from the range of possible values at each step to speed up calculations.

The sensitivity of $[O^m]$ to solar forcing of the 11-year cycle in units of $0.01 \cdot \text{MgII}$ index was estimated for different altitude intervals dividing $MgII^{Amp}$ by the corresponding averaged $[O^m]$ values, see the right panel in Fig. 4.4 for details. The $[O^m]$ time series was employed as an example of a long anomaly time series to estimate the solar parameter $MgII^{Amp}$, the mean value represented by *Offset* and the linear long-term trend *LT*. This enabled assuming that the solar parameter $MgII^{Amp}$ was not biased, and the sensitivity of $[O^m]$ to solar forcing was determined using the fit Eq. (4.1) correctly. To test the correctness of the $[O^m]$ sensitivity to solar forcing, the sensitivity of $[O^a]$ to solar forcing of the 11-year cycle was estimated using the standard technique of linear regression analysis also referred to as regression in the left panel in Fig. 4.4. This was also done for Lyman- α in units of $\text{photon cm}^{-2} \text{s}^{-1}$. The obtained sensitivities were converted to those in units of 100 sfu using the linear ordinary least squares bisector regression [Isobe et al., 1990] to take uncertainties in both pairs of proxy time series into account simultaneously. Note that 1 sfu (solar flux unit) corresponds to $10^{-22} \text{ W m}^{-2} \text{ Hz}^{-1}$ and is the unit of the irradiance at 10.7 cm [Tapping, 2013]. Finally, sensitivity

values in all mentioned altitude ranges were converted to relative differences in $[O^m]$ (or $[O^a]$) between the maximum and minimum phases of the 11-year cycle of solar activity, see Fig. 4.4 and the first two rows in Tables 1 and 2 in Lednyts'kyy et al. [2017].

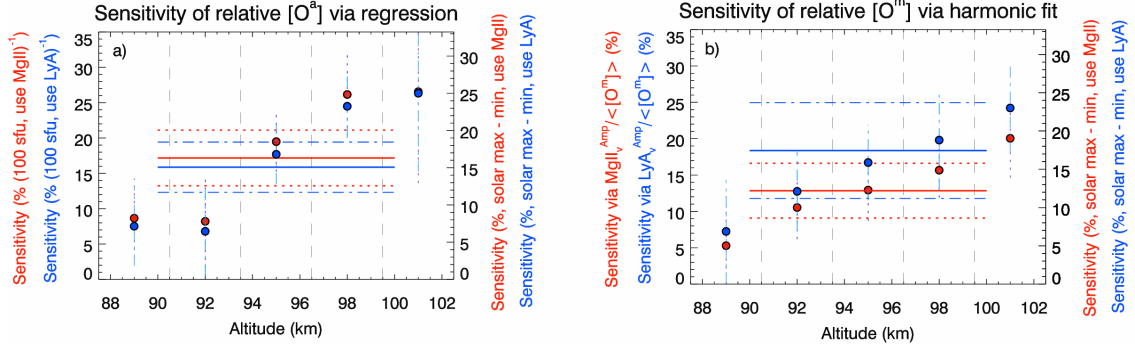


Figure 4.4.: Sensitivities of annually ($[O^a]$) and monthly ($[O^m]$) averaged $O(^3P)$ to the 11-year cycle solar forcing determined using the linear regression technique and the multiple-linear regression technique – also referred to as harmonic fit Eq. (4.1) – are shown in the left and right panels, respectively. The nine year time series of $[O^a]$ and $[O^m]$ were retrieved using the well-known cubic equation of McDade et al. [1986] with the adjusted values of empirical coefficients. $[O^a]$ and $[O^m]$ analyzed in the five indicated altitude ranges are shown by colored circles, while those ones obtained for the altitude range 90. . .100 km are shown by colored solid lines. The dashed colored horizontal lines represent the 68% confidence level of the obtained sensitivity values. Colors of circles and lines denote the proxy indicator of solar activity used to determine sensitivity values as follows: red color denotes the MgII index time series, and blue color denotes the Lyman- α time series. Ordinates on the left side of the panels show the $[O(^3P)]$ sensitivity values used to estimate the $[O(^3P)]$ relative percentage changes. Ordinates on the right side of the panels show the estimated $[O(^3P)]$ relative percentage changes between phases of the solar maximum and minimum. The corresponding numerical values of the $[O^a]$ and $[O^m]$ sensitivity to solar forcing are shown in Table 1 in Lednyts'kyy et al. [2017]. The figure was discussed during Talk III, see section D, and in Lednyts'kyy et al. [2017] by using their Fig. 9.

The $[O(^3P)]$ sensitivity to the 11-year solar forcing estimated using both analysis techniques was found to be strongly dependent on altitude values: $\sim 5\%$ at ~ 90 km and $\sim 25\%$ at ~ 100 km. The sensitivities estimated for Lyman- α were found to be higher than those estimated for MgII index, but they agree well with each other within their uncertainties. It is difficult to draw a conclusion why the Lyman- α sensitivities were found to be systematically higher than the MgII index sensitivities due to a lack of data. This may be related to a more dominant influence of solar irradiance represented by Lyman- α at 121.6 nm on $O(^3P)$ increasing

with rising altitude values than that one of MgII index at ~ 285 nm. This is consistent with the downward transport of $O(^3P)$ [Colegrove et al., 1965] from the thermosphere to the studied altitudes in the MLT. Although there is a difference of $\sim 30\%$ between values of $[O_{SABER}^{\text{quench}}]$ and $[O_{SABER}^{\text{cubic}}]$, sensitivity values were found to be in good agreement with each other within their uncertainties. The determined sensitivity values agree with the sensitivity values discussed in known experimental [Kaufmann et al., 2014, Zhu et al., 2015] and model [Marsh et al., 2007, Schmidt et al., 2006] studies.

The standard techniques of cross-correlation and SEA analysis applied to $[O(^3P)]$ anomaly time series on the day-to-day scale ($[O^d]$) enabled the identification of a statistically significant solar 27-day signature in $[O(^3P)]$ with a relative amplitude of $\sim 1\%$. The time lag of the signature is about 10. . . 12 days, i.e., the maximal $[O(^3P)]$ response occurs about 10. . . 12 days after the peak of the 27-day solar forcing. The $[O^d]$ sensitivity to the 27-day solar forcing was identified in the MLT region on the basis of experimental data sets for the first time, and it is in good agreement with the simulation results obtained by Gruzdev et al. [2009] using the HaMburg Model of the Neutral and Ionized Atmosphere (HAMMONIA). Note that the found time lag is a quarter of the 27-day cycle larger in comparison to the known model results [Gruzdev et al., 2009]. This discrepancy can not be explained by dynamical or photochemical contributions alone as proposed by Thomas et al. [2015] in terms of the 27-day signatures in a number of atmospheric parameters in the polar summer mesopause. It can be assumed that a pure photochemical mechanism was effectively implemented in HAMMONIA. Taking this assumption into account enables assuming that an additional time lag equal to a quarter of the 27-day cycle might be required due to the downward transport of $O(^3P)$ from the lower thermosphere, where most of $O(^3P)$ is produced photochemically according to Colegrove et al. [1965]. It should be noted that SCIAMACHY observations were carried out from a sun-synchronous orbit at $\sim 22:00$ LT, and the studied $[O(^3P)]$ anomaly time series were obtained in the latitude range $0^\circ \dots 20^\circ$ N, where diurnal tides dominate comparing to eddy diffusion. It is assumed that dynamical contributions to SCIAMACHY VER $\{O(^1S - ^1D)\}$ time series used to retrieve the $[O(^3P)]$ time series are aliased by tides because of SCIAMACHY's sun-synchronous sampling. Section 4.6 in Lednyts'kyy et al. [2017] provides details focusing on other possible sources of the mentioned time shift in the $[O(^3P)]$ response to the solar forcing.

The standard techniques of spectral analysis methods were applied in the frequency and time domains, i.e., the generalized Lomb-Scargle (GLS) [Zechmeister and Kürster, 2009] and the wavelet analysis [Torrence and Webster, 1999] techniques, respectively. Peaks in the GLS spectrum were found to be corresponding to the period value of ~ 27 days and the other close to it periods. This might imply that atmospheric waves possibly causing the 27-day variations in vertical advection due to semidiurnal tide modulations might alter the 27-day solar signature in $[O(^3P)]$ [Angelats i Coll and Forbes, 1998, Burrage et al., 1996, Liu et al., 2008, Ward, 1999]. Oscillations with periods of 25. . . 29 days (or 23. . . 32 days) might

be caused by nonlinear interactions between annual (or semiannual) and 27-day variations [Luo et al., 2001, Pancheva et al., 2003]. Note that the atmospheric response to solar forcing is not homogeneous, neither in horizontal nor in vertical direction, and solar induced regional $O(^3P)$ anomalies may disappear by transport [Lee et al., 2013].

Comparing sensitivities of $[O(^3P)]$ to the 11-year and 27-day solar forcing, it becomes evident that the corresponding sensitivity values agree well with each other within their uncertainties during the descending phase of the last (23rd) 11-year cycle of solar activity. Values of the 27-day sensitivity estimated in $[O(^3P)]$ on the day-to-day scale for the solar minimum phase are low that might result from a lower absorption of the extreme ultraviolet photons in the Earth's thermosphere, which is expected to be cooler (and, therefore, lower in density) than it had ever been, according to Solomon et al. [2010], since the beginning of the space age as satellite-borne measurements started.

4.5. Sensitivity of $O(^3P)$ to the lunar gravitational forcing – Article III

The Earth's atmosphere is affected by the gravitational forces of the Earth, the Moon, the Sun and other celestial bodies. These forces are considered, whereas internal forces (vertical convection, mass and heat transfer, etc.) and electromagnetic forces (between the geomagnetic and interplanetary magnetic fields, etc.) are neglected in the tide-generating theories [Chapman and Lindzen, 1970, Sidorenkov, 2009]. Additionally, planets of the solar system interfere with the solar activity [Scafetta and Willson, 2013]. The Moon is the nearest celestial body for the Earth with a higher gravitational influence than that of the planets. The Full Moon occurs in the middle of the 27.322 day sidereal lunar month and at the middle of the 29.531 day synodic lunar month. During a sidereal lunar month, one rotation of the Earth's center of gravity occurs around the mass center of the Earth-Moon system. The following relationship between the local lunar time (τ), the local solar time (t) and the lunar phase angle (ν):

$$\tau = t - \nu \quad (4.2)$$

was applied by von Savigny et al. [2015] and illustrated using their Fig. 1 for the fixed local solar time of SCIAMACHY measurements, i.e., $t \approx 22:00$ LT. Values of lunar phase angle ν were determined using the HORIZONS system provided by the JPL at <http://ssd.jpl.nasa.gov/horizons.cgi> as the angle between the vector from the Sun's center to the test point and the vector from the test point to the Moon. The fixed value of $t \approx 22:00$ LT and the local lunar time τ were considered as input parameters in the HORIZONS system employed to calculate ν values. Equation (4.2) was applied by von Savigny et al. [2015] for different values of the local lunar time τ on the basis of known ν values of the lunar phase angle and $t \approx 22:00$ LT. Specifically, the nine year data sets of the lunar

phase angle, the SCIAMACHY $\text{VER}\{\text{O}(^1S - ^1D)\}$ and $[\text{O}(^3P)]$ ($[\text{O}_{\text{SABER}}^{\text{quench}}]$) were retrieved working on this doctoral thesis to estimate their response in the MLT to the Moon's gravitational force. Note that the SCIAMACHY $[\text{O}_{\text{SABER}}^{\text{quench}}]$ data sets was retrieved according to the extended cubic equation on the basis of the SABER data sets.

The SEA technique was applied by averaging the $[\text{O}(^3P)]$ and other mentioned anomaly time series, see von Savigny et al. [2015] for details. The statistically significant tidal signature in the $[\text{O}(^3P)]$ anomaly time series was found with relative amplitudes of $\sim 1.3\%$ in the MLT region ~ 10.3 hours after the peak in lunar gravitational forcing. The signature of the $[\text{O}(^3P)]$ response to lunar gravitational forcing is comparable with the signature of the $[\text{O}(^3P)]$ response to the solar 27-day forcing characterized by the relative amplitude of $\sim 1\%$ with respect to solar forcing. Additionally, the Global Scale Wave Model (GSWM) was used in this study for necessary simulations (e.g., of the vertical winds) to reproduce OH(3-1) rotational temperature in the MLT [Forbes et al., 2013] and to validate the tidal signature detected in SCIAMACHY OH(3-1) rotational temperature [von Savigny et al., 2012b]. Clear and significant semi-diurnal lunar tidal signatures with relative amplitudes of a few percent and phases (also referred to as time lags) of about 11 lunar hours are in good agreement with each other, and the observed signatures were found to be driven by vertical motions of air. The simulation results concerning downward motions of air indicated the downward transport of $\text{O}(^3P)$ that led to increasing values of $\text{VER}\{\text{O}(^1S - ^1D)\}$ and OH(3-1) VER. The phase relationship between GSWM vertical winds and SCIAMACHY OH(3-1) rotational temperatures enabled suggesting that downward shift in the observed OH* emission altitude led to a presumably adiabatic heating during downward motions and to increasing values of OH(3-1) rotational temperature. Note that von Savigny et al. [2015] detected statistically significant lunar semidiurnal tidal signatures in airglow and other time series in the MLT experimentally for the first time.

4.6. Validation of the $[\text{O}(^3P)]$ retrievals carried out using the proposed Multiple Airglow Chemistry model – Articles V and VI

The MAC model was accurately applied to retrieve concentrations of chemical species and to evaluate VER profiles used to retrieve concentrations. All relevant photochemical reactions of the MAC model and a corresponding VER profile were considered to retrieve concentrations, whereas the VER profile only was divided by the corresponding transition probability to evaluate concentrations. To evaluate a VER profile, retrieved concentrations were multiplied by the corresponding transition probability, see Appendix A in

Lednyts'kyy and von Savigny [2019] for details. The employed *in situ* VER profiles were denoted retrieved VER profiles, they were compared with evaluated VER profiles. Additionally, retrieved and evaluated concentration values were also compared with each other to verify the MAC calculations. The employed profiles of VER and atmospheric parameters – e.g. atmospheric density required to calculate $[N_2]$ and $[O_2]$ as well as temperature – are characterized by different levels of the data sets' self-consistency. For instance, all mentioned profiles measured *in situ* simultaneously using devices aboard one sounding rocket during the WADIS-2 rocket campaign were described in chapter 2. These profiles are considered to be self-consistent which enabled Grygalashvily et al. [2019] to propose a photochemical model based on derived reaction rates.

The following VER profiles were employed to test MAC calculations carried out using reactions involving the corresponding O and O_2 states: (1) $VER\{O_2(b - X)\}$ obtained *in situ* during the WADIS-2 rocket campaign were employed to test MAC reactions involving $O_2(^5\Pi, c, b, X)$, (2) $VER\{O(^1S - ^1D)\}$, $VER\{O_2(b - X)\}$ and $VER\{O_2(a - X)\}$ obtained *in situ* and remotely during the WAVE2004 rocket campaign were employed to test MAC reactions involving $O(^1S, ^1D, ^3P)$ and $O_2(^5\Pi, c, b, a, X)$, (3) $VER\{O_2(b - X)\}$ obtained *in situ* during the WAVE2000 rocket campaign were employed to test MAC reactions involving $O_2(^5\Pi, c, b, X)$, (4) $VER\{O(^1S - ^1D)\}$, $VER\{O_2(A - X)\}$, $VER\{O_2(A' - a)\}$, $VER\{O_2(b - X)\}$ and $VER\{O_2(a - X)\}$ obtained *in situ* during the ETON campaign were employed to test MAC reactions involving $O(^1S, ^1D, ^3P)$ and $O_2(^5\Pi, A, A', c, b, a, X)$. Together with profiles of atmospheric parameters (temperature, $[N_2]$ and $[O_2]$), the above list represents the employed profiles shown with the nearly decreasing level of the data sets' self-consistency because profiles of atmospheric parameters were obtained for the corresponding campaigns as follows: (1) *in situ*, (2) remotely, (3) obtained remotely and simulated, and (4) simulated.

As mentioned at the end of section 3.2, there were three modifications of the MAC model tested for their validity on the basis of $[O(^3P)]$ profiles obtained *in situ* during the following campaigns: (1) the ETON campaign employed to test MAC reactions involving or excluding $O_2(A)$ and $O_2(A')$ in the case of excluding O_3 , H, CO_2 , OH^* and HO_2 , (2) the WAVE2004 campaign employed to test MAC reactions involving or excluding O_3 , H, CO_2 , OH^* and HO_2 in the case of excluding $O_2(A)$ and $O_2(A')$, and (3) the WAVE2000 and WADIS-2 campaigns employed to test MAC reactions involving only $O_2(c, b)$ and $O_2(X)$.

The first modification of the MAC model was implemented to derive rate values of the unknown and poorly constrained reactions on the basis of the multiple VER profiles obtained for the ETON rocket campaign. Values of temperature, $[N_2]$ and $[O_2]$ were obtained using the NRLMSISE-00 model. Calculations were carried out with the MAC model excluding O_3 , H, CO_2 , OH^* and HO_2 for two cases regarding O_2 states as follows: (1) involving $O_2(A)$ and $O_2(A')$, see Fig. 4.5, and (2) excluding $O_2(A)$ and $O_2(A')$ (i.e., setting $VER\{O_2(A - X)\}$ and $VER\{O_2(a - X)\}$ values to zero), see Fig. 5 in Lednyts'kyy and von Savigny [2019].

For the two cases of the first modification of the MAC model, the *in situ* (referred to as retrieved) VER profiles and the evaluated VER profiles are shown in the left panel of Fig. 4.5, see also the left panel of Fig. 5 in Lednyts'kyy and von Savigny [2019]. The retrieved and evaluated VER profiles are in good agreement with each other by sight. Next, the retrieved and evaluated concentration profiles obtained on the basis of respective VER profiles at various MAC retrieval steps and shown in the middle panels in these figures were also compared with each other. The retrieved and evaluated concentration profiles are also in good agreement with each other by sight.

The *in situ* and retrieved $[O(^3P)]$ profiles shown in the right panels in these figures are also in good agreement with each other by sight which validates the MAC calculations. The $[O(^3P)]$ profiles were retrieved at steps 2.1, 2.2, 2.3, 3.2, 4.1 and 5.1 using the MAC model. Because the $[O(^3P)]$ profiles retrieved involving $O_2(A)$ and $O_2(A')$ and shown in Fig. 4.5 are in good agreement with those retrieved excluding $O_2(A)$ and $O_2(A')$ and shown in Fig. 5 in Lednyts'kyy and von Savigny [2019], it was concluded that the contribution of processes involving $O_2(A)$ and $O_2(A')$ can be neglected. Note that $O_2(^5\Pi)$ and the Herzberg states were tested in the MAC model to be the $O(^1S)$ precursors as suggested by Krasnopolsky [2011] as well as Stott and Thrush [1989] and Steadman and Thrush [1994]. Because of the minor contribution of $O_2(A)$ and $O_2(A')$ to the $O(^1S)$ production, $O_2(c)$ can be considered to be the major $O(^1S)$ precursor responsible for the green line emission which was backed up by Bates [1988b], Greer et al. [1981], Hickey et al. [1997], Krasnopolsky [1981], Llewellyn et al. [1980], Snively et al. [2010], Solheim and Llewellyn [1979] and Huang and George [2014].

The second modification of the MAC model was implemented to test the MAC calculations on the basis of the multiple VER profiles obtained for the ETON and WAVE2004 campaigns. Values of temperature, $[N_2]$ and $[O_2]$ were obtained as follows: simulated using the NRLMSISE-00 model for the ETON campaign, and calculated using the SABER instrument for the WAVE2004 campaign. Values of $[O_3]$, $[H]$, $[CO_2]$ (and those of the retrieved $[OH^*]$ and $[HO_2]$) were neglected for the ETON campaign, but calculated on the basis of data sets obtained during the WAVE2004 campaign and using the SABER instrument. This enabled carrying out calculations with the MAC model for the WAVE2004 campaign excluding $O_2(A)$ and $O_2(A')$ for two cases regarding SABER species as follows: (1) involving O_3 , H , CO_2 , $O(^1D)$, OH^* and HO_2 , see Fig. 4.6, and (2) excluding O_3 , H , CO_2 , $O(^1D)$, OH^* and HO_2 , i.e., setting their concentration values to zero, see Fig. 11 in Lednyts'kyy et al. [2019]. Note that for the WAVE2004 campaign, $[OH]$ and $[HO_2]$ were retrieved on the basis of $[O(^3P)]$, $[CO_2]$, $[H]$ and $[O_3]$ as a part of the prior retrieval procedure, see Fig. 3.3 for details.

The retrieved and evaluated VER profiles shown in the left panel in Fig. 4.6 for the first case – involving O_3 , H , CO_2 , $O(^1D)$, OH^* and HO_2 , but excluding $O_2(A)$ and $O_2(A')$ – are in good agreement with each other by sight for the WAVE2004 campaign. This is also the case for the concentration profiles retrieved and evaluated for the first case and shown in the middle panel in this figure, and the performed

calculations were concluded to be verified. The *in situ* and retrieved $[O(^3P)]$ profiles shown in the right panel in the figure are also in good agreement with each other by sight validating the MAC calculations for the first case. Because the $[O(^3P)]$ profiles retrieved for the first case involving OH and HO₂, see Fig. 4.6, are in good agreement with those retrieved for the second case excluding OH and HO₂, see Fig. 11 in Lednyts'kyy and von Savigny [2019], it can be concluded that the contribution of processes involving OH and HO₂ can be neglected. Note that values of the $[O(^3P)]$ profiles retrieved on the basis of $VER\{O_2(b - X)\}$ profiles and shown in the right panels in Figs. 4.5 and 4.6 are almost equal to those retrieved on the basis of VER profiles employed at different steps.

The third modification of the MAC model was implemented to verify the MAC calculations and to test them for validity on the basis of the $VER\{O_2(b - X)\}$ profile obtained *in situ* for the WADIS-2 and WAVE2000 campaigns. For the WADIS-2 campaign, values of temperature, $[N_2]$ and $[O_2]$ were obtained *in situ*. For the WAVE2000 campaign, values of $[N_2]$ and $[O_2]$ were simulated using the NRLMSISE-00 model, and values of temperature were either simulated using the NRLMSISE-00 model or obtained remotely using the MU RADAR [Murayama et al., 2001]. Calculations were carried out with the MAC model involving only $O_2(c, b)$ and $O_2(X)$.

Calculations carried out for the WADIS-2 campaign on the basis of $VER\{O_2(b - X)\}$ profiles were shown in Fig. 4.7 as follows: (1) with 3 km vertical sampling to show the $[O(^3P)]$ profiles retrieved using the MAC model and the model of Grygalashvyly et al. [2019], and (2) with 1 km vertical sampling to show the $[O(^3P)]$ profiles retrieved only using the MAC model. Note that the 3 km vertical sampling was chosen by Grygalashvyly et al. [2019] to show the obtained profiles of $[O(^3P)]$ and $VER\{O_2(b - X)\}$ in their Figs. 4 and 5, presumably, because of the 3 km vertical sampling of the $VER\{O_2(b - X)\}$ profile shown in their Fig. 1. Because the $[O(^3P)]$ profiles retrieved using both models are very similar, they were compared with the *in situ* $[O(^3P)]$ profile which indicates very similar results and supports the MAC calculations. It follows from comparisons during the verification procedure using Fig. 4.5 for the ETON campaign, Fig. 4.6 for the WAVE2004 campaign, Fig. 4.7 for the WADIS-2 campaign and Figs. 7 and 8 in Lednyts'kyy et al. [2019] for the WAVE2000 campaign that the results of calculations carried out with the MAC model are consistent with each other and coherent with measured values.

The influence of variability in such MAC model input parameters as VER, temperature and atmospheric density on the retrieved $[O(^3P)]$ profiles was studied for the ETON and WAVE2004 campaigns on the basis of multiple emissions measured during these campaigns. Note that variations in VER values caused by the imperfect collocation of measurement sites (*in situ* or remotely) during the WAVE2004 campaign are similar to uncertainties of VER values obtained for the ETON campaign. Specifically, providing ETON measurements, Greer et al. [1986] reported uncertainties in *in situ* peak $[O(^3P)]$ values of about 40% and uncertainties in *in situ* peak VER values of up to 20%. The identified variations in VER

and temperature values cause the most prominent changes in the MAC products, whereas variations in atmospheric density values cause small changes. It can be concluded that a 5% temperature change and a 20% VER change lead to $[O(^3P)]$ changes of about 10%, while a 5% variation in atmospheric density causes a $\sim 2\%$ effect in $[O(^3P)]$. Note that the influence of variability in the MAC model input parameters was also described in section 4.1 in Lednyts'kyy and von Savigny [2019] and section 4.4 in Lednyts'kyy et al. [2019].

The influence of variability in unknown or poorly constrained reaction rates on the retrieved $[O(^3P)]$ profiles was studied for the ETON campaign because the number of measured emissions exceeds that during measured another campaigns. Tuning values of unknown or poorly constrained reaction rates, deactivation processes were found to be (1) strong between $O_2(c^1\Sigma_u^-)$ and $O_2(b^1\Sigma_g^+)$, (2) weak between $O_2(A'^3\Delta_u)$ and $O_2(c^1\Sigma_u^-)$, (3) almost completely absent between $O_2(A'^3\Sigma_u^+)$ and $O_2(A'^3\Delta_u)$ as well as $O_2(c^1\Sigma_u^-)$ and $O_2(a^1\Delta_g)$. Note that the influence of variability in unknown or poorly constrained reaction rates was also described in section 3.4 in Lednyts'kyy and von Savigny [2019].

At the end of section 3.2 it was discussed that rate values of the three-body recombination reaction (at least with O_2 as a third body) determined adopting the hard-sphere concept are, presumably, incorrect. Note that increased rate values of the three-body recombination processes implemented in the MAC model led to $O(^3P)$ loss and were backed up by convincing results regarding the verification and validation of the MAC calculations carried out for the ETON, WADIS-2, WAVE2000 and WAVE2004 campaigns. Different additional $O(^3P)$ loss processes were considered in the MAC model implicitly adjusting the association rate values of $O_2(b, a, X)$, see section 3.2 in this doctoral thesis and sections 4.3 and 5 in Lednyts'kyy and von Savigny [2019] for details. Although quenching of the known vibrational O_2 states was implemented in the MAC model for $O_2(b, a)$, quenching of other identified vibrational O_2 states has not been taken into account yet. Krasnopolsky [2011] summarized studies regarding quenching reactions involving a limited number of available vibrationally excited O_2 states and emphasized that other vibrationally excited O_2 states might significantly contribute to quenching processes. Because of this and the fact that the set of quenching reactions currently implemented in the MAC model might not be complete, it follows that the additional $O(^3P)$ loss processes implicitly considered in the MAC model are necessary. The MAC model will be extended to take quenching of another identified vibrational O_2 states into account.

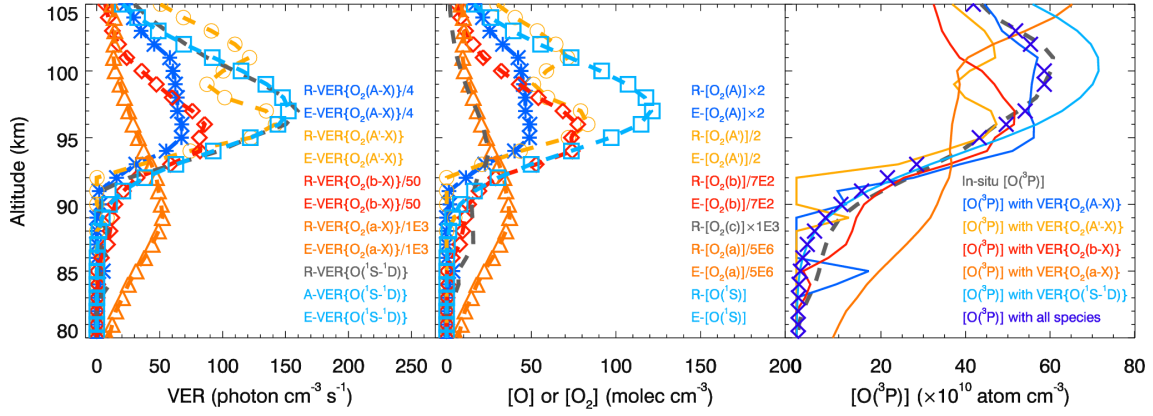


Figure 4.5.: Retrieved and evaluated profiles obtained with the MAC model involving $O_2(A)$ and $O_2(A')$ for the ETON campaign. Retrieved VER profiles shown in the left panel by the dashed lines and denoted in the figure legend by the character R were read out from Greer et al. [1986]. Profiles of $R\text{-VER}\{O_2(A - X)\}$, $R\text{-VER}\{O_2(b - X)\}$ and $R\text{-VER}\{O_2(a - X)\}$ were retrieved using the P227H rocket launched at $\sim 22:11$ UT. Profiles of $R\text{-VER}\{O_2(A - X)\}$, $R\text{-VER}\{O_2(A' - a)\}$, $R\text{-VER}\{O_2(b - X)\}$ and $R\text{-VER}\{O(^1S - ^1D)\}$ were retrieved using the P229H rocket launched at $\sim 22:58$ UT, i.e., after the P227H rocket. The middle panel of the figure shows concentrations of excited O_2 and O species retrieved (see the dashed lines and the character R) and evaluated (see the symbols and the character E) on the basis of the corresponding R-VER profiles at steps 2.1, 2.2, 2.3, 3.1, 3.2 and 4.1, see Fig. 3.3. Specifically, values of an *in situ* R-VER profile were divided by the respective transition probability to evaluate corresponding concentrations, these concentration profiles are indicated by the character E. All relevant processes including the respective transitions were considered to retrieve corresponding concentrations, these concentration profiles are indicated by the character R. Evaluated VER profiles indicated by the character E were obtained multiplying retrieved concentrations with the transition probability and shown in the left panel by symbols colored according to abbreviations in the legend. The right panel of the figure shows $[O(^3P)]$ profiles. The retrieved $[O(^3P)]$ profiles shown in colored lines and crosses were obtained at different retrieval steps using the MAC model, see legend and Fig. 3.3 for details. Note that in each panel of the figure, the legend text and profiles are shown using the same colors chosen to indicate the particular retrieval steps. The *in situ* $[O(^3P)]$ profile shown by dashed gray lines and obtained for the time of the P229H rocket is in the best agreement with $[O(^3P)]$ values obtained at the final retrieval step 5.1. Values of temperature (T), $[N_2]$ and $[O_2]$ were obtained using the NRLMSISE-00 model for the time and place of the P229H rocket. The profiles shown in the figure were discussed during Talk VIII, see section D, and in Lednys'kyy and von Savigny [2019] by using their Figs. 3 and 4.

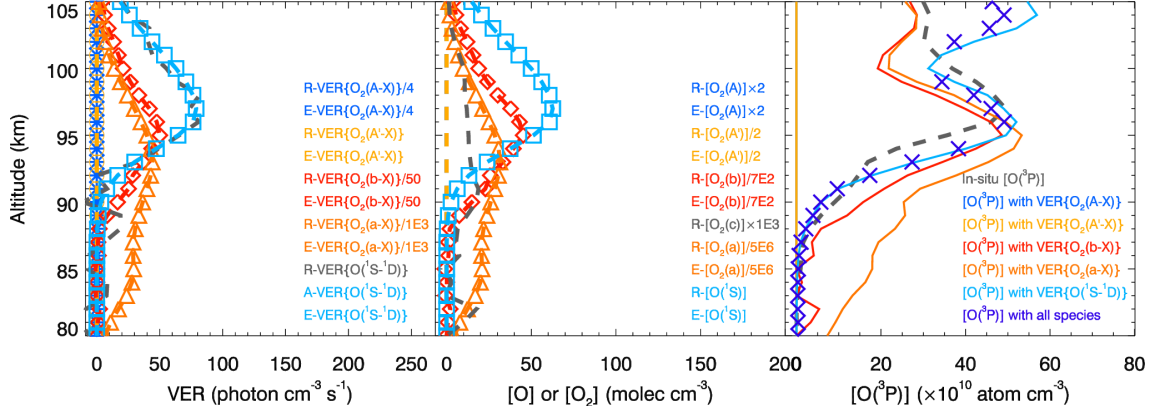


Figure 4.6.: Similar to Fig. 4.5, but excluding O₂(A) and O₂(A') for measurements obtained with the S-310-29 rocket launched during the WAVE2004 campaign and SABER measurements. The used data sets were obtained on 17th January 2004 as follows: (1) VER{O₂(b - X)} and VER{O(¹S - ¹D)} were obtained by using the S-310-33 rocket launched at ~15:30 UT during the WAVE2004 campaign and (2) VER{O₂(a - X)}, temperature, [N₂], [O₂], [CO₂], [H] and [O₃] were obtained by using the SABER orbit/event 1123/39 at ~16:20 UT. Profiles of *in situ* VER (R-VER) and evaluated VER (E-VER) shown in the left panel as well as retrieved and evaluated concentration profiles shown in the middle and right panels were obtained at steps 2.3, 3.2, 4.1 and 5.1 using the MAC model. The representation of profiles using lines and symbols as well as abbreviations shown in the legend are the same as in Fig. 4.5. The profiles shown in the figure were discussed during Talks VII and VIII, see section D, and in Lednyts'kyy et al. [2019] by using their Figs. 9 and 10.

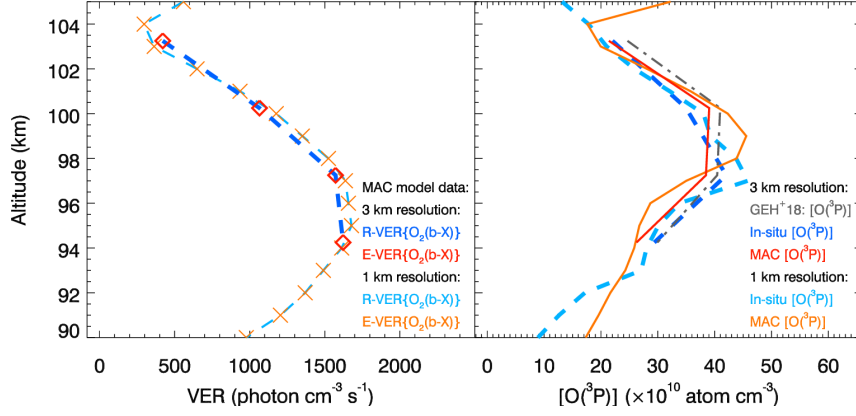


Figure 4.7.: The left panel shows the *in situ* and evaluated $\text{VER}\{\text{O}_2(b-X)\}$ profiles, and the right panel shows the *in situ* and retrieved $[\text{O}(\text{}^3P)]$ profiles for the WADIS-2 campaign. The *in situ* VER and $[\text{O}(\text{}^3P)]$ profiles are shown with vertical samplings of 3 and 1 km by the blue and cyan dashed lines, respectively. The evaluated VER profiles are shown with the same vertical samplings by the red and orange symbols, respectively. The retrieved MAC $[\text{O}(\text{}^3P)]$ profiles are shown with the same vertical samplings by the red and orange solid lines, respectively, while the $[\text{O}(\text{}^3P)]$ profile retrieved according to Grygalashvily et al. [2019] (GEH⁺18) is shown with the 3 km vertical sampling by the gray dash-dotted line. The *in situ* $\text{VER}\{\text{O}_2(b-X)\}$ and $[\text{O}(\text{}^3P)]$ profiles are compared with those calculated with the MAC model, and the validated MAC calculations are concluded to be consistent with each other. Although the shapes of the MAC and GEH⁺18 $[\text{O}(\text{}^3P)]$ profiles are very similar, the MAC values are slightly lower than the GEH⁺18 values. Note that the *in situ* $[\text{O}(\text{}^3P)]$ profile values above 100 km are closer to the MAC profile values than the GEH⁺18 profile values, while those below 97 km are closer to the GEH⁺18 profile values than the MAC profile values. The figure was discussed during Talk IX, see section D, and in Lednyts'kyy et al. [2019] by using their Fig. 6.

5. Summary and outlook

The main research results achieved working on this doctoral thesis are as follows.

Algorithms applied to retrieve nightglow Volume Emission Rate (VER) profiles using spectra of the oxygen green line emission measured remotely using the SCIAMACHY instrument were worked out and optimized. Firstly, each spectrum was analyzed for emissions using the band-pass filter applied for further processing of the oxygen green line emissions. Then, preprocessed nightglow spectra were employed to calculate Limb Emission Rate (LER) profiles. Finally, VER profiles were retrieved on the basis of LER profiles assuming homogeneously emitting atmospheric layers and using a first-order linear Bayesian approach combined with the Regularized Total Least Squares (RTLS) minimization approach implemented with the minimal use of the non-informed *a priori* knowledge.

Simple O_2 and O excitation mechanisms involving not identified excited O_2 and O states were employed in retrievals of the $[O(^3P)]$ near-global time series. Specifically, the established models resulted in the well-known and extended cubic equations and were employed with modified values of reaction rates and empirical coefficients. These values were adjusted working on this doctoral thesis for phases of different solar activity to study two cases of the $O(^3P)$ quenching. The $[O(^3P)]$ retrievals using both cubic equations were carried out on the basis of three sources of such parameters as temperature, $[N_2]$ and $[O_2]$: two models (NRLMSISE-00 and SD-WACCM4) and one measuring instrument (SABER). The retrieved $[O(^3P)]$ time series were verified on the basis of remote measurements considering different verification steps. This resulted in the conclusion that the optimal source of the employed parameters is the SABER instrument, data sets of which were employed to retrieve $[O(^3P)]$ using the extended cubic equation. The $[O(^3P)]$ retrievals carried out using both cubic equations on the basis of the SABER parameters were tested for their validity for two rocket campaigns, see Fig. 4.3, and the development of the MAC model on a new photochemical basis was started on the basis of *in situ* measurements.

The $[O(^3P)]$ sensitivity to lunar and solar forcing was estimated for the $[O(^3P)]$ time series obtained using the established cubic equations. The solar forcing was studied in $[O(^3P)]$ for the 27-day cycle of solar activity for the first time as well as for the phases of the 11-year cycle of solar activity. The phase of minimal solar activity during the end of the solar cycle 23 was an extremely long one since the beginning of the space age for the first time. Note that the $[O(^3P)]$ sensitivity to

the 11-year cycle of solar activity was studied for the extremely long phase of minimal solar activity for the first time. The $[O(^3P)]$ sensitivities to the 11-year and 27-day cycles of solar activity agree with each other within their uncertainties for the two proxies of solar activity: Mg II index and Lyman- α . The results achieved thanks to the multiple-linear regression optimized using the step-wise procedure implemented to carry out calculations with the minimal degree of freedom were backed up by the results obtained using the standard techniques.

Involving identified excited O_2 and O states in reactions implemented in the MAC model in a new photochemical scheme, reaction rates were updated or derived on the basis *in situ* measurements carried out during the ETON rocket campaign. New insights on the established photochemical models, see, e.g., Mlynczak et al. [1993] and Huang and George [2014], were obtained while these models were combined. Then, they were extended with complementary processes considered in the MAC model and proposed as part of this doctoral thesis. The approach of Yankovsky et al. [2016] was adopted and optimized to solve the system of reactions in the photochemical steady state, see the calculation scheme illustrated in Fig. 3.3. For instance, the Slinger et al. [2004a] hypothesis stating the collisional induced conversions among O_2 states from the $O_2(^5\Pi)-O_2(A, A', c)$ -group was tested using the MAC model. Because the MAC calculations involving $O_2(^5\Pi, A, A', c, b, a, X)$ lead to nearly the same results comparing to those obtained with the MAC calculations involving $O_2(^5\Pi, c, b, a, X)$, the conversions involving the $O_2(^5\Pi)-O_2(A, A')$ -group were explicitly confirmed in calculations proposing the MAC model. Results of the MAC calculations enabled concluding that (1) the $O_2(^5\Pi)-O_2(A, A')$ -group and $O_2(c)$ are the $O_2(b)$ precursors, (2) the $O_2(^5\Pi)-O_2(A, A')$ -group and $O_2(c, b)$ are the $O_2(a)$ precursors, (3) the $O_2(^5\Pi)-O_2(A, A')$ -group and $O_2(c, b, a)$ are the $O_2(X)$ precursors, and (4) $O_2(c)$ is the main $O(^1S)$ precursor.

Each measured emission profile was employed to retrieve concentrations of the corresponding excited states of O_2 or O used to retrieve a particular $[O(^3P)]$ profile in each step. This increased the accuracy of the MAC calculations because each particular $[O(^3P)]$ profile was compared to the other ones retrieved in other retrieval steps and compared with the *in situ* $[O(^3P)]$ profile. This validation procedure was accurately carried out for the ETON rocket campaign and the other three rocket campaigns. For two of these campaigns, remotely and *in situ* measured data sets were employed from the collocated measurement sites which positively backed up these photochemical calculations comparing to others based only on the climatologically averaged data sets.

The number of airglow emissions measured simultaneously *in situ* during the ETON and WAVE2004 campaigns enabled coupling O_2 or O states which was confirmed by results of the verification and validation tools. The data sets measured during the WADIS-2 campaign are self-consistent because they were obtained using the rocket-borne devices simultaneously. Convincing results validating calculations using the implemented O_2 and O modules of the MAC model

applied on the basis of the WADIS-2 *in situ* VER $\{\text{O}_2(b - X)\}$ profile back up the MAC model for this and the other three rocket campaigns.

In summary, the proposed MAC approach enables considering (1) the strong coupling among the triplet states $\text{O}_2(A, A')$ and $\text{O}_2(X)$, (2) the $\text{O}_2(^5\Pi)$ – $\text{O}_2(A, A')$ –group implemented according to the modified hypothesis of Slanger et al. [2004a] that refuted the hypothesis of Huestis [2002], (3) the implementation of the moderate $\text{O}(^1S)$ quenching with multiple species including $\text{O}_2(a)$, (4) the suggestion that the rate value of the three-body recombination reaction with O_2 as a third body is arguable (this also led to the implementation of the additional $\text{O}(^3P)$ loss processes), (5) the concept of the implicit consideration of reactions involving $\text{O}_2(^5\Pi)$ by employing the association rate value of $\text{O}_2(^5\Pi)$ applied to adjust the association rate values of $\text{O}_2(b, a, X)$, (6) the implementation of each retrieval step using a particular steady-state continuity equation to retrieve the corresponding concentrations of one of the $\text{O}_2(A, A', c, b, a)$ and $\text{O}(^1S, ^1D)$ states, (7) the concept of the $[\text{O}(^3P)]$ retrievals carried out sequentially on the basis of multiple emissions which enabled the final retrieval step carried out on the basis of the retrieved concentrations of the $\text{O}_2(A, A', c, b, a)$ and $\text{O}(^1S, ^1D)$ states. The $[\text{O}(^3P)]$ retrievals carried out sequentially resulted in the unambiguous verification and validation worked out and applied for the four rocket campaigns. The obtained results enabled explaining the origin of the $\text{O}_2(b, a, X)$ precursors and the $\text{O}(^1S)$ precursor.

The main topics of potential further research based on this doctoral thesis as follows.

The O , O_2 and OH^* modules implemented in the MAC model should be extended to consider different vibrational states (ν) of OH^* and the electronically excited O_2 molecules. This might explain the additional $\text{O}(^3P)$ loss processes implemented in the current version of the MAC model. Sharma et al. [2015] emphasized the role of $\text{O}(^1D)$ in the reaction of OH^* with $\text{O}(^3P)$ resulting in HO_2^* as an intermediate product. Consequently, the $[\text{O}(^1D)]$ retrieval should be worked out for correct modeling of $\text{OH}(\nu)$. The concept of the Multiple Airglow and Ion Chemistry model introduced during Talks V and VI mentioned in the Appendix D should be worked out in the future version of the MAC model. In focus of this is the agreement between shapes of the following vertical profiles: $[\text{O}(^3P)]$ and electronic density [Friedrich et al., 1999] and $[\text{OH}(\nu)]$ and electronic density [Wu et al., 2017].

Bibliography

- Ångström, J. A. (1869). Spectrum des nordlichts. *Annalen der Physik*, 213(5):161–163.
- Andrews, D. G. (2010). *An Introduction to Atmospheric Physics*. An Introduction to Atmospheric Physics. Cambridge University Press.
- Angelats i Coll, M. and Forbes, J. M. (1998). Dynamical influences on atomic oxygen and 5577 Å emission rates in the lower thermosphere. *Geophysical Research Letters*, 25(4):461–464.
- Baker, D. J. and Romick, G. J. (1976). The rayleigh: interpretation of the unit in terms of column emission rate or apparent radiance expressed in SI units. *Applied Optics*, 15(8):1966–1968.
- Balakrishnan, N., Kharchenko, V., and Dalgarno, A. (1998). Slowing of energetic O(³P) atoms in collisions with N₂. *Journal of Geophysical Research: Space Physics*, 103(A10):23393–23398.
- Baldwin, M. P., Gray, L. J., Dunkerton, T. J., Hamilton, K., Haynes, P. H., Randel, W. J., Holton, J. R., Alexander, M. J., Hirota, I., Horinouchi, T., Jones, D. B. A., Kinnarsley, J. S., Marquardt, C., Sato, K., and Takahashi, M. (2001). The quasi-biennial oscillation. *Reviews of Geophysics*, 39(2):179–229.
- Bates, D. R. (1951). Rate of formation of molecules by radiative association. *Monthly Notices of the Royal Astronomical Society*, 111(3):303.
- Bates, D. R. (1978). Forbidden oxygen and nitrogen lines in the nightglow. *Planetary and Space Science*, 26(10):897–912.
- Bates, D. R. (1979). On the proposals of chapman and of barth for O(¹S) formation in the upper atmosphere. *Planetary and Space Science*, 27(5):717–718.
- Bates, D. R. (1981). The green light of the night sky. *Planetary and Space Science*, 29(10):1061–1067.
- Bates, D. R. (1988a). Excitation and quenching of the oxygen bands in the nightglow. *Planetary and Space Science*, 36(9):875–881. Special Issue: Atomic Oxygen Abundance in Thermosphere.
- Bates, D. R. (1988b). Excitation of 557.7 nm OI line in nightglow. *Planetary and Space Science*, 36(9):883–889.

- Bates, D. R. (1992). Nightglow emissions from oxygen in the lower thermosphere. *Planetary and Space Science*, 40(2):211 – 221.
- Bates, D. R. and Nicolet, M. (1950). The photochemistry of atmospheric water vapor. *Journal of Geophysical Research*, 55(3):301–327.
- Baulch, D. L., Cox, R. A., Hampson Jr., R. F., Kerr, J. A., Troe, J., and Watson, R. T. (1980). Evaluated kinetic and photochemical data for atmospheric chemistry. *Journal of Physical and Chemical Reference Data*, 9(2):295–472.
- Becker, E. and Schmitz, G. (2002). Energy deposition and turbulent dissipation owing to gravity waves in the mesosphere. *Journal of the Atmospheric Sciences*, 59(1):54–68.
- Beig, G., Keckhut, P., Lowe, R. P., Roble, R. G., Mlynczak, M. G., Scheer, J., Fomichev, V. I., Offermann, D., French, W. J. R., Shepherd, M. G., Semenov, A. I., Remsberg, E. E., She, C. Y., Lübken, F. J., Bremer, J., Clemesha, B. R., Stegman, J., Sigernes, F., and Fadnavis, S. (2003). Review of mesospheric temperature trends. *Reviews of Geophysics*, 41(4):n/a–n/a. 1015.
- Beig, G., Scheer, J., Mlynczak, M. G., and Keckhut, P. (2008). Overview of the temperature response in the mesosphere and lower thermosphere to solar activity. *Reviews of Geophysics*, 46(3):n/a–n/a. RG3002.
- Bovensmann, H., Burrows, J. P., Buchwitz, M., Frerick, J., Noël, S., Rozanov, V. V., Chance, K. V., and Goede, A. P. H. (1999). Sciamachy: Mission Objectives and Measurement Modes. *Journal of the Atmospheric Sciences*, 56(2):127–150.
- Brasseur, G. and Offermann, D. (1986). Recombination of atomic oxygen near the mesopause: Interpretation of rocket data. *Journal of Geophysical Research: Atmospheres*, 91(D10):10818–10824.
- Brasseur, G. and Solomon, S. (2005). *Aeronomy of the middle atmosphere: chemistry and physics of the stratosphere and mesosphere*. Dordrecht Springer.
- Burkholder, J. B., Sander, S. P., Abbatt, J., Barker, J. R., Huie, R. E., Kolb, C. E., Kurylo, M. J., Orkin, V. L., Wilmouth, D. M., and Wine, P. H. (2015). Chemical kinetics and photochemical data for use in atmospheric studies. Evaluation No. 18. JPL publication 15-10. *Jet Propulsion Laboratory, Pasadena*.
- Burrage, M. D., Vincent, R. A., Mayr, H. G., Skinner, W. R., Arnold, N. F., and Hays, P. B. (1996). Long-term variability in the equatorial middle atmosphere zonal wind. *Journal of Geophysical Research: Atmospheres*, 101(D8):12847–12854.
- Burrows, J. P., Hölzle, E., Goede, A. P. H., Visser, H., and Fricke, W. (1995). SCIAMACHY – scanning imaging absorption spectrometer for atmospheric cartography. *Acta Astronautica*, 35(7):445–451. Earth Observation.
- Campbell, I. M. and Gray, C. N. (1973). Rate constants for $O(^3P)$ recombination and association with $N(^4S)$. *Chemical Physics Letters*, 18(4):607–609.

- Capitelli, M., Colonna, G., and D'Angola, A. (2012). *Fundamental Aspects of Plasma Chemical Physics: Thermodynamics*. Springer-Verlag New York.
- Carraway, E. R., Demas, J. N., and DeGraff, B. A. (1991). Luminescence quenching mechanism for microheterogeneous systems. *Analytical Chemistry*, 63(4):332–336.
- Chapman, S. (1931). Bakerian lecture. Some phenomena of the upper atmosphere. *Proceedings of the Royal Society of London A: Mathematical, Physical and Engineering Sciences*, 132(820):353–374.
- Chapman, S. (1937). LXVI. On the production of auroral and night-sky light. *The London, Edinburgh, and Dublin Philosophical Magazine and Journal of Science*, 23(156):657–665.
- Chapman, S. and Lindzen, R. S. (1970). *Atmospheric tides: Thermal and Gravitational*. D. Reidel Publishing Company, Dordrecht-Holland.
- Chree, C. (1913). Some phenomena of sunspots and of terrestrial magnetism at kew observatory. *Philosophical Transactions of the Royal Society of London A: Mathematical, Physical and Engineering Sciences*, 212(484-496):75–116.
- Colegrove, F. D., Hanson, W. B., and Johnson, F. S. (1965). Eddy diffusion and oxygen transport in the lower thermosphere. *Journal of Geophysical Research*, 70(19):4931–4941.
- Crutzen, P. J. (1971). *Energy conversions and mean vertical motions in the high latitude summer mesosphere and lower thermosphere*, pages 78–88. D. Reidel Publishing Company, Dordrecht-Holland.
- Dickinson, P. H. G., Bain, W. C., Thomas, L., Williams, E. R., Jenkins, D. B., and Twiddy, N. D. (1980). The determination of the atomic oxygen concentration and associated parameters in the lower ionosphere. *Proceedings of the Royal Society of London A: Mathematical, Physical and Engineering Sciences*, 369(1738):379–408.
- Dudok de Wit, T., Kretzschmar, M., Lilensten, J., and Woods, T. (2009). Finding the best proxies for the solar UV irradiance. *Geophysical Research Letters*, 36(10):n/a–n/a. L10107.
- Dudok de Wit, T. D., Kretzschmar, M., Aboudarham, J., Amblard, P.-O., Auchère, F., and Lilensten, J. (2008). Which solar EUV indices are best for reconstructing the solar EUV irradiance? *Advances in Space Research*, 42(5):903–911.
- Dudok de Wit, T. D. and Watermann, J. (2010). Solar forcing of the terrestrial atmosphere. *Comptes Rendus Geoscience*, 342(4-5):259–272. Atmosphère vue de l'espace / The atmosphere seen from space.

- Eberhart, M., Löhle, S., Steinbeck, A., Binder, T., and Fasoulas, S. (2015). Measurement of atomic oxygen in the middle atmosphere using solid electrolyte sensors and catalytic probes. *Atmospheric Measurement Techniques*, 8(9):3701–3714.
- Esplin, R. W., Zollinger, L., Batty, J. C., Folkman, S. L., Roosta, M., Tansock, J., J., J., Jensen, M., Stauder, J. L., Miller, J., Vanek, M. D., and Robinson, D. M. (1995). SABER instrument design update. *Proc. SPIE*, 2553:253–263.
- Falk, G., Herrmann, F., and Schmid, G. B. (1983). Energy forms or energy carriers? *American Journal of Physics*, 51(12):1074–1077.
- Forbes, J. M., Zhang, X., Bruinsma, S., and Oberheide, J. (2013). Lunar semidiurnal tide in the thermosphere under solar minimum conditions. *Journal of Geophysical Research: Space Physics*, 118(4):1788–1801.
- Friedrich, M., Gumbel, J., and Pilgram, R. (1999). Atomic oxygen in the mesosphere and its relevance for the ionosphere: A summary of empirical evidence. In *European Rocket and Balloon Programs and Related Research*, volume 437, pages 287–290. Proceedings of the 14th European Space Agency Symposium, Potsdam, Germany.
- Garcia, R. R. and Solomon, S. (1985). The effect of breaking gravity waves on the dynamics and chemical composition of the mesosphere and lower thermosphere. *Journal of Geophysical Research: Atmospheres*, 90(D2):3850–3868.
- García-Comas, M., López-Puertas, M., Marshall, B. T., Wintersteiner, P. P., Funke, B., Bermejo-Pantaleón, D., Mertens, C. J., Remsberg, E. E., Gordley, L. L., Mlynarczyk, M. G., and Russell, J. M. (2008). Errors in Sounding of the Atmosphere using Broadband Emission Radiometry (SABER) kinetic temperature caused by non-local-thermodynamic-equilibrium model parameters. *Journal of Geophysical Research: Atmospheres*, 113(D24):n/a–n/a. D24106.
- Gobbi, D., Takahashi, H., Clemesha, B. R., and Batista, P. P. (1992). Equatorial atomic oxygen profiles derived from rocket observations of OI 557.7 nm airglow emission. *Planetary and Space Science*, 40(6):775–781.
- Gottwald, M. and Bovensmann, H. (2011). *SCIAMACHY - Exploring the Changing Earth's Atmosphere*. Springer Science+Business Media B.V.
- Greer, R. G. H., Llewellyn, E. J., Solheim, B. H., and Witt, G. (1981). The excitation of $O_2(b^1\sigma_g^+)$ in the nightglow. *Planetary and Space Science*, 29(4):383–389.
- Greer, R. G. H., Murtagh, D. P., McDade, I. C., Dickinson, P. H. G., Thomas, L., Jenkins, D. B., Stegman, J., Llewellyn, E. J., Witt, G., Mackinnon, D. J., and Williams, E. R. (1986). ETON 1: A data base pertinent to the study of energy transfer in the oxygen nightglow. *Planetary and Space Science*, 34(9):771–788.
- Greer, R. G. H., Murtagh, D. P., McDade, I. C., Llewellyn, E. J., Witt, G., Thrush, B. A., Stott, I. P., and Bowhill, S. A. (1987). Rocket photometry and the lower-thermospheric oxygen nightglow [and discussion]. *Philosophical Transactions*

of the Royal Society of London A: Mathematical, Physical and Engineering Sciences, 323(1575):579–595.

Gritzner, C. and Strelnikov, B. (2013). WADIS: Rough Seas in the Middle Atmosphere. *DLR Countdown*, 3(23):22–25.

Gruzdev, A. N., Schmidt, H., and Brasseur, G. P. (2009). The effect of the solar rotational irradiance variation on the middle and upper atmosphere calculated by a three-dimensional chemistry-climate model. *Atmospheric Chemistry and Physics*, 9(2):595–614.

Grygalashvyly, M., Eberhart, M., Hedin, J., Strelnikov, B., Lübken, F.-J., Rapp, M., Löhle, S., Fasoulas, S., Khaplanov, M., Gumbel, J., and Vorobeva, E. (2019). Atmospheric band fitting coefficients derived from a self-consistent rocket-borne experiment. *Atmospheric Chemistry and Physics*, 19(2):1207–1220.

Gumbel, J., Murtagh, D. P., Espy, P. J., Witt, G., and Schmidlin, F. J. (1998). Odd oxygen measurements during the Noctilucent Cloud 93 rocket campaign. *Journal of Geophysical Research: Space Physics*, 103(A10):23399–23414.

Hedin, A. E. (1983). A revised thermospheric model based on mass spectrometer and incoherent scatter data: MSIS-83. *Journal of Geophysical Research: Space Physics*, 88(A12):10170–10188.

Hickey, M. P., Schubert, G., and Walterscheid, R. L. (1993). Gravity wave-driven fluctuations in the O₂ atmospheric (0–1) nightglow from an extended, dissipative emission region. *Journal of Geophysical Research: Space Physics*, 98(A8):13717–13729.

Hickey, M. P., Walterscheid, R. L., Taylor, M. J., Ward, W., Schubert, G., Zhou, Q., Garcia, F., Kelly, M. C., and Shepherd, G. G. (1997). Numerical simulations of gravity waves imaged over arecibo during the 10-day January 1993 campaign. *Journal of Geophysical Research: Space Physics*, 102(A6):11475–11489.

Hollas, J. M. (2004). *Modern Spectroscopy*. John Wiley & Sons.

Huang, T.-Y. and George, R. (2014). Simulations of gravity wave-induced variations of the OH(8,3), O₂(0,1), and O(¹S) airglow emissions in the MLT region. *Journal of Geophysical Research: Space Physics*, 119(3):2149–2159.

Huestis, D. L. (2002). *Current Laboratory Experiments for Planetary Aeronomy*, pages 245–258. American Geophysical Union.

Isobe, T., Feigelson, E. D., Akritas, M. G., and Babu, G. J. (1990). Linear regression in astronomy. *Astrophysical Journal*, 364:104–113.

Iwagami, N., Ohtsuki, S., Akojima, M., Kubota, M., Murayama, Y., Kawamura, S., Yoshimura, R., Nakamura, T., Yamamoto, H., Sekiguchi, H., Kimura, N., Shiokawa, K., Okada, T., Ishisaka, K., Ashihara, Y., Kaiho, Y., Abo, M., Abe,

- T., Koizumi, Y., and Oyama, K.-I. (2005). Waves in airglow structures experiment 2004: Overview and preliminary results. *Advances in Space Research*, 35(11):1964–1970. Coupling Processes in the MLT Region.
- Iwagami, N., Shibaki, T., Suzuki, T., Sekiguchi, H., Takegawa, N., and Morrow, W. H. (2003). Rocket observations of atomic oxygen density and airglow emission rate in the WAVE2000 campaign. *Journal of Atmospheric and Solar-Terrestrial Physics*, 65(16):1349–1360.
- Iwagami, N., Shibaki, T., Suzuki, T., Yamada, Y., Onishi, H., Takahashi, Y., Yamamoto, H., Sekiguchi, H., Mori, K., Sano, Y., Kubota, M., Murayama, Y., Ishii, M., Oyama, K.-I., Yoshimura, R., Shimoyama, M., Koizumi, Y., Shiokawa, K., Takegawa, N., and Nakamura, T. (2002). The WAVE2000 campaign: Overview and preliminary results. *Journal of Atmospheric and Solar-Terrestrial Physics*, 64(8):1095–1104. PSMOS 2000 Workshop - Planetary Scale Mesopause Observing System.
- Job, G. and Herrmann, F. (2006). Chemical potential – a quantity in search of recognition. *European Journal of Physics*, 27(2):353–371.
- Jöckel, P., Tost, H., Pozzer, A., Kunze, M., Kirner, O., Brenninkmeijer, C. A. M., Brinkop, S., Cai, D. S., Dyroff, C., Eckstein, J., Frank, F., Garny, H., Gottschaldt, K.-D., Graf, P., Grewe, V., Kerkweg, A., Kern, B., Matthes, S., Mertens, M., Meul, S., Neumaier, M., Nützel, M., Oberländer-Hayn, S., Ruhnke, R., Runde, T., Sander, R., Scharffe, D., and Zahn, A. (2016). Earth System Chemistry integrated Modelling (ESCiMo) with the Modular Earth Submodel System (MESSy) version 2.51. *Geoscientific Model Development*, 9(3):1153–1200.
- Johnston, J. E. and Broadfoot, A. L. (1993). Midlatitude observations of the night airglow: Implications to quenching near the mesopause. *Journal of Geophysical Research: Space Physics*, 98(A12):21593–21603.
- Jones, D. B., Campbell, L., Bottema, M. J., Teubner, P. J. O., Cartwright, D. C., Newell, W. R., and Brunger, M. J. (2006). Electron-driven excitation of O₂ under night-time auroral conditions: Excited state densities and band emissions. *Planetary and Space Science*, 54(1):45–59.
- Kane, R. (2002). Some implications using the group sunspot number reconstruction. *Solar Physics*, 205(2):383–401.
- Kaufmann, M., Zhu, Y., Ern, M., and Riese, M. (2014). Global distribution of atomic oxygen in the mesopause region as derived from SCIAMACHY O(¹S) green line measurements. *Geophysical Research Letters*, 41(17):6274–6280.
- Kenner, R. D. and Ogryzlo, E. A. (1982). A direct determination of the rate constant for the quenching of O(¹S) by O₂(a¹Δ_g). *Journal of Photochemistry*, 18(4):379–382.

- Kharchenko, V. A., Dalgarno, A., and Mellott, M. (2002). Kinetics of fast atoms in the terrestrial atmosphere. *Final Report*, pages II, 16.
- Khomich, V. Y., Semenov, A. I., and Shefov, N. N. (2008). *Airglow as an indicator of upper atmospheric structure and dynamics*. Springer.
- Krasnopolsky, V. A. (1981). Excitation of oxygen emissions in the night airglow of the terrestrial planets. *Planetary and Space Science*, 29(9):925 – 929.
- Krasnopolsky, V. A. (1986). Oxygen emissions in the night airglow of the Earth, Venus and Mars. *Planetary and Space Science*, 34(6):511–518.
- Krasnopolsky, V. A. (2011). Excitation of the oxygen nightglow on the terrestrial planets. *Planetary and Space Science*, 59(8):754–766.
- Krauss, M. and Neumann, D. (1975). On the interaction of $O(^1S)$ with $O(^3P)$. *Chemical Physics Letters*, 36(3):372–374.
- Krivolutsky, A. A. and Repnev, A. I. (2012). Impact of space energetic particles on the Earth's atmosphere (a review). *Geomagnetism and Aeronomy*, 52(6):685–716.
- Kubota, M., Kawamura, S., Abo, M., Koizumi, Y., Murayama, Y., Yamamori, M., Shiokawa, K., Otsuka, Y., Uchiumi, M., Igarashi, K., Abe, T., Oyama, K.-I., and Iwagami, N. (2006). A fast-propagating, large-scale atmospheric gravity wave observed in the WAVE2004 campaign. *Journal of Geophysical Research: Atmospheres*, 111(D21):n/a–n/a. D21110.
- Lakowicz, J. R. (2006). *Principles of Fluorescence Spectroscopy*. Springer US.
- Lamarque, J.-F., Emmons, L. K., Hess, P. G., Kinnison, D. E., Tilmes, S., Vitt, F., Heald, C. L., Holland, E. A., Lauritzen, P. H., Neu, J., Orlando, J. J., Rasch, P. J., and Tyndall, G. K. (2012). CAM-chem: description and evaluation of interactive atmospheric chemistry in the Community Earth System Model. *Geoscientific Model Development*, 5(2):369–411.
- Lean, J. (1987). Solar ultraviolet irradiance variations: A review. *Journal of Geophysical Research: Atmospheres*, 92(D1):839–868.
- Lednyts'kyi, O. and von Savigny, C. (2016). Development of a Multiple Airglow Chemistry model and validation with in-situ Airglow measurements. *Midterm HEPP Meeting of the Max Planck Society, Berlin, Germany, 27 October 2016*, N1, 2016.
- Lednyts'kyi, O. and von Savigny, C. (2019). Photochemical modeling of molecular and atomic oxygen based on multiple *in-situ* emissions measured during the Energy Transfer in the Oxygen Nightglow rocket campaign. *Atmospheric Chemistry and Physics Discussions*, 2019:1–60. In review.
- Lednyts'kyi, O., von Savigny, C., Eichmann, K.-U., and Mlynarczyk, M. G. (2015). Atomic oxygen retrievals in the MLT region from SCIAMACHY nightglow limb measurements. *Atmospheric Measurement Techniques*, 8(3):1021–1041.

- Lednyts'kyi, O., von Savigny, C., Sinnhuber, M., Iwagami, N., and Mlynarczyk, M. (2019). Multiple Airglow Chemistry approach for atomic oxygen retrievals on the basis of *in situ* nightglow emissions. *Journal of Atmospheric and Solar-Terrestrial Physics*, 194:105096.
- Lednyts'kyi, O., von Savigny, C., and Weber, M. (2017). Sensitivity of equatorial atomic oxygen in the MLT region to the 11-year and 27-day solar cycles. *Journal of Atmospheric and Solar-Terrestrial Physics*, 162:136–150. Layered Phenomena in the Mesopause Region.
- Lee, J. N., Wu, D. L., and Ruzmaikin, A. (2013). Interannual variations of MLS carbon monoxide induced by solar cycle. *Journal of Atmospheric and Solar-Terrestrial Physics*, 102:99–104.
- Liu, G., Shepherd, G. G., and Roble, R. G. (2008). Seasonal variations of the nighttime O(¹S) and OH airglow emission rates at mid-to-high latitudes in the context of the large-scale circulation. *Journal of Geophysical Research: Space Physics*, 113(A6):n/a–n/a. A06302.
- Liu, H.-L., Foster, B. T., Hagan, M. E., McInerney, J. M., Maute, A., Qian, L., Richmond, A. D., Roble, R. G., Solomon, S. C., Garcia, R. R., Kinnison, D., Marsh, D. R., Smith, A. K., Richter, J., Sassi, F., and Oberheide, J. (2010). Thermosphere extension of the Whole Atmosphere Community Climate Model. *Journal of Geophysical Research: Space Physics*, 115(A12):n/a–n/a. A12302.
- Llewellyn, E. J., Solheim, B. H., Witt, G., Stegman, J., and Greer, R. G. H. (1980). On the excitation of oxygen emissions in the airglow of the terrestrial planets. *Journal of Photochemistry*, 12(2):179 – 183.
- López-González, M. J., López-Moreno, J. J., and Rodrigo, R. (1992). Altitude and vibrational distribution of the O₂ ultraviolet nightglow emissions. *Planetary and Space Science*, 40(7):913–928.
- Luo, Y., Manson, A. H., Meek, C. E., Igarashi, K., and Jacobi, C. (2001). Extra long period (20–40 day) oscillations in the mesospheric and lower thermospheric winds: Observations in Canada, Europe and Japan, and considerations of possible solar influences. *Journal of Atmospheric and Solar-Terrestrial Physics*, 63(9):835–852. Mesosphere-Thermosphere-Ionosphere Coupling and Energetics.
- Markwardt, C. B. (2009). *Non-linear Least-squares Fitting in IDL with MPFIT*, volume 411, page 251. Astronomical Society of the Pacific.
- Marsh, D. R., Garcia, R. R., Kinnison, D. E., Boville, B. A., Sassi, F., Solomon, S. C., and Matthes, K. (2007). Modeling the whole atmosphere response to solar cycle changes in radiative and geomagnetic forcing. *Journal of Geophysical Research: Atmospheres*, 112(D23):n/a–n/a. D23306.

- McDade, I. C. (1998). The photochemistry of the MLT oxygen airglow emissions and the expected influences of tidal perturbations. *Advances in Space Research*, 21(6):787–794. Proceedings of the C0.1 Symposium of COSPAR Scientific Commission C.
- McDade, I. C., Llewellyn, E. J., Murtagh, D. P., and Greer, R. G. H. (1987). ETON 5: Simultaneous rocket measurements of the OH meinel $\delta\nu=2$ sequence and (8,3) band emission profiles in the nightglow. *Planetary and Space Science*, 35(9):1137–1147.
- McDade, I. C., Murtagh, D. P., Greer, R. G. H., Dickinson, P. H. G., Witt, G., Stegman, J., Llewellyn, E. J., Thomas, L., and Jenkins, D. B. (1986). ETON 2: Quenching parameters for the proposed precursors of $O_2(b^1\Sigma_g^+)$ and $O(^1S)$ in the terrestrial nightglow. *Planetary and Space Science*, 34(9):789–800.
- McIntosh, S. W., Leamon, R. J., Krista, L. D., Title, A. M., Hudson, H. S., Riley, P., Harder, J. W., Kopp, G., Snow, M., Woods, T. N., Kasper, J. C., Stevens, M. L., and Ulrich, R. K. (2015). The solar magnetic activity band interaction and instabilities that shape quasi-periodic variability. *Nature Communications*, 6(6491).
- McIntosh, S. W., Wang, X., Leamon, R. J., Davey, A. R., Howe, R., Krista, L. D., Malanushenko, A. V., Markel, R. S., Cirtain, J. W., Gurman, J. B., Pesnell, W. D., and Thompson, M. J. (2014). Deciphering solar magnetic activity. I. On the relationship between the sunspot cycle and the evolution of small magnetic features. *The Astrophysical Journal*, 792(1):12.
- McLennan, J. C. and Shrum, G. M. (1925). On the Origin of the Auroral Green Line 5577 Angstrom, and Other Spectra Associated with the Aurora Borealis. *Proceedings of the Royal Society of London A: Mathematical, Physical and Engineering Sciences*, 108(747):501–512.
- Meier, R. R. (1991). Ultraviolet spectroscopy and remote sensing of the upper atmosphere. *Space Science Reviews*, 58(1):1–185.
- Mertens, C. J., Mlynczak, M. G., López-Puertas, M., Wintersteiner, P. P., Picard, R. H., Winick, J. R., Gordley, L. L., and Russell III, J. M. (2003). Retrieval of kinetic temperature and carbon dioxide abundance from nonlocal thermodynamic equilibrium limb emission measurements made by the SABER experiment on the TIMED satellite. *Proc. SPIE*, 4882:162–171.
- Minaev, B. F., Murugan, N. A., and Ågren, H. (2013). Dioxygen spectra and bioactivation. *International Journal of Quantum Chemistry*, 113(14):1847–1867.
- Mlynczak, M. G., Hunt, L. A., Mast, J. C., B., T. M., Russell, J. M., Smith, A. K., Siskind, D. E., Yee, J.-H., Mertens, C. J., Javier M.-T., F., Earl Thompson, R., Drob, D. P., and Gordley, L. L. (2013a). Atomic oxygen in the mesosphere and lower thermosphere derived from SABER: Algorithm theoretical basis and measurement uncertainty. *Journal of Geophysical Research: Atmospheres*, 118(11):5724–5735.

- Mlynczak, M. G., Hunt, L. A., Thomas M., B., Martin-Torres, F. J., Mertens, C. J., Russell, J. M., Remsberg, E. E., López-Puertas, M., Picard, R., Winick, J., Wintersteiner, P., Thompson, R. E., and Gordley, L. L. (2010). Observations of infrared radiative cooling in the thermosphere on daily to multiyear timescales from the TIMED/SABER instrument. *Journal of Geophysical Research: Space Physics*, 115(A3):n/a–n/a. A03309.
- Mlynczak, M. G., Hunt, L. H., Mertens, C. J., Marshall, B. T., Russell, J. M., López-Puertas, M., Smith, A. K., Siskind, D. E., Mast, J. C., Thompson, R. E., and Gordley, L. L. (2013b). Radiative and energetic constraints on the global annual mean atomic oxygen concentration in the mesopause region. *Journal of Geophysical Research: Atmospheres*, 118(11):5796–5802.
- Mlynczak, M. G. and Solomon, S. (1991). Middle atmosphere heating by exothermic chemical reactions involving odd-hydrogen species. *Geophysical Research Letters*, 18(1):37–40.
- Mlynczak, M. G. and Solomon, S. (1993). A detailed evaluation of the heating efficiency in the middle atmosphere. *Journal of Geophysical Research: Atmospheres*, 98(D6):10517–10541.
- Mlynczak, M. G., Solomon, S., and Zaras, D. S. (1993). An updated model for $O_2(a^1\Delta_g)$ concentrations in the mesosphere and lower thermosphere and implications for remote sensing of ozone at $1.27\ \mu\text{m}$. *Journal of Geophysical Research: Atmospheres*, 98(D10):18639–18648.
- Murayama, Y., Igarashi, K., Koizumi, Y., Shimoyama, M., Oyama, K.-I., Nakamura, T., and Tsuda, T. (2001). Observation of Wind and Temperature of the Mesosphere and Lower Thermosphere with MF and MU Radars. *Research Report on S-310-29 Sounding Rocket*, pages 37–46.
- Murtagh, D. P., Mcdade, I. C., Greer, R. G. H., Stegman, J., Witt, G., and Llewellyn, E. J. (1986). ETON 4: An experimental investigation of the altitude dependence of the $O_2(A^3\Sigma_u^+)$ vibrational populations in the nightglow. *Planetary and Space Science*, 34(9):811–817.
- Nagy, A. F., Balogh, A., Cravens, T. E., Mendillo, M., and Müller-Wodarg, I. (2008). *Comparative Aeronomy*, pages 267–310. Springer-Verlag New York.
- Noël, S., Bovensmann, H., Wuttke, M. W., Burrows, J. P., Gottwald, M., Krieg, E., Goede, A. P. H., and Muller, C. (2002). Nadir, limb, and occultation measurements with SCIAMACHY. *Advances in Space Research*, 29(11):1819–1824.
- Owens, J. K., Torr, D. G., Torr, M. R., Chang, T., Fennelly, J. A., Richards, P. G., Morgan, M. F., Baldridge, T. W., Fellows, C. W., Dougani, H., Swift, W., Tejada, A., Orme, T., Germany, G. A., and Yung, S. (1993). Mesospheric nightglow spectral survey taken by the ISO Spectral Spatial Imager on ATLAS 1. *Geophysical Research Letters*, 20(6):515–518.

- Pancheva, D., Mitchell, N., Middleton, H., and Muller, H. (2003). Variability of the semidiurnal tide due to fluctuations in solar activity and total ozone. *Journal of Atmospheric and Solar-Terrestrial Physics*, 65(1):1–19.
- Pautet, P.-D., Taylor, M. J., Pendleton, W. R., Zhao, Y., Yuan, T., Esplin, R., and McLain, D. (2014). Advanced mesospheric temperature mapper for high-latitude airglow studies. *Applied Optics*, 53(26):5934–5943.
- Pejaković, D. A., Copeland, R. A., Cosby, P. C., and Slanger, T. G. (2007). Studies on the production of $O_2(a^1\Delta_g, \nu = 0)$ and $O_2(b^1\Sigma_g^+, \nu = 0)$ from collisional removal of $O_2(A^3\Sigma_u^+, \nu=6-10)$. *Journal of Geophysical Research: Space Physics*, 112(A10):n/a–n/a. A10307.
- Picone, J. M., Hedin, A. E., Drob, D. P., and Aikin, A. C. (2002). NRLMSISE-00 empirical model of the atmosphere: Statistical comparisons and scientific issues. *Journal of Geophysical Research: Space Physics*, 107(A12):SIA 15–1–SIA 15–16. 1468.
- Remsberg, E. E., Marshall, B. T., García-Comas, M., Krueger, D., Lingenfelter, G. S., Martin-Torres, J., Mlynczak, M. G., Russell, J. M., Smith, A. K., Zhao, Y., Brown, C., Gordley, L. L., López-González, M. J., López-Puertas, M., She, C.-Y., Taylor, M. J., and Thompson, R. E. (2008). Assessment of the quality of the Version 1.07 temperature-versus-pressure profiles of the middle atmosphere from TIMED/SABER. *Journal of Geophysical Research: Atmospheres*, 113(D17):n/a–n/a. D17101.
- Rezac, L., Kutepov, A., Russell III, J. M., Feofilov, A. G., Yue, J., and Goldberg, R. A. (2015). Simultaneous retrieval of T(p) and CO₂ VMR from two-channel non-LTE limb radiances and application to daytime SABER/TIMED measurements. *Journal of Atmospheric and Solar-Terrestrial Physics*, 130–131:23–42.
- Rodgers, C. D. (1990). Characterization and error analysis of profiles retrieved from remote sounding measurements. *Journal of Geophysical Research*, 95(D5):5587–5595.
- Rodgers, C. D. (2000). *Inverse methods for atmospheric sounding: Theory and practice*. Series on Atmospheric, Oceanic and Planetary Physics, Vol. 2. World Scientific.
- Rodrigo, R., López-Moreno, J. J., López-Puertas, M., and Molina, A. (1988). *Progress in Atmospheric Physics*, pages 3–32. Springer Netherlands.
- Russell, J. P., Lowe, R., and Ward, W. (2004). Atomic oxygen annual and semi-annual variations in the mesopause region for mid and equatorial latitudes. *Journal of Atmospheric and Solar-Terrestrial Physics*, 66(6–9):451–461.
- Russell III, J. M., Mlynczak, M. G., Gordley, L. L., Tansock, J., and Esplin, R. (1999). An overview of the SABER experiment and preliminary calibration results. *Space Dynamics Lab Publications*, pages 277–288.

- Sandu, A. and Sander, R. (2006). Technical note: Simulating chemical systems in Fortran90 and Matlab with the Kinetic PreProcessor KPP-2.1. *Atmospheric Chemistry and Physics*, 6(1):187–195.
- Scafetta, N. and Willson, R. C. (2013). Empirical evidences for a planetary modulation of total solar irradiance and the TSI signature of the 1.09-year Earth-Jupiter conjunction cycle. *Astrophysics and Space Science*, 348(1):25–39.
- Schmidt, C., Höppner, K., and Bittner, M. (2013). A ground-based spectrometer equipped with an InGaAs array for routine observations of OH(3-1) rotational temperatures in the mesopause region. *Journal of Atmospheric and Solar-Terrestrial Physics*, 102:125–139.
- Schmidt, H., Brasseur, G. P., Charron, M., Manzini, E., Giorgetta, M. A., Diehl, T., Fomichev, V. I., Kinnison, D., Marsh, D., and Walters, S. (2006). The HAMMONIA chemistry climate model: Sensitivity of the mesopause region to the 11-year solar cycle and CO₂ doubling. *Journal of Climate*, 19(16):3903–3931.
- Sedlak, R., Hannawald, P., Schmidt, C., Wüst, S., and Bittner, M. (2016). High-resolution observations of small-scale gravity waves and turbulence features in the OH airglow layer. *Atmospheric Measurement Techniques*, 9(12):5955–5963.
- Semenov, A. I. (1997). Long-term changes in the height profiles of ozone and atomic oxygen in the lower thermosphere. *Geomagnetism and Aeronomy*, 37(3):354–360.
- Semenov, A. I. and Shefov, N. N. (1997). The empirical model of nocturnal variations in the 557.7 nm emission of atomic oxygen: 3. Emitting layer altitude. *Geomagnetism and Aeronomy*, 37(4):470–474.
- Sharma, R. D., Wintersteiner, P. P., and Kalogerakis, K. S. (2015). A new mechanism for OH vibrational relaxation leading to enhanced CO₂ emissions in the nocturnal mesosphere. *Geophysical Research Letters*, 42(11):4639–4647.
- Sharp, W. E., Zaccheo, T. S., Browell, E. V., Ismail, S., Dobler, J. T., and Llewellyn, E. J. (2014). Impact of ambient O₂(a¹Δ_g) on satellite-based laser remote sensing of O₂ columns using absorption lines in the 1.27 μm region. *Journal of Geophysical Research: Atmospheres*, 119(12):7757–7772. 2013JD021324.
- Sheese, P. E., McDade, I. C., Gattinger, R. L., and Llewellyn, E. J. (2011). Atomic oxygen densities retrieved from Optical Spectrograph and InfraRed Imaging System observations of O₂ A-band airglow emission in the mesosphere and lower thermosphere. *Journal of Geophysical Research: Atmospheres*, 116(D1):n/a–n/a. D01303.
- Shematovich, V. I., Bisikalo, D. V., Krauss, S., Hausleitner, W., and Lammer, H. (2011). Influence of the hot oxygen corona on the satellite drag in the earth’s upper atmosphere. *Solar System Research*, 45(3):231–239.

- Sidorenkov, N. S. (2009). *The interaction between Earth's rotation and geophysical processes*. WILEY-VCH.
- Sima, D. M., Van Huffel, S., and Golub, G. H. (2004). Regularized Total Least Squares based on Quadratic Eigenvalue Problem Solvers. *BIT Numerical Mathematics*, 44(4):793–812.
- Skupin, J., Noël, S., Wuttke, M. W., Gottwald, M., Bovensmann, H., Weber, M., and Burrows, J. P. (2005). SCIAMACHY solar irradiance observation in the spectral range from 240 to 2380 nm. *Advances in space research*, 35(3):370–375.
- Slanger, T. G. and Copeland, R. A. (2003). Energetic oxygen in the upper atmosphere and the laboratory. *Chemical Reviews*, 103(12):4731–4766. PMID: 14664631.
- Slanger, T. G., Cosby, P. C., and Huestis, D. L. (2004a). Co-variation of nightglow emission from the $O_2(A^3\Sigma_u^+)$ and $O_2(c^1\Sigma_u^-)$ states and the oxygen green line, observed with the Keck I/II telescopes. *Journal of Atmospheric and Solar-Terrestrial Physics*, 66(6-9):617–622.
- Slanger, T. G., Cosby, P. C., and Huestis, D. L. (2004b). A new O_2 band system: The $c^1\Sigma_u^- - b^1\Sigma_g^+$ transition in the terrestrial nightglow. *Journal of Geophysical Research: Space Physics*, 108(A2):n/a–n/a. 1089.
- Smith, A. K. (2012). Global dynamics of the MLT. *Surveys in Geophysics*, 33(6):1177–1230.
- Smith, A. K., Marsh, D. R., and Szymczak, A. C. (2003). Interaction of chemical heating and the diurnal tide in the mesosphere. *Journal of Geophysical Research: Atmospheres*, 108(D5):n/a–n/a. 4164.
- Smith, G. P. and Robertson, R. (2008). Temperature dependence of oxygen atom recombination in nitrogen after ozone photolysis. *Chemical Physics Letters*, 458(1-3):6–10.
- Smith, I. W. M. (1984). The role of electronically excited states in recombination reactions. *International Journal of Chemical Kinetics*, 16(4):423–443.
- Snively, J. B., Pasko, V. P., and Taylor, M. J. (2010). OH and OI airglow layer modulation by ducted short-period gravity waves: Effects of trapping altitude. *Journal of Geophysical Research: Space Physics*, 115(A11).
- Snow, M., Weber, M., Machol, J., Viereck, R., and Richard, E. (2014). Comparison of Magnesium II core-to-wing ratio observations during solar minimum 23/24. *Journal of Space Weather and Space Climate*, 4:A04.
- Solheim, B. H. and Llewellyn, E. J. (1979). An indirect mechanism for the production of $O(^1S)$ in the aurora. *Planetary and Space Science*, 27(4):473–479.

- Solomon, S. C. and Qian, L. (2005). Solar extreme-ultraviolet irradiance for general circulation models. *Journal of Geophysical Research: Space Physics*, 110(A10).
- Solomon, S. C., Woods, T. N., Didkovsky, L. V., Emmert, J. T., and Qian, L. (2010). Anomalously low solar extreme-ultraviolet irradiance and thermospheric density during solar minimum. *Geophysical Research Letters*, 37(16):n/a–n/a. L16103.
- Steadman, J. A. and Thrush, B. A. (1994). A laboratory study of the mechanism of the oxygen airglow. *Journal of Atmospheric Chemistry*, 18(4):301–317.
- Stegman, J. and Murtagh, D. P. (1991). The molecular oxygen band systems in the U. V. nightglow: Measured and modelled. *Planetary and Space Science*, 39(4):595–609.
- Stevens, B., Giorgetta, M., Esch, M., Mauritsen, T., Crueger, T., Rast, S., Salzmann, M., Schmidt, H., Bader, J., Block, K., Brokopf, R., Fast, I., Kinne, S., Kornblueh, L., Lohmann, U., Pincus, R., Reichler, T., and Roeckner, E. (2013). Atmospheric component of the MPI-M Earth System Model: ECHAM6. *Journal of Advances in Modeling Earth Systems*, 5(2):146–172.
- Stott, I. P. and Thrush, B. A. (1989). Laboratory studies of the mechanism of the oxygen airglow. *Proceedings of the Royal Society of London A: Mathematical, Physical and Engineering Sciences*, 424(1866):1–17.
- Strelnikov, B., Szewczyk, A., Strelnikova, I., Latteck, R., Baumgarten, G., Lübken, F.-J., Rapp, M., Fasoulas, S., Löhle, S., Eberhart, M., Hoppe, U.-P., Dunker, T., Friedrich, M., Hedin, J., Khaplanov, M., Gumbel, J., and Barjatya, A. (2017). Spatial and temporal variability in MLT turbulence inferred from in situ and ground-based observations during the WADIS-1 sounding rocket campaign. *Annales Geophysicae*, 35(3):547–565.
- Sugiura, M. and Fanselau, G. (1966). Lunar phase numbers v and v' for years 1850–2050. *IAGA-IAMAP Joint Committee on Lunar Effects*, page 219. X-612-66-401.
- Swenson, G. R., Mende, S. B., and Llewellyn, E. J. (1989). Imaging observations of lower thermospheric $O(^1S)$ and O_2 airglow emissions from STS 9: Implications of height variations. *Journal of Geophysical Research: Space Physics*, 94(A2):1417–1429.
- Tapping, K. F. (2013). The 10.7cm solar radio flux (F10.7). *Space Weather*, 11(7):394–406.
- Thomas, G. E., Thurairajah, B., Hervig, M. E., von Savigny, C., and Snow, M. (2015). Solar-induced 27-day variations of mesospheric temperature and water vapor from the AIM SOFIE experiment: Drivers of polar mesospheric cloud variability. *Journal of Atmospheric and Solar-Terrestrial Physics*, 134:56–68.

- Thorne, A. P., Litzén, U., and Johansson, S. (1999). *Spectrophysics: Principles and applications*. Springer.
- Torr, M. R., Torr, D. G., and Laher, R. R. (1985). The O₂ atmospheric 0-0 band and related emissions at night from Spacelab 1. *Journal of Geophysical Research: Space Physics*, 90(A9):8525–8538.
- Torrence, C. and Webster, P. J. (1999). Interdecadal changes in the ENSO-Monsoon System. *Journal of Climate*, 12(8):2679–2690.
- Vlasov, M. N., Nicolls, M. J., Kelley, M. C., Smith, S. M., Aponte, N., and González, S. A. (2005). Modeling of airglow and ionospheric parameters at arecibo during quiet and disturbed periods in October 2002. *Journal of Geophysical Research: Space Physics*, 110(A7):n/a–n/a. A07303.
- von Savigny, C. (2017). Airglow in the Earth atmosphere: basic characteristics and excitation mechanisms. *ChemTexts*, 3(4):14.
- von Savigny, C., Eichmann, K.-U., Llewellyn, E. J., Bovensmann, H., Burrows, J. P., Bittner, M., Hppner, K., Offermann, D., Taylor, M. J., Zhao, Y., Steinbrecht, W., and Winkler, P. (2004). First near-global retrievals of OH rotational temperatures from satellite-based Meinel band emission measurements. *Geophysical Research Letters*, 31(15):n/a–n/a. L15111.
- von Savigny, C., Eichmann, K.-U., Robert, C. E., Burrows, J. P., and Weber, M. (2012a). Sensitivity of equatorial mesopause temperatures to the 27-day solar cycle. *Geophysical Research Letters*, 39(21):n/a–n/a. L21804.
- von Savigny, C. and Lednyts'kyi, O. (2013). On the relationship between atomic oxygen and vertical shifts between OH Meinel bands originating from different vibrational levels. *Geophysical Research Letters*, 40(21):5821–5825.
- von Savigny, C., Lednyts'kyi, O., Forbes, J. M., and Zhang, X. (2015). Lunar semidiurnal tide in the terrestrial airglow. *Geophysical Research Letters*, 42(9):3553–3559.
- von Savigny, C., McDade, I. C., Eichmann, K.-U., and Burrows, J. P. (2012b). On the dependence of the OH* meinel emission altitude on vibrational level: SCIAMACHY observations and model simulations. *Atmospheric Chemistry and Physics*, 12(18):8813–8828.
- Ward, W. E. (1999). A simple model of diurnal variations in the mesospheric oxygen nightglow. *Geophysical Research Letters*, 26(23):3565–3568.
- Wei, Y., Pu, Z., Zong, Q., Wan, W., Ren, Z., Fraenz, M., Dubinin, E., Tian, F., Shi, Q., Fu, S., and Hong, M. (2014). Oxygen escape from the Earth during geomagnetic reversals: Implications to mass extinction. *Earth and Planetary Science Letters*, 394:94 – 98.

- Wraight, P. C. (1982). Association of atomic oxygen and airglow excitation mechanisms. *Planetary and Space Science*, 30(3):251–259.
- Wu, Y. J., Williams, E., Chang, S. C., Chou, J. K., Hsu, R. R., Friedrich, M., Kuo, C. L., Chen, A. B., Peng, K. M., Su, H. T., Frey, H. U., Mende, S. B., Takahashi, Y., and Lee, L. C. (2017). The leading role of atomic oxygen in the collocation of elves and hydroxyl nightglow in the low-latitude mesosphere. *Journal of Geophysical Research: Space Physics*, pages n/a–n/a. 2016JA023681.
- Yankovsky, V. A., Kuleshova, V. A., Manuilova, R. O., and Semenov, A. O. (2007). Retrieval of total ozone in the mesosphere with a new model of electronic-vibrational kinetics of O₃ and O₂ photolysis products. *Izvestiya, Atmospheric and Oceanic Physics*, 43(4):514–525.
- Yankovsky, V. A., Martysenko, K. V., Manuilova, R. O., and Feofilov, A. G. (2016). Oxygen dayglow emissions as proxies for atomic oxygen and ozone in the mesosphere and lower thermosphere. *Journal of Molecular Spectroscopy*, 327(Supplement C):209 – 231. New Visions of Spectroscopic Databases, Volume II.
- Young, R. A. and Sharpless, R. L. (1963). Chemiluminescent reactions involving atomic oxygen and nitrogen. *The Journal of Chemical Physics*, 39(4):1071–1102.
- Yung, Y. L. and DeMore, W. B. (1998). *Photochemistry of Planetary Atmospheres*. Oxford University Press.
- Zechmeister, M. and Kürster, M. (2009). The generalised Lomb-Scargle periodogram. A new formalism for the floating-mean and Keplerian periodograms. *Astronomy and Astrophysics*, 496(2):577–584.
- Zhu, Y., Kaufmann, M., Ern, M., and Riese, M. (2015). Nighttime atomic oxygen in the mesopause region retrieved from SCIAMACHY O(¹S) green line measurements and its response to solar cycle variation. *Journal of Geophysical Research: Space Physics*, 120(10):9057–9073. 2015JA021405.

Appendix

A. Articles of the cumulative doctoral thesis

Author contributions

Article I: von Savigny, C., and Lednyts'kyi, O.: On the relationship between atomic oxygen and vertical shifts between OH Meinel bands originating from different vibrational levels, *Geophysical Research Letters*, **40**, 21, 5821–5825, DOI: 10.1002/2013GL058017, 2013.

O. Lednyts'kyi retrieved time series of volume emission rate (VER) of the oxygen green line emission ($\text{VER}\{\text{O}(^1S - ^1D)\}$) and time series of atomic oxygen concentrations ($[\text{O}(^3P)]$). C. von Savigny retrieved VER time series of OH(3-1) and OH(6-2). C. von Savigny analyzed all time series and demonstrated that vertical shifts between the two OH bands are correlated with $[\text{O}(^3P)]$. The manuscript was written by C. von Savigny and edited by O. Lednyts'kyi.

Article II: Lednyts'kyi, O., von Savigny, C., Eichmann, K.-U., and Mlynczak, M. G.: Atomic oxygen retrievals in the MLT region from SCIAMACHY night-glow limb measurements, *Atmospheric Measurement Techniques*, **8**, 3, 1021–1041, DOI:10.5194/amt-8-1021-2015, 2015.

O. Lednyts'kyi retrieved time series of limb emission rate (LER) of the oxygen green line emission ($\text{LER}\{\text{O}(^1S - ^1D)\}$), $\text{VER}\{\text{O}(^1S - ^1D)\}$ and $[\text{O}(^3P)]$. O. Lednyts'kyi analyzed all time series and analyzed time series of $[\text{O}(^3P)]$ retrieved on the basis of such atmospheric parameters as temperature, atmospheric density and $[\text{O}(^3P)]$ as well as SCIAMACHY $\text{VER}\{\text{O}(^1S - ^1D)\}$ profiles. C. von Savigny advised the implementation of the $\text{LER}\{\text{O}(^1S - ^1D)\}$ retrieval and suggested to employ three sources of the mentioned atmospheric parameters. C. von Savigny negotiated to obtain time series of $[\text{O}(^3P)]$ simulated using the SD-WACCM4 model. K.-U. Eichmann provided SCIAMACHY spectral measurements required to retrieve time series of $\text{LER}\{\text{O}(^1S - ^1D)\}$. M. Mlynczak provided time series of the mentioned atmospheric parameters measured using the SABER instrument. The manuscript was written by O. Lednyts'kyi, edited by C. von Savigny and commented by other co-authors.

Article III: von Savigny, C., Lednyts'kyi, O., Forbes, J., and Zhang, X.: Lunar semidiurnal tide in the terrestrial airglow, *Geophysical Research Letters*, **42**, 9, 3553–3559, DOI: 10.1002/2015GL063567, 2015.

O. Lednyts'kyi retrieved and analyzed time series of lunar phase angles, $\text{VER}\{\text{O}(^1S - ^1D)\}$ and $[\text{O}(^3P)]$. C. von Savigny retrieved and analyzed time series of OH(3-1) emission rates, OH emission altitude and OH(3-1) rotational temperature. J. Forbes and X. Zhang provided time series of the vertical lunar tidal winds simulated using the GSWM-09 model. The manuscript was written by C. von Savigny and co-edited by O. Lednyts'kyi, J. Forbes and X. Zhang.

Article IV: Lednyts'kyi, O., von Savigny, C., and Weber, M.: Sensitivity of equatorial atomic oxygen in the MLT region to the 11-year and 27-day solar cycles, *Journal of Atmospheric and Solar-Terrestrial Physics*, **162**, 136–150, DOI: 10.1016/j.jastp.2016.11.003, 2017.

The article IV is only available to subscribers of the journal.

O. Lednyts'kyi retrieved time series of $\text{VER}\{\text{O}(^1S - ^1D)\}$ and $[\text{O}(^3P)]$. O. Lednyts'kyi analyzed these time series and those of the solar proxies: MgII index and Lyman- α . C. von Savigny advised the implementation of cross-correlation, superposed epoch analysis and the linear-regression methods applied to estimate sensitivity. O. Lednyts'kyi implemented all methods including the multiple-linear regression. M. Weber provided time series of MgII index. The manuscript was written by O. Lednyts'kyi and co-edited by C. von Savigny and M. Weber.

Article V: Lednyts'kyi, O., and von Savigny, C.: Photochemical modeling of molecular and atomic oxygen based on multiple *in-situ* emissions measured during the Energy Transfer in the Oxygen Nightglow rocket campaign, *Atmospheric Chemistry and Physics Discussions*, **2019**, 1–60, DOI: 10.5194/acp-2019-221, in review, 2019.

O. Lednyts'kyi worked out the concept of the MAC approach proposed by Torr et al. (1985), developed corresponding software, performed needed computations and prepared the manuscript of the article. C. von Savigny contributed to planning the work activities regarding the article, discussed the results, contributed to the manuscript of the article, corrected and edited it.

Article VI: Lednyts'kyi, O., von Savigny, C., Sinnhuber, M., Iwagami, N., and Mlynczak, M.: Multiple Airglow Chemistry approach for atomic oxygen retrievals on the basis of *in situ* nightglow emissions, *Journal of Atmospheric and Solar-Terrestrial Physics*, **194**, 105096, DOI: 10.1016/j.jastp.2019.105096, 2019.

The article VI is only available to subscribers of the journal.

O. Lednyts'kyy: Conceptualization, Data curation, Formal analysis, Investigation, Methodology, Resources, Software, Validation, Visualization, Writing - original draft, Writing - review & editing. C. von Savigny: Formal analysis, Funding acquisition, Investigation, Project administration, Resources, Supervision, Writing - review & editing. M. Sinnhuber: Formal analysis, Funding acquisition, Investigation, Project administration, Resources, Supervision, Writing - review & editing. N. Iwagami: Data curation, Formal analysis, Investigation, Resources, Supervision, Writing - review & editing. M. Mlynczak: Data curation, Investigation, Resources, Supervision, Writing - review & editing.

The place and date of approval: Greifswald, November 18, 2019

Signature of Olexandr Lednyts'kyy:

The place and date of approval: Greifswald, November 18, 2019

Signature of the supervisor
Christian von Savigny:

Article I

von Savigny, C., and Lednyts'kyy, O.: On the relationship between atomic oxygen and vertical shifts between OH Meinel bands originating from different vibrational levels, *Geophysical Research Letters*, **40**, 21, 5821–5825, DOI: 10.1002/2013GL058017, 2013.

On the relationship between atomic oxygen and vertical shifts between OH Meinel bands originating from different vibrational levels

C. von Savigny¹ and O. Lednyts'kyi¹

Received 13 September 2013; revised 16 October 2013; accepted 22 October 2013; published 4 November 2013.

[1] OH Meinel emissions from different vibrational levels are known to occur at slightly different altitudes in the terrestrial airglow. Earlier model studies suggested quenching by atomic oxygen to be a principal cause of these vertical shifts. Here we employ the tropical mesopause region—characterized by pronounced semiannual variations—as a natural laboratory to test the hypothesis that vertical shifts between different OH Meinel bands are a consequence of quenching by atomic oxygen. Nighttime satellite measurements of OH(3–1) and OH(6–2) volume emission rate profiles and atomic oxygen with Scanning Imaging Absorption Spectrometer for Atmospheric Chartography on Envisat are used for this purpose. Upper mesospheric atomic oxygen profiles are retrieved from measurements of the O(¹S–¹D) green line emission. The results demonstrate that vertical shifts between the OH bands investigated are indeed correlated with the amount of atomic oxygen in the upper mesosphere, corroborating the hypothesis. **Citation:** von Savigny, C., and O. Lednyts'kyi (2013), On the relationship between atomic oxygen and vertical shifts between OH Meinel bands originating from different vibrational levels, *Geophys. Res. Lett.*, 40, 5821–5825, doi:10.1002/2013GL058017.

1. Introduction

[2] The OH Meinel bands are one of the most prominent features of the terrestrial airglow. They are caused by the exothermic recombination of O₃ and H and lead to a global emission layer with a mean nighttime altitude of about 87 km and a width of 8–10 km. Spectrally resolved observations of OH emissions allow retrievals of OH rotational temperature and provide important information on middle atmospheric climate change [e.g., *Espy and Stegman*, 2002]. One critical aspect for the interpretation of these temperature time series is the altitude and shape of the OH emission layer. Long-term or solar cycle variations in the OH emission rate profile will complicate the determination of OH rotational temperature changes. Another important aspect is the finding that OH Meinel emissions from different vibrational levels are associated with different vertical emission rate profiles [e.g., *Adler-Golden*, 1997]. In a recent study, *von Savigny et al.* [2012a] used Scanning Imaging Absorption Spectrometer for Atmospheric Chartography (SCIAMACHY) satellite observations and model results to show that the

OH(ν') emissions originating from different vibrational levels ν' do not peak at the same altitude, but emissions from higher levels are shifted upward by roughly 0.5 km per vibrational level. Model simulations suggested that the vertical shifts are mainly due to quenching by atomic oxygen. Qualitatively, the vertical shifts occur, because the lifetime of OH(ν') increases with decreasing vibrational level ν' , making quenching by O more likely for smaller ν' . This—in combination with the vertical gradient of atomic oxygen around 87 km—leads to the observed vertical shifts between OH(ν') emissions from different ν' . In this study we use SCIAMACHY measurements of OH(3–1) and OH(6–2) emission rate profiles at wavelengths of about 1500 nm and 835 nm, respectively, as well as atomic oxygen density profiles to experimentally test the hypothesis, whether vertical shifts between different Meinel emission bands are indeed correlated to the amount of atomic oxygen.

2. Brief Instrumental Description

[3] SCIAMACHY, the Scanning Imaging Absorption Spectrometer for Atmospheric Chartography [*Bovensmann et al.*, 1999] on Envisat was a grating spectrometer with eight spectral channels observing scattered, reflected, and transmitted solar radiation in nadir, limb scatter, and solar/lunar occultation geometry in the 220 nm to 2380 nm spectral range. Additionally, limb emission measurements were performed on the Earth's nightside covering the 75–150 km tangent height range. Envisat was launched on 1 March 2002 into a polar, sun-synchronous orbit with a 10:00 A.M. descending node. The Envisat mission ended unexpectedly on 8 April 2012 due to a spacecraft failure. For this study we only employed nighttime limb observations carried out at a fixed local solar time of around 22:00 LT (local time). The nighttime limb measurements are only made throughout the year at latitudes between 0° and 30°N. In terms of the stability of the SCIAMACHY tangent height information, *Bramstedt et al.* [2012] found tangent height drifts of less than 20 m/yr.

3. Data Products

3.1. OH(3–1) and OH(6–2) Volume Emission Rate Profiles

[4] The OH volume emission rate profiles were retrieved from SCIAMACHY limb observations of the OH(3–1) and OH(6–2) bands using the same technique and wavelength range (1515–1546 nm for the OH(3–1) band and 837.5–848 nm for the OH(6–2) band, respectively) as in *von Savigny et al.* [2012a]. The only difference is that the inversion was applied to individual measurements rather than monthly averaged data. An example of the time and altitude

¹Institute of Physics, Ernst-Moritz-Arndt-University of Greifswald, Greifswald, Germany.

Corresponding author: C. von Savigny, Institute of Physics, Ernst-Moritz-Arndt-University of Greifswald, Greifswald, Germany. (csavigny@physik.uni-greifswald.de)

©2013. American Geophysical Union. All Rights Reserved.
0094-8276/13/10.1002/2013GL058017

dependence of the OH(3–1) volume emission rates is shown in Figure 1b. Based on the OH(3–1) and OH(6–2) volume emission rate (VER) profiles, mean emission altitudes $z_{\text{OH}(3-1/6-2)}$ were determined by weighting altitude with the VER profile:

$$z_{\text{OH}} = \frac{\int_0^{\infty} \text{VER}(z') z' dz'}{\int_0^{\infty} \text{VER}(z') dz'} \quad (1)$$

[5] Monthly and zonal averages of these weighted emission altitudes are displayed in Figure 1c. The OH(6–2) and OH(3–1) emission altitudes differ by about 1–1.5 km, as expected.

3.2. Atomic Oxygen Profile Retrievals

[6] Atomic oxygen density profiles in the mesopause region were derived from monthly and zonally averaged vertical volume emission rate profiles of the oxygen O(¹S–¹D) green line at 557.7 nm also retrieved from SCIAMACHY nighttime limb measurements. The photochemical model is based on a two-step Barth transfer scheme and model parameters by McDade *et al.* [1986]. In addition to the reactions considered by McDade *et al.* [1986], quenching of O(¹S) by ground state atomic oxygen was also taken into account [Khomich *et al.*, 2008]. The uncertainty of measured green line limb emission rates is determined as the signal standard deviation in the emission-free part of spectrum around the green line emission. The inversion to vertical volume emission rate profiles was regularized using a total least squares method [Sima *et al.*, 2004]. The uncertainty of the derived atomic oxygen density profiles contains contributions from photochemical parameter uncertainty, smoothing error, and measurement noise. In this study, temperature, O₂, and N₂ density profiles are taken from the NRLMSISE-00 atmospheric model [Picone *et al.*, 2002]. Sample green line volume emission rate and inferred atomic oxygen profiles—monthly and zonally averaged for January 2008 and latitudes between 0° and 10° N—are shown in Figure 2. The oxygen green line volume emission rate profiles and the retrieved atomic oxygen profiles are in good agreement with other published results [e.g., Russell and Lowe, 2003; Shepherd *et al.*, 2006].

[7] Note that the SCIAMACHY O green line observations were performed simultaneously with the measurements of OH emission rates and OH rotational temperatures which are also used in this study.

3.3. OH(3–1) Rotational Temperature Measurements

[8] OH(3–1) rotational temperatures are derived from SCIAMACHY limb emission observations of the P_{1/2}(2) to P_{1/2}(4) rotational lines of the OH(3–1) Meinel band on the Earth's nightside, as described by von Savigny *et al.* [2012b]. Temperature is retrieved from limb emission spectra at about 85 km tangent height. The mean emission altitude—weighted by the vertical emission rate profile—is then similar to that of ground-based observations, i.e., about 87 km.

4. Results and Discussion

[9] We first discuss the general behavior of the observed parameters, before addressing the relationship between atomic oxygen and the vertical shifts between different OH

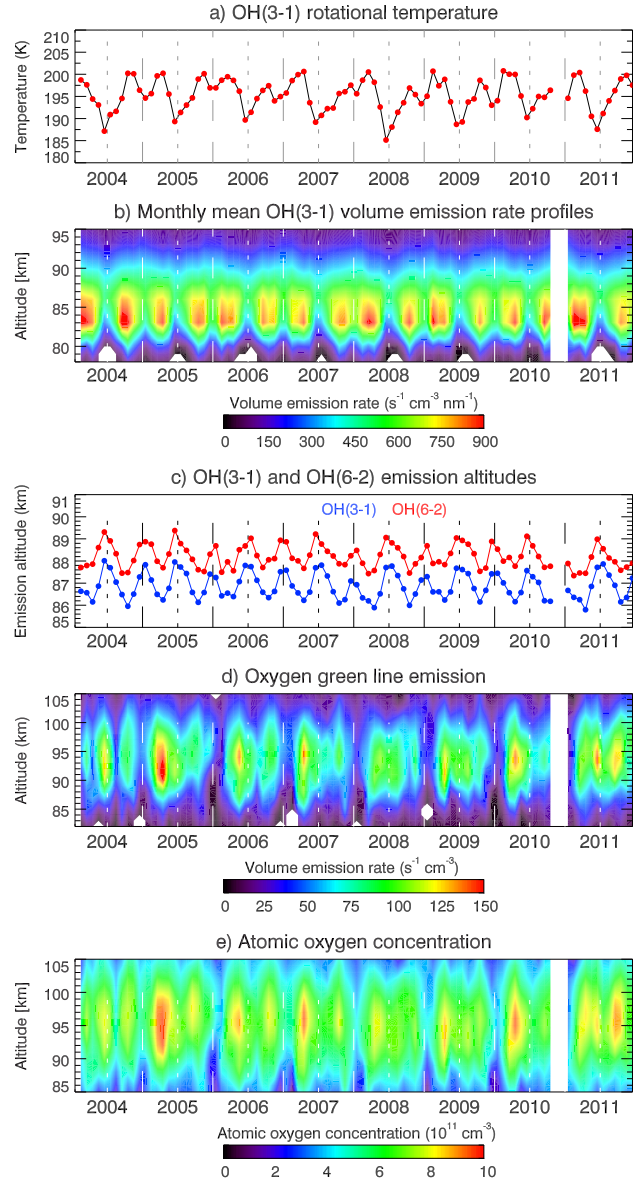


Figure 1. Time series of monthly and zonally averaged parameters retrieved from SCIAMACHY nightglow measurements for the period January 2004 to December 2011 and the 0° to 10°N latitude bin. (a) OH(3–1) rotational temperature; (b) OH(3–1) volume emission rate; (c) OH(6–2) and OH(3–1) emission altitudes weighted by the corresponding emission rate profile; (d) oxygen green line volume emission rate; (e) atomic oxygen concentration. The missing data in January 2004 and November and December 2010 are due to gaps in SCIAMACHY nighttime limb measurements.

Meinel bands. Figure 1 shows the time series of all parameters introduced above for the period from January 2004 to December 2011 and for the 0°–10°N latitude range. The year 2003 is not included in the present analysis, because several longer gaps exist in nighttime limb measurements in 2003. All quantities displayed show pronounced semiannual variations with equinox maxima for OH rotational temperature, OH emission rate, green line emission rate, and atomic oxygen, in agreement with previous experimental and

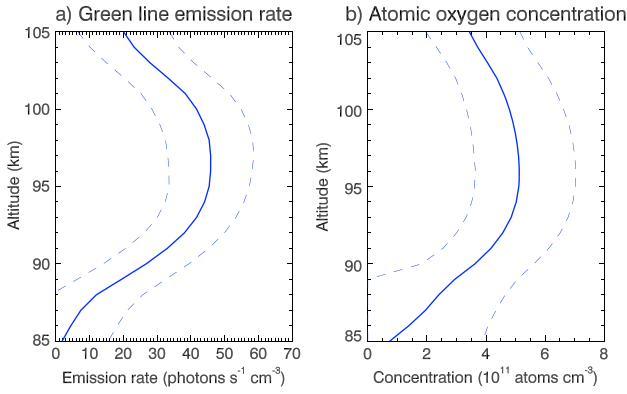


Figure 2. (a) Sample monthly and zonally averaged O(¹S–¹D) volume emission rate profile retrieved from SCIAMACHY limb measurements in April 2007 and for the 0°–10°N latitude band. The dashed lines indicate the uncertainty of the monthly mean emission rate profile. (b) Atomic oxygen concentration profile inferred from the volume emission rate profile shown in Figure 2a using the methodology described in the text. The dashed lines indicate the oxygen concentration uncertainty.

modeling studies [e.g., Liu *et al.*, 2008]. The weighted OH(6–2) and OH(3–1) emission altitudes, however, assume minima around equinox. According to Marsh *et al.* [2006], the semiannual variation in OH emission rate at low latitudes is a consequence of the semiannual variation of the amplitude of the diurnal tide—with maxima around equinox. Because of the strong tidal modulation of the OH and oxygen green line airglow emissions [e.g., Zhang *et al.*, 2001], it is important to remember that SCIAMACHY samples the atmosphere at 22:00 LT for the measurements used here.

[10] Temperature maxima near the equinoxes are indicative of enhanced downward transport associated with adiabatic heating. The enhanced downward motion—relative to solstice conditions—is also consistent with enhanced atomic oxygen concentrations and subsequently enhanced oxygen green line and OH emission rates as well as minima in OH emission altitudes.

[11] We now use the quantities retrieved from SCIAMACHY nightglow measurements for testing the hypothesis that the vertical shift between the OH(6–2) and the OH(3–1) emission rate profiles is affected by the abundance of atomic oxygen. We first use an indirect method employing the OH(3–1) emission altitude as an inverse proxy for the amount of atomic oxygen. As Figure 1 demonstrates, the mean OH emission altitude and the atomic oxygen concentration are anti-correlated, consistent with the heuristic argument of downward transport of atomic oxygen [e.g., Cho and Shepherd, 2006]. We now select three latitude bins of 10° width between the equator and 30°N. These specific latitude bins were chosen, because (a) only there the SCIAMACHY nighttime limb emission measurements cover the entire year and (b) the strong semiannual variation in mesopause parameters at low latitudes—including atomic oxygen—can be expected to lead to an observable variation in the vertical shifts between the OH(6–2) and the OH(3–1) bands. The Figure 3 (left column) shows scatterplots of the dependence of the mean altitude difference between the OH(6–2) and the

OH(3–1) bands on the mean OH(3–1) altitude. The small blue points correspond to individual months, and the larger red points show the averaged seasonal cycle, i.e., averages over all Januaries, Februaries, etc. Apparently, the plotted quantities are anti-correlated with correlation coefficients varying between –0.38 and –0.43 for individual months and between –0.49 and –0.82 for the average seasonal cycle. Considering the relatively large total number of months analyzed (i.e., 93), the correlation coefficients for the individual month time series are significant at the 99% confidence level. Because of the negative correlation between atomic oxygen and the mean OH emission altitude, the results are consistent with a positive correlation between atomic oxygen and the vertical shift between the mean OH(6–2) and OH(3–1) emission altitudes.

[12] In the next step, we use atomic oxygen retrievals directly to check whether seasonally enhanced atomic oxygen is associated with larger vertical shifts between the OH(6–2) and the OH(3–1) bands. Rather than using atomic

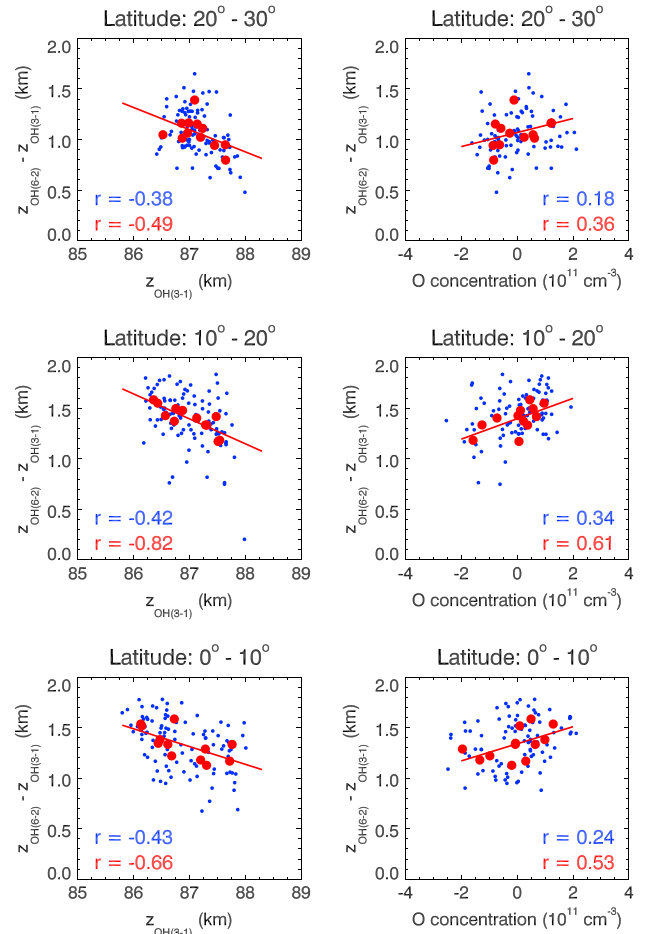


Figure 3. (left column) Dependence of the difference in mean OH(6–2) and OH(3–1) emission altitudes on the mean OH(3–1) emission altitude for different latitude bins. (right column) Dependence of the difference in mean OH(6–2) and OH(3–1) emission altitudes on the anomaly of the atomic oxygen amount weighted by the OH(6–2) emission rate profile. Small blue circles correspond to individual months, and the larger red circles show averages over all Januaries, Februaries, etc.

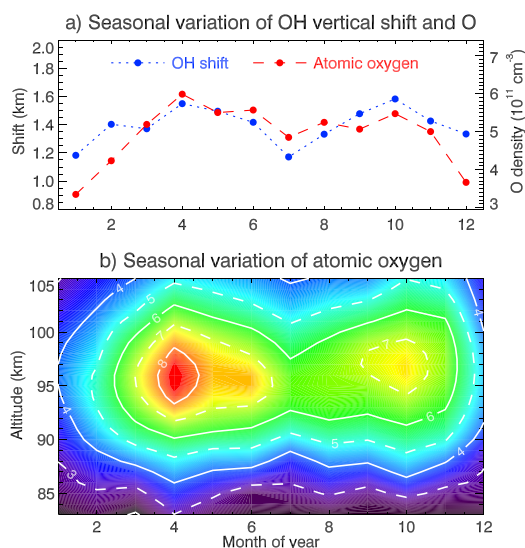


Figure 4. (a) Average seasonal variation of the difference in mean OH(6-2) and OH(3-1) emission altitude (blue circles and dotted line) and the atomic oxygen profile weighted by the OH(6-2) emission rate profiles (red circles and dashed line). (b) Average seasonal and altitude variation of retrieved atomic oxygen concentrations. Both panels correspond to the 10°N–20°N latitude range.

oxygen concentrations at a fixed altitude or within a fixed altitude range, we weighted the atomic oxygen profile with the OH(6-2) volume emission rate profile, in order to properly consider the seasonal variation of the OH emission altitude. Additionally, to reduce the effect of the atomic oxygen changes associated with the 11 year solar cycle, we determined an atomic oxygen anomaly time series by removing the 12 month running mean from the OH-weighted oxygen profile time series. The Figure 3 (right column) shows scatterplots of the dependence of the OH-weighted altitude difference on atomic oxygen anomalies for the same three latitude bins. Again, the small blue circles show individual months, while the larger red circles display the averaged seasonal cycle. The correlation coefficients range from 0.18–0.34 for the individual months and from 0.36–0.61 for the average seasonal cycle. In terms of the individual month time series, correlation coefficients exceeding 0.21 and 0.27, respectively, are significant at the 95% and 99% confidence levels, respectively.

[13] Figure 4a shows the mean seasonal cycle—averaged over all years considered—in OH profile weighted atomic oxygen and the difference in mean OH(6-2) and OH(3-1) emission altitude for the 10°N–20°N latitude bin. Both quantities show a semiannual variation, as expected from Figure 1, but the atomic oxygen time series also has a discernible annual component with a minimum at the beginning of the year. This may indicate that quenching by atomic oxygen is not the only process affecting the vertical shifts between different Meinel bands. The annual component in atomic oxygen is also seen in Figure 4b, showing the seasonal and altitude variation of atomic oxygen.

[14] In summary, the results are consistent with the hypothesis that vertical shifts between different Meinel bands are at least partly caused by quenching by atomic oxygen. This finding is—to our best knowledge—reported here

for the first time and confirms the model simulations by *von Savigny et al.* [2012a].

[15] We now briefly discuss the implications of this finding for ground-based rotational temperature measurements. The seasonally varying vertical shift between the OH(6-2) and the OH(3-1) bands will introduce a variable shift in altitude ranges sampled by spectrometers observing different OH Meinel bands. The vertical shifts vary by about 0.5 km (Figure 3). This effect is therefore significantly smaller than the semiannual altitude variation of the individual OH emissions, reaching 2 km peak to peak (see Figure 1c). Based on the estimates by *von Savigny et al.* [2012a], a 2 km shift in emission altitude changes the observed temperature by about 2.5 K, because a slightly different altitude region is sampled.

5. Conclusions

[16] SCIAMACHY measurements of OH emission rate profiles and atomic oxygen in the nighttime low-latitude mesopause region were used to test the hypothesis that vertical shifts between different OH Meinel bands are caused by quenching by atomic oxygen. The OH(6-2) and OH(3-1) bands were studied for this purpose, and atomic oxygen concentration profiles were derived from simultaneous observations of the oxygen green line emission. The results demonstrate that the difference in mean OH(6-2) and OH(3-1) emission altitudes is indeed positively correlated with the amount of atomic oxygen. The seasonal variability of the mean emission altitude difference between the OH(6-2) and the OH(3-1) bands is only about 0.5 km. However, because of the importance of OH rotational temperature measurements for our understanding of middle atmosphere climate change, all physical and chemical processes affecting variability in OH emission altitude need to be understood.

[17] **Acknowledgments.** This work was supported Ernst-Moritz-Arndt-University of Greifswald. The authors are indebted to K.-U. Eichmann for assistance with the handling of SCIAMACHY data. SCIAMACHY is jointly funded by Germany, the Netherlands, and Belgium.

[18] The Editor thanks Gordon Shepherd for his assistance in evaluating this paper.

References

- Adler-Golden, S. (1997), Kinetic parameters for OH nightglow modeling consistent with recent laboratory measurements, *J. Geophys. Res.*, **102**, 19,969–19,976.
- Bovensmann, H., et al. (1999), SCIAMACHY: Mission objectives and measurement modes, *J. Atmos. Sci.*, **56**, 127–150.
- Bramstedt, K., et al. (2012), Precise pointing knowledge for SCIAMACHY solar occultation measurements, *Atmos. Meas. Tech.*, **5**, 2867–2880.
- Cho, Y.-M., and G. G. Shepherd (2006), Correlation of airglow temperature and emission rate at Resolute Bay (74.68°N), over four winters (2001–2005), *Geophys. Res. Lett.*, **33**, L06815, doi:10.1029/2005GL025298.
- Espy, P. J., and J. Stegman (2002), Trends and variability of mesospheric temperature at high latitudes, *Phys. Chem. Earth*, **27**, 543–553.
- Khomich, V. Y., A. I. Semenov, and N. N. Shefov (2008), *Airglow as an Indicator of Upper Atmospheric Structure and Dynamics*, 739 p., Springer, Berlin, Germany.
- Liu, G., G. G. Shepherd, and R. G. Roble (2008), Seasonal variations of the nighttime O(¹S) and OH airglow emission rates at mid-to-high latitudes in the context of the large-scale circulation, *J. Geophys. Res.*, **113**, A06302, doi:10.1029/2007JA012854.
- Marsh, D. R., A. K. Smith, M. G. Mlynarczyk, and J. M. Russell III (2006), SABER observations of the OH Meinel airglow variability near the mesopause, *J. Geophys. Res.*, **111**, A10S05, doi:10.1029/2005JA011451.
- McDade, I. C., et al. (1986), ETON 2: Quenching parameters for the precursors of O₂(b¹Σ_g⁺) and O(¹S) in the terrestrial nightglow, *Planet. Space Sci.*, **34**, 789–800.
- Picone, J. M., A. E. Hedin, D. P. Drob, and A. C. Aikin (2002), NRLMSISE-00 empirical model of the atmosphere: Statistical

- comparisons and scientific issues, *J. Geophys. Res.*, *107*(A12), 1468, doi:10.1029/2002JA009430.
- Russell, J. P., and R. P. Lowe (2003), Atomic oxygen profiles (80–94 km) derived from Wind Imaging Interferometer/Upper Atmospheric Research Satellite measurements of the hydroxyl airglow: 1. Validation of technique, *J. Geophys. Res.*, *108*(D21), 4662, doi:10.1029/2003JD003454.
- Shepherd, M. G., G. Liu, and G. G. Shepherd (2006), Mesospheric semi-annual oscillation in temperature and nightglow emission, *J. Atmos. Sol. Terr. Phys.*, *68*(3-5), 379–389.
- Sima, S. M., S. van Huffel, and G. H. Golub (2004), Regularized total least squares based on quadratic eigenvalue solvers, *BIT Numer. Math.*, *44*, 739–812.
- von Savigny, C., I. C. McDade, K.-U. Eichmann, and J. P. Burrows (2012a), On the dependence of the OH* Meinel emission altitude on vibrational level: SCIAMACHY observations and model results, *Atmos. Chem. Phys.*, *12*, 8813–8828.
- von Savigny, C., K.-U. Eichmann, C. E. Robert, J. P. Burrows, and M. Weber (2012b), Sensitivity of equatorial mesopause temperatures to the 27-day solar cycle, *Geophys. Res. Lett.*, *39*, L21804, doi:10.1029/2012GL053563.
- Zhang, S. P., R. G. Roble, and G. G. Shepherd (2001), Tidal influence on the oxygen and hydroxyl nightglows: Wind Imaging Interferometer observations and thermosphere/ionosphere/mesosphere electrodynamics general circulation model, *J. Geophys. Res.*, *106*(A10), 21,381–21,393.

Article II

Lednyts'kyy, O., von Savigny, C., Eichmann, K.-U., and Mlynczak, M. G.: Atomic oxygen retrievals in the MLT region from SCIAMACHY nightglow limb measurements, *Atmospheric Measurement Techniques*, **8**, 3, 1021–1041, DOI:10.5194/amt-8-1021-2015, 2015.



Atomic oxygen retrievals in the MLT region from SCIAMACHY nightglow limb measurements

O. Lednyts'kyy¹, C. von Savigny¹, K.-U. Eichmann², and M. G. Mlynczak³

¹Institute of Physics, Ernst-Moritz-Arndt-University of Greifswald, Greifswald, Germany

²Institute of Environmental Physics, University of Bremen, Bremen, Germany

³NASA Langley Research Center, Hampton, VA, USA

Correspondence to: O. Lednyts'kyy (olexandr.lednytskyy@uni-greifswald.de)

Received: 10 September 2014 – Published in Atmos. Meas. Tech. Discuss.: 30 October 2014

Revised: 30 January 2015 – Accepted: 6 February 2015 – Published: 4 March 2015

Abstract. Vertical distributions of atomic oxygen concentration ([O]) in the mesosphere and lower thermosphere (MLT) region were retrieved from sun-synchronous SCIAMACHY/Envisat (SCanning Imaging Absorption spectroMeter for Atmospheric CHartographY on board the Environmental Satellite) limb measurements of the oxygen 557.7 nm green line emission in the terrestrial nightglow. A band pass filter was applied to eliminate contributions from other emissions, the impact of measurement noise and auroral activity. Vertical volume emission rate profiles were retrieved from integrated limb-emission rate profiles under the assumption that each atmospheric layer is horizontally homogeneous and absorption and scattering can be neglected. The radiative transfer problem was solved using regularized total least squares minimization in the inversion procedure. Atomic oxygen concentration profiles were retrieved from data collected for altitudes in the range 85–105 km with approximately 4 km vertical resolution during the time period from August 2002 to April 2012 at approximately 22:00 local time. The retrieval of [O] profiles was based on the generally accepted two-step Barth transfer scheme including consideration of quenching processes and the use of different available sources of temperature and atmospheric density profiles. A sensitivity analysis was performed for the retrieved [O] profiles to estimate maximum uncertainties assuming independent contributions of uncertainty components. Errors in photochemical model parameters depending on temperature uncertainties and random errors of model parameters contribute less than 50 % to the overall [O] retrieval error. The retrieved [O] profiles were compared with reference [O] profiles provided by SABER/TIMED (Sounding of the At-

mosphere using Broadband Emission Radiometry instrument on board the Thermosphere, Ionosphere, Mesosphere Energetics and Dynamics satellite) or by the NRLMSISE-00 (Naval Research Laboratory Mass Spectrometer and Incoherent Scatter radar Extended model, year: 2000) and SD-WACCM4 (Whole Atmosphere Community Climate Model with Specified Dynamics, version 4). A comparison of the retrieved [O] profiles with the reference [O] profiles led to the conclusion that the photochemical model taking into account quenching of O(¹S) by O₂, O(³P), and N₂ and the SABER/TIMED model as a source of temperature and density profiles are the most appropriate choices for our case. The retrieved [O] profile time series exhibits characteristic seasonal variations in agreement with satellite observations based on analysis of OH Meinel band emissions and atmospheric models. A pronounced 11-year solar cycle variation can also be identified in the retrieved atomic oxygen concentration time series.

1 Introduction

Atomic oxygen (O) is the most abundant chemically active trace gas in the Earth's mesosphere/lower thermosphere (MLT) region. It plays a critical role for O₃ and indirectly for OH* formation as well as the energy balance in the MLT region. Being generated through photolysis of molecular oxygen by ultraviolet radiation during daytime, atomic oxygen is subsequently destroyed through three-body recombination and other chemical processes. Atomic oxygen fuels exothermic chemical reactions (Mlynczak and Solomon,

1993) and causes radiative cooling of the MLT region that occurs through collisions of O with molecules (CO_2 , NO), later resulting in infrared emissions (Jursa, 1985). The green line emission of $\text{O}(^1\text{S}-^1\text{D})$ is visible at night due to the long photochemical lifetime (on the order of months at 100 km altitude) of ground state atomic oxygen $\text{O}(^3\text{P})$, which is excited to $\text{O}(^1\text{S})$ through the two-step process known as the Barth transfer scheme.

Decades of ground-based observations of the $\text{O}(^1\text{S}-^1\text{D})$ airglow emission rate (first performed by the fourth Baron Rayleigh in 1928; Egerton, 1949) were followed by rocket measurements. Ground-based observations of integrated airglow emission rates are constrained by specific geophysical locations for a given day. A limited number of direct measurements of atomic oxygen concentration ([O]) profiles (McDade et al., 1986; Iwagami et al., 2003; Yoshimura et al., 2003; Melo et al., 1996; Gobbi et al., 1992; Kita et al., 1992) were performed to support the hypothesis that a Barth-type mechanism is involved in producing $\text{O}(^1\text{S})$ in the MLT region. Simultaneous direct measurements of atomic oxygen density and nightglow emission rate profiles were provided by the Energy Transfer in the Oxygen Nightglow (ETON) rocket campaign to develop the well-known empirical airglow models (e.g., McDade et al., 1986).

Satellite limb measurements of the atomic oxygen 557.7 nm green line emission rates enable the continuous retrieval of [O] profiles and on a near-global basis. The SCanning Imaging Absorption spectroMeter for Atmospheric CHartographY (SCIAMACHY) on board the Environmental Satellite (Envisat) observed the atmosphere in a dedicated mesosphere/thermosphere limb mode that enabled vertically resolved measurements of the nightglow green line emission to be made. On the basis of the obtained measurements the retrieval of [O] profiles is possible.

The basic purpose of our study is such a retrieval of [O] profiles in the MLT region within the time period from August 2002 to April 2012 at approximately 22:00 local time (LT). The retrieval was performed according to the following scheme. The $\text{O}(^1\text{S}-^1\text{D})$ nighttime green line spectra measured by SCIAMACHY were averaged (see Sect. 2.1) and integrated to limb-emission rate (LER) profiles in 5° latitude bins with daily and monthly resolution (see Sect. 3). Vertical volume emission rate (VER) profiles were retrieved from LER profiles applying linear inversion supported by regularized total least squares (RTLS) minimization (see Sect. 4). The well-known cubic equation (McDade et al., 1986) and its extension (Gobbi et al., 1992; Semenov, 1997; Khomich et al., 2008) were used to retrieve [O] profiles (see Sect. 5) on the basis of temperature and density profiles provided by different available sources and VER profiles retrieved from SCIAMACHY nightglow observations. Temperature and density profiles were provided by the Naval Research Laboratory Mass Spectrometer and Incoherent Scatter radar Extended model, year: 2000, (NRLMSISE-00) semi-empirical atmospheric model (Picone et al., 2002), the Whole

Atmosphere Community Climate Model with Specified Dynamics, version 4, (SD-WACCM4) model (Liu et al., 2010) and by measurements with the Sounding of the Atmosphere using Broadband Emission Radiometry (SABER) instrument (Mlynczak, 1997; Russell et al., 1999) on the Thermosphere, Ionosphere, Mesosphere Energetics and Dynamics (TIMED) spacecraft.

Random and systematic errors were estimated for the obtained data sets at each step of the retrieval. The uncertainty components were assumed to contribute to the total error independently. Successive linear addition of the estimated uncertainty components (Kennedy et al., 2011) was performed at each step of the retrieval procedure to calculate the maximum error. A verification of the retrieved [O] profiles was performed through their comparison with reference [O] profiles provided by the NRLMSISE-00 and SD-WACCM4 models as well as SABER retrievals (see Sect. 6). A selection of the appropriate photochemical model (cubic or extended cubic equation) and the choice of the appropriate source of temperature and density profiles was made at the corresponding steps of the verification.

The optimized [O] retrieval (based on VER profiles provided by SCIAMACHY measurements, see Sect. 5) might also be applied to VER profiles provided by other satellite instruments: e.g., Wind Imaging Interferometer (WINDII), Optical Spectrograph and Infrared Imager System (OSIRIS) and Imager of Sprites and Upper Atmospheric Lightning (ISUAL). Hydroxyl and oxygen green line nightglow observations from the WINDII on board the Upper Atmosphere Research Satellite from 1991 to 2004 were already used to retrieve [O] profiles (Russell et al., 2005). Daytime and nighttime O_2 A-band airglow measurements with the OSIRIS on board the Odin satellite from 2001 to date were also used to retrieve [O] profiles (Sheese et al., 2011). Gao et al. (2012) used green line airglow measurements with the ISUAL on board the FORMOSAT-2 satellite to retrieve [O] profiles. In a very recent study, SCIAMACHY $\text{O}(^1\text{S}-^1\text{D})$ green line observations were employed by Kaufmann et al. (2014) in combination with a slightly modified version of the McDade et al. (1986) photochemical model to retrieve atomic oxygen profiles. Differences between the Kaufmann et al. (2014) retrieval and the one presented in this study will be discussed below in Sect. 7.3.

2 Description of instruments and models used

2.1 SCIAMACHY on board the satellite Envisat

The Envisat-1 designed by the European Space Agency carries 10 instruments (total weight about 8 tons). One of them, SCIAMACHY (Burrows et al., 1995; Bovensmann et al., 1999), observed the atmospheric radiation field in limb, nadir and solar/lunar occultation geometry. On 1 March 2002 Envisat was launched into a sun-synchronous orbit with an

inclination of 98.5° and a period of 100 min, thus performing about 14.4 orbits per day at a mean altitude of 799.8 km (Gottwald et al., 2006). The grating spectrometer SCIAMACHY provided measurements in eight spectral channels within a wavelength range of 220–2380 nm and a spectral resolution of 0.22–1.48 nm.

The limb-emission observations on the Earth's nightside additionally performed by SCIAMACHY at a fixed local solar time (around 22:00 LT) were used in the study presented here. This dedicated mesosphere/thermosphere mode, covering the 75–150 km tangent height range, is characterized by a nominal difference between two adjacent tangent heights of 3.3 km and 0.045° vertical field of view (Cardaci, 2010; Kaiser et al., 2004). The geometrical field of view is approximately 2.4–2.6 km in the vertical direction at the tangent point depending on tangent height and satellite altitude (Kaiser et al., 2004). Note that the SCIAMACHY nighttime limb-emission measurements are performed continuously throughout the year only at latitudes between 0 and 30° N.

The communication link to Envisat-1 and hence SCIAMACHY operations was interrupted in April 2012. The nighttime limb measurements from August 2002 to April 2012 were pre-processed by the German Aerospace Center (DLR) and data quality reports (SOST-DLR, 2013a, b, c), and data anomaly reports (SOST-DLR, 2012) were provided. The data used in our study were pre-processed from Level 1c SCIAMACHY format to the orbital measurements of the green line emission spectra. Level 1 data version 7.0x were used in this study and the data were calibrated using all calibration flags (Gottwald et al., 2006) required to obtain fully calibrated SCIAMACHY limb radiances. The spectral resolution of the SCIAMACHY spectra in channel three used in this study is about 0.2 nm.

2.2 SABER on board the satellite TIMED

SABER infrared radiometer (Mlynczak, 1997; Russell et al., 1999) on board the National Aeronautics and Space Administration (NASA) TIMED satellite measures a number of middle atmospheric parameters and NASA provides the data online via their website (SABER, 2014). SABER measurements are made within the latitude range 54° S– 87° N or 87° N– 54° S with coverage alternating every 60 days. The vertical resolution of SABER measurements is approximately 2 km (Mertens et al., 2009). Nighttime hydroxyl emission rates measured with SABER are used to calculate atomic oxygen mixing ratios (Mlynczak et al., 2013). In our study, SABER level 2A data (version 2.0) for the years 2002–2012 were interpolated to 1.0 km altitude grid resolution and averaged within the time interval 21:00–23:00 LT to compare them with SCIAMACHY measurements made at around 22:00 LT. Atmospheric density and temperature profiles provided by SABER were used in the SCIAMACHY [O] retrieval as discussed in Sect. 5. The concentrations of

molecular oxygen ($[O_2]$) and molecular nitrogen ($[N_2]$) were calculated from atmospheric density profiles assuming constant mixing ratios. The decrease of the $[O_2]/[N_2]$ ratio with altitude according to NRLMSISE-00 data is not reliable as pointed out by Picone et al. (2002), because credible mesospheric $[O_2]$ data are absent in the NRLMSISE-00 database. If the mixing ratio correction based on NRLMSISE-00 $[O_2]$ and $[N_2]$ profiles were applied in our O retrieval, SCIAMACHY [O] values would fall by 4 % in the altitude range 100–105 km. We supposed in our SCIAMACHY O retrieval that a constant mixing ratio is valid at altitudes up to 105 km, which is also assumed in the SABER O retrieval (Smith, 2010). The atomic oxygen mixing ratio profiles based on SABER measurements were converted into [O] profiles and used as reference [O] profiles for the verification of the retrieved [O] profiles (see Sect. 7).

2.3 NRLMSISE-00 and SD-WACCM4 models

NRLMSISE-00 incorporates ground-based, rocket and satellite-borne measurements. A set of parametric equations of diffusive equilibrium (Akins et al., 2003) is used to interpolate or extrapolate the data. Heliogeophysical conditions which influence the parameters relevant for the photochemical model were employed for the [O] retrieval in our study. These parameters, F10.7 (10.7 cm solar radio flux) and Ap-index (planetary equivalent daily amplitude), were taken from databases provided by the National Oceanic and Atmospheric Administration (NOAA, 2014a). The NRLMSISE-00 model provided online (NRLMSISE-00, 2014) was used to simulate the concentration profiles of individual atmospheric constituents (i.e., [O], $[O_2]$, $[N_2]$) and temperature profiles for the specifically chosen heliogeophysical conditions and geographical locations at 22:00 LT with 1.0 km altitude grid resolution.

In this study we also use atomic oxygen and atmospheric background parameters modeled with SD-WACCM4; see Garcia et al. (2007) for a description of a previous version of the model. SD-WACCM4 is nudged to Goddard Earth Observing System Model, version 5, (GEOS-5) meteorological fields below about 50 km altitude. The SD-WACCM4 data set used in this study covers the period from April 2010 to March 2011 and was previously also employed by Hoffmann et al. (2012) and Kowalewski et al. (2014). The geopotential height profiles provided by SD-WACCM4 were converted to geometrical height profiles. Temperature profiles, atmospheric pressure profiles and [O] profiles were interpolated from the geometrical height grid to an altitude grid with 1.0 km resolution. The $[O_2]$ and $[N_2]$ profiles required for the present study were calculated from SD-WACCM4 pressure and temperature profiles assuming the ideal gas law and constant O_2 and N_2 mixing ratios. To extract the required atmospheric parameters at 22:00 LT we sampled the corresponding longitude of the SD-WACCM4 output provided

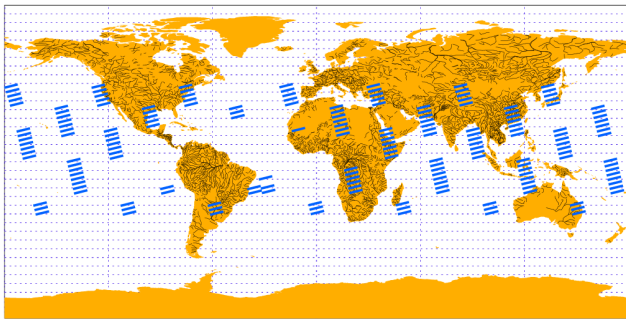


Figure 1. Geographical location and coverage of nighttime limb-emission observations performed by SCIAMACHY on 9 September 2010 in the dedicated mesosphere/thermosphere mode.

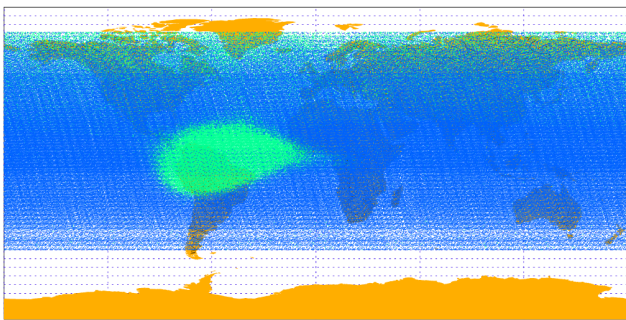


Figure 2. Geographical locations of nighttime limb-emission observations performed by SCIAMACHY between 2 August 2002 and 8 April 2012. Limb measurements marked in green are excluded because they are affected by Aurora Borealis, highly energetic particles in the South Atlantic Anomaly or by an enhanced offset possibly related to contaminating emissions associated with the OH(7-1) transition (Blackwell et al., 1960) and the NO + O air-afterglow continuum (e.g., von Savigny et al., 1999).

with daily resolution at 00:00 UTC, as in Kowalewski et al. (2014).

3 Determination of green line limb-emission profiles

The nightglow limb spectral measurements provided by SCIAMACHY were screened and measurements from certain orbits were excluded according to measurement errors presented in the SOST-DLR quality and anomaly reports (SOST-DLR, 2013a, b, c, 2012; see Sect. 2.1).

The geographical position and extent of the air volumes observed by SCIAMACHY nighttime limb measurements on a single day are presented in Fig. 1. The duration of a single measurement is about 60 s and the horizontal resolution is about $1000\text{ km} \times 630\text{ km}$. The geographical positions of all nighttime limb measurements performed during the period from 2 August 2002 to 8 April 2012 are shown in Fig. 2. For the retrieval we used the limb measurements marked in blue in Fig. 2 but not the measurements that are affected by Aurora

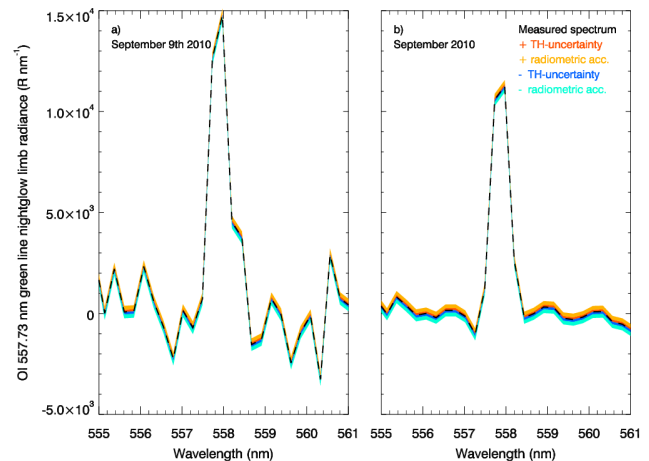


Figure 3. Sample daily (a) and monthly (b) averaged green line emission spectra (calculated by averaging 12 (a) and 480 (b) orbital spectral measurements) at 95 km altitude for the 20–25° N latitude range with uncertainty components σ_h^+ (orange), σ_a^+ (yellow), σ_h^- (light blue) and σ_a^- (cyan). See Sects. 3 and 6.1 for further details.

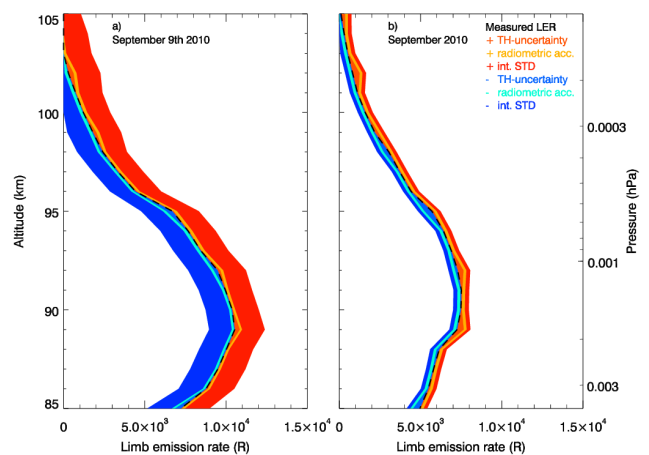


Figure 4. Sample daily (a) and monthly (b) averaged green line LER profiles for the 20–25° N latitude range with uncertainty components σ_h^+ (orange), σ_a^+ (yellow) introduced for determining P_{+1} and calculated for LER_{+1} and σ_l (red) calculated directly for LER_{+1} . Similarly, σ_h^- (light blue) and σ_a^- (cyan) are introduced when calculating P_{-1} and are propagated to determine LER_{-1} . σ_l (blue) is directly calculated for LER_{-1} . See Sects. 3 and 6.1 for further details.

Borealis, by highly energetic particles or by contaminating emissions.

The measured spectra within the tangent height range from 75 to 128 km with 3.3 km vertical sampling were interpolated to 1.0 km altitude grid resolution within the spectral range 555–561 nm. For each individual spectrum the emission spectra averaged over the 110–126 km tangent height range were subtracted from the spectrum at each tangent height. The subtraction of the 110–126 km average is because

of contributions from other emissions, the impact of noise and auroral activity. Then each spectrum was separated into three parts corresponding to the following wavelength intervals: from 555 to 557 nm (background emissions and noise), from 557 to 559 nm (green line emission) and from 559 to 561 nm (background emissions and noise) (see Fig. 3). The spectral baseline underneath the green line was determined using the background and noise intervals and was subtracted from the spectral data in the green line interval. Each individual spectrum was analyzed with the help of a band pass filter based on the application of variance and mean value thresholds within the wavelength intervals from 555 to 557 nm and from 559 to 561 nm. Measurement noise detection based on the variance threshold was only applied within the wavelength interval from 557 to 559 nm. The empirical choice and application of the threshold values are discussed below.

Envisat, as it passes through the South Atlantic Anomaly at an altitude of approximately 800 km, is exposed to high-energy particles within the lowest of the three Van Allen belts. The varying solar activity (Hudson et al., 2008) and solar coronal mass ejections, e.g., the Halloween event in 2003, caused measurement interruptions (reported by SOST-DLR in data quality and anomaly reports). Spectra were excluded from the retrieval if the variance within the background wavelength intervals exceeded the variance threshold value of $50 \times 10^6 \text{ Rayleigh}^2 \text{ nm}^{-2}$ (1 Rayleigh equals $10^{10} \text{ photons s}^{-1} \text{ m}^{-2}$).

The geographical position of limb spectral measurements was used to exclude them from further processing in the case when contamination by auroral events was expected. The size of the auroral oval (Newell et al., 2002) varies constantly with each minute depending on the hemispheric power index provided by NOAA (2014b) that was used as a measure of the auroral activity in this study. The shape of the aurora oval was approximated with a circle centered at the north geomagnetic pole (80° N , 72° W) according to the International Geomagnetic Reference Field (IGRF-11) model. The area of such a circle is supposed to vary according to the value of the hemispheric power index so that spectra measured at geographical locations within this circle were excluded from daily and monthly averaging. In addition to this aurora position filter, the variance threshold value of $60 \times 10^6 \text{ Rayleigh}^2 \text{ nm}^{-2}$ was also applied within the green line wavelength interval to exclude non-valid spectral measurements.

The Q and P branch components of the OH(7-1) band emissions (Blackwell et al., 1960) can contribute to the green line emissions within the wavelength interval from 555 to 561 nm. There are no other sources of nightglow emissions contributing to the spectra of the analyzed green line emissions to be additionally considered, except the one due to the $\text{NO} + \text{O}$ air-afterglow reaction, which is, however, typically at least 2 orders of magnitude weaker than the $\text{O}(^1\text{S})$ green line (von Savigny et al., 1999). These contaminating emissions may affect the spectral baseline. Spectra were excluded

from the retrieval if the absolute mean value in the background wavelength intervals exceeded the threshold value of $500 \text{ Rayleigh nm}^{-1}$. Figure 3 presents sample daily (a) and monthly (b) spectra that are calculated by averaging 12 (a) and 480 (b) orbital spectral measurements at the altitude of 95 km in the latitude range $20\text{--}25^\circ \text{ N}$. Each spectral measurement processed was integrated over the green line wavelength interval from 557 to 559 nm. The green line LER profiles were daily or monthly averaged and converted to Rayleigh. Zonal averaging in 5° latitude bins was applied additionally because the zonal atmospheric motion in the MLT is much faster than the meridional motion. Daily and monthly averaged sample LER profiles within the latitude range $20\text{--}25^\circ \text{ N}$ are presented in Fig. 4.

4 Retrieval of volume emission rate profiles

The main task of this step of the retrieval procedure is to invert LER profiles (being a function of tangent height h) to vertical VER profiles (as a function of geometric altitude z), given that the elements of the LER profiles are integrals of the VER along the line of sight (LOS). The Earth's atmosphere, represented by the flattened Earth model WGS84 (e.g., NIMA, 2000; Larson and Wertz, 1999) is assumed to be composed of homogeneously emitting layers of 1 km thickness. The geometrical distances (optical paths) along the LOS passing through subsequent layers of the model atmosphere were calculated using the Pythagorean theorem.

A linear model was used to map (Rodgers, 2000) VER profiles from their state space into measurement space of LER profiles. Note that extinction due to scattering and self-absorption is negligible for this specific application. The forward model is mathematically represented by the following linear relationship:

$$\mathbf{y} = \mathbf{F}(\mathbf{x}, \mathbf{b}) + \epsilon = \mathbf{K}\mathbf{x} + \epsilon, \quad (1)$$

where LER profiles are represented by the measurement vector \mathbf{y} , VER profiles are represented by the state vector \mathbf{x} , \mathbf{F} is the functional representation of the forward model, the vector term \mathbf{b} represents the random error of model parameters (one of the model parameters relevant for this retrieval step is an offset in tangent height registration) and ϵ is a statistical uncertainty that includes both the uncertainty in \mathbf{y} and in the elements of the weighting function matrix \mathbf{K} (see Sect. 6). The inverse problem is even-determined for the chosen retrieval altitude grid resolution of 1.0 km, being the same for the standard tangent height grid resolution.

A least squares method was employed to solve the inverse problem, minimizing the prediction error assuming linear system inconsistencies due to noise in \mathbf{y} . Phillips–Tikhonov regularization was chosen to avoid physically meaningless solutions such as oscillations due to, e.g., numerical sensitivity of the inversion.

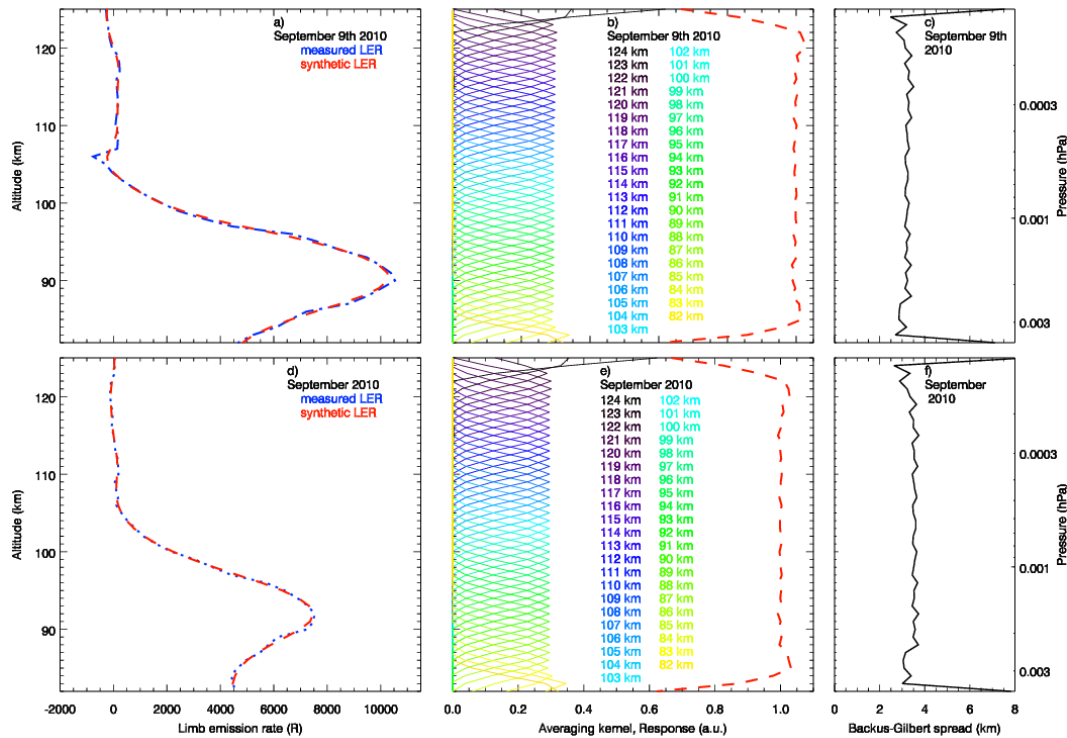


Figure 5. Characteristics and diagnostics of the inversion procedure in sample daily (top row) and monthly averages (bottom row) for the latitude range 20–25° N: comparison of the measured LER profile and the synthetic LER profile (panels **a** and **d**); averaging kernel and the resulting area (response curve marked red) (panels **b** and **e**); the vertical resolution (Backus–Gilbert spread) (panels **c** and **f**).

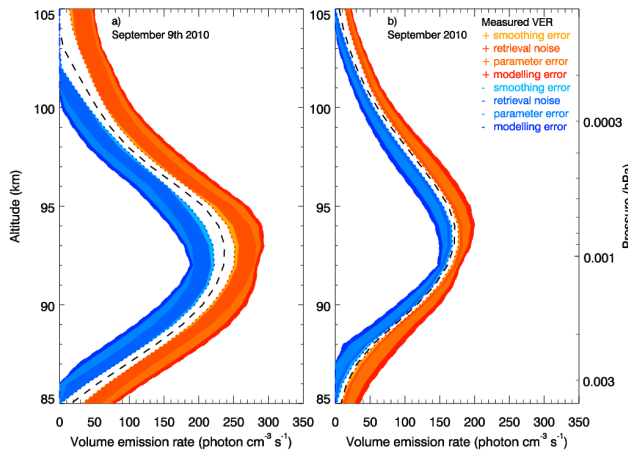


Figure 6. Sample daily (**a**) and monthly (**b**) averaged green line VER profiles for the 20–25° N latitude range with uncertainty ($\sigma_{S_{\text{tot}}}$) components σ_{S_s} (yellow), σ_{S_m} (light red), σ_{S_b} (orange), σ_{S_f} (red) introduced and calculated for the VER_{+1} retrieval, σ_{S_s} (cyan marked), σ_{S_m} (light blue), σ_{S_b} (dark cyan) and σ_{S_f} (blue) introduced and calculated for the VER_{-1} retrieval. See Sects. 4, 4.3, 6.1 and 7.1 for further details.

The determination of SCIAMACHY tangent heights is characterized by uncertainties, but the tangent height error drift is, at less than 20 m year⁻¹, very small (Bramstedt, 2012). Because the resulting tangent height uncertainties affect the weighting function matrix **K**, the total least squares method with regularization was applied to reduce potential numerical instabilities and oscillations due to uncertainties in **y** and **K**.

At first, an inversion was performed using a constrained least squares approach:

$$\mathbf{x} = (\mathbf{K}^T \mathbf{K} + \gamma_r \mathbf{H}^T \mathbf{H})^{-1} \mathbf{K}^T \mathbf{y} = \mathbf{G}_r \mathbf{y}, \quad (2)$$

where the positive semi-definite regularization matrix **H** (Wang and Yuan, 2003) is scaled with the regularization parameter γ_r (lower index r means “restricted”, i.e., without considering S_e and S_a) and the restricted gain matrix **G_r** (also known as the generalized inverse matrix). To determine the value of γ_r the automated RTLS procedure (see Sect. 4.2) was applied.

At the next step, the diagonal noise covariance matrix **S_e** (corresponding to the 1 σ error of the current LER profile **y**) was introduced. Uncertainty information of measured LER profiles represented by **S_e** needs to be appropriately balanced with the a priori covariance matrix **S_a** related to the retrieved target VER profiles **x**. The first-order linear Bayesian

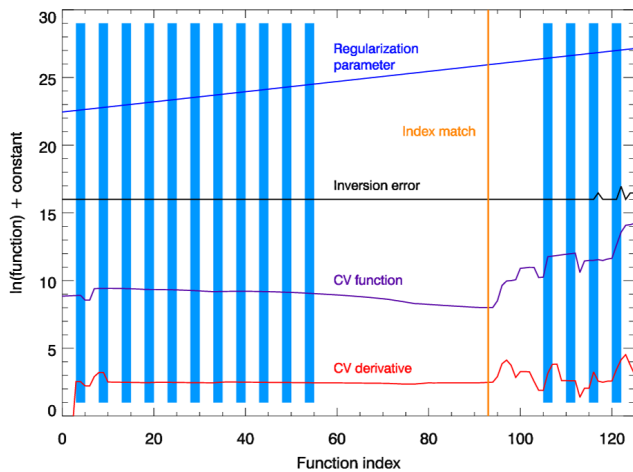


Figure 7. Illustration of the regularized total least squares (RTLS) minimization used for the identification of the optimal regularization parameter γ_r . Shading (with vertical blue lines) of the regions in the range of possible regularization parameters means their rejection from the retrieval, absence of shading means their acceptance. The cross-validation (CV) function (see Eq. 9) is used to locate its minimum and to determine the index of γ_r . Alternatively, the peak of the CV derivative occurring where the steepest slope of the CV function occurs can be used to locate the index of γ_r . The index of the optimal regularization parameter γ_r is marked by an orange line.

approach (Rodgers, 2000) was implemented to solve Eq. (3) extended with \mathbf{S}_e and \mathbf{S}_a (see Sect. 4.1).

4.1 Implementation of the inversion procedure

The maximum a posteriori solution obtained after generalization for independent components of the state vector \mathbf{x} (Rodgers, 2000) is given by:

$$\mathbf{x} = \mathbf{S}_a \mathbf{K}^T (\mathbf{K} \mathbf{S}_a \mathbf{K}^T + \mathbf{S}_e + \gamma \mathbf{H}^T \mathbf{H})^{-1} \mathbf{y} = \mathbf{G} \mathbf{y}, \quad (3)$$

where the positive semi-definite regularization matrix \mathbf{H} (Wang and Yuan, 2003) is scaled with the regularization parameter γ and the retrieval gain matrix \mathbf{G} . The inversion procedure becomes insensitive to the application of covariance matrices if the a priori matrix \mathbf{S}_a is calculated with help of the \mathbf{S}_e matrix.

Under the assumption (based on similarities in statistical distributions of \mathbf{S}_a and \mathbf{S}_e for our case) that \mathbf{S}_a is calculated from \mathbf{S}_e , Eq. (3) gives us

$$\text{diag}(\mathbf{K} \mathbf{S}_a \mathbf{K}^T) \approx \text{diag}(\mathbf{S}_e). \quad (4)$$

A comparison of Eq. (2) and Eq. (3) gives that γ , γ_r and \mathbf{S}_a are related as follows:

$$\gamma = \gamma_r \cdot \text{diag}(\mathbf{S}_a). \quad (5)$$

Once γ_r is determined (see Eq. 2) using the RTLS procedure (see Sect. 4.2), γ can be calculated.

The presented γ calculation procedure is supported by evident equivalence of the VER profiles retrieved according to Eq. (2) (optimized for using γ_r) and Eq. (3) (optimized for using γ). The calculation procedure is supported also by the fact that the measurement vector \mathbf{y} is similar to the synthetic vector $\mathbf{s} = \mathbf{K} \mathbf{x}$. In fact, the curve representing the synthetic vector \mathbf{s} fits the curve representing the measurement vector \mathbf{y} . The relative difference between \mathbf{s} and \mathbf{y} is less than 0.1 (or 10 %) for data sets on a daily timescale and less than 0.05 (or 5 %) on a monthly timescale in the altitude range 82–100 km. Figure 5 presents the results for LER profiles (\mathbf{y}) and synthetic profiles based on the retrieved VER profiles averaged for a sample day (Fig. 5a) and a sample month (Fig. 5d). Figure 6 presents sample daily and monthly averaged VER profiles (\mathbf{x}) within the latitude range 20–25° N.

The shape of the averaging kernel represented by a row of the matrix $\mathbf{A} = \mathbf{G} \mathbf{K}$ is, in our case, a simple peak. The area of the averaging kernels is defined by

$$a(z) = \int \mathbf{A}(z, z') dz', \quad (6)$$

where z is the nominal altitude of the peak of the related averaging kernel. It characterizes the measurement response as a measure of the relative contribution of the observations and the a priori information to the retrieved VER profile (Rodgers, 2000). Figure 5 presents the averaging kernel rows (colored lines) and the measurement response (red dashed line) for a sample day (Fig. 5b) and a sample month (Fig. 5e) for the 20–25° N latitude range. The area of the averaging kernels – characterizing the measurement response – is close to 1 within the altitude range from 86 to 122 km with some deviations at the edges of this altitude range.

The vertical resolution of the retrieved VER profiles (usually defined as the “width” of the averaging kernels) was evaluated using the Backus–Gilbert spread $r(z)$ that characterizes the prevalence of useful information against noise at the geometric altitude z (Rodgers, 1990):

$$r(z) = \frac{12}{a(z)^2} \int (z - z')^2 \mathbf{A}(z, z')^2 dz'. \quad (7)$$

Figure 5 shows the vertical resolution according to Backus–Gilbert spread for a sample day (Fig. 5c) and a sample month (Fig. 5f) within the latitude range 20–25° N. The approximately 3.7 km vertical resolution of the retrieved VER profiles is slightly coarser than the vertical sampling of the measured LER profiles of approximately 3.3 km.

4.2 Regularized total least squares minimization

The automated RTLS procedure (Sima et al., 2004) was applied to determine the value of the regularization parameter γ_r (see Eq. 5).

Partial solutions \mathbf{x}_i of the regularized problem are calculated as a function of a fixed γ_r :

$$\mathbf{x}_i = (\mathbf{K}_{-i}^T \mathbf{K}_{-i} + \gamma_r \mathbf{H}^T \mathbf{H})^{-1} \mathbf{K}_{-i}^T \mathbf{y}_{-i} = \mathbf{G}_{CV} \mathbf{y}_{-i}, \quad (8)$$

where \mathbf{K}_{-i} is the matrix \mathbf{K} with rows i set to zero, and \mathbf{y}_{-i} is a measurement vector with elements i set to zero (Sima et al., 2004). The fitting bias associated with ignoring parts of the data is measured on the basis of the calculated set of $\mathbf{x}_i(\gamma_r)$ using the orthogonal distances composing the cross-validation (CV) function:

$$\text{CV} = \sum_{i=1}^N \frac{\|\mathbf{K}_{-i}\mathbf{x}_i - \mathbf{y}_{-i}\|^2}{\|\mathbf{x}_i\|^2 + 1}, \quad (9)$$

where \mathbf{G}_{CV} is retrieval gain matrix corresponding to the CV function. The optimal γ_r is found at the minimum of the CV function (Sima et al., 2004). The RTLS algorithm was implemented with the LAPACK functions LUDC, LUSOL and LUMPROVE used in Interactive Data Language version 8.2 to solve the reduced inversion equation (see Eq. 2).

The range of possible regularization parameters was selected empirically to speed up the process of the γ_r calculation. The range not shaded with blue color in Fig. 7 represents the acceptable range of possible regularization parameters (in this figure the violet line corresponds to the CV function, the red line to the derivative of the CV function with respect to the index and the blue line to the regularization parameter function). Instabilities due to numerical random errors are present in the left part of the CV function curve where the value of the regularization parameter γ_r is too small and the retrieval is under-regularized (see the blue-shaded zone on the left in Fig. 7). Small values of regularization parameters cause roughness of the curve representing the retrieved state vector \mathbf{x} . Too high values of the regularization parameter result in spikes of the inversion error curve corresponding to the scaled norm function $\|\mathbf{G}_{\text{CV}}^{-1}\mathbf{G}_{\text{CV}} - \mathbf{I}\|$ (see the black line in the blue-shaded zone on the right in Fig. 7). High values of regularization parameters mean that the retrieval is over-regularized leading to flatness of the retrieved state vector \mathbf{x} curve.

The optimal γ_r is found automatically within the acceptable (not shaded) range. Within the acceptable range of γ_r the minimum of the CV function curve is identified to determine the optimal γ_r . If the minimum of the CV function is located beyond the acceptable range, the steepest slope of the CV function is identified using the derivative of the CV function.

4.3 Retrieval errors due to inversion

The retrieval error is characterized by the total retrieval error \mathbf{S}_{tot} (Rodgers, 2000) estimated for the retrieved VER profiles (see Eq. 3) as follows:

$$\mathbf{S}_{\text{tot}} = \mathbf{S}_m + \mathbf{S}_s + \mathbf{S}_b + \mathbf{S}_f, \quad (10)$$

with the measurement error covariance matrix \mathbf{S}_m related to random and systematic errors, the smoothing error covariance matrix \mathbf{S}_s , the error covariance matrix \mathbf{S}_b related to random errors of model parameters that are not retrieved (see

Sects. 4 and 6) and the covariance matrix \mathbf{S}_f corresponding to the systematic forward model parameter error.

The covariance matrix \mathbf{S}_m due to retrieval system noise is given by

$$\mathbf{S}_m = \mathbf{G}\mathbf{S}_e\mathbf{G}^T, \quad (11)$$

with the retrieval gain matrix \mathbf{G} (see Eq. 3)

$$\mathbf{G} = \mathbf{S}_a\mathbf{K}^T(\mathbf{K}\mathbf{S}_a\mathbf{K}^T + \mathbf{S}_e + \gamma\mathbf{H}^T\mathbf{H})^{-1}. \quad (12)$$

The covariance matrix \mathbf{S}_s due to smoothing error is given by

$$\mathbf{S}_s = (\mathbf{A} - \mathbf{I})\mathbf{S}_n(\mathbf{A} - \mathbf{I})^T, \quad (13)$$

with averaging kernel matrix $\mathbf{A} = \mathbf{G}\mathbf{K}$, the identity matrix \mathbf{I} and covariance matrix of the states' ensemble \mathbf{S}_n about the mean state $\bar{\mathbf{x}}$ (Rodgers, 2000): $\mathbf{S}_n = \mathbf{E}[(\mathbf{x} - \bar{\mathbf{x}}) \cdot (\mathbf{x} - \bar{\mathbf{x}})^T]$.

The diagonal matrix \mathbf{S}_b is the error covariance matrix containing the inverse and squared standard deviation (SD) of VER profiles with respect to uncertainties in the model parameters. The SD was found as the difference of the averaged VER profiles due to perturbations of h' representing the uncertainty in the tangent height determination (± 500 m, see Sect. 6.1). The covariance matrix \mathbf{S}_f due to forward model errors caused by approximations and imperfections of the forward model is given by

$$\mathbf{S}_f = \mathbf{G}\mathbf{K}\mathbf{S}_b\mathbf{K}^T\mathbf{G}^T. \quad (14)$$

5 Retrieval of atomic oxygen concentration profiles

The retrieval of atomic oxygen concentration profiles from the obtained green line VER profiles is based on the generally accepted two-step Barth transfer scheme and approximations derived from the measurements provided by the ETON rocket campaign (McDade et al., 1986). The $\text{O}(^1\text{S}-^1\text{D})$ SCIAMACHY nightglow green line emission spectra were processed according to the retrieval approach presented in Sect. 4 resulting in the retrieved VER profiles. The [O] retrieval is based on the well-known cubic equation (McDade et al., 1986), which represents the empirically derived relation between VER and [O] profiles; see Eq. (15).

The two-step Barth transfer scheme is represented by chemical reactions (see Reactions (1), (2) and the resulting Reaction (10) for the green line emission in Table 1) accompanied by quenching. The quenching of O_2^* as well as the quenching of $\text{O}(^1\text{S}_0)$ by O_2 was considered by McDade et al. (1986). In addition, Gobbi et al. (1992), Semenov (1997), Semenov and Shefov (2005) and Khomich et al. (2008) also considered quenching of $\text{O}(^1\text{S}_0)$ by $\text{O}(^3\text{P})$ or N_2 . The simplest of the [O] retrieval approaches based on the cubic equation does not account for the quenching of $\text{O}(^1\text{S}_0)$ by $\text{O}(^3\text{P})$ or N_2 , and the retrieved [O] profiles using this approach are

Table 1. Photochemical reactions according to the two-step Barth transfer scheme (see Reactions (1), (2) and the resulting Reaction (10) for the green line emission) accompanied by quenching. The quantities listed in the column named *intermediate coefficients* correspond to the notation by Khomich et al. (2008) and the coefficients employed here (see Eq. 15) follow the notation by Gobbi et al. (1992) and McDade et al. (1986) and are listed in the column entitled *used coefficients*. See Sect. 5 for further details.

Item #	Chemical reaction	Intermediate coefficient	Used coefficient
1	$O(^3P) + O(^3P) + (O_2, N_2) \rightarrow O_2^* + (O_2, N_2)$	α_{O_2}	κ_1
2	$O_2^* + O(^3P) \rightarrow O_2 + O(^1S_0)$	α_O	C(1)
3	$O_2^* + O(^3P) \rightarrow O_2 + O(^3P)$	β_O^*	
4	$O_2^* + N_2 \rightarrow O_2 + N_2$	$\beta_{N_2}^*$	C(2)
5	$O_2^* + O_2 \rightarrow O_2 + O_2$	$\beta_{O_2}^*$	
6	$O_2^* \rightarrow O_2 + h\nu$	A^*	C(0)
7	$O(^1S_0) + O(^3P) \rightarrow 2O(^3P, ^1D_2)$	β_O	$^1\kappa_5$
8	$O(^1S_0) + N_2 \rightarrow O(^3P, ^1D_2) + N_2^*$	β_{N_2}	$^2\kappa_5$
9	$O(^1S_0) + O_2 \rightarrow O(^3P, ^1D_2) + O_2^*$	β_{O_2}	$^3\kappa_5$
10	$O(^1S_0) \rightarrow O(^1D_2) + h\nu (\lambda = 557.7 \text{ nm})$	A_{558}	
11	$O(^1S_0) \rightarrow O(^3P_1) + h\nu (\lambda = 297.2 \text{ nm})$	A_{297}	A_{1S}
12	$O(^1S_0) \rightarrow O(^3P_2) + h\nu (\lambda = 295.8 \text{ nm})$	A_{296}	

Table 2. Einstein coefficients (A_{558} , A_{1S}), excitation parameters (C(0), C(1), C(2)) and factors (k_1 , $^1\kappa_5$, $^2\kappa_5$, $^3\kappa_5$) for rate coefficients (κ_1 , $^1\kappa_5$, $^2\kappa_5$, $^3\kappa_5$). The values are presented in the table according to their position in the Eq. (15) that gives the retrieved atomic oxygen concentration (see Table 1, Sect. 5 and Appendix for details).

[O] error bound	A_{558}	A_{1S}	C(0)	C(1)	C(2)	k_1	$^1\kappa_5$	$^2\kappa_5$	$^3\kappa_5$
−1	1.26 s^{-1}	1.105 s^{-1}	9	204	14	5.051	4.467	4.5	1.38
0	1.16 s^{-1}	1.228 s^{-1}	13	224	17	4.700	5.000	5.0	2.32
+1	1.06 s^{-1}	1.350 s^{-1}	17	244	20	4.349	5.533	5.5	3.26

denoted as $[O^{\text{cubic}}]$. The [O] retrieval approach based on the extended cubic equation accounts for the quenching of $O(^1S)$ by $O(^3P)$ and N_2 , and the retrieved [O] profiles using such an approach are denoted as $[O^{\text{quench}}]$.

According to the differences of these model approaches, the following equation based on the coefficients represented in Table 2 was used in the [O] retrieval:

$$\text{VER} = \kappa_1 [O]^2 ([N_2] + [O_2]) \cdot \frac{[O]}{(C(0) + C(1)[O] + C(2)[O_2])} \cdot \frac{A_{558}}{(A_{1S} + \sum_i (^i\kappa_5 [M_i]))}, \quad (15)$$

where A_{558} (s^{-1}) is the transition probability of $O(^1S \rightarrow ^1D)$, A_{1S} (s^{-1}) is the inverse radiative lifetime of $O(^1S)$, κ_1 ($\text{cm}^3 \text{ s}^{-1}$) is the rate coefficient for the three-body recombination of atomic oxygen and $^i\kappa_5$ ($\text{cm}^3 \text{ s}^{-1}$) is the rate coefficient for quenching of $O(^1S)$ by M_i , $i = 1, 2, 3$. The dimensionless variables C(0), C(1) and C(2) are the empirical $O(^1S)$ excitation parameters; $[M_i] = ([O], [N_2], [O_2])$ represents concentrations of the respective species, $i = 1, 2, 3$.

The first term on the right-hand side of the Eq. (15) describes rate of O_2^* production, the first and second terms describe the production of $O(^1S)$ and all three terms on right-

hand side describe the $O(^1S \rightarrow ^1D)$ emission rate. Recombination of ground state atomic oxygen with rate κ_1 causes production of metastable oxygen O_2^* . Subsequent deactivation of O_2^* by ground state O leads to $O(^1S)$ production. Metastable molecular oxygen undergoes quenching described by parameters C(1), C(2) and radiative relaxation described by radiative lifetime $C(0)^{-1}$ so that the second term on the right-hand side of the Eq. (15) represents conversion to $O(^1S)$. The influence of $[O_2]$ and $[N_2]$ was accounted for by the approximated parameters C(0), C(1) and C(2) (McDade et al., 1986). The quenching of $O(^1S)$ by $O(^3P)$ or N_2 (described by Reactions (7) and (8) in Table 1 and introduced by Gobbi et al., 1992; Semenov, 1997; Semenov and Shefov, 2005; Khomich et al., 2008) is considered in the third term on the right-hand side of the Eq. (15).

The numerical approximation employed by Semenov (1997), Semenov and Shefov (2005) and Khomich et al. (2008) was applied to find the solution of Eq. (15) for $^i\kappa_5 \neq 0$, $i = 1, 2, 3$ that corresponds to retrieving $[O^{\text{quench}}]$ profiles. The atomic oxygen concentration $[O^{\text{cubic}}]$ was retrieved as the exact solution of the cubic equation resulting from the Eq. (15) for $^1\kappa_5 = ^2\kappa_5 = 0$.

The discussed model approach for retrieving [O] profiles according to Eq. (15) requires parameters such as SCIAMACHY VER profiles, temperature-dependent rate coefficients κ and atmospheric density ($[\text{N}_2] + [\text{O}_2]$) profiles. Both $[\text{O}^{\text{quench}}]$ and $[\text{O}^{\text{cubic}}]$ retrievals were performed for all available sources of temperature and atmospheric density profiles.

In an ideal case, simultaneous measurements of all quantities required to calculate atomic oxygen profiles (i.e., temperature (T), $[\text{N}_2]$, $[\text{O}_2]$ and VER profiles) are available. Unfortunately, such a data set is not available. So, in our case, the available SCIAMACHY VER profiles were combined with T , $[\text{O}_2]$, $[\text{N}_2]$ profiles from NRLMSISE-00, SD-WACCM4 and SABER to calculate $[\text{O}^{\text{quench}}]$ and $[\text{O}^{\text{cubic}}]$ profiles according to Eq. (15). The presented retrievals $[\text{O}^{\text{cubic}}]$ and $[\text{O}^{\text{quench}}]$ are in the following discussion additionally denoted with lower indices showing the source of the T , $[\text{O}_2]$ and $[\text{N}_2]$ profile data as $[\text{O}^{\text{cubic}}_{\text{MSIS00}}]$, $[\text{O}^{\text{cubic}}_{\text{WACCM4}}]$, $[\text{O}^{\text{cubic}}_{\text{SABER}}]$ and $[\text{O}^{\text{quench}}_{\text{MSIS00}}]$, $[\text{O}^{\text{quench}}_{\text{WACCM4}}]$, $[\text{O}^{\text{quench}}_{\text{SABER}}]$. The retrieved [O] profiles were compared with atomic oxygen concentration profiles extracted from NRLMSISE-00, SD-WACCM4 and SABER denoted as $[\text{O}^{\text{MSIS00}}]$, $[\text{O}^{\text{WACCM4}}]$ and $[\text{O}^{\text{SABER}}]$, respectively. Figures 10 and 11 show different possible sample daily and monthly averaged [O] profiles within the latitude range 20–25° N.

6 Error analysis

The error analysis was done assuming independent contributions of uncertainty components to the maximum uncertainty of the retrieved data set, so correlations of the uncertainty components were neglected. The uncertainty components considered are assumed, first of all, to include random errors and systematic errors. The model parameters (that are not retrieved and related to random errors) correspond to the vector \mathbf{b} (see Sect. 4). The components of the vector \mathbf{b} are discussed at the relevant steps of the retrieval considering:

1. the error in the determination of the tangent height information affecting the VER retrieval (see Sect. 6.1)
2. the error in atmospheric density (represented by the sum of molecular oxygen $[\text{O}_2]$ and nitrogen $[\text{N}_2]$ concentrations) and temperature profiles affecting the [O] retrieval (see Sect. 6.2).

Successive additions of the uncertainty components to the solution were performed at each step of the retrieval. These steps result in (1) the spectral data set \mathbf{P} , (2) LER profiles, (3) VER profiles and (4) atomic oxygen concentration profiles. The error bounds (denoted by subscript ± 1) were estimated in a way to avoid assumptions about the parameter distributions, e.g., that they are Gaussian.

At each step of the retrieval the relevant uncertainty components were accounted for (Kennedy et al., 2011) resulting in the unperturbed retrieval values ($\mathbf{P}_0 \Rightarrow$

$\mathbf{LER}_0 \Rightarrow \mathbf{VER}_0 \Rightarrow [\text{O}]_0$) and their upper and lower bounds ($\mathbf{P}_{+1} \Rightarrow \mathbf{LER}_{+1} \Rightarrow \mathbf{VER}_{+1} \Rightarrow [\text{O}]_{+1}$ and $\mathbf{P}_{-1} \Rightarrow \mathbf{LER}_{-1} \Rightarrow \mathbf{VER}_{-1} \Rightarrow [\text{O}]_{-1}$). The uncertainty components considered at a given step of the retrieval were taken into account for the error bounds at the next step of the retrieval.

6.1 Error analysis for the retrieval of volume emission rate profiles

The maximum tangent height (h) error of the SCIAMACHY limb measurements is assumed to be ± 500 m ($h' = 500$ m) (von Savigny et al., 2009). Modeled in a discrete mode (by applying $\pm h'$), perturbations of h were considered to resemble the random error of the determination of the tangent height. The uncertainty of the measured spectrum \mathbf{P} is composed of two additive altitude-dependent components caused by variations of h (related to a random error vector σ_h) and radiometric accuracy (related to a systematic error vector σ_a). The altitude-dependent vector of SDs σ_h was calculated using spectra \mathbf{P} and perturbed spectra denoted as \mathbf{P}^{temp} : $\sigma_h^+ = |\mathbf{P}^{\text{temp}}(+h') - \mathbf{P}|$ and $\sigma_h^- = |\mathbf{P} - \mathbf{P}^{\text{temp}}(-h')|$.

A radiometric accuracy of the SCIAMACHY spectral measurements of 4 % ($a = 4$ %) (Noël et al., 1998) was assumed to calculate the altitude-dependent vector of SDs σ_a of the averaged spectra: $\sigma_a^+ = |\mathbf{P}^{\text{temp}}(+a) - \mathbf{P}|$ and $\sigma_a^- = |\mathbf{P} - \mathbf{P}^{\text{temp}}(-a)|$. Subtracting $(\sigma_a^- + \sigma_h^-)$ from \mathbf{P} yields the lower bound of the ± 1 error bar of spectral data; its upper bound \mathbf{P}_{+1} is calculated as $\mathbf{P}_{+1} = \mathbf{P} + (\sigma_a^+ + \sigma_h^+)$. The unchanged retrieval spectrum \mathbf{P}_0 is equal to \mathbf{P} . Figure 3 presents sample daily (Fig. 3a) and monthly (Fig. 3b) averaged green line spectra at the altitude of 95 km within the latitude range 20–25° N.

Each spectral data set (\mathbf{P}_{-1} , \mathbf{P}_0 and \mathbf{P}_{+1}) was processed (see Sect. 3) separately to calculate the corresponding LER profiles denoted by upper index temp: $\mathbf{LER}_{-1}^{\text{temp}}$, $\mathbf{LER}_0^{\text{temp}}$ and $\mathbf{LER}_{+1}^{\text{temp}}$. The emission-free spectral intervals (see Sect. 3) of \mathbf{P}_0 were used to calculate the uncertainty component (related to the random error vector σ_l) of the LER when integrating over the green line spectral interval. The altitude-dependent vector of SDs σ_l of \mathbf{LER}_0 was subtracted from $\mathbf{LER}_{-1}^{\text{temp}}$, which resulted in the lower error bound \mathbf{LER}_{-1} . The upper bound is $\mathbf{LER}_{+1} = \mathbf{LER}_{+1}^{\text{temp}} + \sigma_l$. The unchanged LER profile \mathbf{LER}_0 is equal to $\mathbf{LER}_0^{\text{temp}}$. Figure 4 presents sample daily (Fig. 4a) and monthly (Fig. 4b) averaged LER profiles within the latitude range 20–25° N with calculated uncertainty components.

The inversion scheme described above and supported by RTLS was applied to \mathbf{LER}_{-1} , \mathbf{LER}_0 and \mathbf{LER}_{+1} to calculate VER profiles denoted with the upper index temp: $\mathbf{VER}_{-1}^{\text{temp}}$, $\mathbf{VER}_0^{\text{temp}}$ and $\mathbf{VER}_{+1}^{\text{temp}}$. From the diagonal elements of the error covariance matrix \mathbf{S}_{tot} (see Eq. (10), Sect. 4.3) square roots were taken, resulting in the altitude-dependent vector of SDs $\sigma_{\text{S}_{\text{tot}}}$. The uncertainties $\sigma_{\text{S}_{\text{tot}}}$ of

VER_0 were subtracted from VER_{-1}^{temp} , resulting in the lower error bound VER_{-1} . The upper bound is $VER_{+1} = VER_{+1}^{\text{temp}} + \sigma_{S_{\text{tot}}}$. The unchanged VER profile VER_0 is equal to VER_0^{temp} . Figure 6 presents sample daily (Fig. 6a) and monthly (Fig. 6b) averaged VER profiles within the latitude range 20–25° N with calculated uncertainty components of $\sigma_{S_{\text{tot}}}$.

6.2 Error analysis for the retrieval of atomic oxygen concentration profiles

The maximum and minimum values of photochemical parameters (see Eq. 15) were used to estimate the contribution of photochemical model errors to the error in retrieved [O] profiles. The ranges of coefficients and other parameters used in the photochemical model (see Eq. 15) to determine the ± 1 error bar of the [O] profiles are presented in Table 2.

Each VER profile (VER_{-1} , VER_0 and VER_{+1}) was processed (see Sect. 5) assuming that simultaneously varied photochemical parameters cause maximum uncertainty of [O] separately, yielding [O] profiles denoted with the upper index temperature: $[O]_{-1}^{\text{temp}}$, $[O]_0^{\text{temp}}$ and $[O]_{+1}^{\text{temp}}$.

Moreover, model parameters that affect the [O] retrieval, but are not retrieved, are considered at this step, i.e., temperature and the sum of molecular oxygen [O₂] and nitrogen [N₂] concentrations. To determine the influence of temperature and [O₂] + [N₂] on the resulting random error, temperature was perturbed by $T' = 5$ K and [O₂] + [N₂] by $D' = 10$ %. The altitude-dependent vector of SDs σ_T was determined as: $\sigma_T^+ = |[\mathbf{O}(+T')]_0^{\text{temp}} - [\mathbf{O}]_0^{\text{temp}}|$ and $\sigma_T^- = |[\mathbf{O}]_0^{\text{temp}} - [\mathbf{O}(-T')]_0^{\text{temp}}|$. The altitude-dependent SDs σ_D in perturbations of D' were calculated as follows: $\sigma_D^- = |[\mathbf{O}(-D')]_0^{\text{temp}} - [\mathbf{O}]_0^{\text{temp}}|$ and $\sigma_D^+ = |[\mathbf{O}]_0^{\text{temp}} - [\mathbf{O}(+D')]_0^{\text{temp}}|$. The cumulative uncertainties due to perturbations in T' and D' contribute simultaneously to the ± 1 error bar of [O] causing maximum uncertainty: $\sigma_{TD}^+ = \sigma_T^+ + \sigma_D^+$ and $\sigma_{TD}^- = \sigma_T^- + \sigma_D^-$.

The uncertainties σ_{TD}^- of $[O]_0^{\text{temp}}$ were subtracted from $[O]_{-1}^{\text{temp}}$, resulting in the lower error bound $[O]_{-1}$. The upper bound is $[O]_{+1} = [O]_{+1}^{\text{temp}} + \sigma_{TD}^+$. The unchanged [O] profile $[O]_0$ is equal to $[O]_0^{\text{temp}}$. Figure 8 shows sample daily and monthly averaged atomic oxygen concentration ($[O]_{\text{SABER}}^{\text{quench}}$) profiles within the latitude range 20–25° N.

7 Results and discussion

In this section we first present results of the error analysis introduced in Sect. 6. Then the derived [O] densities are assessed via comparisons with NRLMSISE-00 and SD-WACCM4 model results as well as with TIMED/SABER retrievals. The verification of the [O] retrieval compares retrieved with reference [O] profiles and ideally allows a well-founded choice between the cubic and the extended cubic

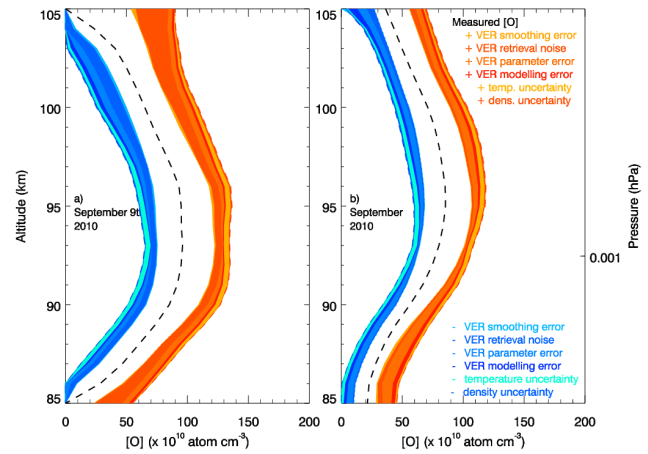


Figure 8. Sample daily (a) and monthly (b) averaged atomic oxygen concentration ($[O]_{\text{SABER}}^{\text{quench}}$) profiles for the 20–25° N latitude range with uncertainty components σ_{S_s} (yellow), σ_{S_m} (light red), σ_{S_b} (orange), σ_{S_f} (red) introduced for retrieving VER_{+1} and propagated to $[O]_{+1}$, while σ_{TD}^+ (light yellow and dark orange marked components) is calculated directly for the determination of $[O]_{+1}$. Similarly, σ_{S_s} (cyan), σ_{S_m} (light blue), σ_{S_b} (dark cyan) and σ_{S_f} (blue) are introduced for calculating VER_{-1} and are propagated to $[O]_{-1}$, while σ_{TD}^- (light cyan and dark cyan marked components) is directly calculated when determining $[O]_{-1}$. See Sects. 5, 6.2 and 7.1 for further details.

equations and a selection of the most appropriate source of temperature and density profiles from the different available sources. The verification was carried out in several steps including comparisons of reference and retrieved [O] profiles for

1. sample profiles (see Sect. 7.2)
2. climatologies of relative differences (see Sect. 7.3)
3. climatologies of correlation coefficients (see Sect. 7.4).

In Sect. 7.5 we present first results of seasonal [O] variations in the SCIAMACHY and the reference data sets and of the complete SCIAMACHY [O] data set covering the period from August 2002 to April 2012.

7.1 Results of error analysis

The calculated uncertainty components in the retrieved VER profiles are represented by VER_{+1} and VER_{-1} in Fig. 6 with daily (Fig. 6a) and monthly (Fig. 6b) averaging within the latitude range 20–25° N. The distribution of uncertainty components of the retrieved [O] profiles is presented in Fig. 8 with daily (Fig. 8a) and monthly (Fig. 8b) averaging within the same latitude range. The magnitudes of the errors, which are typical of the entire data set, are listed in Tables 3–8 in the supplementary material. The estimated magnitude of the maximum error (up to 60 % on the daily timescale and up to 47 % on the monthly timescale in the altitude

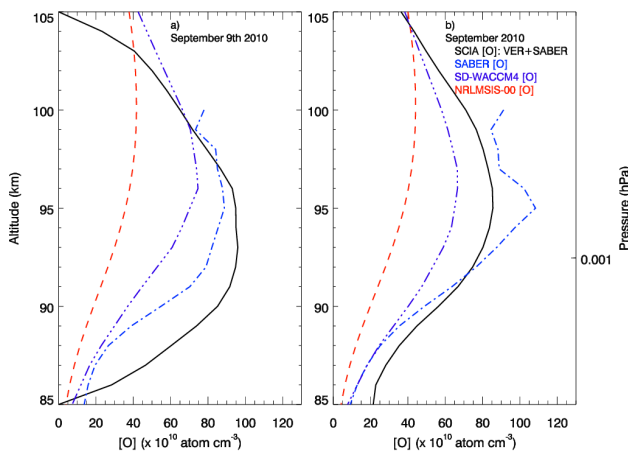


Figure 9. Sample daily (a) and monthly (b) averaged atomic oxygen concentration profiles (black solid $[O]_{\text{SABER}}^{\text{quench}}$) compared with profiles measured by SABER (blue dash dot $[O]_{\text{SABER}}$) and modeled with SD-WACCM4 (violet dash dot dot $[O]_{\text{WACCM4}}$) and NRLMSISE-00 (red dashed $[O]_{\text{MSISE00}}$) for the 20–25° N latitude range and at local times between 21:00 and 23:00.

range 90–100 km; see the last two columns of Tables 3–8) is bigger than the magnitude of the root-sum-square (RSS) error for other satellite derivations of $[O]$ (less than 25 % for SABER (Mlynchak et al., 2013) and less than 44 % for OSIRIS (Sheese et al., 2011)). Note that the maximum error can be equal to the RSS error if all absolute error components are equal, otherwise the estimation of maximum uncertainty results in a bigger error than an RSS error.

The averaged errors in the altitude range 90–100 km were used to calculate the relative errors of each error component to the total error so that added partial errors result in 100 % of the error (see the last two columns of Tables 3–8). The retrieval noise σ_{S_m} component is represented by relatively large colored zones in Fig. 6 and in Fig. 8 and corresponds to 54 and 37 % partial error, respectively. The corresponding colored zone is smaller in the monthly averaged profiles (21 and 12 %) because of a larger number of averaged profiles. The modeling error σ_{S_f} in VER and $[O]$ profiles is relatively small (12 and 9 % on the daily timescale as well as 24 and 16 % on the monthly timescale, respectively) compared to the total uncertainty $\sigma_{\text{S}_{\text{tot}}}$ (100 %) associated with the inversion procedure.

The $[O]$ profile error associated with temperature errors assumes the highest values within the altitude range where the $[O]$ peak occurs. Similar behavior, but to a lesser extent, is characteristic for the $[O]$ profile uncertainty caused by errors in atmospheric density (the sum of $[O_2]$ and $[N_2]$).

7.2 Verification step 1

Figure 9 shows atomic oxygen concentration ($[O]_{\text{SABER}}^{\text{quench}}$) profiles and reference $[O]$ profiles provided by SABER,

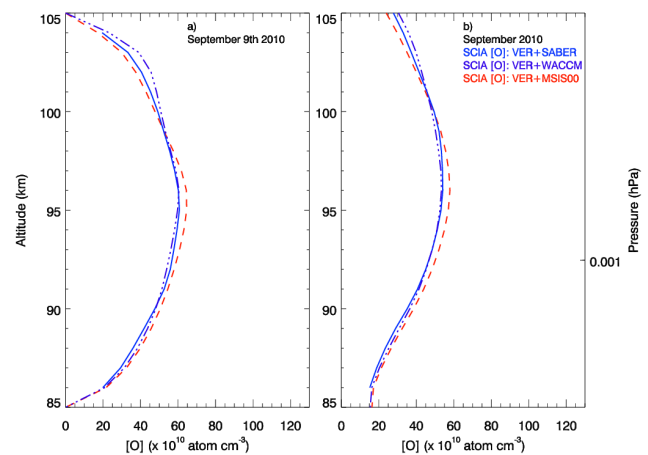


Figure 10. Sample daily (a) and monthly (b) averaged atomic oxygen concentration profiles ($[O]_{\text{SABER}}^{\text{cubic}}$ – blue solid, $[O]_{\text{WACCM4}}^{\text{cubic}}$ – violet dash-dotted, $[O]_{\text{MSISE00}}^{\text{cubic}}$ – red dashed) according to the cubic equation (McDade et al., 1986) for different sources of background atmospheric profiles and for the 20–25° N latitude range.

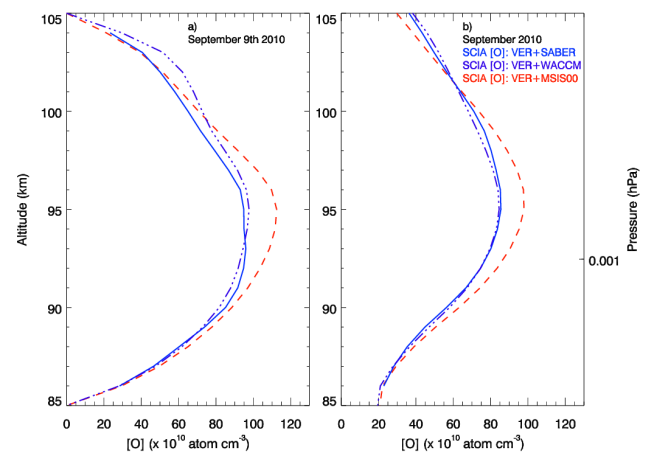


Figure 11. Sample daily (a) and monthly (b) averaged atomic oxygen concentration profiles ($[O]_{\text{SABER}}^{\text{quench}}$ – blue solid, $[O]_{\text{WACCM4}}^{\text{quench}}$ – violet dash-dotted, $[O]_{\text{MSISE00}}^{\text{quench}}$ – red dashed) according to the extended cubic equation by Gobbi et al. (1992) and Khomich et al. (2008) for different sources of background atmospheric profiles and for the 20–25° N latitude range.

NRLMSISE-00 and SD-WACCM4 in the altitude range 85–105 km in the latitude bin 20–25° N for a sample day (9 September 2010) and month (September 2010). The altitude dependence of $[O]_{\text{SABER}}^{\text{quench}}$ in comparison with $[O]_{\text{SABER}}$, $[O]_{\text{MSISE00}}$ and $[O]_{\text{WACCM4}}$ exhibits some deviations in the altitude range 85–87 km. These deviations correspond to low values of the measurement response (see Fig. 5) in the altitude range 82–87 km. The comparisons shown in Fig. 9 allow the preliminary conclusion that SABER as the source of temperature and density profiles (which we need to retrieve

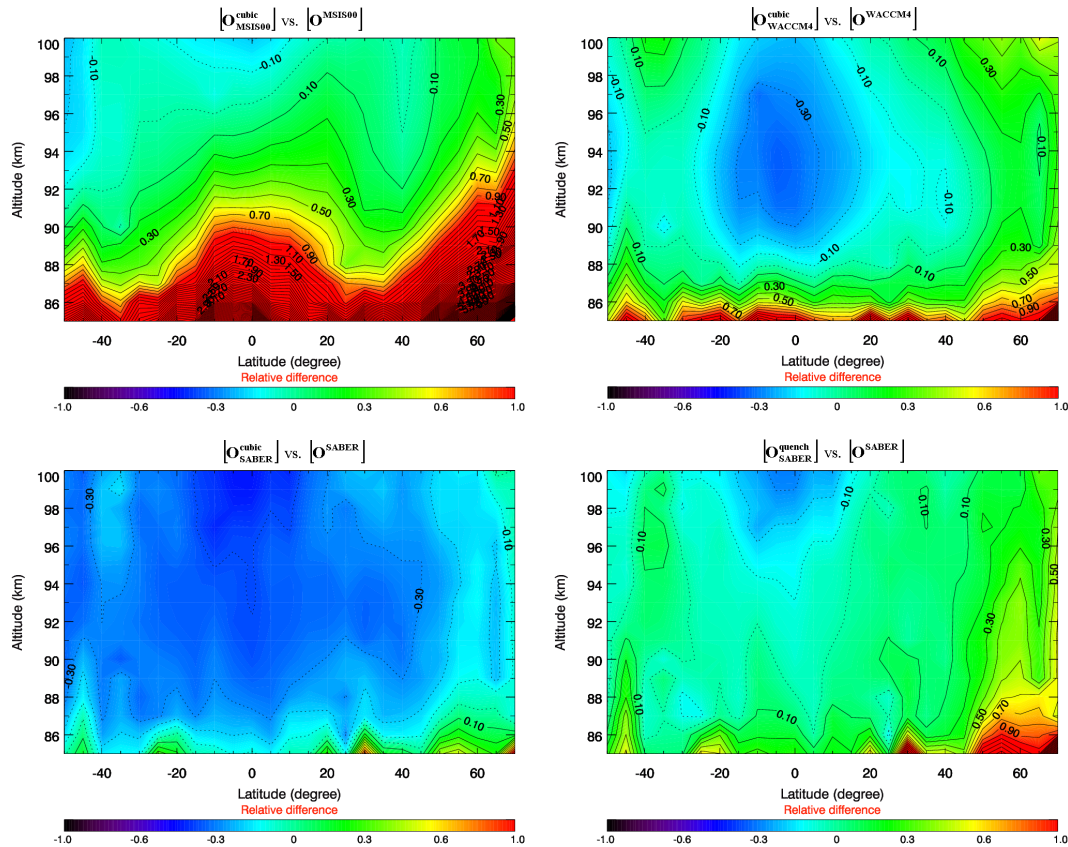


Figure 12. Relative differences in monthly averaged atomic oxygen fields from April 2010 to March 2011: $[O^{\text{cubic}}_{\text{MSIS00}}]$ compared with reference $[O^{\text{MSIS00}}]$ (top left), $[O^{\text{cubic}}_{\text{WACCM4}}]$ compared with reference $[O^{\text{WACCM4}}]$ (top right), $[O^{\text{cubic}}_{\text{SABER}}]$ compared with reference $[O^{\text{SABER}}]$ (bottom left) and $[O^{\text{quench}}_{\text{SABER}}]$ compared with reference $[O^{\text{SABER}}]$ (bottom right).

$[O]$ profiles from SCIAMACHY VER profiles) seems to be preferable.

Figure 9 allows the conclusion to be drawn that the reference $[O^{\text{MSIS00}}]$ profiles are characterized by lower concentrations in comparison with the retrieved $[O^{\text{quench}}_{\text{SABER}}]$ profiles. We use the absolute of the mean relative difference ($\langle |\epsilon| \rangle$) determined according to the equation $\langle |\epsilon| \rangle = \langle |([O]^{\text{current}} - [O]^{\text{reference}})/[O]^{\text{reference}}| \rangle$ averaged over the altitude range 90–100 km to quantify differences between different $[O]$ profiles. For $[O^{\text{MSIS00}}]$ ($[O]^{\text{current}}$) in comparison with $[O^{\text{quench}}_{\text{SABER}}]$ ($[O]^{\text{reference}}$) we obtain $\langle |\epsilon| \rangle \approx 0.6$ on the daily timescale and ≈ 0.54 on the monthly timescale. For $[O^{\text{WACCM4}}]$ in comparison with $[O^{\text{quench}}_{\text{SABER}}]$ we obtain $\langle |\epsilon| \rangle \approx 0.27$ on the daily timescale and ≈ 0.24 on the monthly timescale. For $[O^{\text{SABER}}]$ in comparison with $[O^{\text{quench}}_{\text{SABER}}]$ we obtain $\langle |\epsilon| \rangle \approx 0.13$ on the daily timescale and ≈ 0.14 on the monthly timescale.

Figures 10 and 11 (with data corresponding to the same altitude, latitude and time ranges as in Fig. 9) present $[O]$ profiles retrieved from SCIAMACHY VER profiles according to the cubic ($[O^{\text{cubic}}]$) and extended cubic ($[O^{\text{quench}}]$)

approaches (see Eq. 15) and show that $[O^{\text{quench}}]$ concentrations are higher than the $[O^{\text{cubic}}]$ concentrations. $\langle |\epsilon| \rangle$ for $[O^{\text{cubic}}_{\text{WACCM4}}]$ in comparison with $[O^{\text{cubic}}_{\text{SABER}}]$ is about 0.02 on the daily and monthly timescale. $\langle |\epsilon| \rangle$ for $[O^{\text{cubic}}_{\text{MSIS00}}]$ in comparison with $[O^{\text{cubic}}_{\text{SABER}}]$ is about 0.05 on the daily timescale and 0.06 on the monthly timescale. $\langle |\epsilon| \rangle$ for $[O^{\text{quench}}_{\text{WACCM4}}]$ in comparison with $[O^{\text{quench}}_{\text{SABER}}]$ is about 0.05 on the daily timescale and 0.02 on the monthly timescale. $\langle |\epsilon| \rangle$ for $[O^{\text{quench}}_{\text{MSIS00}}]$ in comparison with $[O^{\text{quench}}_{\text{SABER}}]$ is about 0.13 on the daily timescale and 0.11 on the monthly timescale. This leads to the preliminary conclusion that NRLMSISE-00 does not seem to be a reliable source of temperature and density profiles. A comparison between Figs. 9, 10 and 11 indicates that $[O^{\text{quench}}_{\text{SABER}}]$ profiles are (by sight) in better agreement with $[O^{\text{SABER}}]$ profiles than $[O^{\text{cubic}}]$ profiles are. This implies that the extended cubic equation seems to be preferable for the retrieval of $[O]$ profiles.

7.3 Verification step 2

Relative differences (ϵ) between different $[O]$ profiles were calculated according to the equation $\epsilon = ([O]^{\text{current}} -$

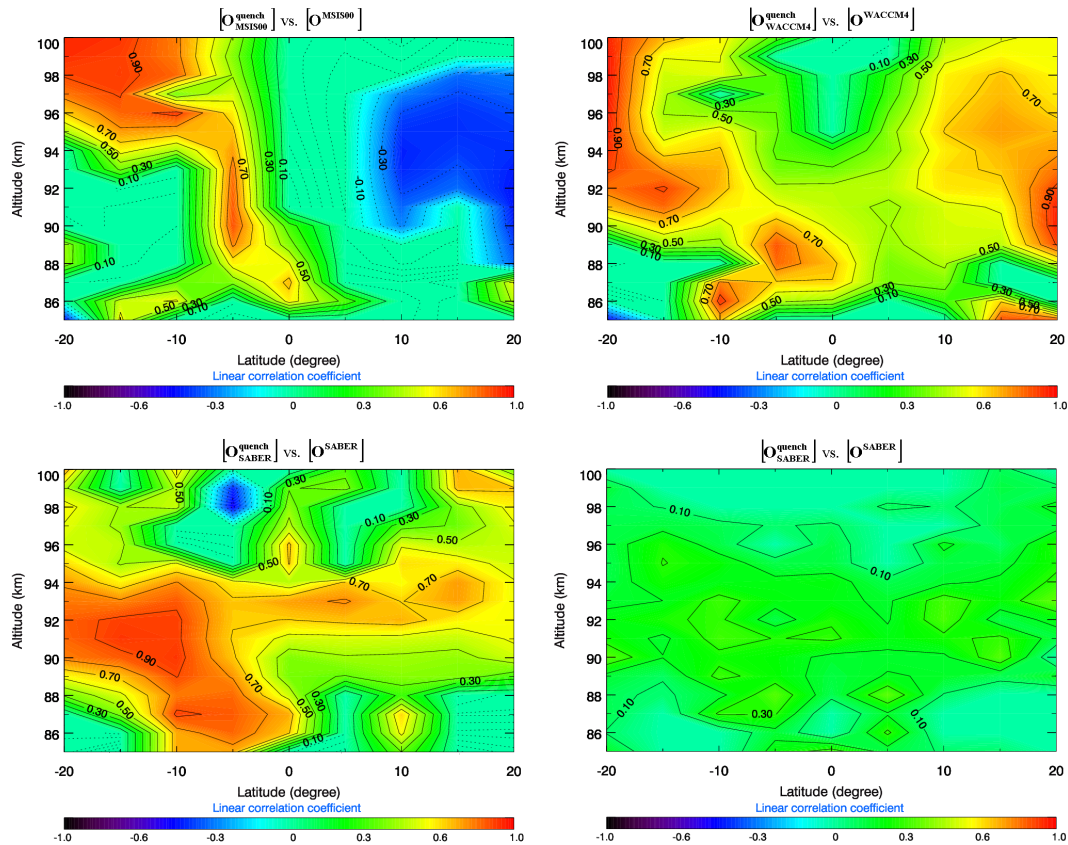


Figure 13. Correlation coefficients for atomic oxygen fields from April 2010 to March 2011: monthly averaged $[O_{\text{MSIS00}}^{\text{quench}}]$ cross-correlated with $[O_{\text{MSIS00}}]$ (top left), monthly averaged $[O_{\text{WACCM4}}^{\text{quench}}]$ cross-correlated with $[O_{\text{WACCM4}}]$ (top right), monthly averaged $[O_{\text{SABER}}^{\text{quench}}]$ cross-correlated with $[O_{\text{SABER}}]$ (bottom left) and daily averaged $[O_{\text{SABER}}^{\text{quench}}]$ cross-correlated with $[O_{\text{SABER}}]$ (bottom right).

$[O]^{\text{reference}})/[O]^{\text{reference}}$. Figure 12 presents sample distributions of relative $[O]$ differences as a function of latitude and altitude in the time period from April 2010 to March 2011 which corresponds to SD-WACCM4 data that we had at our disposal.

Provided that $\langle |\epsilon| \rangle$ in the following text is averaged over altitude range 86–100 km, the latitude range 50°S – 70°N and the time period from April 2010 to March 2011, we find that $\langle |\epsilon| \rangle$ for $[O_{\text{MSIS00}}^{\text{cubic}}]$ ($[O_{\text{current}}]$) in comparison with $[O_{\text{MSIS00}}]$ ($[O_{\text{reference}}]$) is about 0.81 on the monthly timescale. The mean absolute relative difference between $[O_{\text{MSIS00}}^{\text{quench}}]$ and $[O_{\text{MSIS00}}]$ (not shown in Fig. 12) of $\langle |\epsilon| \rangle \approx 1.74$ is at least twice as large as the value for $[O_{\text{MSIS00}}^{\text{cubic}}]$ vs. $[O_{\text{MSIS00}}]$. The mean absolute relative difference between $[O_{\text{WACCM4}}^{\text{quench}}]$ and $[O_{\text{WACCM4}}]$ (not shown in Fig. 12) is ≈ 0.65 . $\langle |\epsilon| \rangle$ for $[O_{\text{WACCM4}}^{\text{cubic}}]$ in comparison with $[O_{\text{WACCM4}}]$ is about 0.24 and exhibits the same anomaly cluster with high negative $\langle |\epsilon| \rangle$ of unknown origin in the subtropical region as for $[O_{\text{WACCM4}}^{\text{quench}}]$ vs. $[O_{\text{WACCM4}}]$. For $[O_{\text{SABER}}^{\text{quench}}]$ in comparison with $[O_{\text{SABER}}]$ we obtain $\langle |\epsilon| \rangle \approx 0.19$, which is smaller than $\langle |\epsilon| \rangle$ for $[O_{\text{SABER}}^{\text{cubic}}]$ vs. $[O_{\text{SABER}}]$

of about 0.28. This enables the preliminary conclusion that NRLMSISE-00 is not an adequate source of $[O]$ profiles. We use SABER temperature and density profiles for future analysis and the extended cubic approach to retrieve $[O]$ profiles.

We now briefly discuss differences between the O retrievals from SCIAMACHY O green line observations derived in this study with similar retrievals – also from SCIAMACHY O green line measurements – recently presented by Kaufmann et al. (2014). Kaufmann et al. (2014) also compared their retrievals to co-located SABER measurements and found an approximately 30 % low bias compared to SABER atomic oxygen. Since the photochemical model employed by Kaufmann et al. (2014) is essentially the one by McDade et al. (1986) – corresponding to our $[O_{\text{SABER}}^{\text{cubic}}]$ data set (see lower left panel of Fig. 12) – we come to a similar conclusion as Kaufmann et al. (2014): our SCIAMACHY $[O_{\text{SABER}}^{\text{cubic}}]$ retrievals are at least 30 % lower in comparison with $[O_{\text{SABER}}]$.

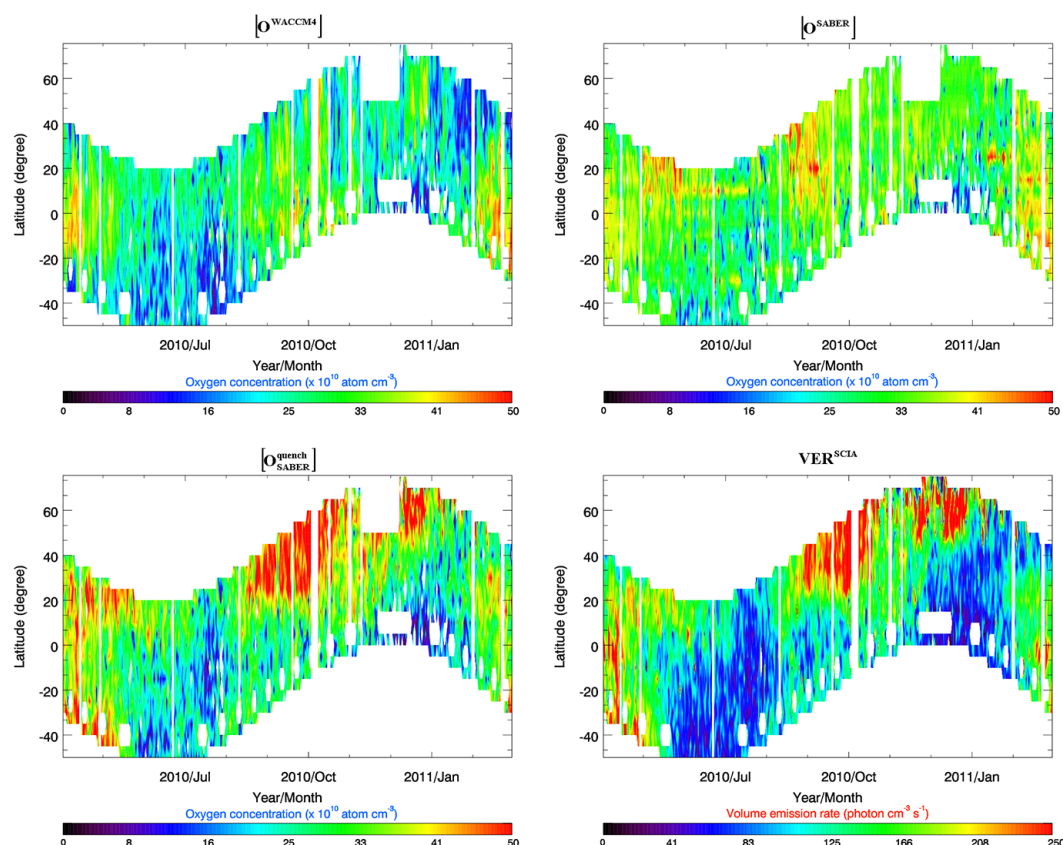


Figure 14. Seasonal variations of daily and vertically averaged (between 85 and 100 km) atomic oxygen fields from April 2010 to March 2011: $[O^{\text{WACCM4}}]$ (top left), $[O^{\text{SABER}}]$ (top right) and $[O^{\text{quench}}_{\text{SABER}}]$ (bottom left). The bottom right panel shows daily and vertically integrated (also from 85 to 100 km) SCIAMACHY volume emission rates.

7.4 Verification step 3

The Pearson's cross-correlation analysis between the retrieved and the reference [O] profiles was performed within the time period from April 2010 to March 2011. The calculated correlation coefficients were analyzed using the Fischer t test. Figure 13 shows sample correlation coefficient fields as a function of latitude and altitude for monthly averaged (top row and bottom left panel) and daily averaged (bottom right panel) [O]. Regions with correlation coefficients significant at the 68 % confidence level are indicated by solid contour lines, while areas characterized by lower significance are characterized by dotted contour lines and missing contour labels.

The cross correlation between SCIAMACHY and NRLMSISE-00 [O] profiles (top left panel in Fig. 13) indicates that there exists a phase shift of about 180° in the seasonal variations in the northern tropical region. In a recent study, Sheese et al. (2011) reported on a similar 180° phase shift of $[O^{\text{MSIS00}}]$ compared to daytime OSIRIS [O] profile measurements. In addition, Russell et al. (2005) found a 180° phase shift in the tidal signature in MSIS-90 [O] compared to

WINDII [O] measurements and model simulations with the TIME-GCM model.

The correlation between SCIAMACHY ($[O^{\text{quench}}_{\text{WACCM4}}]$) and SD-WACCM $[O^{\text{WACCM4}}]$ profiles (top right panel) is characterized by relatively high correlation coefficients of more than 0.65 in large parts of the latitude/height ranges shown. Directly above the equator the correlation is lower, particularly above the [O] peak.

The correlation coefficient field for monthly averaged $[O^{\text{quench}}_{\text{SABER}}]$ vs. $[O^{\text{SABER}}]$ does not contain the areas of negative (NRLMSISE-00) or extensive areas with low (SD-WACCM4) values that indicate discrepancies of the retrieved $[O^{\text{quench}}_{\text{SABER}}]$ compared to $[O^{\text{MSIS00}}]$ or $[O^{\text{WACCM4}}]$. The correlation of $[O^{\text{quench}}_{\text{SABER}}]$ with the SABER measurements on a daily basis (bottom right panel) shows a similar pattern than for the monthly averaged data but with lower correlation coefficients, as expected. We notice the presence of relatively high correlation coefficient values in the altitude range 88–95 km for monthly averaged $[O^{\text{quench}}_{\text{SABER}}]$ vs. $[O^{\text{SABER}}]$. The distribution of correlation coefficient values for monthly and daily averaged data are quite similar by sight (see bottom left and bottom right panels in Fig. 13). The high correlation

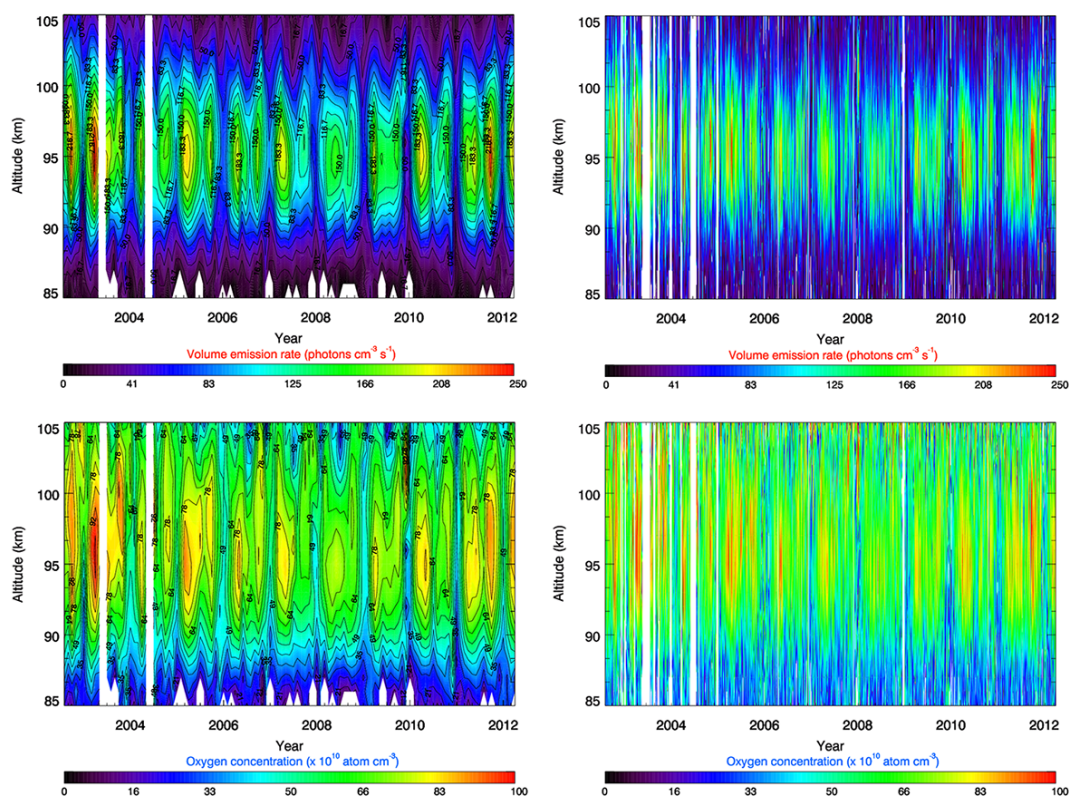


Figure 15. Temporal evolution of VER profiles (top panels) and $[O]_{\text{SABER}}^{\text{quench}}$ (bottom panels) with monthly (left panels) and daily (right panels) resolution for the 10–20° N latitude range from August 2002 to April 2012.

coefficients in the range 88–95 km may be related to the fact that the atomic oxygen profile retrievals from SABER and SCIAMACHY measurements are based on different airglow emissions that peak at different altitudes. The SABER nighttime atomic oxygen profiles are retrieved from the Meinel band VER (OH^* near $2\mu\text{m}$) profiles, which peak at about 87 km. In contrast, the O green line emissions used to retrieve atomic oxygen profiles from SCIAMACHY nighttime measurements peak near 95 km. [O] profiles can only be retrieved well from the different airglow emissions at altitudes with non-negligible emissions. We may therefore expect that the SABER [O] profile retrievals become more and more inaccurate above about 95 km, and the SCIAMACHY becomes more inaccurate below about 87 km.

7.5 Seasonal variations

We now present some first sample results on the morphology of atomic oxygen in the MLT region. More detailed analyses of different aspects of the spatiotemporal variability of atomic oxygen will be the foci of future studies.

Figure 14 shows seasonal variations in vertically averaged (85–100 km) SD-WACCM4 (top left panel), SABER (top right panel) and SCIAMACHY (bottom left panel) atomic oxygen for the time period from April 2010 to March 2011, together with vertically averaged green line volume emission

rates measured with SCIAMACHY (bottom right panel). When focusing at latitudes close to the equator all panels show a dominating semiannual variation with maxima around the equinoxes. However, there are also differences. The enhanced atomic oxygen abundances seen in the SCIAMACHY data (bottom left panel) in boreal fall and winter at latitudes above 20° N – consistent with a similar enhancement in the volume emission rates (bottom left panel) – are not that apparent in the SD-WACCM and SABER data sets. The reason for this discrepancy is currently unknown. We note, however, that similar oxygen anomalies at about 20° N in March 2010 and September 2010 are found in SABER and SCIAMACHY atomic oxygen fields but not in modeled $[O^{\text{WACCM4}}]$.

Figure 15 shows contour plots of O green line volume emission rates (top row) and retrieved atomic oxygen (bottom row) as a function of time and altitude with monthly (left column) and daily (right column) resolution for the 10–20° N latitude range and for the entire SCIAMACHY mission period from August 2002 to April 2012. Note that in case of the results for daily averaging (Figs. 14 and 15), gaps in the SABER temperature data set were filled with monthly averaged temperature data. The measurement gaps indicated by white areas in Fig. 15 are a consequence of missing SCIAMACHY raw data during these periods. The VER as well

as the O profile data presented in Fig. 15 show evidence for pronounced semiannual – with the well-established equinox maxima – and 11-year solar cycle signatures, with the solar cycle signature being more obvious at altitudes above about 95 km than below. An annual component is also visible associated with a major minimum in boreal winter and a minor minimum in boreal summer. These signatures are consistent with earlier studies (e.g., Liu and Shepherd, 2008; von Savigny and Lednyts'kyy, 2013) and will be the foci of future investigations of this comprehensive data set of atomic oxygen profiles in the MLT region.

8 Conclusions

Atomic oxygen concentration profiles in the MLT region were retrieved from SCIAMACHY observations of the O green line emission in the terrestrial nightglow. The inversion of integrated LER profiles to VER profiles was performed with a linear least squares minimization technique with regularization. The employed photochemical model is based on the generally accepted two-step Barth transfer scheme and [O] retrievals were carried out for the standard empirical photochemical model by McDade et al. (1986) as well as for an extended version that also considers quenching of $O(^1S_0)$ by $O(^3P)$ or N_2 .

A comprehensive sensitivity analysis was carried out to determine the effect of various error contributions occurring at the different steps of the [O] profile retrieval. Using the sensitivity analysis results, an error budget for the [O] profile retrievals from SCIAMACHY green line nightglow observations was established based on successive linear addition of the estimated uncertainty components in order to avoid any assumptions concerning distributions of model parameters and other error components. The errors were averaged in the altitude range 90–100 km and partial contributions of each error component relative to the total error were calculated in percent (added partial errors result in 100 % of the error shown in the last two columns of Tables 3–8 in the supplementary material). At the retrieval step leading to LER

profiles (see Sects. 3 and 6.1), the maximum uncertainty calculation includes the effect of errors in tangent height registration (partial contribution of 21.6 % for September 2010 to the total error), limited radiometric accuracy (partial contribution of 31.7 %) and spectrum integrating uncertainties (partial contribution of 46.7 %). At the retrieval step resulting in VER profiles (see Sects. 4, 4.3, 6.1 and 7.1) the maximum uncertainty calculation includes the impact of modeling errors (partial contribution of 24.3 % for September 2010), parameter errors (partial contribution of 46.4 %) measurement errors (partial contribution of 20.6 %) and smoothing errors (partial contribution of 8.7 %). At the retrieval step resulting in [O] profiles (see Sects. 5, 6.2, 7.1), the maximum uncertainty calculation includes the impact of modeling errors (partial contribution of 15.8 % for September 2010), parameter errors (partial contribution of 31.4 %), measurement errors (partial contribution of 12.1 %), smoothing errors (partial contribution of 4.3 %), temperature uncertainty values (partial contribution of 29.8 %) and density uncertainty values (partial contribution of 6.6 %).

The retrieved [O] profiles were compared to simulations with NRLMSISE-00 and SD-WACCM4 and to observations with SABER. The comparisons showed that NRLMSISE-00 [O] concentrations are significantly lower than the other ones.

Seasonal variations found in atomic oxygen anomalies in SABER and SCIAMACHY data sets are not so evident in SD-WACCM4 model simulations. The SCIAMACHY [O] profiles are in better agreement with co-located SABER observations when the extended photochemical model – considering quenching of $O(^1S)$ by $O(^3P)$ or N_2 – is used. This is an indication that the extended photochemical model is more appropriate to retrieve [O] profiles from the O green line emission than the standard photochemical model.

The implemented retrieval scheme was applied to the entire SCIAMACHY data set covering the period from August 2002 to April 2012, providing one of the most comprehensive atomic oxygen data sets in the MLT region. This data set will be evaluated in the near future to investigate seasonal, long-term, as well as solar cycle variations, both at the 11-year and 27-day temporal scale.

Appendix A

This appendix provides explanations for Table 2 showing upper and lower boundaries of the photochemical model parameters relevant for the retrieval of atomic oxygen profiles from $O(^1S)$ green line airglow measurements (see Sect. 5). The maximum and minimum values of A_{558} were taken from the works of Nakayama et al. (2006) (1.26 s^{-1}) – also used by Gao et al. (2012) – and Snively et al. (2010) (1.06 s^{-1}), respectively. The A_{558} values used by McDade et al. (1986) (1.18 s^{-1}), Makhoul et al. (1998) (1.18 s^{-1}), Semenov (1997) (1.215 s^{-1}) and Khomich et al. (2008) (1.215 s^{-1}) are between these maximum/minimum values.

The maximum and minimum values of A_{1S} were taken from McDade et al. (1986) (1.35 s^{-1} , based on research of Nicolaides et al., 1971) and Snively et al. (2010) (1.105 s^{-1}), respectively. The dimensionless values $C(0)$, $C(1)$ and $C(2)$ correspond to the fitting coefficients C^O/C^{O_2} , C^O and C^{O_2} (see McDade et al., 1986), which represent quenching by the different species (the *used coefficients* typically correspond to multiple reactions represented by the *intermediate coefficients*; see Table 1). The maximum and minimum values of $C(0)$, $C(1)$ and $C(2)$ used here were taken from McDade et al. (1986).

The rate coefficients are calculated in this study as follows:

$$\kappa_1 = k_1 \times 10^{-33} \cdot (300/T)^2,$$

$$^1\kappa_5 = ^1k_5 \times 10^{-11} \cdot e^{-305/T},$$

$$^2\kappa_5 = ^2k_5 \times 10^{-17} \text{ and}$$

$$^3\kappa_5 = ^3k_5 \times 10^{-12} \cdot e^{-(812-1.82 \times 10^{-3} \cdot T^2)/T}.$$

A value of $k_1 = 4.7$ was used for the standard retrieval and the temperature dependence of κ_1 was taken from McDade et al. (1986), as also done by Gao et al. (2012). The uncertainty range of k_1 (see Table 1) was estimated according to the uncertainties typical for the laboratory work performed by Campbell and Gray (1973). In terms of the temperature dependence of $^1\kappa_5$, we used the same expression as in Semenov (1997), Khomich et al. (2008) and von Savigny and Lednyts'kyi (2013). The uncertainty range of 1k_5 was taken from Slanger and Black (1976) and is also used by Witt et al. (1979). The value of $^2\kappa_5$ was taken from Okabe (1978) and it is used to calculate the maximum and minimum values by assuming a 10 % uncertainty. Gobbi et al. (1992) and Nakayama et al. (2006) also used a $^2\kappa_5$ value within 10 % of the Okabe (1978) value. The value of 3k_5 , its uncertainty range and the temperature dependence of $^3\kappa_5$ were taken from Capetanakis et al. (1993), as was done by von Savigny and Lednyts'kyi (2013) as well.

Finally, we note that the temperature dependence of κ_1 and $^2\kappa_5$ was originally used by McDade et al. (1986) with temperature profiles provided by MSIS-83 atmospheric model.

The Supplement related to this article is available online at doi:10.5194/amt-8-1021-2015-supplement.

Acknowledgements. This work was partly funded by Ernst-Moritz-Arndt-University of Greifswald. SCIAMACHY is jointly funded by Germany, the Netherlands and Belgium. SCIAMACHY Level 1 data was kindly provided by the European Space Agency. We are indebted to the SABER team and NASA for making SABER data available. The authors thank Ian C. McDade (York University, Toronto), Stefan Kowalewski (IUP Bremen) and Martin Kaufmann (Forschungszentrum Jülich) for helpful discussions.

Edited by: F. Khosrawi

References

- Akins, K. A., Healy, L. M., Coffey, S. L., and Picone, J. M.: Comparison of MSIS and Jacchia atmospheric density models for orbit determination and propagation, proceedings of the 13th AAS/AIAA space flight mechanics meeting, Ponce, Puerto Rico, Adv. Astronaut. Sci., 114, 951–970, 2003.
- Blackwell, D. E., Ingham, M. F., and Rundle, H. N.: The night-sky spectrum $\lambda\lambda$ 5000–6500 Å, *Astrophys. J.*, 131, 15–24, doi:10.1086/146801, 1960.
- Bovensmann, H., Burrows, J. P., Buchwitz, M., Frerick, J., Noël, S., Rozanov, V. V., Chance, K. V., and Goede, A. P. H.: SCIAMACHY: mission objectives and measurement modes, *J. Atmos. Sci.*, 2, 127–150, doi:10.1175/1520-0469(1999)056<0127:SMOAMM>2.0.CO;2, 1999.
- Bramstedt, K., Noël, S., Bovensmann, H., Gottwald, M., and Burrows, J. P.: Precise pointing knowledge for SCIAMACHY solar occultation measurements, *Atmos. Meas. Tech.*, 5, 2867–2880, doi:10.5194/amt-5-2867-2012, 2012.
- Burrows, J. P., Hölzle, E., Goede, A. P. H., Visser, H., and Fricke, W.: SCIAMACHY – scanning imaging absorption spectrometer for atmospheric chartography, *Acta Astronaut.*, 35, 445–451, doi:10.1016/0094-5765(94)00278-T, 1995.
- Campbell, I. M. and Gray, C. N.: Rate constants for $O(^3P)$ recombination and association with $N(^4S)$, *Chem. Phys. Lett.*, 18, 607–609, 1973.
- Capetanakis, F. P., Sondermann, F., Höser, S., and Stuhl, F.: Temperature dependence of the quenching of $O(^1S)$ by simple inorganic molecules, *J. Chem. Phys.*, 98, 7883, doi:10.1063/1.464596, 1993.
- Cardaci, M.: ENVISAT-1 products specifications, vol. 15, SCIAMACHY Products Specifications, available at: http://earth.esa.int/pub/ESA_DOC/ENVISAT/Vol15_Sciamachy_3L_1.1.pdf (last access: 15 March 2014), 2010.
- Egerton, A. C.: Lord Rayleigh, 1875–1947, *Obit. Not. Fell. R. Soc.*, 6, 502–538, 1949.
- Gao, H., Nee, J.-B., and Xu, J.: The emission of oxygen green line and density of O atom determined by using ISUAL and SABER measurements, *Ann. Geophys.*, 30, 695–701, doi:10.5194/angeo-30-695-2012, 2012.
- Garcia, R. R., Marsh, D. R., Kinnison, D. E., Boville, B. A., and Sassi, F.: Simulation of secular trends in the middle atmosphere, 1950–2003, *J. Geophys. Res.*, 112, D09301, doi:10.1029/2006JD007485, 2007.
- Gobbi, D., Takahashi, H., Clemesha, B. R., and Batista, P. P.: Equatorial atomic oxygen profiles derived from rocket observations of OI 557.7 nm airglow emission, *Planet. Space Sci.*, 40, 775–781, 1992.
- Gottwald, M., Bovensmann, H., Lichtenberg, G., Noël, S., von Bargen, A., Slijkhuis, S., PETERS, A., Hoozevee, R., von Savigny, C., Buchwitz, M., Kokhanovsky, A., Richter, A., Rozanov, A., Holzer-Popp, T., Bramstedt, K., Lambert, J.-C., Skupin, J., Wittrock, F., Schrijver, H., and Burrows, J. P.: SCIAMACHY – Monitoring the Changing Earth's Atmosphere, DLR, Freiburger Graphische Betriebe, 167 pp., 2006.
- Hoffmann, C. G., Kinnison, D. E., Garcia, R. R., Palm, M., Notholt, J., Raffalski, U., and Hochschild, G.: CO at 40–80 km above Kiruna observed by the ground-based microwave radiometer KIMRA and simulated by the Whole Atmosphere Community Climate Model, *Atmos. Chem. Phys.*, 12, 3261–3271, doi:10.5194/acp-12-3261-2012, 2012.
- Hudson, M. K., Kress, B. T., Mueller, H.-R., Zastrow, J. A., and Blake, J. B.: Relationship of the Van Allen radiation belts to solar wind drivers, *J. Atmos. Sol.-Terr. Phys.*, 70, 708–729, doi:10.1016/j.jastp.2007.11.003, 2008.
- Iwagami, N., Shibaki, T., Suzuki, T., Sekiguchi, H., Takegawa, N., and Morrow, W. H.: Rocket observations of atomic oxygen density and airglow emission rate in the WAVE2000 campaign, *J. Atmos. Sol.-Terr. Phys.*, 65, 1349–1360, doi:10.1016/j.jastp.2003.08.002, 2003.
- Jursa, A. S.: Handbook of Geophysics and Space Environment, Air Force Research Laboratory, Space Vehicles Directorate, Battlespace Environment Division, 4th Edn., available at: http://www.cnofs.org/Handbook_of_Geophysics_1985/pdf_menu.htm (last access: 15 March 2014), 1985.
- Kaiser, J. W., von Savigny, C., Eichmann, K.-U., Noël, S., Bovensmann, H., Frerick, J., and Burrows, J. P.: Satellite-pointing retrieval from atmospheric limb-scattering of solar UV-B radiation, *Can. J. Phys.*, 82, 1041–1052, doi:10.1139/p04-071, 2004.
- Kaufmann, M., Zhu, Y., Ern, M., and Riese, M.: Global distribution of atomic oxygen in the mesopause region as derived from SCIAMACHY $O(^1S)$ green line measurements, *Geophys. Res. Lett.*, 41, 6274–6280, doi:10.1002/2014GL060574, 2014.
- Kennedy, J. J., Rayner, N. A., Smith, R. O., Parker, D. E., and Saunby, M.: Reassessing biases and other uncertainties in sea-surface temperature observations measured in situ since 1850, part 2: biases and homogenisation *J. Geophys. Res.*, 116, D14104, doi:10.1029/2010JD015220, 2011.
- Khomich, V. Y., Semenov, A. I., and Shefov, N. N.: Airglow as an Indicator of Upper Atmospheric Structure and Dynamics, Springer, 739 pp., 2008.
- Kita, K., Iwagami, K., and Ogawa, T.: Rocket observations of oxygen night airglows: excitation mechanisms and oxygen atom concentration, *Planet. Space Sci.*, 40, 1269–1288, 1992.
- Kowalewski, S., von Savigny, C., Palm, M., McDade, I. C., and Notholt, J.: On the impact of the temporal variability of the collisional quenching process on the mesospheric OH emission layer: a study based on SD-WACCM4 and SABER, *Atmos. Chem. Phys.*, 14, 10193–10210, doi:10.5194/acp-14-10193-2014, 2014.

- Larson, W. J. and Wertz, J. R.: Space Mission Analysis and Design, Microcosm Press and Kluwer Academic Publishers, Springer Netherlands, 920 pp., 1999.
- Liu, G. and Shepherd, G. G.: An investigation of the solar cycle impact on the lower thermosphere $O(^1S)$ nightglow emission as observed by WINDII/UARS, *Adv. Space Res.*, 42, 933–938, doi:10.1016/j.asr.2007.10.008, 2008.
- Liu, H. L., Foster, B. T., Hagan, M. E., McInerney, J. M., Maute, A., Qian, L., Richmond, A. D., Roble, R. G., Solomon, S. C., Garcia, R. R., Kinnison, D., Marsh, D. R., Smith, A. K., Richter, J., Sassi, F., and Oberheide, J.: Thermosphere extension of the whole atmosphere community climate model, *J. Geophys. Res.*, 115, A12302, doi:10.1029/2010JA015586, 2010.
- Makhlouf, U. B., Picard, R. H., Winick, J. R., and Tuan, T. F.: A model for the response of the atomic oxygen 557.7 nm and the OH Meinel airglow to atmospheric gravity waves in a realistic atmosphere, *J. Geophys. Res.*, 103, 6261–6269, 1998.
- McDade, I. C., Murtagh, D. P., Greer, R. G. H., Dickinson, P. H. G., Witt, G., Stegman, J., Llewellyn, E. J., Thomas, L., and Jenkins, D. B.: ETON 2: Quenching parameters for the precursors of $O_2(b^1\Sigma_g^+)$ and $O(^1S)$ in the terrestrial nightglow, *Planet. Space Sci.*, 34, 789–800, 1986.
- Melo, S. M. L., Takahashi, H., Clemesha, B. R., Batista, P. P., and Simonich, D. M.: Atomic oxygen concentrations from rocket airglow observations in the equatorial region, *J. Atmos. Terr. Phys.*, 58, 1935–1942, 1996.
- Mertens, C. J., Russell, J. M., III, Mlynczak, M. G., She, C.-Y., Schmidlin, F. J., Goldberg, R. A., Lopez-Puertas, M., Wintersteiner, P. P., Picard, R. H., Winick, J. R., and Xu, X.: Kinetic temperature and carbon dioxide from broadband infrared limb emission measurements taken from the TIMED/SABER instrument, *Adv. Space Res.*, 43, 15–27, doi:10.1016/j.asr.2008.04.017, 2009.
- Mlynczak, M. G.: Energetics of the mesosphere and lower thermosphere and the SABER experiment, *Adv. in Space Res.*, 20, 1177–1183, doi:10.1016/S0273-1177(97)00769-2, 1997.
- Mlynczak, M. G. and Solomon, S.: A detailed evaluation of the heating efficiency in the middle atmosphere, *J. Geophys. Res.*, 98, 10517–10541, doi:10.1029/93JD00315, 1993.
- Mlynczak, M. G., Hunt, L. H., Mast, J. C., Marshall, B. T., Russell III, J. M., Smith, A. K., Siskind, D. E., Yee, J.-H., Mertens, C. J., Martin-Torres, F. J., Thompson, R. E., Drob, D. P., and Gordley, L. L.: Atomic oxygen in the mesosphere and lower thermosphere derived from SABER: Algorithm theoretical basis and measurement uncertainty, *J. Geophys. Res.*, 118, 5724–5735, doi:10.1002/jgrd.50401, 2013.
- Nakayama, T., Takahashi, K., Matsumi, Y., and Fujiwara, H.: Laboratory study of $O(^1S)$ formation process in the photolysis of O_3 and its atmospheric implications, *J. Atmos. Chem.*, 53, 107–122, doi:10.1007/s10874-006-0597-3, 2006.
- National Imagery and Mapping Agency: Department of Defense World Geodetic System 1984, Its Definition and Relationships with Local Geodetic Systems, Technical report 8350.2, 2000, available at: <http://earth-info.nga.mil/GandG/publications/tr8350.2/wgs84fin.pdf> (last access: 15 March 2014), 2000.
- Newell, P. T., Sotirelis, T., Ruohoniemi, J. M., Carbary, J. F., Liou, K., Skura, J. P., Meng, C.-I., Deehr, C., Wilkinson, D., and Rich, F. J.: OVATION: Oval variation, assessment, tracking, intensity, and online nowcasting, *Ann. Geophys.*, 20, 1039–1047, doi:10.5194/angeo-20-1039-2002, 2002.
- Nicolaides, C., Sinanoğlu, O., and Westhaus, P.: Theory of atomic structure including electron correlation. IV, Method for forbidden-transition probabilities with results for [O I], [O II], [O III], [N I], [N II] and [C I], *Phys. Rev. A*, 4, 1400–1410, doi:10.1103/PhysRevA.4.1400, 1971.
- NOAA: National Geophysical Data Center, Kp/Ap dataset, available at: ftp://ftp.ngdc.noaa.gov/STP/GEOMAGNETIC_DATA/INDICES/KP_AP/ (last access: 15 March 2014), 2014a.
- NOAA: Hemispheric Power Data lists, available at: <http://www.swpc.noaa.gov/ftplib/lists/hpi/> (last access: 15 March 2014), 2014b.
- Noël, S., Bovensmann, H., Burrows, J. P., Frerick, J., Chance, K. V., Goede, A. H. P., and Muller, C.: The SCIAMACHY instrument on ENVISAT-1, in: *Sensors, Systems, and Next-Generation Satellites II*, Vol. 3498 of Proc. SPIE, edited by: Fujisada, H., 94–104, 1998.
- NRLMSISE-00: Atmosphere Model, available at: <http://ccmc.gsfc.nasa.gov/modelweb/models/nrlmsise00.php> (last access: 15 March 2014), 2014.
- Okabe, H.: Photochemistry of small molecules, A Wiley-Interscience publication, ISBN 0-471-65304-7, 1978.
- Picone, J. M., Hedin, A. E., Drob, D. P., and Aikin, A. C.: NRLMSISE-00 empirical model of the atmosphere: Statistical comparisons and scientific issues, *J. Geophys. Res.*, 107, 1468, doi:10.1029/2002JA009430, 2002.
- Rodgers, C. D.: Characterization and error analysis of profiles retrieved from remote sounding measurements, *J. Geophys. Res.*, 95, 5587–5595, 1990.
- Rodgers, C. D.: *Inverse Methods for Atmospheric Sounding: Theory and Practice*, Series on Atmospheric, Oceanic and Planetary Physics, Vol. 2, World Scientific Publishing, 2000.
- Russell, J. M., III, Mlynczak, M. G., Gordley, L. L., Tansock, J., and Esplin, R.: An overview of the SABER experiment and preliminary calibration results, *Proc. SPIE*, 3756, 277–288, doi:10.1117/12.366382, 1999.
- Russell, J. P., Ward, W. E., Lowe, R. P., Roble, R. G., Shepherd, G. G., and Solheim, B.: Atomic oxygen profiles (80 to 115 km) derived from wind imaging interferometer/upper atmospheric research satellite measurements of the hydroxyl and greenline airglow: local time – latitude dependence, *J. Geophys. Res.*, 110, D15305, doi:10.1029/2004JD005570, 2005.
- SABER: level 2A data (version 2.0), available at: http://saber.gats-inc.com/browse_data.php (last access: 15 March 2014), updated in 2014.
- Semenov, A. I.: Long-term changes in the height profiles of ozone and atomic oxygen in the lower thermosphere, *Geomagn. Aeronomy+*, 37, 354–360, 1997.
- Semenov, A. I. and Shefov, N. N.: Model of the vertical profile of the atomic oxygen concentration in the mesopause and lower ionosphere region, *Geomagn. Aeronomy+*, 45, 797–808, 2005.
- Sheese, P. E., McDade, I. C., Gattinger, R. L., and Llewellyn, E. J.: Atomic oxygen densities retrieved from optical spectrograph and infrared imaging system observations of O_2 A-band airglow emission in the mesosphere and lower thermosphere, *J. Geophys. Res.*, 116, D01303, doi:10.1029/2010JD014640, 2011.

- Sima, D. M., van Huffel, S., and Golub, G. H.: Regularized total least squares based on quadratic eigenvalue problem solvers, *BIT*, 44, 739–812, 2004.
- Slanger, T. G. and Black, G.: $O(^1S)$ production from oxygen atom recombination, *J. Chem. Phys.*, 64, 3767, doi:10.1063/1.432692, 1976.
- Smith, A. K., Marsh, D. R., Mlynczak, M. G., Mast, J. C.: Temporal variations of atomic oxygen in the upper mesosphere from SABER, *J. Geophys. Res.*, 115, D18309, doi:10.1029/2009JD013434, 2010.
- Snively, J. B., Pasko, V. P., and Taylor, M. J.: OH and OI airglow layer modulation by ducted short-period gravity waves: effects of trapping altitude, *J. Geophys. Res.*, 115, A11311, doi:10.1029/2009JA015236, 2010.
- SOST-DLR: Anomaly Reports, available at: http://www.atmos.caf.dlr.de/projects/scops/instrument_monitoring/anomaly_reports_actual.html (last access: 15 March 2014), updated on 10 May 2012.
- SOST-DLR, data quality – thermal performance, available at: http://www.atmos.caf.dlr.de/projects/scops/instrument_monitoring/data_quality_thermal.html (last access: 15 March 2014), updated on 30 January 2013a.
- SOST-DLR: data quality – pointing (2008–2012) performance, available at: http://www.atmos.caf.dlr.de/projects/scops/instrument_monitoring/data_quality_pointing_2008_2012.html (last access: 15 March 2014), updated on 31 January 2013b.
- SOST-DLR: Data quality – pointing (2002–2007) performance, available at: http://www.atmos.caf.dlr.de/projects/scops/instrument_monitoring/data_quality_pointing_2002_2007.html (last access: 15 March 2014), updated on 31 January 2013c.
- von Savigny, C. and Lednyts'kyy, O.: On the relationship between atomic oxygen and vertical shifts between OH Meinel bands originating from different vibrational levels, *Geophys. Res. Lett.*, 40, 1–5, doi:10.1002/2013GL058017, 2013.
- von Savigny, C. H. A., McDade, I. C., Shepherd, G. G., and Rochon, Y.: Lower thermospheric nitric oxide concentrations derived from WINDII observations of the green nightglow continuum at 553.1 nm, *Ann. Geophys.*, 17, 1439–1446, doi:10.1007/s00585-999-1439-9, 1999.
- von Savigny, C., Bovensmann, H., Bramstedt, K., Dikty, S., Ebojje, F., Jones, A., Noël, S., Rozanov, A., and Sinnhuber, B.-M.: Indications for long-term trends and seasonal variations in the SCIAMACHY Level 1 version 6.03 tangent height information, *Techn. Note IUP scia pointing 2009-01*, Issue 2, University of Bremen, Bremen, Germany, 2009.
- Wang, Y. F. and Yuan, Y. X.: A trust region algorithm for solving distributed parameter identification problem, *J. Comp. Mathem.*, 21, 759–772, 2003.
- Witt, G., Stegman, J., Solheim, B. H., and Llewellyn, E. J.: A measurement of the $O_2(b^1\Sigma_g^+ - X^3\Sigma_g^-)$ atmospheric band and the OI(1S) green line in the nightglow, *Planet. Space Sci.*, 27, 341–350, 1979.
- Yoshimura, R., Iwagami, N., and Oyama, K.-I.: Rocket measurement of electron density and atomic oxygen density modulated by atmospheric gravity waves, *Adv. Space Res.*, 32, 837–842, doi:10.1016/S0273-1177(03)00422-8, 2003.

Article III

von Savigny, C., Lednyts'kyy, O., Forbes, J., and Zhang, X.: Lunar semidiurnal tide in the terrestrial airglow, *Geophysical Research Letters*, **42**, 9, 3553–3559, DOI: 10.1002/2015GL063567, 2015.

RESEARCH LETTER

10.1002/2015GL063567

Key Points:

- First observation of statistically significant lunar semidiurnal tides in airglow
- Coherent behavior of the lunar tidal signatures in all studied parameters
- Observed temperature lunar tide in good agreement with GSWM simulations

Correspondence to:

C. von Savigny,
csavigny@physik.uni-greifswald.de

Citation:

von Savigny, C., O. Lednyts'kyy, J. M. Forbes, and X. Zhang (2015), Lunar semidiurnal tide in the terrestrial airglow, *Geophys. Res. Lett.*, 42, 3553–3559, doi:10.1002/2015GL063567.

Received 24 FEB 2015

Accepted 2 APR 2015

Accepted article online 8 APR 2015

Published online 5 May 2015

Lunar semidiurnal tide in the terrestrial airglow

C. von Savigny¹, O. Lednyts'kyy¹, J. M. Forbes², and X. Zhang²
¹Institute of Physics, Ernst-Moritz-Arndt-Universität Greifswald, Greifswald, Germany, ²Department of Aerospace Engineering Sciences, University of Colorado, Boulder, Colorado, USA

Abstract We report on lunar semidiurnal tidal signatures in several parameters of the terrestrial airglow, including OI green line emission rates, OH(3-1) emission rates, as well as OH emission altitude, atomic oxygen, and OH(3-1) rotational temperature in the mesosphere/lower thermosphere region. The parameters were retrieved from spaceborne measurements of nightglow emissions at low latitudes with the Scanning Imaging Absorption Spectrometer for Atmospheric Cartography instrument on the Envisat satellite. The identified lunar tidal signatures in airglow emissions have amplitudes of a few percent and are highly significant statistically. Moreover, the signatures observed in the different parameters analyzed show a coherent behavior consistent with the view that they are caused by vertical motions associated with vertical transport of atomic oxygen and adiabatic cooling/heating. The observed lunar semidiurnal tidal signature in temperature is in good agreement with model simulations with the global scale wave model.

1. Introduction

The Moon's gravitational field is responsible for tidal signatures in the Earth's atmosphere. The semidiurnal lunar tide with a period of 12.421 h is the most important of these signatures. It was identified in surface pressure for the first time in 1842 based on measurements on St. Helena [Sabine, 1847]. Chapman [1918] presented the first successful identification of the lunar semidiurnal tide at extratropical latitudes based on 64 years of hourly surface pressure measurements at Greenwich.

In terms of the Earth's MLT (mesosphere/lower thermosphere) region, the lunar semidiurnal tide has been successfully identified in temperature [e.g., Forbes *et al.*, 2013] and winds [e.g., Stening *et al.*, 2003; Sandford and Mitchell, 2007; Zhang and Forbes, 2013]. Forbes *et al.* [2013] showed that the observed semidiurnal lunar tidal signature in MLT temperature can be reproduced reasonably well by simulations with the global scale wave model (GSWM). Lunar tidal signatures in several other MLT parameters have been discussed quite controversially in the literature. Indications for lunar tidal signatures in airglow emissions were reported in several studies. However, most authors pointed out that the observed signatures were not statistically significant [e.g., Davidson, 1963; Huruhta, 1965; Forbes and Geller, 1972; Semenov and Shefov, 1997; Khomich *et al.*, 2008]. A few studies deal with lunar semidiurnal variations in ground-based visual observations of noctilucent clouds (NLC) [Kropotkina and Shefov, 1975; Gadsden, 1985; Gadsden and Schröder, 1989; Dalin *et al.*, 2006]. However, the identified lunar tidal periods differ significantly between these studies, and the relative amplitudes of the identified lunar tidal signatures in NLC occurrence frequency—up to approximately 30%—have to date not been confirmed by nonvisual observations (e.g., satellite- or ground-based lidar observations) and have to be considered unrealistically large.

In this study, we employ spaceborne measurements of several MLT parameters retrieved from nightglow measurements with the Scanning Imaging Absorption Spectrometer for Atmospheric Cartography (SCIAMACHY) instrument on Envisat to demonstrate the statistically significant existence of lunar semidiurnal tidal signatures in airglow measurements for the first time—to our best knowledge.

2. Brief Instrumental Description

All measurement results presented in this study are based on spaceborne measurements with SCIAMACHY, the Scanning Imaging Absorption Spectrometer for Atmospheric Cartography on the ESA (European Space Agency) Envisat spacecraft [Bovensmann *et al.*, 1999]. SCIAMACHY was a passive grating spectrometer performing spectroscopic measurements in nadir, solar/lunar occultation, and limb geometry from August 2002 to April 2012. SCIAMACHY covered the 220 nm to 2380 nm spectral range in eight spectral channels with a

wavelength-dependent spectral resolution between 0.2 and 1.5 nm. For this study only the mesosphere/lower thermosphere limb measurements on the Earth's nightside were used. It is also relevant for this study that Envisat orbits the Earth in a sun-synchronous orbit, and all measurements presented here were made at 22:00 local solar time.

3. Data Products

OH rotational temperatures are retrieved from SCIAMACHY nightglow measurements of the OH(3-1) Meinel emission originating at altitudes near 87 km using the method described by *von Savigny et al.* [2004]. The OH(3-1) temperature retrievals were previously used to study solar 27 day effects in the tropical mesopause region [*von Savigny et al.*, 2012a] using an analysis technique similar to the one applied here to extract lunar tidal signatures. The OH(3-1) vertical volume emission rate (VER) profiles were retrieved from SCIAMACHY limb measurements using a constrained linear least squares inversion scheme with statistical weighting as described by *von Savigny et al.* [2012b]. The VER profiles cover the 1515–1546 nm spectral range, which is usually employed for OH(3-1) rotational temperature retrievals [e.g., *von Savigny et al.*, 2004]. The OH(3-1) emission altitudes shown in this study are centroid altitudes, i.e., correspond to altitude weighted by the OH(3-1) emission rate profile. The OI green line VER profiles were retrieved using the approach described by *Lednyts'kyy et al.* [2015]. Atomic oxygen concentration profiles in the 85–105 km altitude range were retrieved from the green line VER profiles based on the two-step Barth transfer scheme (details also provided by *Lednyts'kyy et al.* [2015]). The retrieved atomic oxygen concentrations were found to be in good agreement [*Lednyts'kyy et al.*, 2015] with colocated retrievals from OH airglow measurements with the Sounding of the Atmosphere using Broadband Emission Radiometry/Thermosphere Ionosphere Mesosphere Energetics and Dynamics (SABER/TIMED) instrument.

4. The Global Scale Wave Model

The SCIAMACHY observations are in this study compared to simulations with the global scale wave model [e.g., *Hagan et al.*, 1995]. The GSWM solves the linearized tidal equations taking into account meridional gradients in the background atmosphere, mean winds, and various dissipation processes. The model results used here were calculated with model version GSWM-09 described by *Zhang et al.* [2010] and are based on the implementation of the M_2 migrating lunar forcing as described by *Forbes* [1982]. Solar thermal forcing is switched off, and the atmospheric tidal forcing due to the solid Earth and oceans is neglected here. The GSWM model results used here were previously analyzed in a somewhat different context by *Forbes et al.* [2013].

5. Results and Discussion

Here we employ SCIAMACHY measurements between January 2003 and December 2011 and perform a superposed epoch analysis with lunar time as the independent variable. The measured parameters were daily and zonally averaged as well as averaged over the 0° to 20°N latitude bin—because only at these latitudes SCIAMACHY nighttime limb measurements are available throughout the year. Based on the known local solar time t of the measurements and the lunar phase angle ν , the daily value of the lunar time τ corresponding to the SCIAMACHY measurements can be determined by $\tau = t - \nu$ [e.g., *Forbes et al.*, 2013]. Figure 1 provides an illustration of this relationship for the specific conditions of the SCIAMACHY nightglow measurements used in this study.

Before averaging the different epochs, anomaly time series are determined by removing an 18 day running mean from each individual time series. The choice of an 18 day running mean is slightly arbitrary, but tests showed that the results obtained using a 15 day or 20 day running mean are very similar, in agreement with similar tests performed for identifying a solar 27 day signature in noctilucent clouds [*Robert et al.*, 2010]. The anomaly time series for OH rotational temperature, OH emission rate, OI emission rate, and atomic oxygen were then smoothed with a 3 day running mean in order to reduce variability. The OH emission altitudes were smoothed with a 5 day running mean, because of larger variability present in the time series. The epoch averaging is then performed for 1 h lunar time bins ranging for 0 to 12 lunar hours, following the approach used by *Forbes et al.* [2013]. Amplitude, phase, and their uncertainties were determined by least squares fitting of sinusoidal functions to the epoch-averaged anomalies. The phase here corresponds to the lunar time of the maximum value. The amplitude uncertainties correspond to the propagated standard errors of the mean of the averaged anomalies for each lunar time bin.

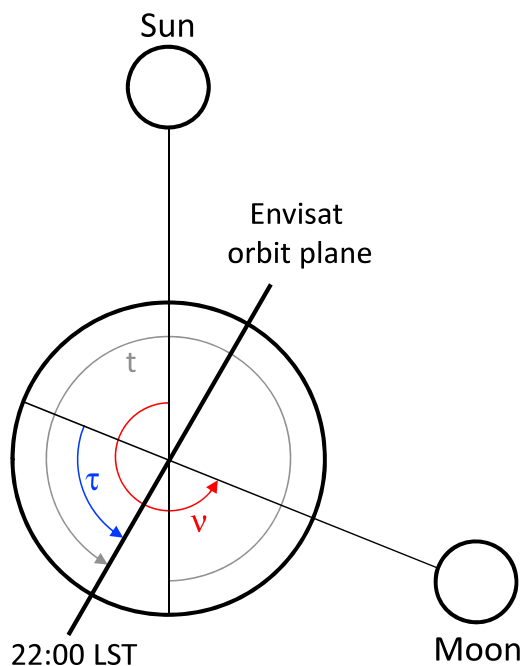


Figure 1. Illustration of the relationship between the lunar phase angle ν , local solar time t , and local lunar time τ . Due to Envisat's sun-synchronous orbit the local solar time of the SCIAMACHY measurements used here is always 22:00.

amplitudes for all three parameters are a factor of 7–11 larger than their uncertainties, making the signatures highly significant [Chapman and Lindzen, 1970].

Figure 3a shows the lunar semidiurnal signature identified in SCIAMACHY OH(3-1) rotational temperature (black line and symbols) in comparison with GSWM simulations (green solid line) for the same altitude and latitude range. The red solid line corresponds to the fit to the observed temperatures. The amplitude of the measured signature is about 30% smaller than that of the simulated signature, and the phases differ by about 1 lunar hour. A significant part of this difference is likely due to amplitude suppression associated with phase cancellation effects in constructing vector averages over 10 years of data. It is also likely that the GSWM model does not emulate dissipation of the tide with sufficient accuracy. However, the overall agreement between modeled and measured lunar tidal signature can be considered good.

Figure 3b compares the centroid OH(3-1) emission altitudes (black line and symbols) with GSWM simulations of the vertical lunar tidal winds (blue solid line). Again, the red solid line shows a sinusoidal fit to the OH(3-1) emission altitude. The phases of the tidal signatures in vertical winds and the OH(3-1) emission altitude differ by 3.5 lunar hours, corresponding to a phase shift of slightly more than 90° . This implies that the modeled tidal variation in vertical wind is consistent with the observed signature in OH emission altitude; i.e., the OH emission altitude is increasing for positive (i.e., upward directed) vertical winds and decreasing for negative vertical winds. This finding is an additional evidence that the observed signature in OH emission altitude is caused by the lunar semidiurnal tide.

We now discuss the relation between the lunar tidal signatures identified in the different mesopause parameters. Apparently, the tidal signatures in atomic oxygen, OH emission rate, and temperature are more or less in phase, while OH(3-1) emission altitude is out-of-phase relative to the OH(3-1) emission. The latter relation has been reported in several earlier studies for thermal tidal variations [e.g., Yee *et al.*, 1997], the semiannual variation and other sources of variability in the MLT region [Liu and Shepherd, 2006; von Savigny, 2015] and the results presented here indicate that this “universal scaling” [von Savigny, 2015] between OH emission altitude and emission rate also holds—in a qualitative sense—for the lunar semidiurnal tide.

As mentioned above, there exists a phase difference between the lunar tidal signatures in the OH and the OI green line airglow emissions of about 1.4 h (see Figure 2), which may be related to the altitude difference of

Figure 2 shows the lunar time dependence of the epoch-averaged relative anomalies (in %) of the vertically integrated OH(3-1) emission rate (a), the OI green line emission vertically integrated over the 90–100 km altitude range (b), and inferred atomic oxygen concentrations averaged over the same altitude range (c). The red solid lines correspond to the fitted sinusoidal functions. The error bars correspond to the standard errors of the mean of the epoch-averaged anomaly values. All three quantities exhibit clear semidiurnal lunar tidal signatures with relative amplitudes on the order of a few percent. The phases are around 11 lunar hours. The phases of the green line emission and atomic oxygen agree within uncertainties, which is expected, because atomic oxygen was derived from the green line measurements. The difference between the phases in OH and OI green line emissions is discussed below. We also note that the ampli-

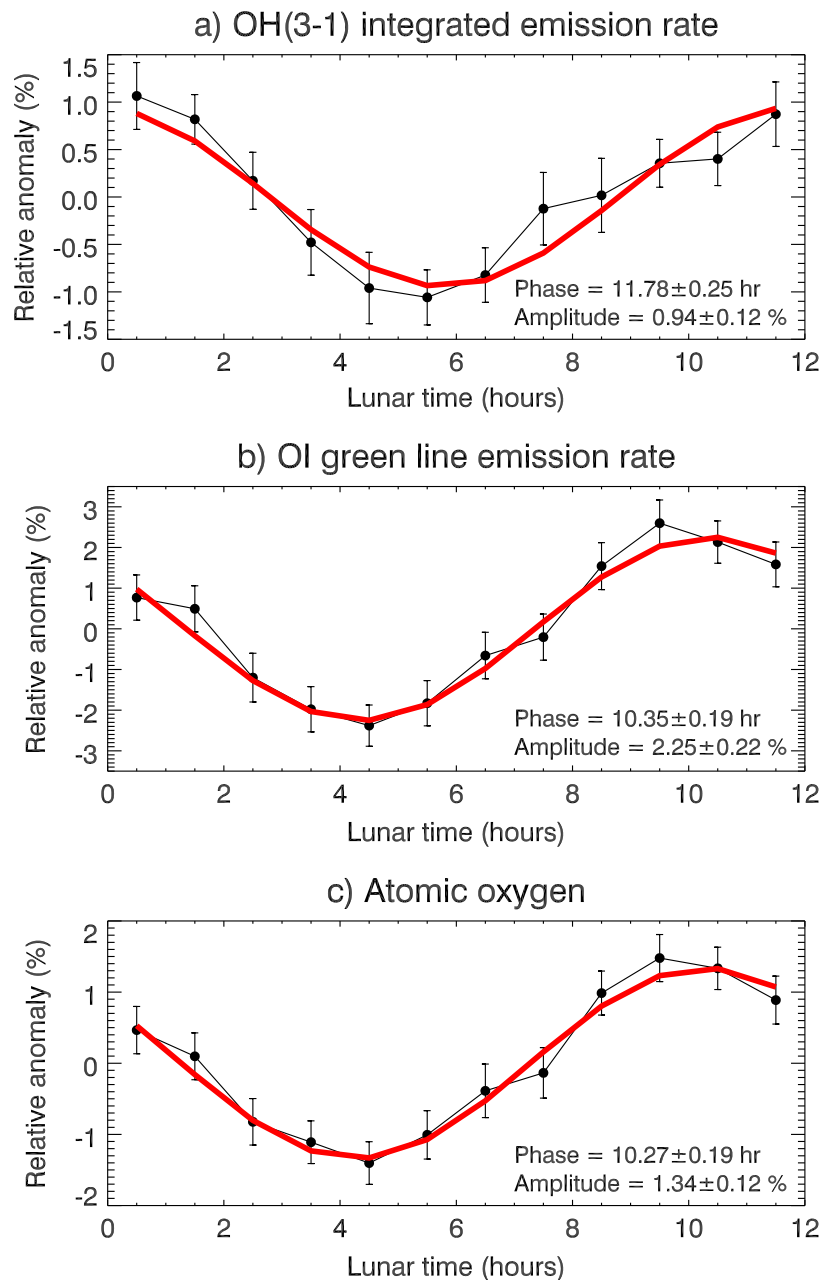


Figure 2. Epoch-averaged anomalies of (a) OH(3-1) integrated emission rate, (b) OI green line emission rate, and (c) inferred atomic oxygen as a function of lunar time. The red solid lines show least squares fit sinusoidal functions.

the two emissions. The centroid altitudes of the emissions are about 87 km for OH [e.g., von Savigny, 2015] and about 95 km for the OI green line [e.g., Lednyts'kyy et al., 2015]. If we compare the lunar tidal phases in GSWM temperature and vertical wind at 87 km and 95 km—and averaged over the $[0^\circ, 20^\circ\text{N}]$ latitude range—we obtain differences of 1.0 h for temperature and 2.5 h for the vertical wind, respectively, the sign being consistent with the observed phase differences. This means that the observed phase differences are in qualitative and reasonable quantitative agreement with the GSWM results.

In summary, we have identified statistically significant lunar semidiurnal tidal signatures in all parameters investigated—the signatures having amplitudes of at least 4.7 times their uncertainties. In addition, we observe coherent tidal signatures in all quantities retrieved that are consistent with the heuristic picture that

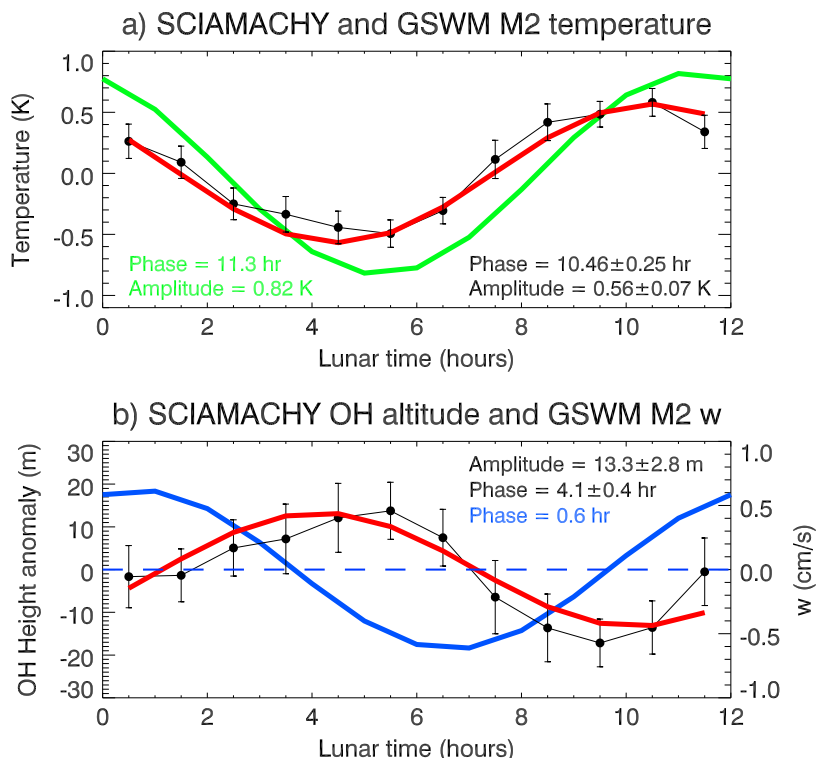


Figure 3. (a) Comparison of epoch-averaged SCIAMACHY OH(3-1) rotational temperature (black circles and line) with GSWM simulations of the lunar semidiurnal tide at 87 ± 5 km altitude and the $[0^\circ, 20^\circ\text{N}]$ latitude range. The red solid line shows a sinusoidal function least squares fit to the SCIAMACHY data points. (b) Epoch-averaged OH(3-1) emission altitude (black circles and left ordinate) and GSWM simulations of vertical wind speed (blue line and right ordinate) as a function of lunar time. The red solid line again shows a fit to the SCIAMACHY data points.

downward motion leads to increased airglow emissions due to downward transport of atomic oxygen—for both, the OI green line emission ($\propto [\text{O}]^3$) and the OH emission ($\propto [\text{O}]$)—and to a downward shift in the OH emission altitude, as well as a temperature increase that may be interpreted as being caused by adiabatic heating. This interpretation is also supported by the phase relationship between GSWM vertical winds and the SCIAMACHY OH temperature measurements.

5.1. Comparison to Previous Results

We now compare the results presented here with experimental results available in the literature. While there was significant interest in lunar tidal signatures in airglow emissions in the decade following the International Geophysical Year 1957/1958, rather few observational studies have been published on this topic in the last three decades.

Khomich et al. [2008] reported relative lunar semidiurnal variations in OH emission rate of about 2%, which is fairly consistent with the results presented here. *Semenov and Shefov* [1997] found lunar tidal signatures in vertically integrated OI green line emission rates on the order of 1–2%, also in agreement with the results presented here. However, in both of these studies the statistical significance of the presented results is questioned.

Khomich et al. [2008] also present results (their Figure 4.7) on the lunar tidal signature in OH emission altitude and report peak-to-peak variations of about 10 km, which is several orders of magnitude larger than the results presented here.

Several recent studies deal with lunar semidiurnal tidal signatures in middle atmospheric and lower thermospheric temperature. *Forbes et al.* [2013] compared lunar semidiurnal tidal signatures in SABER/TIMED temperature measurements with model simulations with the GSWM and found good overall agreement in terms of tidal amplitude and phase. The amplitude of the temperature tidal signature retrieved from the

SABER measurements is about 1 K or less for the altitude and latitude range relevant for the present study; i.e., the SABER results by Forbes *et al.* [2013] are in good agreement with the SCIAMACHY results presented here. The SABER temperature data set was also used in the recent study by Paulino *et al.* [2013] to investigate the lunar semidiurnal tide and its seasonal, latitudinal, and longitudinal variation. The amplitudes of the extracted lunar tidal signatures in the [0°, 20°N] latitude range relevant for the present study vary between about 0 and 1 K, in good agreement with our results. Paulino *et al.* [2013] reported tidal phases of about 10 h near 90 km altitude and in the [0°, 20°N] latitude range, which agrees very well with the results presented here.

6. Conclusions

This study presents statistically significant lunar semidiurnal tidal signatures in several different terrestrial airglow parameters, including OI green line emission rates, OH(3-1) emission rates, as well as OH emission altitude, atomic oxygen, and temperature in the MLT region. The data sets were retrieved from SCIAMACHY/Envisat nightglow measurements at tropical latitudes from 2003 to 2011. The tidal signature in OH rotational temperature is in good agreement with model simulations with the global scale wave model. Apart from the presence of statistically significant lunar tidal signatures in different parameters, we find a coherent relationship between the studied parameters suggesting that the observed signatures are to a large extent driven by vertical motions. All these findings provide robust evidence that lunar semidiurnal tidal signatures are indeed present in the terrestrial airglow.

Acknowledgments

This work was supported by Ernst-Moritz-Arndt-Universität Greifswald and by the German Ministry of Education and Research (BMBF) within the priority program ROMIC (project OHcycle, grant 01LG1215A). J.M.F. and X.Z. acknowledge support under NASA award NNX12AJ58G as part of the Heliophysics Guest Investigator Program. We are indebted to the European Space Agency for making SCIAMACHY Level 1 data available. Further information on the data used in this study can be obtained upon request via email to the author (csavigny@physik.uni-greifswald.de).

The Editor thanks two anonymous reviewers for their assistance in evaluating this paper.

References

- Bovensmann, H., J. P. Burrows, M. Buchwitz, J. Frerick, S. Noël, V. V. Rozanov, K. V. Chance, and A. P. H. Goede (1999), SCIAMACHY: Mission objectives and measurement modes, *J. Atmos. Sci.*, **56**, 127–150.
- Chapman, S. (1918), The lunar atmospheric tide at Greenwich, 1854–1917, *Q. J. R. Meteorol. Soc.*, **44**(188), 271–280.
- Chapman, S., and R. S. Lindzen (1970), *Atmospheric Tides: Thermal and Gravitational*, 200 pp., Gordon and Breach, New York.
- Dalin, P. A., N. N. Pertsev, and V. A. Romejko (2006), Significance of lunar impact on noctilucent clouds, *J. Atmos. Sol. Terr. Phys.*, **68**, 1653–1663.
- Davidson, T. W. (1963), Measurements of lunar time variations in the intensity of oxygen 5577 Å airglow, *Planet. Space Sci.*, **11**, 1133–1138.
- Forbes, J. M. (1982), Atmospheric tides: II. The solar and lunar semidiurnal components, *J. Geophys. Res.*, **87**, 5241–5252.
- Forbes, J. M., and M. A. Geller (1972), Lunar semidiurnal variation in O I (5577 Å) nightglow, *J. Geophys. Res.*, **77**(16), 2942–2947.
- Forbes, J. M., X. Zhang, S. Bruinsma, and J. Oberheide (2013), Lunar semidiurnal tide in the thermosphere under solar minimum conditions, *J. Geophys. Res. Space Physics*, **118**, 1788–1801, doi:10.1029/2012JA017962.
- Gadsden, M. (1985), Observations of noctilucent clouds from north-west Europe, *Ann. Geophys.*, **3**(1), 119–126.
- Gadsden, M., and W. Schröder (1989), *Noctilucent Clouds*, 165 pp., Springer, New York.
- Hagan, M. E., J. M. Forbes, and F. Vial (1995), On modeling migrating solar tides, *Geophys. Res. Lett.*, **22**(8), 893–896.
- Huruhata, M. (1965), Lunar tidal effect on the oxygen green line in the night airglow, *J. Geophys. Res.*, **70**(23), 5979–5980.
- Khomich, V. Y., A. I. Semenov, and N. N. Shefov (2008), *Airglow as an Indicator of Upper Atmospheric Structure and Dynamics*, 739 pp., Springer, Berlin.
- Kropotkina, Y. P., and N. N. Shefov (1975), Influence of lunar tides on the probability of appearance of noctilucent clouds. Russian Academy of Sciences, *Phys. Atmos. Ocean*, **11**(11), 1184–1186.
- Lednyts'kyy, O., C. von Savigny, K.-U. Eichmann, and M. G. Mlynarczyk (2015), Atomic oxygen retrievals in the MLT region from SCIAMACHY nightglow limb measurements, *Atmos. Meas. Tech.*, **8**, 1021–1041, doi:10.5194/amt-8-1021-2015.
- Liu, G., and G. G. Shepherd (2006), An empirical model for the altitude of the OH nightglow emission, *Geophys. Res. Lett.*, **33**, L09805, doi:10.1029/2005GL025297.
- Paulino, A. R., P. P. Batista, and I. S. Batista (2013), A global view of the atmospheric lunar semidiurnal tide, *J. Geophys. Res. Atmos.*, **118**, 13,128–13,139, doi:10.1002/2013JD019818.
- Robert, C. E., C. von Savigny, N. Rahpoe, H. Bovensmann, J. P. Burrows, M. T. DeLand, and M. J. Schwartz (2010), First evidence of a 27 day solar signature in noctilucent cloud occurrence frequency, *J. Geophys. Res.*, **115**, D00I12, doi:10.1029/2009JD012359.
- Sabine, E. (1847), On the lunar atmospheric tide at St. Helena, *Philos. Trans. R. Soc.*, **137**, 45–50.
- Sandford, D. J., and N. J. Mitchell (2007), Lunar tides in the mesosphere over Ascension Island (8°S, 14.4°W), *Ann. Geophys.*, **25**, 9–12, doi:10.5194/angeo-25-9-2007.
- Semenov, A. I., and N. N. Shefov (1997), An empirical model of nocturnal variations in the 557.7 nm emission of atomic oxygen: 1. Intensity, *Geomagn. Aeron.*, **37**(2), 215–221.
- Stening, R. J., T. Tsuda, and T. Nakamura (2003), Lunar tidal winds in the upper atmosphere over Jakarta, *J. Geophys. Res.*, **108**(A5), 1192, doi:10.1029/2002JA009528.
- von Savigny, C. (2015), Variability of OH(3-1) emission altitude from 2003 to 2011: Long-term stability and universality of the emission rate-altitude relationship, *J. Atmos. Sol. Terr. Physics*, doi:10.1016/j.jastp.2015.02.001, in press.
- von Savigny, C., et al. (2004), First near-global retrieval of OH rotational temperatures from satellite-based Meinel band emission measurements, *Geophys. Res. Lett.*, **31**, L15111, doi:10.1029/2004GL020410.
- von Savigny, C., K.-U. Eichmann, C. E. Robert, J. P. Burrows, and M. Weber (2012a), Sensitivity of equatorial mesopause temperatures to the 27-day solar cycle, *Geophys. Res. Lett.*, **39**, L21804, doi:10.1029/2012GL053563.
- von Savigny, C., I. C. McDade, K.-U. Eichmann, and J. P. Burrows (2012b), On the dependence of the OH* Meinel emission altitude on vibrational level: SCIAMACHY observations and model simulations, *Atmos. Chem. Phys.*, **12**, 8813–8828, doi:10.5194/acp-12-8813-2012.
- Yee, J. H., G. Crowley, R. G. Roble, W. R. Skinner, M. D. Burrage, and P. B. Hays (1997), Global simulations and observations of O(¹S), O2(¹Σ) and OH mesospheric nightglow emissions, *J. Geophys. Res.*, **102**, 19,949–19,968.

- Zhang, J. T., and J. M. Forbes (2013), Lunar tidal winds between 80 and 110 km from UARS/HRDI wind measurements, *J. Geophys. Res. Space Physics*, *118*, 5296–5304, doi:10.1002/jgra.50420.
- Zhang, X., J. M. Forbes, and M. E. Hagan (2010), Longitudinal variation of tides in the MLT region: 1. Tides driven by tropospheric net radiative heating, *J. Geophys. Res.*, *115*, A06316, doi:10.1029/2009JA014897.

Article IV

Lednyts'kyi, O., von Savigny, C., and Weber, M.: Sensitivity of equatorial atomic oxygen in the MLT region to the 11-year and 27-day solar cycles, *Journal of Atmospheric and Solar-Terrestrial Physics*, **162**, 136–150, DOI: 10.1016/j.jastp.2016.11.003, 2017.

The article IV is only available to subscribers of the journal.

Article V

Lednyts'kyi, O., and von Savigny, C.: Photochemical modeling of molecular and atomic oxygen based on multiple *in-situ* emissions measured during the Energy Transfer in the Oxygen Nightglow rocket campaign, *Atmospheric Chemistry and Physics Discussions*, **2019**, 1–60, DOI: 10.5194/acp-2019-221, in review, 2019.



Photochemical modeling of molecular and atomic oxygen based on multiple *in-situ* emissions measured during the Energy Transfer in the Oxygen Nightglow rocket campaign

Olexandr Lednyts'kyi¹ and Christian von Savigny¹

¹University of Greifswald, Greifswald, Germany

Correspondence: O. Lednyts'kyi (olexandr.lednytskyi@uni-greifswald.de), ORCID: 0000-0002-8343-6357

Abstract. Electronically excited states of molecular and atomic oxygen (six of O₂ and two of O) were implemented in the proposed Multiple Airglow Chemistry (MAC) model as minor species coupled with each other as well as with the ground states of O₂ and O to represent the photochemistry in the upper Mesosphere and Lower Thermosphere (MLT) region. The MAC model is proposed combining chemical processes of the well-known photochemical models related to identified O₂ and O species and some additional processes. Concentrations of excited O₂ and O species were retrieved using the MAC model on the basis of the multiple *in-situ* nightglow emissions measured during the Energy Transfer in the Oxygen Nightglow (ETON) rocket campaign. The proposed retrieval procedure to obtain concentrations of these MLT minor species is implemented avoiding *a priori* data sets. Unknown and poorly constrained reaction rates were tuned and reaction rates of the well-known models were updated with the MAC model comparing *in-situ* and evaluated emission profiles as well as *in-situ* and retrieved O concentration profiles. As a result, precursors of O₂ and O species responsible for transitions considered in the MAC model are identified and validated by calculations with the MAC model.

1 Introduction

Airglow is a permanent global atmospheric phenomenon that can be hardly seen without appropriate instruments. Ångström (1869) used such instruments and observed the green line emission at 557.7 nm in the nightglow (airglow at night) from the Earth's surface in 1868 for the first time. The origin of airglow was considered to be the same as the origin of aurora, a sporadic arc-like atmospheric phenomenon, which fascinated numerous spectators for many thousands of years.

Table 1 provides an overview of relatively strong airglow emissions detected in the upper Mesosphere and Lower Thermosphere (MLT) *in-situ* and remotely. The Energy Transfer in the Oxygen Nightglow (ETON) rocket campaign conducted in March 1982 and discussed in Section 2 was conceptualized to obtain *in-situ* profiles of airglow Volume Emission Rates (VER) and other atmospheric parameters like atomic oxygen (O) in the ground state (O(³P)) to verify and validate photochemical models describing airglow.

O(³P) is a chemically active MLT trace gas which is a critical component of the energy budget of the MLT region. O(³P) is also required to retrieve carbon dioxide (CO₂) concentrations, profiles of kinetic temperature and pressure (Remsberg et al.,



2008; García-Comas et al., 2008; Rezac et al., 2015). $O(^3P)$ is also a major component of the neutral bath gas in the upper thermosphere significantly contributing to the nighttime ionosphere (Shematovich et al., 2011; Wei et al., 2014).

The transition $O(^1S - ^1D)$ from the second excited O state ($O(^1S)$) to the first one ($O(^1D)$) is detected as the 557.7 nm green line emission. The Chapman excitation scheme and the Barth excitation transfer scheme were proposed in 1931 and 1962, respectively, to explain the origin of the green line emission in the MLT. The Chapman excitation scheme considers a collision of two $O(^3P)$ atoms and a third body represented by $O(^3P)$ to produce $O(^1S)$ (Chapman, 1931, 1937). The Barth excitation transfer scheme considers (1) a collision of two $O(^3P)$ atoms and a third body represented by an abundant molecule, e.g. molecular nitrogen (N_2) and oxygen (O_2), to produce O_2 in a not identified excited state O_2^* , and (2) an energy transfer from O_2^* to $O(^3P)$ so that $O(^1S)$ is produced (Bates, 1979). Comparing both excitation schemes Bates (1979) interpreted the Chapman excitation process to consist of four steps as follows: (1) two $O(^3P)$ atoms collide (2) creating a common surface of potential energy of, presumably, an electronically excited O_2 molecule in the upper Herzberg state (Greer et al., 1987), (3) after its collision with a third $O(^3P)$ atom (4) one vibrationally excited O_2 molecule and one $O(^1S)$ atom are created. One of the differences between the Chapman and Barth excitation schemes is the kind of a third body being an $O(^3P)$ atom or an abundant molecule in the MLT, respectively. The energy transfer considered in the Barth scheme includes O_2^* acting as the $O(^1S)$ precursor, but the Chapman scheme does not include it. Photochemical models proposed to implement the Chapman and Barth schemes are hereafter referred to be of the first (one-step) and the second (two-step) type, respectively.

Airglow emissions are very complex atmospheric phenomena so that photochemical models are often proposed to derive unknown or poorly constrained reaction rates, which can be backed up by reaction rates determined in the ground-based laboratory with the use of the Stern-Volmer method. The Stern-Volmer method is applied to analyze concentration dependent kinetics in a homogeneous system, to which a quencher was added (Lakowicz, 2006). According to the Stern-Volmer method, excited and quenching chemical species are considered in a system of a few photochemical reactions so that steady-state methods can be applied to describe emissions. Then measurements of lifetimes or concentrations of emitting species enable determining the true pseudo-first order decay required to calculate the rate coefficient of the considered quenching reaction. However, the same values of the pseudo-first order decay rate are possible for both the dynamic quenching and the static quenching at the given temperature (Lakowicz, 2006). Dynamic quenching reduces the apparent fluorescent lifetime, and static quenching rather reduces the apparent concentration of fluorescent species during inelastic collisions (Lakowicz, 2006). Unfortunately, reactive collisions responsible for the static quenching are not so well understood compared to the products of the dynamic quenching that can introduce difficulties calculating the rate coefficient of the considered quenching reaction.

If no more than one emission, e.g. $VER\{O(^1S - ^1D)\}$ in McDade et al. (1986), is considered in the model of the second type then the resulting mass conservation (continuity) equation is of the third degree with respect to $[O(^3P)]$, and the respective solutions can be easily interpreted. As for the $O_2(b - X)$ transition, McDade et al. (1986) developed photochemical models of the first and second types to describe transitions from $O_2(b)$ (the second electronically excited state of molecular oxygen, O_2) to $O_2(X)$ (the electronic ground state of O_2). This transition in the Atmospheric band was measured *in-situ* in the Earth's atmosphere during the ETON campaign to retrieve $VER\{O_2(b - X)\}$. The model of the second type with the $O_2(b)$ precursor and $O_2(b)$ was proposed to explain non-linearities detected in quenching processes simulated by using the model of the first



type with $O_2(b)$ only. McDade et al. (1986) used known reaction rates and tuned poorly constrained reaction rates of these quenching processes in the atmosphere so that simulated profiles match the *in-situ* observations. The processes considered in the models of the first and second types and provided in Table 2 were developed by McDade et al. (1986) to describe atmospheric airglow emissions and to verify the obtained results in the ground-based laboratory using the Stern-Volmer relationship.

- 5 The total number of reactions considered in the models of López-González et al. (1992b) and McDade et al. (1986) with the $O(^1S)$ precursor (O_2^*) and $O(^1S)$ was limited to ten, and these reactions are separated in two groups according to the Barth excitation transfer scheme. A full overview of these reactions including O_2 in a not identified excited state O_2^* is not provided in this short overview excepting two reactions. Specifically, López-González et al. (1992b) considered the reaction $O(^1S) + O(^3P) \rightarrow \text{products}$, which McDade et al. (1986) did not consider. But McDade et al. (1986) considered the reaction
- 10 $O_2^* + N_2 \rightarrow \text{products}$, which López-González et al. (1992b) did not consider. Possible reasons to limit the list of all possible reactions in these models are as follows: (1) the Barth excitation transfer scheme can be represented by the most important (e.g., ten) reactions, (2) the system of a few reactions can be easily represented by a low degree polynomial equation regarding $[O(^3P)]$, (3) additional reactions would introduce difficulties to derive their rates, which can also be considered in ratio values tuned as empirical coefficients, and (4) the choice of approaches applied to derive empirical coefficients is limited depending
- 15 on the considered reactions, e.g., compare approaches applied by McDade et al. (1986) and López-González et al. (1992b).

These reasons limit the applicability of the mentioned methods used to analyze laboratory results and atmospheric measurements, which are usually studied without propagation in time. The computational simulation of a chemical kinetics system enables studying the time evolution of chemical species by using the ordinary differential equations (ODE) system matrix and initial conditions, see, e.g., Sandu and Sander (2006) for an overview of zero-dimensional box models developed to integrate

20 ODEs numerically in time. Unfortunately, computer modeling depends on *a priori* data sets used to initialize a box model. *In-situ* atmospheric measurements may be influenced by gravity waves and atmospheric tides at the particular moments of time that hinders the use of box models on the basis of such measurements. This article here studies the MLT photochemistry on the basis of the *in-situ* ETON measurements with the use of steady state continuity equations, i.e. without propagation in time, and without *a priori* data sets used for it.

- 25 The ETON multiple airglow emissions are described in Section 2, they can be applied simultaneously in the model proposed in this study to decrease uncertainties when tuning unknown and poorly constrained reaction rates with the use of the verification and validation procedures.

The first application of multiple emissions measured remotely with spectrometers in a model considering several O_2 states seems to be done by Torr et al. (1985) analyzing data sets from the shuttle Spacelab 1. In fact, these data sets were extremely

30 scattered in the time and place that might have stopped Torr et al. (1985) combining identified O_2 states in one model. Instead, they considered a number of photochemical models with some excited O_2 states in each model so that all discussed excited O_2 states appeared to be uncoupled with each other. Note that Torr et al. (1985) also considered $O_2(c)$ as the $O(^1S)$ precursor according to Greer et al. (1981), and applied the $O(^1S)$ quenching with $O_2(a)$ according to Bates (1981) and Kenner and Ogryzlo (1982).



In summary, this investigation was conducted to study the following topics regarding the new photochemical model proposed here: (1) processes of the $O(^1S)$ formation and quenching, see Section 3.1, (2) processes including identified O_2 states, see Sections 3.2.1, 3.2.2 and 3.3, and (3) the $O(^1S)$ precursor represented by one O_2 state or a group of them, see Section 4.4.

The $O(^3P)$ retrieval scheme was proposed to be solved in subsequent steps as described in Appendix A on the basis of multiple airglow emission profiles that was discussed by Lednyts'kyy and von Savigny (2016) and Lednyts'kyy et al. (2018). Note that *a priori* data are not required to initiate calculations with in the MAC model. Concentrations of O_2 in higher excited states are calculated earlier at these retrieval steps, and are used to calculate concentrations of O_2 in lower excited states at the other retrieval steps. It should be noted that a limited number of multiple airglow emissions available from the ETON measurements or other sources can be also applied to retrieve $[O(^3P)]$ values at some of the mentioned retrieval steps, see Sections 2 and 5 for details.

2 Data sets applied in the Multiple Airglow Chemistry (MAC) model

In-situ measurements obtained during the Energy Transfer in the Oxygen Nightglow (ETON) campaign and simulations using the most recent version of the MSIS (Mass Spectrometer Incoherent Scatter) semi-empirical model are in the focus of this section.

Volume Emission Rates (VER) of the nightglow emissions measured *in-situ* during the ETON campaign and the corresponding statistical errors provided by Greer et al. (1986) were used in this study. The ETON campaign is comprised of measurements obtained during coordinated launches of seven sounding rockets at South Uist ($\sim 57^\circ 16' N$, $\sim 7^\circ 19' W$) in Scotland, Great Britain, in westerly direction on 23rd March 1982 from $\sim 21:27$ UT to $\sim 23:55$ UT (Greer et al., 1986, 1987).

The maximal number of VER profiles related to various O_2 and O transitions were obtained by two ETON rockets, which are discussed here. As for the Infrared Atmospheric band emissions at $1.27 \mu m$, they were measured with a photometer aboard only one ETON rocket: the P227H rocket launched at $\sim 22:11$ UT. The Herzberg I and Atmospheric band emissions at 320 and 761.9 nm, respectively, were also measured by the P227H rocket. The P229H rocket was launched at $\sim 22:58$ UT right after the P227H rocket and provided measurements of the Herzberg I, Chamberlain and Atmospheric band emissions at 330, 370 and 761.9 nm, respectively, as well as the oxygen green line emission at 557.7 nm. It should be noted that the Chamberlain band emissions were measured by the P229H rocket only. The absolute accuracy of $\pm 20\%$ in VER peak values for the Infrared Atmospheric band emissions and better than $\pm 10\%$ in other wavelength ranges (Greer et al., 1986) introduces uncertainties in the $[O(^3P)]$ retrievals.

In-situ measurements of atomic oxygen (O) concentrations ($[O]$) in the ground state ($[O(^3P)]$) were carried out directly by the rockets P232H and P234H launched at $\sim 21:49$ UT and $\sim 23:55$ UT, respectively. $[O(^3P)]$ values were determined directly using the resonance fluorescence and absorption technique at ~ 130 nm (Greer et al., 1986) and were interpolated for the launch time of the other ETON rockets. The statistical (and the systematic) error was less than about $\pm 10\%$ (and about $\pm 30\%$) at about 100 km (where $[O(^3P)]$ peak values are measured) and increased up to $\pm 50\%$ (and about $\pm 20\%$) at other altitudes (where $[O(^3P)]$ low values are measured) (Greer et al., 1986).



The most recent version of the MSIS model, NRLMSISE-00 (Naval Research Laboratory MSIS Extended, 2000), was used to obtain the following input parameters required to run the MAC model: temperature (T), molecular nitrogen concentrations ($[N_2]$) and $[O_2]$. Because the highest number of O_2 and O transitions were sounded by the P229H rocket compared to those using the P227H rocket, the time of *in-situ* measurements obtained by the P229H rocket at ~ 97 km over South Uist in Scotland were specified for the NRLMSISE-00 model. It should be mentioned that McDade et al. (1986) developed the well-known cubic equation deriving empirical coefficients by using the MSIS-83 model, which is not available anymore.

The input parameters required to run the established models and the proposed MAC model are profiles of T, $[N_2]$, $[O_2]$ and VER values. The following abbreviations of *in-situ* VER profiles are used in this study: VER $\{O_2(A-X)\}$ (Herzberg I band, HzI), VER $\{O_2(A'-a)\}$ (Chamberlain band, Cha), VER $\{O_2(b-X)\}$ (Atmospheric band, Atm), VER $\{O(^1S-^1D)\}$ (green line, GrL) and VER $\{O_2(a-X)\}$ (Infrared Atmospheric band, IRAtm). Some of O_2 transitions listed in Table 1 correspond to these VER profiles. Note that the other listed O_2 transitions were also considered in the proposed MAC model, see Section 3.3 for details. It is worth mentioning that all of these O_2 transitions were measured remotely using the instrument SCIAMACHY (SCanning Imaging Absorption spectroMeter for Atmospheric CHartographY) aboard the satellite ENVISAT (ENVironmental SATellite) launched by the European Space Agency (Burrows et al., 1995; Bovensmann et al., 1999). Gravity waves and atmospheric tides influence *in-situ* measurements, but averaging of the long time measurement series in latitude intervals enabled suppressing effects caused by gravity waves, although tidal effects were still present, see, e.g., Lednyts'kyy et al. (2017) for analysis of the SCIAMACHY datasets.

It should be mentioned that Lednyts'kyy and von Savigny (2016) tuned unknown or poorly constrained reaction rates considered in the MAC model on the basis of data sets obtained during the ETON campaign. The corresponding reaction rates are shown in Tables 9 ... 12. Then, the MAC model was applied on the basis of data sets obtained during three campaigns as follows: the WADIS-2 (WAVE propagation and DISSIPATION in the middle atmosphere), WAVE2000 (WAVes in airglow structures Experiment, 2000) and WAVE2004 campaigns, see the next publication. The WADIS-2 rocket provided all data sets required to retrieve $[O(^3P)]$ values. Data sets measured *in-situ* with rockets launched during the WAVE2000 and WAVE2004 campaigns were combined with the collocated data sets measured remotely. Convincing retrieval results enabled validating tuned reaction rates and calculations carried out with the MAC model.

3 Development of the MAC model

3.1 The $O(^1S)$ nightglow model with O_2^* as the $O(^1S)$ precursor

The established photochemical models of McDade et al. (1986), Gobbi et al. (1992) and Semenov (1997) related to the oxygen green line emission are described in this section in short, see Lednyts'kyy et al. (2015) for details.

McDade et al. (1986) considered processes provided in Table 2 that resulted in two photochemical models according to the two-step Barth excitation transfer scheme implemented in each model and involving precursors of $O_2(b)$ and $O(^1S)$, respectively. McDade et al. (1986) also implemented one model according to the one-step excitation scheme and related to $O_2(b)$, but excluding the $O_2(b)$ precursor. Both models related to $O_2(b)$ were used to retrieve $[O(^3P)]$ on the basis of Volume



Table 1. Relevant optical transitions of terrestrial airglow in the Earth’s atmosphere. Emissions (see column “Emission”) observed in the wavelength range shown in column “ λ ” are denoted by abbreviations (see column “Ident.”) and transition types (see column “Type”). Typical intensity values of an integrated (limb) emission rate profile are given for nightglow (see column “Int.” before the comma) and, if available, dayglow (see column “Int.” after the comma). Altitudes of the corresponding emission rate peaks are shown in column “Alt.”. Atomic oxygen emissions are denoted by abbreviations as follows: **GrL** is for the green line emission at 557.7 nm, **ReL** – the red line emissions at 630.0 and 636.4 nm, **UVL** and **UVL*** – the ultraviolet line emissions at 297.2 and 295.8 nm, respectively. Molecular oxygen emissions are denoted by abbreviations as follows: **IRAtm** is for the InfraRed Atmospheric band emission at 1270 nm, **Atm** – the Atmospheric band emission at 761.9 nm, **Nox** – the Atmospheric band emission at 1908 nm, **Hzi** – the Herzberg I band emissions, **BG** – the Broida-Gaydon band emissions, **Cha** – the Chamberlain band emissions, **HziII** – the Herzberg III band emissions, **HziII** – the Herzberg II band emissions, **cbK** – the New system band emissions measured by using the Keck I/II instrument (Slanger et al., 2004a), **RJ** – the Richards-Johnson band emissions. References are marked with upper indices as follows: sc is for Slanger and Copeland (2003), mc – McConkey et al. (1966), na – Nagy et al. (2008), md – McDade (1998), na – Nagy et al. (2008), kh – Khomich et al. (2008).

Emission	Ident.	λ (nm)	Int., night, day	Alt.(km)
$O_2(A^3\Sigma_u^+ - b^1\Sigma_g^+)$	BG	300...1100 ^{kh}		
$O_2(A^3\Sigma_u^+ - X^3\Sigma_g^-)$	Hzi	240...520 ^{kh}	600 R, 600 R	98.8 ^{kh}
$O_2(A'^3\Delta_u - a^1\Delta_g)$	Cha	300...870 ^{kh}	150 R, 150 R	98.3 ^{kh}
$O_2(A'^3\Delta_u - X^3\Sigma_g^-)$	HziII	260...600 ^{kh}	70 ^{kh} R	97.7 ^{kh}
$O_2(c^1\Sigma_u^- - b^1\Sigma_g^+)$	cbK	384...550 ^{sc}	30 R	
$O_2(c^1\Sigma_u^- - a^1\Delta_g)$	RJ	280...1000 ^{kh}		
$O_2(c^1\Sigma_u^- - X^3\Sigma_g^-)$	HziII	250...530 ^{kh}	50 R, 50 R	98.1 ^{kh}
$O(^1S - ^1D)$	GrL	557.7	300 R, 4...13 kR	97 ^{md}
$O(^1S - ^3P_1)$	UVL	297.2	30 R, 0.4...1.3 kR	
$O(^1S - ^3P_2)$	UVL*	295.8	0.1 ^{mc} R	
$O(^1D - ^3P_2, ^3P_1)$	ReL	630.0, 636.4	0...50 R, 50 kR	250 ^{na}
$O_2(b^1\Sigma_g^+ - a^1\Delta_g)$	Nox	1908		
$O_2(b^1\Sigma_g^+ - X^3\Sigma_g^-)\{0-0\}$	Atm	761.9 ^{na}	5 kR, 100 kR	94 ^{md}
$O_2(a^1\Delta_g - X^3\Sigma_g^-)\{0-0\}$	IRAtm	1270 ^{na}	50 kR	90 ^{md}

Emission Rates (VER) of the Atmospheric band emissions. All processes of the $O_2(b)$ -model involving the $O_2(b)$ precursor are provided in the upper part of Table 2. In fact, reactions related to O_2^{**} ($R_{u1.1-2}^P$, $R_{u3.1-3}^P$ and $R_{u4.0}^P$) are absent in the model implemented without the $O_2(b)$ precursor. The model implemented without the $O_2(b)$ precursor exhibits non-linearities in quenching processes, but the model implemented with the $O_2(b)$ precursor (O_2^{**}) does not result in such non-linearities

5 (McDade et al., 1986). Note that McDade et al. (1986) described the green line emission considering the $O(^1S)$ precursor according to the Barth excitation transfer scheme. In fact, the well-known quadratic equation resulting from the model with the $O_2(b)$ precursor and the well-known cubic equation resulting from the model with the $O(^1S)$ precursor were concluded by McDade et al. (1986) to be favorable comparing to models based on the one-step (Chapman) excitation scheme. It is worth



mentioning that Grygalashvyly et al. (2018) proposed a model combining the Chapman and Barth excitation schemes, which were implemented in both $O_2(b)$ -models of McDade et al. (1986) separately. Applying self-consistent data sets (see Section 2) and fitting retrieved data sets, Grygalashvyly et al. (2018) applied methods of McDade et al. (1986) to derive new values of empirical coefficients, which were initially derived by McDade et al. (1986) for the well-known quadratic equation. The newly
 5 derived coefficients were preferred by Grygalashvyly et al. (2018) to be applied in their model.

The well-known cubic equation of McDade et al. (1986) provided here in the full form and in the short form was used here to retrieve $[O(^3P)]$ on the basis of VER of the green line emission (VER₅₅₈ also referred to as VER $\{O(^1S - ^1D)\}$).

The well-known cubic equation provided by McDade et al. (1986) in the full form is as follows:

$$\frac{A_{558}\kappa_1[O(^3P)]^3([N_2] + [O_2])}{VER_{558}(A_{1S} + {}^3\kappa_5[O_2])} = \frac{1}{\beta\delta} \frac{A^*}{\beta_O^*} + \frac{1}{\beta\delta} [O(^3P)] + \frac{1}{\beta\delta} \frac{\beta_{O_2}^*}{\beta_O^*} [O_2] + \frac{1}{\beta\delta} \frac{\beta_{O_2}^*}{\beta_O^*} R \frac{\beta_{N_2}^*}{\beta_{O_2}^*} [O_2], \quad (1)$$

10 where $R \approx 4$ represents the mean $[N_2]/[O_2]$ ratio valid in the altitude range 80...120km according to McDade et al. (1986). All reaction rates shown in Eq. (1) correspond to the ones provided in the lower part of Table 2. Ratios of some of these reaction rate values were derived by McDade et al. (1986), see empirical coefficients in Eq. (2) of Murtagh et al. (1990), on the basis of the ETON *in-situ* measurements as well as simulated temperature, $[N_2]$ and $[O_2]$ profiles.

The well-known cubic equation and the derived empirical coefficients in particular were verified by Murtagh et al. (1990),
 15 who provided the well-known cubic equation in the short form as follows:

$$VER_{558} = \kappa_1 [O(^3P)]^2 ([N_2] + [O_2]) \cdot \frac{\frac{[O]}{C(0) + C(1)[O(^3P)] + C(2)[O_2]}}{\frac{A_{558}}{A_{1S} + {}^3\kappa_5[O_2]}}, \quad (2)$$

where the rate coefficient of the $R_{g1.2}$ reaction provided in Table 2 is ${}^3\kappa_5 = 4 \cdot 10^{-12} \exp(-865/T) \text{ molec}^{-1} \text{ cm}^3 \text{ s}^{-1}$, the Einstein coefficients of the reactions $R_{g3.0}$ and $R_{g(3-4).0}$ are $A_{558} = 1.18 \text{ s}^{-1}$ and $A_{1S} = 1.35 \text{ s}^{-1}$, the rate β_{κ_1} of the three-
 20 body recombination reaction $R_{v1.1-2}^P$ is the product of $\kappa_1 = 4.7 \cdot 10^{-33} (300/T)^2 \text{ molec}^{-2} \text{ cm}^6 \text{ s}^{-1}$ and an empirical β value. The $R_{v1.1-2}^P$ reaction refers to the first step of the Barth excitation transfer scheme describing the production of O_2^* , the $O(^1S)$ precursor. The rates β_O^* , $\beta_{N_2}^*$, $\beta_{O_2}^*$ of the $R_{v3.1-3}^P$ reactions describe the O_2^* quenching. The $R_{v2.1}^P$ reaction with the rate value $\delta\beta_O^*$, where δ is an empirical value, refers to the second step of the Barth excitation transfer scheme resulting in $O(^1S) + O_2$.

The values of the empirical coefficients C(0), C(1) and C(2) are equal to 0, 211 and 15, respectively, and these values are used
 25 in this study for retrievals using the well-known cubic equation according to Murtagh et al. (1990). Note that these empirical coefficients were derived by McDade et al. (1986) using the semi-empirical models including MSIS-83, which is not available nowadays. The NRLMSISE-00 model mentioned in Section 2 is used in this study to simulate temperature, $[N_2]$ and $[O_2]$ profiles. McDade et al. (1986) used various available models that resulted in other values of temperature, $[N_2]$ and $[O_2]$ profiles and different values of the empirical coefficients. The minimal values of C(0), C(1) and C(2) from all obtained ones, which are
 30 related to the $O(^1S)$ precursor, were found by McDade et al. (1986) to be equal to 13 ± 4 , 183 ± 10 and 9 ± 3 , respectively, and their maximal values were found to be equal to 23 ± 9 , 224 ± 20 and 17 ± 3 , respectively.



Table 2. Processes of the $O(^1S)$ nightglow model with O_2^* as the $O(^1S)$ precursor were proposed by McDade et al. (1986) and modified by Lednyts'kyy et al. (2015) according to Gobbi et al. (1992) and Semenov (1997). Odd oxygen processes related to $O_2(b)$ were described with the well-known quadratic equation of McDade et al. (1986). Odd oxygen processes related to $O(^1S)$ were described by using two models. The first model excluded two processes, $R_{g1.2}$ and $R_{g2.1}$, and resulted in the well-known cubic Eq. (2) of McDade et al. (1986). The second model included two processes, $R_{g1.2}$ and $R_{g2.1}$, and resulted in the extended cubic Eq. (3) of Lednyts'kyy et al. (2015). The processes marked with a character P were not considered proposing the MAC model, but were used in the 1st step (prior) retrieval of $[O(^3P)]$. Odd oxygen processes related to $O(^1S)$ represent the two-step Barth transfer scheme (see reactions $R_{v1.1-2}$, $R_{v2.1}$ and the resulting reaction $R_{g3.0}$) accompanied by quenching. The symbolic representation of the reaction rates shown above the arrows in the second column of this table was adopted from Khomich et al. (2008) and used in Section 3.1. The symbolic representation shown in the third column of this table was used by Lednyts'kyy et al. (2015). For instance, the reaction rate β_O (Khomich et al., 2008) corresponds to γ_{3P}^{SP} (Lednyts'kyy and von Savigny, 2016), β_{O_2} (Khomich et al., 2008) corresponds to $\gamma_{O_2}^{SP}$ (Lednyts'kyy and von Savigny, 2016), A_{558} (Khomich et al., 2008) corresponds to γ_{557n7}^A (Lednyts'kyy and von Savigny, 2016) and $A_{558} + (A_{297} + A_{296})$ (Khomich et al., 2008) corresponds to γ_{1S3Pe}^A (Lednyts'kyy and von Savigny, 2016). Processes marked with a character P were used at the prior retrieval steps applied to calculate $[O(^1S)]$ (see Section A1.1) and $[O(^3P)]$ (see Sections 3.1 and 3.4).

R#	Odd oxygen processes related to $O_2(b)$	Symbol
$R_{u1.1-2}^P$	$O(^3P) + O(^3P) + \{N_2, O_2\} \xrightarrow{\alpha\kappa_1, \alpha\kappa_1} O_2^{**} + \{N_2, O_2\}$	$\alpha\kappa_1$
$R_{u2.1}^P$	$O_2^{**} + O_2 \xrightarrow{\gamma, {}^3\kappa_3} O_2(b) + O_2$	C^{O_2}
$R_{u3.1-3}^P$	$O_2^{**} + \{O(^3P), N_2, O_2\} \xrightarrow{{}^1\kappa_3, {}^2\kappa_3, {}^3\kappa_3} \text{All products}$	C^O
$R_{u4.0}^P$	$O_2^{**} \xrightarrow{\beta_u^A} O_2 + h\nu$	A_u
$R_{u5.1-3}^P$	$O_2(b) + \{O(^3P), N_2, O_2\} \xrightarrow{{}^1\kappa_2, {}^2\kappa_2, {}^3\kappa_2} \text{Quenched products}$	${}^i\kappa_2$
$R_{b5.0}$	$O_2(b) \xrightarrow{\beta_{762}^A} O_2 + h\nu(\lambda = 762 \text{ nm})$	A_{762}
$R_{b6.0}$	$O_2(b) \xrightarrow{\beta_{Atm}^A} O_2 + h\nu(\text{Atmospheric band})$	A_{Atm}
R#	Odd oxygen processes related to $O(^1S)$	Symbol
$R_{v1.1-2}^P$	$O(^3P) + O(^3P) + \{N_2, O_2\} \xrightarrow{\alpha_{O_2}, \alpha_{O_2}} O_2^* + \{N_2, O_2\}$	$\beta\kappa_1$
$R_{v2.1}^P$	$O_2^* + O(^3P) \xrightarrow{\delta, \beta_{O_2}^* = \alpha_O} O(^1S) + O_2$	$C(1)$
$R_{v3.1-3}^P$	$O_2^* + \{O(^3P), N_2, O_2\} \xrightarrow{\beta_O^*, \beta_{N_2}^*, \beta_{O_2}^*} O_2 + \{O(^3P), N_2, O_2\}$	$C(2)$
$R_{v4.0}^P$	$O_2^* \xrightarrow{A^*} O_2 + h\nu$	$C(0)$
$R_{g1.1}$	$O(^1S) + O(^3P) \xrightarrow{\beta_O} O(^1D) + O(^1D)$	${}^1\kappa_5$
$R_{g2.1}$	$O(^1S) + N_2 \xrightarrow{\beta_{N_2}} O(^3P) + N_2$	${}^2\kappa_5$
$R_{g1.2}$	$O(^1S) + O_2 \xrightarrow{\beta_{O_2}} O(^3P) + O_2$	${}^3\kappa_5$
$R_{g3.0}$	$O(^1S) \xrightarrow{A_{558}} O(^1D) + h\nu(\lambda = 557.7 \text{ nm})$	A_{558}
$R_{g(3-4).0}$	$O(^1S) \xrightarrow{A_{558} + (A_{297} + A_{296})} \{O(^1D), O(^3P)\} + h\nu$	A_{1S}



Gobbi et al. (1992) suggested that processes of the enhanced $O(^1S)$ quenching with $O(^3P)$ and N_2 should also be considered in the well-known Eq. (2). The extended cubic equation provided by Gobbi et al. (1992) is as follows:

$$VER_{558} = \kappa_1 [O(^3P)]^2 ([N_2] + [O_2]) \cdot \frac{[O(^3P)]}{C(0) + C(1)[O(^3P)] + C(2)[O_2]} \cdot \frac{A_{558}}{A_{1S} + {}^1\kappa_5 [O(^3P)] + {}^2\kappa_5 [N_2] + {}^3\kappa_5 [O_2]}, \quad (3)$$

5 where the rate coefficients corresponding to the reactions $R_{g1.1}$, $R_{g2.1}$ and $R_{g1.2}$ are ${}^1\kappa_5 = 2 \cdot 10^{-14} \text{ molec}^{-1} \text{ cm}^3 \text{ s}^{-1}$, ${}^2\kappa_5 = 5 \cdot 10^{-17} \text{ molec}^{-1} \text{ cm}^3 \text{ s}^{-1}$ and ${}^3\kappa_5 = 4.9 \cdot 10^{-12} \exp(-885/T) \text{ molec}^{-1} \text{ cm}^3 \text{ s}^{-1}$, respectively. The other coefficients are shown and described for Eq. (2). The photochemical model resulting in the extended cubic equation is hereafter referred to as the G-model in short according to the surname of the first author in Gobbi et al. (1992), who proposed this model.

The $O(^1S)$ quenching with N_2 is not effective according to Atkinson and Welge (1972) because the ${}^2\kappa_5$ value is five orders
 10 lower than the ${}^3\kappa_5$ value of the $O(^1S)$ quenching with O_2 . Therefore, the $O(^1S)$ quenching with N_2 was neglected (${}^2\kappa_5 = 0$) by Semenov (1997), who considered a relatively high ${}^1\kappa_5$ value of $5 \cdot 10^{-11} \exp(-305/T) \text{ molec}^{-1} \text{ cm}^3 \text{ s}^{-1}$ compared to the ${}^1\kappa_5$ value of $2 \cdot 10^{-14} \text{ molec}^{-1} \text{ cm}^3 \text{ s}^{-1}$ used by Gobbi et al. (1992). The low ${}^1\kappa_5$ value was obtained by Krauss and Neumann (1975) theoretically and approved experimentally by Kenner and Ogryzlo (1982), but Johnston and Broadfoot (1993) and a number of other scientists including Khomich et al. (2008) used the high ${}^1\kappa_5$ value.

15 Semenov (1997) developed the photochemical model that resulted in the cubic equation as follows:

$$VER_{558} = \alpha_{O_2} [O(^3P)]^2 ([N_2] + [O_2]) \cdot \frac{\alpha_O [O(^3P)]}{A^* + \beta_{N_2}^* [N_2] + \beta_O^* [O(^3P)] + \beta_{O_2}^* [O_2]} \cdot \frac{A_{558}}{A_{1S} + {}^1\kappa_5 [O(^3P)] + {}^3\kappa_5 [O_2]}, \quad (4)$$

where $\alpha_{O_2} = \beta\kappa_1$ and $\alpha_O = \delta\beta_O^*$, see the notation of process rates provided in Table 2. The notation of other process rates shows that Eq. (4) can be transformed into Eq. (3) by using $A^* + \beta_{N_2}^* [N_2] := C(0)$, $\beta_O^* := C(1)$, $\beta_{O_2}^* := C(2)$ and ${}^2\kappa_5 =$
 20 $0 \text{ molec}^{-1} \text{ cm}^3 \text{ s}^{-1}$.

The $O(^1S)$ quenching with $O_2(a)$ is very effective according to Bates (1981) and Kenner and Ogryzlo (1982), but the direct inclusion of $O_2(a)$ in Eq. (3) would increase its order so that the number of the obtained solutions would be very complicated to interpret. Therefore, the high ${}^1\kappa_5$ value of the $O(^1S)$ quenching with $O(^3P)$ was adopted by Lednyts'kyy et al. (2015) in order to implicitly include the $O(^1S)$ quenching with $O_2(a)$ and to keep the order of the polynomial in Eq. (3). In this
 25 context it is worth mentioning that – according to Garcia and Solomon (1985) – $O(^1S)$ quenching reactions are not completely established. The direct correspondence of Eq. (4) (with defined empirical coefficients $C(0)$, $C(1)$ and $C(2)$) and Eq. (3) to each other enabled specifying how the specific relationship between values of $[O(^3P)]$ and VER_{558} can be used to solve both Eqs. (4) and (3) applying the analytical method of Semenov (1997).



The well-known cubic Eq. (2) represents the reduced form of the extended Eq. (3). Indeed, the reaction rates $^1\kappa_5$ and $^2\kappa_5$ are not equal to zero in the extended Eq. (3) to represent the $O(^1S)$ quenching with O_2 , $O(^3P)$ and N_2 . On the contrary, if they are equal to zero then the extended Eq. (3) becomes identical to the well-known Eq. (2). The other values of reaction rates and empirical coefficients were proposed by Lednyts'kyy et al. (2015) to be the same in both Eqs. (2) and (3) and calculated by
 5 Lednyts'kyy et al. (2015) according to the discussion provided in the next paragraph. The $[O(^3P)]$ retrievals obtained by using Eqs. (2) and (3) were verified by Lednyts'kyy et al. (2015), analyzed by von Savigny and Lednyts'kyy (2013), von Savigny et al. (2015) and Lednyts'kyy et al. (2017) and validated here, see Section 3.4 for details.

Gobbi et al. (1992) used *in-situ* measurements obtained during the solar minimum phase at the transition from solar cycle 21 to cycle 22, but the ETON *in-situ* measurements were obtained during the solar maximum phase of the 21st solar cycle. It
 10 is worth being mentioned that Gobbi et al. (1992) used Eq. (3) instead of Eq. (2) with the same empirical coefficients derived by McDade et al. (1986). Lednyts'kyy et al. (2015) adjusted values of these empirical coefficients applied here according to publications related to various phases of solar activity. This was done to reflect differences in ultraviolet irradiance and optical depth values during phases of the solar maximum and minimum. Indeed, Dudok de Wit et al. (2009) and Meier (1991) reported that the irradiance in the extreme ultraviolet wavelength range 30...121 nm affects thermospheric $O(^3P)$, O_2 , N_2 , N
 15 and N_2O ionization. Colegrove et al. (1965) emphasized that $O(^3P)$ is generated in the lower thermosphere and transported downwards to the mesosphere. Equation (2) of Murtagh et al. (1990) was extended by Lednyts'kyy et al. (2015) with the empirical coefficient $C(0) \neq 0$ because the first term on the right hand side of Eq. (1) is not equal to zero so that $C(0)$ should be introduced. However, the influence of $C(0)$ on solutions of Eq. (2) is negligible compared to $C(1)[O(^3P)]$ or $C(2)[O_2]$ so that the exact $C(0)$ value is not important. The NRLMSISE-00 model was applied adjusting the empirical coefficients $C(0)$, $C(1)$
 20 and $C(2)$ instead of the MSIS-83 model applied by McDade et al. (1986).

In summary, polynomial equations of the second and the third orders with respect to $[O(^3P)]$ (McDade et al., 1986) are used to retrieve $[O(^3P)]$, see left panels in Figs. 4 and 5 in Section 3.4. The extended cubic Eq. (3) was solved for this study using the analytical method of Semenov (1997) also described by Khomich et al. (2008). As for the well-known cubic Eq. (2), it solved for this study using the program available at <https://idlastro.gsfc.nasa.gov/ftp/contrib/freudenreich/cuberoot.pro> within
 25 the Astronomy User's Library distributed by the National Aeronautics and Space Administration. Note that values of reaction rates and empirical coefficients provided by Lednyts'kyy et al. (2015) were used according to the extended cubic Eq. (3) for $O(^3P)$ retrievals in this study. As for the well-known cubic Eq. (2) used for $O(^3P)$ retrievals in this study, values of reaction rates and empirical coefficients provided by Murtagh et al. (1990).

Photochemical models based on identified O_2 states and their coupling with each other are described in the following Section
 30 3.2.

3.2 Models with identified excited O_2 states

A short review regarding approaches developing photochemical models is provided in Section 1. The established photochemical models described in the following sections include $O_2(b, a, X)$ in the first model, see Section 3.2.1, and $O_2(c, b, X)$ in the second model, see Section 3.2.1, developed using available data sets.



3.2.1 The modified kinetic model of O_2 and O_3 photolysis products

A photochemical model taking $O_2(b, a, X)$ states and $O(^1D, ^3P)$ states into account was developed by Mlynczak et al. (1993) with the use of the basic daytime $O_2(a)$ kinetic model employed by Thomas (1990). The model of Mlynczak et al. (1993) was extended by Sharp et al. (2014) by including the three-body recombination reaction producing $O_2(a)$ during night time, see the
 5 $R_{a1.1-2}$ reactions provided in Table 3. The model of Sharp et al. (2014) also included processes related to the laser excitation, but these processes are not relevant for the present study and are excluded.

All other processes of the model proposed by Sharp et al. (2014) are shown in Table 3. The modified kinetic model with these processes is hereafter referred to as the M-model in short according to the surname of the first author in Mlynczak et al. (1993). Processes marked with a character E and shown in Table 3 were excluded from the resulting M-model because they
 10 were not found in the latest version of the 2015 database of the Jet Propulsion Laboratory (Burkholder et al., 2015).

The M-model was verified on the basis of a few emission lines (with high signal to noise ratios) from possible band emissions measured remotely. Some of these strongest O_2 nightglow emissions are provided in Table 1. One of them in the Infrared Atmospheric band is represented by the vibrational transition $0-0$ of the forbidden electronic transition $a^1\Delta_g, \nu' = 0 - X^3\Sigma_g^-, \nu'' = 0$ ($O_2(a-X)\{0-0\}$). Note that processes of the M-model were used to develop the MAC model on the basis of VER profiles
 15 from the ETON campaign including VER values of $O_2(a-X)\{0-0\}$ (VER $\{O_2(a-X)\}$). Note that Yankovsky et al. (2016) developed the new YM2011 model considering $O(^1D)$ and various electronic-vibrationally excited levels in the new model of electronic-vibrational kinetics: 3 of $O_2(b, \nu \leq 2)$, 6 of $O_2(a, \nu \leq 5)$ and 35 of $O_2(X, \nu \leq 35)$. In contrast to the YM2011 model, reaction rates in the modified kinetic model of Mlynczak et al. (1993) refer to a specific portion of vibrational states from their statistical equilibrium in each O_2 electronic state. Yankovsky et al. (2016) and Yankovsky et al. (2007) reported
 20 on differences among O_3 altitude profiles obtained by using the modified kinetic model of Mlynczak et al. (1993) and the YM2011 model.

3.2.2 The extended $O(^1S)$ nightglow model with $O_2(c)$ as the $O(^1S)$ precursor

A photochemical model taking $O_2(c, b, X)$ states and $O(^1S, ^1D, ^3P)$ states into account was developed by Huang and George (2014) on the basis of the photochemical $O(^1S)$ nightglow model proposed by Hickey et al. (1997). The first implementation
 25 of $O_2(c)$ as the $O(^1S)$ precursor seems to be carried out by Torr et al. (1985) on the basis of multiple emissions simultaneously measured from the Spacelab 1 shuttle. The $O(^1S)$ precursor was also assumed to be $O_2(c)$ by Greer et al. (1981) describing *in-situ* measurements of the ETON campaign and Hickey et al. (1997).

Huang and George (2014) tuned some rates of quenching reactions on the basis of measurements of the green line emissions at 557.7 nm and the Atmospheric band emissions at 864.5 nm. The vibrational transition $0-1$ of the electronic transition
 30 $b^1\Sigma_g^+, \nu' = 1 - X^3\Sigma_g^-, \nu'' = 0$ at 864.5 nm can be observed from the Earth's surface and it is denoted as $O_2(b-X)\{0-1\}$. Volume Emission Rates (VER) of the $O_2(b-X)\{0-1\}$ transition are about 30 times less intense than VER $\{O_2(b-X)\}$ of the $O_2(b-X)\{0-0\}$ transition at 762.2 nm in the Atmospheric band (Meinel, 1950). Prof. Huang provided rate coefficients of the model of Huang and George (2014) for VER $\{O_2(b-X)\}$ of the $O_2(b-X)\{0-0\}$ transition, but the same reactions were



Table 3. Processes of the model of Mlynčzak et al. (1993) modified by Sharp et al. (2014) are hereafter referred to as the M-model, see Section 3.2.1. Processes of O_2 and O_3 photolysis occur at sunlight conditions. The processes marked with a character M are not considered in the MAC model shown in Tables 6 and 7 because they were not listed in the online version of the JPL 2015-year database (Burkholder et al., 2015) and were replaced by other relevant up-to-date processes.

$R_{\#}$	Odd oxygen processes related to $O_2(b)$, $O_2(a)$ and $O(^1D)$
$R_{s1.2-3}$	$O_2 + h\nu \xrightarrow{\sigma_{PD}^{LA}, \sigma_{PD}^{Sc}} O(^3P) + \{O(^1D), O(^1D)\}$
$R_{s2.3}$	$O_3 + h\nu \xrightarrow{\sigma_{aD}^{Ha}} O(^1D) + O_2(a)$
$R_{s3.1}$	$O_2 + h\nu(\lambda = 762\text{nm}) \xrightarrow{\sigma_{b1}^{O_2^1}} O_2(b)$
$R_{b2.1}^E$	$O_2(b) + O_3 \xrightarrow{\beta_{O_3}^{ba}} O_2(a) + O_2 + O(^3P)$
$R_{b2.2-5}$	$O_2(b) + \{O, N_2, O_2, CO_2\} \xrightarrow{\beta_{3P}^{ba}, \beta_{N_2}^{ba}, \beta_{O_2}^{ba}, \beta_{CO_2}^{ba}} O_2(a) + \{O, N_2, O_2, CO_2\}$
$R_{b5.0}$	$O_2(b) \xrightarrow{\beta_{62}^A} O_2 + h\nu(\lambda = 762\text{nm})$
$R_{b6.0}$	$O_2(b) \xrightarrow{\beta_{Aim}^A} O_2 + h\nu(\text{Atmospheric band})$
$R_{a1.1-2}$	$O(^3P) + O(^3P) + \{N_2, O_2\} \xrightarrow{\alpha_{N_2}^{Pa}, \alpha_{O_2}^{Pa}} O_2(a) + \{N_2, O_2\}$
$R_{a2.2-4}$	$O_2(a) + \{O, N_2, O_2\} \xrightarrow{\alpha_{3P}^{ax}, \alpha_{N_2}^{ax}, \alpha_{O_2}^{ax}} O_2 + \{O, N_2, O_2\}$
$R_{a3.0}$	$O_2(a) \xrightarrow{\alpha_{1u27}^A} O_2 + h\nu(\lambda = 1.27\mu\text{m})$
$R_{a4.0}$	$O_2(a) \xrightarrow{\alpha_{IRA}^A} O_2 + h\nu(\text{IR Atmospheric band})$
$R_{r2.1,3}$	$O(^1D) + \{N_2, O_2\} \xrightarrow{\rho_{N_2}^{DP}, \rho_{Ob}^{DP}} O(^3P) + \{N_2, O_2(b)\}$
$R_{r2.2}^E$	$O(^1D) + O_2 \xrightarrow{\rho_{O_2}^{DP}} O(^3P) + O_2$

used for the transitions $O_2(b-X)\{0-0\}$ and $O_2(b-X)\{0-1\}$. All processes of the model of Huang and George (2014) are hereafter referred to as processes of the H-model with the capital H for the surname of the first author in Huang and George (2014).

It should be noted that both transitions $O_2(b-X)\{0-0\}$ and $O_2(b-X)\{0-1\}$ can be observed remotely from space, e.g. using the SCIAMACHY instrument mentioned in Section 2 because radiation was measured using the SCIAMACHY instrument simultaneously and contiguously in the wavelength range from 240 to 1750nm (Bovensmann et al., 1999).

As for a photochemical model considering electronic-vibrational kinetics according to the Barth excitation transfer scheme, Makhlof et al. (1998) proposed to consider $O_2(c, \nu' \geq 3)$ instead of O_2^* as the $O(^1S)$ precursor based on conclusions of Krasnopolsky (1981). The results of Makhlof et al. (1998) were obtained for $O_2(c, \nu' = 0 \dots 16)$ regarding the oxygen green line emission simulating gravity wave-driven fluctuations like Huang and George (2014) did. Nevertheless, rate values of the $O_2(c, \nu' = 0, 1)$ quenching used by Makhlof et al. (1998) differ from those ones used by Huang and George (2014) implying that these rate values derived by tuning the H-model depend on the used data sets. It should be mentioned that tuning results for the M-model also depended on the used data sets, see Section 3.2.1.



Table 4. Processes of the extended $O(^1S)$ nightglow model (Hickey et al., 1997; Huang and George, 2014) hereafter referred to as the H-model, see Section 3.2.2. The MAC model includes all processes listed here and also the processes shown in Tables 6 and 7.

$R_{\#}$	Odd oxygen processes related $O_2(c)$, $O_2(b)$ and $O(^1S)$
$R_{c1.1-2}$	$O(^3P) + O(^3P) + \{N_2, O_2\} \xrightarrow{s_{N_2}^{pc}, s_{O_2}^{pc}} O_2(c) + \{N_2, O_2\}$
$R_{c2.1}$	$O_2(c) + O(^3P) \xrightarrow{s_{IS}^{cs}} O_2 + O(^1S)$
$R_{c3.1-2}$	$O_2(c) + \{O(^3P), O_2\} \xrightarrow{s_{3P}^{cb}, s_{O_2}^{cb}} O_2(b) + \{O(^3P), O_2\}$
$R_{c7.1}$	$O_2(c) + O(^3P) \xrightarrow{s_{3P}^{cs}} O_2 + O(^3P)$
$R_{c8.0}$	$O_2(c) \xrightarrow{s_{HI}^A} O_2 + h\nu(\text{Herzberg II band})$
$R_{b1.1-2}$	$O(^3P) + O(^3P) + \{N_2, O_2\} \xrightarrow{\beta_{N_2}^{pb}, \beta_{O_2}^{pb}} O_2(b) + \{N_2, O_2\}$
$R_{b4.2-4}$	$O_2(b) + \{O(^3P), N_2, O_2\} \xrightarrow{\beta_{3P}^{bx}, \beta_{N_2}^{bx}, \beta_{O_2}^{bx}} O_2 + \{O(^3P), N_2, O_2\}$
$R_{b5.0}$	$O_2(b) \xrightarrow{\beta_{762}^A} O_2 + h\nu(\lambda = 762 \text{ nm})$
$R_{b6.0}$	$O_2(b) \xrightarrow{\beta_{Atm}^A} O_2 + h\nu(\text{Atmospheric band})$
$R_{g1.2}$	$O(^1S) + O_2 \xrightarrow{\gamma_{O_2}^{sp}} O(^3P) + O_2$
$R_{g3.0}$	$O(^1S) \xrightarrow{\gamma_{557.7}^A} O(^1D) + h\nu(\lambda = 557.7 \text{ nm})$
$R_{g4.0}$	$O(^1S) \xrightarrow{\gamma_{IS3Pe}^A} O(^3P) + h\nu$
$R_{x1.1-2}$	$O(^3P) + O(^3P) + \{N_2, O_2\} \xrightarrow{\chi_{N_2}^{px}, \chi_{O_2}^{px}} O_2 + \{N_2, O_2\}$

3.3 Processes of the MAC model

Processes of the proposed MAC model extend a combination of the processes adopted from the G-model, see Section 3.1, the M-model, see Section 3.2.1 and the H-model, see Section 3.2.2. Rate values of the processes considered in these models were updated using the JPL 2015 database (Burkholder et al., 2015) and the database of the National Institute of Standards and Technology (NIST) available at <https://www.nist.gov/pml/productsservices/physical-reference-data> as well as other high ranking sources listed in Huestis (2002) and Jones et al. (2006).

The following processes were adopted in the MAC model from the M-model of Mlynczak et al. (1993) and Sharp et al. (2014), see Table 3 in Section 3.2.1. These processes are related to:

1. the photolysis of O_2 and O_3 ($R_{s1.2-3}$, $R_{s3.1}$, $R_{s2.3}$),
2. the Atmospheric band emission ($R_{b2.1}^E$, $R_{b2.2-5}$, $R_{b5.0}$, $R_{b6.0}$),
3. the Infrared Atmospheric band emission ($R_{a1.1-2}$, $R_{a2.2-4}$, $R_{a3.0}$, $R_{a4.0}$),
4. the red line emission ($R_{r2.1,3}$, $R_{r2.2}^E$).



It should be noted that the processes $R_{b2.1}^E$ and $R_{r2.2}^E$ were replaced by processes with other products according to Burkholder et al. (2015). These replaced processes and the other processes of the M-model were adopted in the proposed MAC model, they are also referred to as M-processes.

The following processes were adopted in the MAC model from the H-model of Huang and George (2014) and Hickey et al. (1997), see Table 4 in Section 3.2.2. These processes are related to:

1. the singlet Herzberg state ($R_{c1.1-2}$, $R_{c2.1}$, $R_{c3.1-2}$, $R_{c7.1}$, $R_{c8.0}$),
2. the Atmospheric band emission ($R_{b1.1-2}$, $R_{b4.2-4}$, $R_{b5.0}$, $R_{b6.0}$),
3. the green line emission ($R_{g1.2}$, $R_{g3.0}$, $R_{g4.0}$),
4. the three-body recombination ($R_{x1.1-2}$).

10 These processes were all adopted in the proposed MAC model, they are also referred to as H-processes.

The following processes were adopted in the MAC model from the G-model of Gobbi et al. (1992), see Table 2 in Section 3.1. These processes are related to:

1. the green line emission ($R_{g1.1-2}$, $R_{g2.1}$, $R_{g3.0}$, $R_{g(3-4).0}$) and
2. the $O(^1S)$ precursor responsible for the green line emission ($R_{v1.1-2}^P$, $R_{v2.1}^P$, $R_{v3.1-3}^P$, $R_{v4.0}^P$).

15 It should be noted that the G-model processes $R_{v1.1-2}^P$, $R_{v2.1}^P$, $R_{v3.1-3}^P$ and $R_{v4.0}^P$ were replaced by corresponding processes of the H-model which were adopted in the proposed MAC model. All processes of the G-model are also referred to as G-processes.

In addition to the G-, M- and H-processes, complementary processes (C-processes) were proposed to couple $O_2(^5\Pi, A, A', c, b, a, X)$ with each other and $O(^1S, ^1D, ^3P)$ taking the hypotheses of Huestis (2002) and Slanger et al. (2004b) into account and discussed by Lednyts'kyy and von Savigny (2016) and Lednyts'kyy et al. (2018).

20 Huestis (2002) suggested that the de-excitation of O_2 states with higher energy to O_2 states with lower energy only occurs in a cascade that was described by Slanger et al. (2004b) as the integrity of the O_2 electronic states' identity. This enables assuming that the $O(^1S)$ precursor can be represented by one O_2 state or a group of O_2 states according to the hypothesis of the integrity of the O_2 electronic states' identity. In fact, the Barth excitation transfer scheme was formulated with O_2^* considering it as one not identified O_2 state or a one group of many not identified O_2 states coupled in a cascade of de-excitation reactions is also possible.

25 The hypothesis of Huestis (2002) was refuted by Slanger et al. (2004b) on the basis of laboratory measurements discussed by Huestis (2002), Slanger et al. (2004b) and Pejaković et al. (2007) stating that energetically nearly resonant intermolecular processes are responsible for conversions of higher to lower excited O_2 electronic states according to Slanger and Copeland (2003). Specifically, Slanger et al. (2004b) suggested that the de-excitation of O_2 states occurs not in a cascade-like process. They emphasized the presence of a cycle of de-excitation and excitation of $O_2(^5\Pi)$ and the Herzberg O_2 states in high vibrational levels. These O_2 states transform back and forth into each other through collisions. Finally, the $O_2(^5\Pi)-O_2(A, A', c)$ -group is removed converting to very high vibrational levels of $O_2(b, a, X)$ states. It should be noted that $^5\Pi$ is the electronically excited



O_2 state with the higher energy than O_2 in the Herzberg states. This, in contrast to the hypothesis of Huestis (2002), makes it more complicated to operate with the $O(^1S)$ precursor as a group of many not identified O_2 states.

The C-processes related to the Herzberg states $A^3\Sigma_u^+$ and $A'^3\Delta_u$ (hereafter referred to as $O_2(A, A')$) are not considered in the G-, M- and H-models. These C-processes are related to:

- 5 1. the production of $O_2(A)$ ($R_{t1.1-2}$),
2. the de-excitation of $O_2(A)$ to $O_2(A', c, b)$ ($R_{t2.1-3}$, $R_{t3.1-3}$, $R_{t4.1-3}$),
3. the Broida-Gaydon band emission ($R_{t5.0}$),
4. the de-excitation of $O_2(A)$ to $O_2(a, X)$ ($R_{t6.1-3}$, $R_{t7.1-3}$),
5. the Herzberg I band emission ($R_{t8.0}$, $R_{t9.0}$),
- 10 6. the $O(^1S)$ precursor responsible for the green line emission ($R_{t10.1}$, $R_{d9.1}$),
7. the production of $O_2(A')$ ($R_{d1.1-2}$),
8. the de-excitation of $O_2(A')$ to $O_2(c, b, a)$ ($R_{d2.1-2}$, $R_{d3.1-2}$, $R_{d4.1-2}$),
9. the Chamberlain band emission ($R_{d5.0}$, $R_{d6.0}$),
10. the de-excitation of $O_2(A')$ to $O_2(X)$ ($R_{d7.1-2}$),
- 15 11. the Herzberg III band emission ($R_{d8.0}$).

These C-processes are shown here in Table 5, they were considered and discussed by Lednyts'kyy et al. (2018). The corresponding reaction rates are shown in Table 9.

The C-processes related to the G-, M- and H-processes complete the coupling of $O_2(^5\Pi, c, b, a, X)$ with each other and $O(^1S, ^1D, ^3P)$, they are related to:

- 20 1. the photolysis of O_2 and O_3 ($R_{s1.(1,4-5)}$, $R_{s2.(1-2,4-6)}$),
2. the singlet Herzberg state ($R_{c4.0}$, $R_{c5.1-2}$, $R_{c6.0}$, $R_{c7.2}$),
3. the Atmospheric band emission ($R_{b2.1}$, $R_{b4.1,5-6}$),
4. the Infrared Atmospheric band emission ($R_{a2.1}$),
5. the red line emission ($R_{r2.2,4}$, $R_{r1.1-3}$, $R_{r3.0}$),
- 25 6. the green line emission ($R_{g1.3}$, $R_{g2.2}$),
7. three-body recombination and ozone ($R_{x1.1-2}$, $R_{x2.1}$, $R_{x3.1-2}$).



These C-processes are shown here in Tables 6 and 7, they were considered and discussed by Lednyts'kyi and von Savigny (2016). The corresponding reaction rates are shown in Tables 10 ... 12.

Unknown or poorly constrained reaction rates of these complementary processes might be compromised by boundary effects if they were measured in a ground-based laboratory. Therefore, an appropriate photochemical model including many chemical species obtained on the basis of multiple emissions measured *in-situ* in the Earth's atmosphere may be a valuable complement to laboratory experiments conducted on the Earth's surface. In fact, unknown or poorly constrained reaction rates were tuned according to the verification and validation procedures discussed in Section 3.4 and applied on the basis of the ETON *in-situ* measurements. The advantage of the ETON campaign compared to another rocket campaigns is that multiple emissions and $[O(^3P)]$ were measured almost simultaneously. This enables comparing the *in-situ* and retrieved $[O(^3P)]$ using each particular emission profile described in Section 2.

Figure 1 shows processes coupling $O_2(^5\Pi, A, A', c, b, a, X)$ and $O(^1S, ^1D, ^3P)$ with each other, and Fig. 2 shows processes coupling $O_2(^5\Pi, c, b, a, X)$ and $O(^1S, ^1D, ^3P)$ with each other.

Considering the energy required for a spin flip in transitions among the triplet $O_2(A, A', X)$ and singlet $O_2(c, b, a)$ states it can be concluded that transitions from the $O_2(A, A')$ states to the $O_2(X)$ state are more probable than spin forbidden transitions from the $O_2(A, A')$ states to the $O_2(c, b, a)$ states. Therefore, at least two versions of the MAC model can be implemented on the basis of the ETON measurements. The first one involves $O_2(A)$ and $O_2(A')$, and the second one excludes them from the MAC model.

3.4 Verification and validation of calculations carried out with the MAC model

The input parameters of the MAC model are described in Section 2, they are: VER profiles retrieved on the basis of *in-situ* measurements during the ETON rocket campaign (Greer et al., 1986) as well as profiles of temperature (T), $[N_2]$ and $[O_2]$ obtained using the semi-empirical model NRLMSISE-00. Among the mentioned VER profiles are: $VER\{O_2(A - X)\}$ (Herzberg I band, HzI), $VER\{O_2(A' - a)\}$ (Chamberlain band, Cha), $VER\{O_2(b - X)\}$ (Atmospheric band, Atm), $VER\{O_2(a - X)\}$ (Infrared Atmospheric band, IRAtm) and $VER\{O(^1S - ^1D)\}$ (green line, GrL). These VER profiles were retrieved on the basis of the raw integrated data (Greer et al., 1986) that is marked with a character R, e.g. R- $VER\{O_2(A - X)\}$.

Concentrations of various chemical species were retrieved using sequentially applied continuity equations in the steady state, i.e. polynomial equations of the second or the third order. An overview of all retrieval steps of the MAC model is provided in Appendix A devoted to the description of all algorithmic steps used in calculations with the MAC model, see also Table 8 for a short overview. The input-VER profiles shown in Table 8 correspond to O_2 transitions shown in Table 1. In fact, all reactions relevant for the particular chemical species were used in the retrievals, and the retrieved concentration profiles are marked with a character R, e.g. R- $[O_2(A)]$. Additionally, concentrations of the same chemical species were evaluated dividing the R-VER profiles, which correspond to the particular chemical species, by the respective transition probability. The evaluated concentration profiles are marked with a character E, e.g. E- $[O_2(A)]$. As for the evaluated VER profiles, which are marked with a character E as E-VER profiles (e.g. E- $VER\{O_2(A - X)\}$), they are obtained by dividing the retrieved concentrations of the respective same chemical species by the respective transition probability.



Table 5. Processes of the MAC model, continued by processes shown in Tables 6 and 7.

R#	Odd oxygen processes related to $O_2(A)$ and $O_2(A')$
$R_{t1.1-2}$	$O(^3P) + O(^3P) + \{N_2, O_2\} \xrightarrow{\theta_{N_2}^{Pt}, \theta_{O_2}^{Pt}} O_2(A) + \{N_2, O_2\}$
$R_{t2.1-3}$	$O_2(A) + \{O(^3P), N_2, O_2\} \xrightarrow{\theta_{3P}^{td}, \theta_{N_2}^{td}, \theta_{O_2}^{td}} O_2(A') + \{O(^3P), N_2, O_2\}$
$R_{t3.1-3}$	$O_2(A) + \{O(^3P), N_2, O_2\} \xrightarrow{\theta_{3P}^{tc}, \theta_{N_2}^{tc}, \theta_{O_2}^{tc}} O_2(c) + \{O(^3P), N_2, O_2\}$
$R_{t4.1-3}$	$O_2(A) + \{O(^3P), N_2, O_2\} \xrightarrow{\theta_{3P}^{tb}, \theta_{N_2}^{tb}, \theta_{O_2}^{tb}} O_2(b) + \{O(^3P), N_2, O_2\}$
$R_{t5.0}$	$O_2(A) \xrightarrow{\theta_{BG}^A} O_2(b) + h\nu$ (Broida-Gaydon system)
$R_{t6.1-3}$	$O_2(A) + \{O(^3P), N_2, O_2\} \xrightarrow{\theta_{3P}^{ta}, \theta_{N_2}^{ta}, \theta_{O_2}^{ta}} O_2(a) + \{O(^3P), N_2, O_2\}$
$R_{t7.1-3}$	$O_2(A) + \{O(^3P), N_2, O_2\} \xrightarrow{\theta_{3P}^{tx}, \theta_{N_2}^{tx}, \theta_{O_2}^{tx}} O_2 + \{O(^3P), N_2, O_2\}$
$R_{t8.0}$	$O_2(A) \xrightarrow{\theta_{320n}^A} O_2 + h\nu$ ($\lambda = 320$ nm)
$R_{t9.0}$	$O_2(A) \xrightarrow{\theta_{HI}^A} O_2 + h\nu$ (Herzberg I band)
$R_{t10.1}$	$O_2(A) + O(^3P) \xrightarrow{\theta_{IS}^{tx}} O_2 + O(^1S)$
$R_{d1.1-2}$	$O(^3P) + O(^3P) + \{N_2, O_2\} \xrightarrow{\delta_{N_2}^{Pd}, \delta_{O_2}^{Pd}} O_2(A') + \{N_2, O_2\}$
$R_{d2.1-2}$	$O_2(A') + \{O(^3P), O_2\} \xrightarrow{\delta_{3P}^{dc}, \delta_{O_2}^{dc}} O_2(c) + \{O(^3P), O_2\}$
$R_{d3.1-2}$	$O_2(A') + \{O(^3P), O_2\} \xrightarrow{\delta_{3P}^{db}, \delta_{O_2}^{db}} O_2(b) + \{O(^3P), O_2\}$
$R_{d4.1-2}$	$O_2(A') + \{O(^3P), O_2\} \xrightarrow{\delta_{3P}^{da}, \delta_{O_2}^{da}} O_2(a) + \{O(^3P), O_2\}$
$R_{d5.0}$	$O_2(A') \xrightarrow{\delta_{370n}^A} O_2(a) + h\nu$ ($\lambda = 370$ nm)
$R_{d6.0}$	$O_2(A') \xrightarrow{\delta_{Cha}^A} O_2(a) + h\nu$ (Chamberlain band)
$R_{d7.1-2}$	$O_2(A') + \{O(^3P), O_2\} \xrightarrow{\delta_{3P}^{dx}, \delta_{O_2}^{dx}} O_2 + \{O(^3P), O_2\}$
$R_{d8.0}$	$O_2(A') \xrightarrow{\delta_{HIII}^A} O_2 + h\nu$ (Herzberg III band)
$R_{d9.1}$	$O_2(A') + O(^3P) \xrightarrow{\delta_{IS}^{dx}} O_2 + O(^1S)$

The results of calculations carried out using the MAC model are verified by a visual comparison of retrieved and evaluated profiles, i.e. the respective emission and concentration values. Note that the prior step 1 shown in Table 8 and briefly described in Section A1 is omitted for the ETON campaign because such input parameters as $[O_3]$ and $[H]$ are not known *a-priori*. Instead, the short list of the input parameters required to run the MAC model is applied: T , $[N_2]$, $[O_2]$ from the NRLMSISE-00 model and VER profiles from the ETON campaign. For instance, the quadratic continuity equation is solved to retrieve $R-[O_2(A)]$ on the basis of $R-VER\{O_2(A - X)\}$ by using all relevant processes of the MAC model. This retrieval step is shown as the step 2.1 in Table 8 and the step 2.1 described in Section A2.1 in Appendix A. Then, the verification of calculations at the step 2.1 is carried out comparing $R-VER\{O_2(A - X)\}$ with $E-VER\{O_2(A - X)\}$ and $R-[O_2(A)]$ with $E-[O_2(A)]$. The cubic equation is solved at the step 2.2 on the basis of T , $[N_2]$, $[O_2]$, $R-VER\{O_2(A' - a)\}$ and $R-[O_2(A)]$. Then, the verification of calculations at the step 2.2 is carried out comparing $R-VER\{O_2(A' - a)\}$ with $E-VER\{O_2(A' - a)\}$ and $R-[O_2(A')]$ with $E-[O_2(A')]$.



Table 6. Processes shown here comprise the MAC model together with processes shown above in Table 5 and processes shown below in Table 7.

R _#	Odd oxygen processes related to O ₂ (c), O ₂ (b) and O ₂ (a)
R _{c1.1-2}	$O(^3P) + O(^3P) + \{N_2, O_2\} \xrightarrow{s_{N_2}^{Pc}, s_{O_2}^{Pc}} O_2(c) + \{N_2, O_2\}$
R _{c2.1}	$O_2(c) + O(^3P) \xrightarrow{s_{IS}^{cx}} O_2 + O(^1S)$
R _{c3.1-2}	$O_2(c) + \{O(^3P), O_2\} \xrightarrow{s_{3P}^{cb}, s_{O_2}^{cb}} O_2(b) + \{O(^3P), O_2\}$
R _{c4.0}	$O_2(c) \xrightarrow{s_{cbK}^A} O_2(b) + h\nu(\text{New system from Keck I/II})$
R _{c5.1-2}	$O_2(c) + \{O(^3P), O_2\} \xrightarrow{s_{3P}^{ca}, s_{O_2}^{ca}} O_2(a) + \{O(^3P), O_2\}$
R _{c6.0}	$O_2(c) \xrightarrow{s_{RJ}^A} O_2(a) + h\nu(\text{Richards-Johnson system})$
R _{c7.1-2}	$O_2(c) + \{O(^3P), O_2\} \xrightarrow{s_{3P}^{cx}, s_{O_2}^{cx}} O_2 + \{O(^3P), O_2\}$
R _{c8.0}	$O_2(c) \xrightarrow{s_{HII}^A} O_2 + h\nu(\text{Herzberg II band})$
R _{b1.1-2}	$O(^3P) + O(^3P) + \{N_2, O_2\} \xrightarrow{\beta_{N_2}^{Pb}, \beta_{O_2}^{Pb}} O_2(b) + \{N_2, O_2\}$
R _{b2.1-5}	$O_2(b) + \{O_3, O, N_2, O_2, CO_2\} \xrightarrow{\beta_{O_3}^{ba}, \beta_{3P}^{ba}, \beta_{N_2}^{ba}, \beta_{O_2}^{ba}, \beta_{CO_2}^{ba}} O_2(a) + \{O_3, O, N_2, O_2, CO_2\}$
R _{b3.0}	$O_2(b) \xrightarrow{\beta_{Nox}^A} O_2(a) + h\nu(\text{Noxon transition})$
R _{b4.1-6}	$O_2(b) + \{O_3, O, N_2, O_2, CO_2, O_3\} \xrightarrow{\beta_{O_3}^{bx}, \beta_{3P}^{bx}, \beta_{N_2}^{bx}, \beta_{O_2}^{bx}, \beta_{CO_2}^{bx}, \beta_{O_3}^{x3}} O_2 + \{O + O_2, O, N_2, O_2, CO_2, O_3\}$
R _{b5.0}	$O_2(b) \xrightarrow{\beta_{762}^A} O_2 + h\nu(\lambda = 762 \text{ nm})$
R _{b6.0}	$O_2(b) \xrightarrow{\beta_{Atm}^A} O_2 + h\nu(\text{Atmospheric band})$
R _{a1.1-2}	$O(^3P) + O(^3P) + \{N_2, O_2\} \xrightarrow{\alpha_{N_2}^{Pa}, \alpha_{O_2}^{Pa}} O_2(a) + \{N_2, O_2\}$
R _{a2.1-4}	$O_2(a) + \{O_3, O, N_2, O_2\} \xrightarrow{\alpha_{O_3}^{ax}, \alpha_{3P}^{ax}, \alpha_{N_2}^{ax}, \alpha_{O_2}^{ax}} O_2 + \{O + O_2, O, N_2, O_2\}$
R _{a3.0}	$O_2(a) \xrightarrow{\alpha_{127}^A} O_2 + h\nu(\lambda = 1.27 \mu\text{m})$
R _{a4.0}	$O_2(a) \xrightarrow{\alpha_{IRA}^A} O_2 + h\nu(\text{IR Atmospheric band})$

Note that values of the *in-situ* R-VER{O(¹S – ¹D)} profile are less than zero randomly below 92 km due to the measurement noise. Therefore, the *in-situ* R-VER{O(¹S – ¹D)} profile is approximated by the asymmetrical Gaussian distribution described by Semenov (1997) and Khomich et al. (2008) to obtain the shown A-VER{O(¹S – ¹D)} profile and to retrieve the corresponding [O(¹S)] profile.

- 5 The retrieved and evaluated VER profiles indicated by the dashed lines and the symbols, respectively, and shown on the left in Fig. 3 are compared with each other by sight to verify calculations carried out with the MAC model involving O₂(A) and O₂(A'). The retrieved and evaluated VER profiles belonging to each pair regarding the considered excited O₂ state seem to be in perfect agreement with each other by sight. Next, the retrieved and evaluated concentration profiles shown on the right in Fig. 3 by the dashed lines and the symbols, respectively, are also compared with each other for each retrieval step; these
- 10 profiles also seem to be in perfect agreement with each other by sight. The comparison of the retrieved and evaluated products



Table 7. Processes shown here comprise the MAC model together with processes shown above in Tables 5 and 6.

R#	Odd oxygen processes related to $O(^1S)$ and $O(^1D)$
$R_{g1.1-3}$	$O(^1S) + \{O(^3P), O_2, O_3\} \xrightarrow{\gamma_{1D}^{SP}, \gamma_{O_2}^{SP}, \gamma_{O_3}^{SP}} \{2O(^1D), O(^3P) + O_2, 2O_2\}$
$R_{g2.1-2}$	$O(^1S) + \{N_2, O_2(a)\} \xrightarrow{\gamma_{N_2}^{SP}, \gamma_{O_2}^{SP}} O(^3P) + \{N_2, O_2(a)\}$
$R_{g3.0}$	$O(^1S) \xrightarrow{\gamma_{557nm}^A} O(^1D) + h\nu (\lambda = 557.7 \text{ nm})$
$R_{g4.0}$	$O(^1S) \xrightarrow{\gamma_{1S3Pe}^A} O(^3P) + h\nu$
$R_{r1.1-3}$	$O(^1D) + \{O(^3P), O_3, O_2\} \xrightarrow{\rho_{3P}^{DP}, \rho_{2P}^{DP}, \rho_{O_2}^{DP}} \{2O(^3P), 2O(^3P) + O_2, 2O_2\}$
$R_{r2.1-4}$	$O(^1D) + \{N_2, O_2, O_2, CO_2\} \xrightarrow{\rho_{N_2}^{DP}, \rho_{O_2}^{DP}, \rho_{O_2}^{DP}, \rho_{CO_2}^{DP}} O(^3P) + \{N_2, O_2(a), O_2(b), CO_2\}$
$R_{r3.0}$	$O(^1D) \xrightarrow{\rho_{1D3Pe}^A} O(^3P) + h\nu$
R#	Odd oxygen processes related to the loss of atomic oxygen
$R_{x1.1-2}$	$O(^3P) + O(^3P) + \{N_2, O_2\} \xrightarrow{\chi_{N_2}^{Px}, \chi_{O_2}^{Px}} O_2 + \{N_2, O_2\}$
R#	Odd oxygen processes related to catalytic ozone destruction and photolysis
$R_{x2.1}$	$O(^3P) + O_3 \xrightarrow{\chi_{O_2}^{3P}} 2O_2$
$R_{x3.1-2}$	$O_2 + O(^3P) + \{N_2, O_2\} \xrightarrow{\chi_{N_2}^{P3}, \chi_{O_2}^{P3}} O_3 + \{N_2, O_2\}$
$R_{s1.1-5}$	$O_2 + h\nu \xrightarrow{\sigma_{PS}^{UV}, \sigma_{PD}^{LA}, \sigma_{PD}^{Sc}, \sigma_{PP}^{Sb}, \sigma_{PP}^{Hc}} O(^3P) + \{O(^1S), O(^1D), O(^1D), O(^3P), O(^3P)\}$
$R_{s2.1-6}$	$O_3 + h\nu \xrightarrow{\sigma_{aS}^{UV}, \sigma_{PP}^{Ha}, \sigma_{aD}^{Hu}, \sigma_{xD}^{Hu}, \sigma_{aP}^{Ch}, \sigma_{xP}^{Ch}} \{O(^1S) + O_2(a), 3O, O(^1D) + O_2(a), O(^1D) + O_2, O + O_2(a), O + O_2\}$
$R_{s3.1}$	$O_2 + h\nu (\lambda = 762 \text{ nm}) \xrightarrow{\sigma_{b1}^{O_2}} O_2(b)$
R#	Odd hydrogen processes
$R_{h1.1}$	$H + O_3 \xrightarrow{\eta_{OH}^H} OH^* + O_2$
$R_{h2.1}$	$OH^* + O(^3P) \xrightarrow{\eta_{OH}^{3P}} H + O_2$
$R_{h3.1}$	$OH^* + O_3 \xrightarrow{\eta_{HO_2}^{OH}} HO_2 + O_2$
$R_{h4.1}$	$HO_2 + O(^3P) \xrightarrow{\eta_{HO_2}^{3P}} OH^* + 2O_2$
$R_{h5.1-2}$	$H + O_2 + \{N_2, O_2\} \xrightarrow{\eta_{N_2}^H, \eta_{O_2}^H} HO_2 + \{N_2, O_2\}$
$R_{h6.1-3}$	$H + HO_2 \xrightarrow{\eta_{OH}^{HO_2}, \eta_{H_2}^{HO_2}, \eta_{H_2O}^{HO_2}} \{OH^* + OH^*, H_2 + O_2, O(^3P) + H_2O\}$

(VER or concentration profiles) enables concluding that all calculations carried out using the MAC model are consistent with each other and coherent with measurements.

Before we discuss results of the $[O(^3P)]$ retrievals obtained with the proposed MAC model, a short overview of the previously used photochemical models is given to estimate our current situation and to argue whether the proposed MAC model

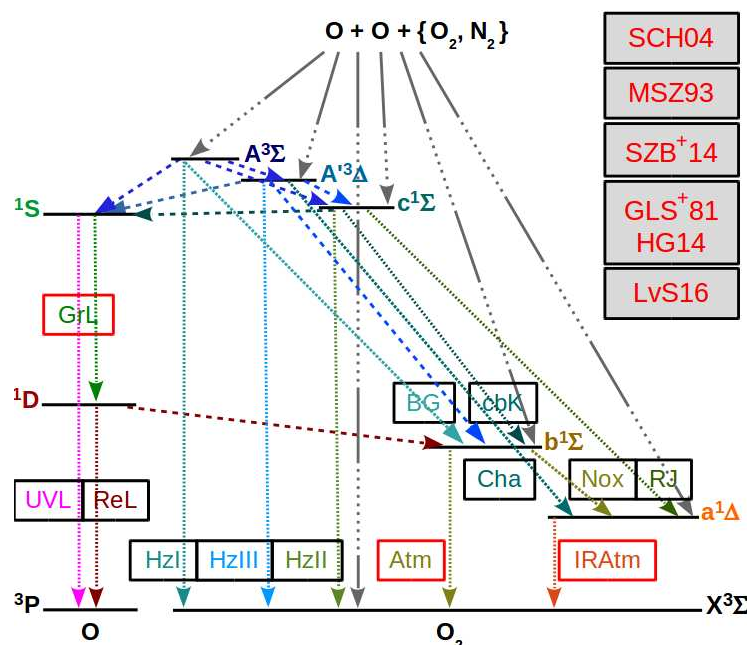


Figure 1. O_2 and O term diagrams showing processes of the MAC model comprised of processes considered in the G-, M- and H-models combined and extended with complementary C-processes completing the MAC model. C-processes are proposed to couple states of $O_2(^5\Pi, A, A', c, b, a, X)$ and $O(^1S, ^1D, ^3P)$ with each other according to the hypothesis of Slanger et al. (2004b) (SCH04) stating that the Herzberg states are in constant collisional communication with the higher excited $^5\Pi$ electronic state. All considered processes of the MAC model are provided in Tables 5, 6 and 7. Three-body recombination (association) reactions are indicated by the gray 10 dots–1 dash line and result in O_2^* and O_2^{**} due to reactions, rate values of which are $\beta\kappa_1$ and $\alpha\kappa_1$, respectively, (McDade et al., 1986). Radiative losses accompanied with quenching processes are indicated by an abbreviation near the fine dashed line, see Table 1 for abbreviations. Radiative losses only are also indicated by an abbreviation, but near the violet 2 dots–3 dashes line. Quenching processes only are indicated by the dashed lines. References shown in the legend as well as the representation of lines and abbreviations regarding various chemical processes are the same as those used in the mentioned above figures. The $O_2(A, A', c)$ Herzberg states are all implemented as possible $O(^1S)$ precursors because their energy in various vibrational levels exceeds the 4.19 eV excitation energy difference with respect to the triplet $O_2(X)$ ground state.

is needed. The published photochemical models based on processes provided in Table 2 resulted in the following continuity equations discussed here with respect to $[O(^3P)]$:

1. the well-known quadratic equation of McDade et al. (1986) (MMG⁺86) was applied to the Atmospheric band emissions at 762.2 nm (see Sections 1 and 3.1),
2. the well-known cubic equation (2) was applied to the green line emissions at 557.7 nm (see Section 3.1) and

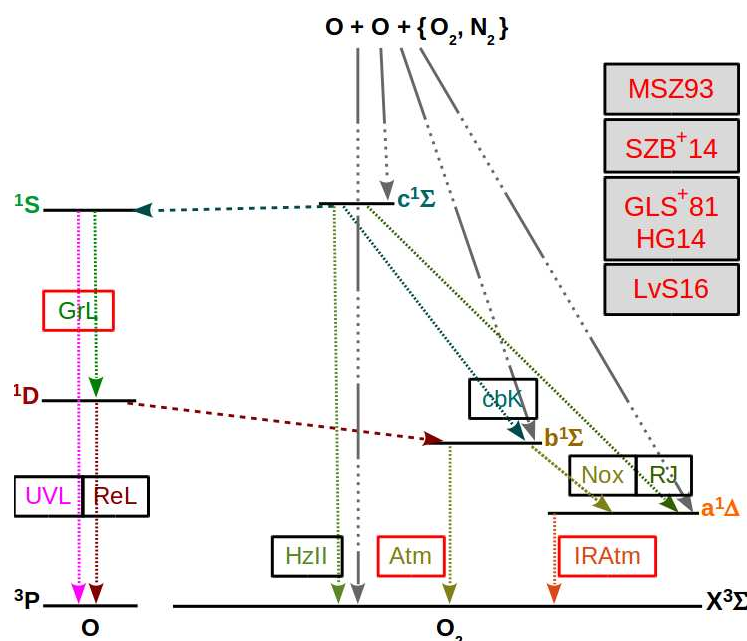


Figure 2. Similar to Fig. 1, but for processes excluding the triplet $O_2(A)$ and $O_2(A')$ Herzberg states from the MAC model. All considered processes of the MAC model indicated in the O_2 and O term diagrams are provided in Tables 6 and 7. The following conclusions drawn by Slanger et al. (2004b) and Krasnopolsky (2011) help to interpret processes indicated here in the O_2 and O term diagrams: (1) the $O_2(A, A')$ and $O_2(X)$ ($X^3\Sigma_g^-$) are triplet states, which are strongly coupled with each other; (2) transitions among the singlet $O_2(c, b, a)$ states ($c^1\Sigma_u^-$, $b^1\Sigma_g^+$, $a^1\Delta_g$) and the triplet $O_2(A, A', X)$ states are less probable because they require a spin flip; (3) the $O_2(c)$ and $O_2(b, a)$ states seem to be rather weakly coupled with each other presumably because of Frank-Condon factors. This enabled neglecting the $O_2(A, A')$ states in the MAC model indicated in Fig. 2.

- the extended cubic equation proposed by Gobbi et al. (1992), see Eq. (3), was applied to the green line emission at 557.7 nm with empirical coefficients of Lednyts'kyy et al. (2015) (LSE⁺15) and solved using the analytical method of Semenov (1997) modified by Lednyts'kyy et al. (2015).

These three continuity equations are applied, and the retrieved $[O(^3P)]$ profiles are shown on the left in Fig. 4. The peak $[O(^3P)]$ profile values retrieved according to the well-known quadratic and cubic equations are lower, but those of the extended cubic equation are higher than the peak values of the *in-situ* ETON $[O(^3P)]$ profile. The $[O(^3P)]$ profile values retrieved according to the well-known and extended cubic equations are almost equidistant with respect to the *in-situ* $[O(^3P)]$ profile values, and can be considered as two profiles of extrema values. One could assume that the arithmetical averaging of the extrema $[O(^3P)]$ profile values might be appropriate to finalize the $[O(^3P)]$ retrievals, see the violet crosses on the left in both figures. Indeed, the averaged peak $[O(^3P)]$ profile values are almost equal to those of the *in-situ* $[O(^3P)]$ profile. However, now we do not see any deeper significance in this finding. Empirical coefficients were derived for these previously used photochemical



Table 8. Overview of the calculation steps carried out using the MAC model. The first column shows the step number. Input-concentrations shown in the third column were retrieved at one of the previous steps and are required together with profiles of input-VER and the other MAC input parameters at the current retrieval step. The other MAC input parameters should be at least comprised of temperature (T), O₂ and N₂ that can be simulated using the NRLMSISE-00 model. If only these MAC input parameters are available, then the prior step 1 described in Section A1 is omitted. Nevertheless, if [O₃] and [H] were also available among the other MAC input parameters, then [O(¹S)], [O(¹D)], [OH*] and [HO₂] would be calculated at the prior step 1 and also used as MAC input parameters at the following steps.

Step #	Input-VER	Input-concentration	Output-concentration
1	–	–	–
2.1	VER{O ₂ (A – X)}	–	[O(³ P)], [O ₂ (A)]
2.2	VER{O ₂ (A' – a)}	[O ₂ (A)]	[O(³ P)], [O ₂ (A')]
2.3	VER{O ₂ (b – X)}	[O ₂ (A)], [O ₂ (A')]	[O(³ P)], [O ₂ (b)]
3.1	–	[O(³ P)], [O ₂ (A)], [O ₂ (A')], [O ₂ (b)]	[O ₂ (c)]
3.2	VER{O ₂ (a – X)}	[O ₂ (A)], [O ₂ (A')], [O ₂ (c)], [O ₂ (b)]	[O(³ P)], [O ₂ (a)]
4.1	VER{O(¹ S – ¹ D)}	[O ₂ (A)], [O ₂ (A')], [O ₂ (c)], [O ₂ (b)], [O ₂ (a)]	[O(³ P)], [O(¹ S)]
5.1	–	[O ₂ (A)], [O ₂ (A')], [O ₂ (c)], [O ₂ (b)], [O ₂ (a)],	[O(³ P)]
5.1	–	[O(¹ S)]	[O(³ P)]

models phenomenologically, i.e. in relation to rates of reactions in which a not identified O₂^{*} is involved. Therefore, [O(³P)] retrievals on a new photochemical basis are required. Note processes of the previously used photochemical models were also used to propose the MAC model, which is applied as follows.

[O(³P)] profiles retrieved using the MAC model involving O₂(A) and O₂(A') are shown on the right in Fig. 4. The *in-situ* [O(³P)] profile is compared with the [O(³P)] profiles obtained at the retrieval steps provided in Table 8. The retrieved profiles are indicated in the same color used to show them in the legend. The peak values of the [O(³P)] profiles retrieved directly on the basis of VER{O₂(A – X)}, VER{O₂(A' – a)}, VER{O₂(b – X)} and VER{O₂(a – X)} are lower than those of the *in-situ* ETON [O(³P)] profile, but the peak values of the [O(³P)] profile retrieved at the pre-last step 4.1 on the basis of VER{O(¹S – ¹D)} are higher. The peak magnitude and altitude values as well as the shape of the [O(³P)] profile retrieved at the last step 5.1 on the basis of all chemical species are approximately the same comparing to those of the *in-situ* ETON [O(³P)] profile.

In the following, the retrieval results obtained with the MAC model excluding O₂(A) and O₂(A') are shown in Fig. 5 and discussed in the comparison to those obtained with the MAC model involving O₂(A) and O₂(A') and shown in Figs. 3 and 4.

Profiles of VER and [O(³P)] obtained at the retrieval steps 2.3, 3.1, 3.2, 4.1 and 5.1 are shown on the left and right of Fig. 5, respectively. In fact, values of E-VER{O₂(A – X)}, E-VER{O₂(A' – a)}, R-[O₂(A)] and R-[O₂(A')] are equal zero, whereas E-[O₂(A)] and E-[O₂(A')] can not be shown because of the division by transition probabilities set to zero at the retrieval steps 2.1 and 2.2 for Fig. 5.

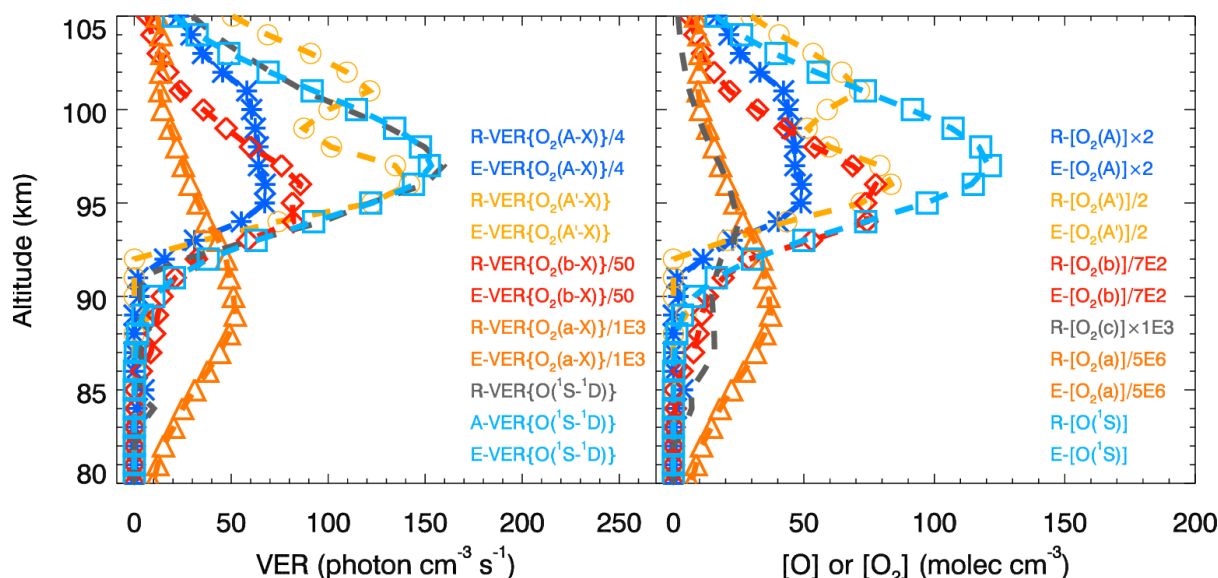


Figure 3. The retrieved VER (R-VER) profiles obtained during the ETON campaign (see Section 2) and the evaluated VER (E-VER) profiles obtained using the MAC model involving $O_2(A)$ and $O_2(A')$ are shown on the left by the dashed lines and symbols. Calculations carried out using the MAC model involving $O_2(A)$ and $O_2(A')$ are verified visually comparing the R-VER and E-VER profiles. Concentrations of various chemical species were retrieved on the basis of the corresponding R-VER profiles and all relevant processes of the MAC model; these concentrations are marked with a character R and shown on the right by the dashed lines. The respective transition probabilities are only used to evaluate concentrations marked with a character E as well as E-VER profiles. Again, the evaluated concentrations are shown with the use of symbols as it as done for E-VER profiles. Two corresponding profiles (R-VER and E-VER as well as of the retrieved and evaluated concentrations) seem to be in perfect agreement with each other by sight. This implies that all calculations carried out with the MAC model are consistent with each other and the results are coherent with measurements. The abbreviations indicating emissions are explained in Table 1, and the sequence of the retrieval steps is provided in Table 8. Values of temperature, $[N_2]$ and $[O_2]$ were obtained by using the NRLMSISE-00 model (see Section 2) for the time and place of the P229H rocket.

Comparing VER and $[O(^3P)]$ profiles shown on the left in Figs. 3 and 5 with each other, it can be concluded that all calculations carried out using the MAC model excluding or involving $O_2(A)$ and $O_2(A')$ are all consistent with each other and coherent with measurements. As far as $R-VER\{O(^1S - ^1D)\}$ with $E-VER\{O(^1S - ^1D)\}$ shown in these figures seem to be in perfect agreement with each other, we can argue about the $O(^1S)$ production implemented via different pathways indicated in Figs. 1 and 2. In fact, our suggestions about the origin of the $O(^1S - ^1D)$ green line emission are also backed up by the comparison of various $[O(^3P)]$ shown on the right in Figs. 4 and 5. Specifically, $O_2(c)$ can be considered the major $O(^1S)$ precursor because the contribution of processes involving $O_2(A)$ and $O_2(A')$ to the $O(^1S)$ production is negligible.

The $[O(^3P)]$ profile values retrieved at the step 3.2 on the basis of $VER\{O_2(a-X)\}$ (Infrared Atmospheric band, IRAtm) are variable, and variabilities are higher than those of the *in-situ* ETON $[O(^3P)]$ profile at altitudes higher than 102 km and lower than 95 km, see Figs. 4 and 5. $[O(^3P)]$ profile values retrieved at the other steps are in good agreement with those of the *in-situ*

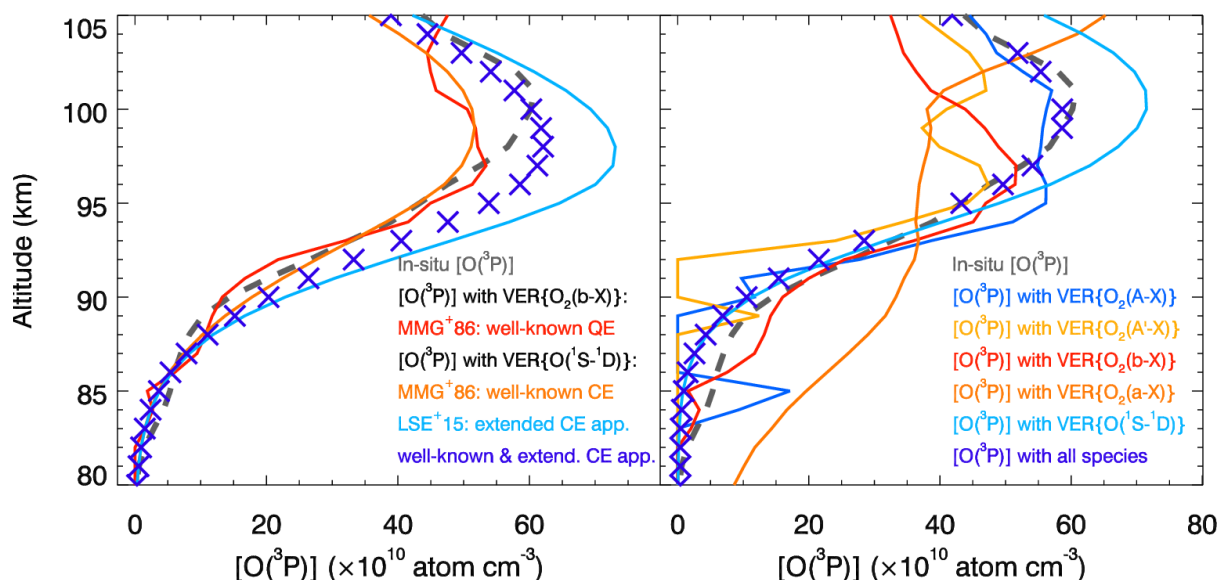


Figure 4. The *in-situ* and retrieved $[O(^3P)]$ profiles are shown and compared with each other. The *in-situ* $[O(^3P)]$ profile obtained during the ETON campaign (see Section 2) is shown with the dashed gray line to validate $[O(^3P)]$ retrievals. The well-known quadratic equation (QE) and the well-known cubic equation (CE) of McDade et al. (1986) (MMG^+86) as well as the extended CE of Lednys'kyy et al. (2015) (LSE^+15) were applied to retrieve $[O(^3P)]$ profiles shown on the left. $[O(^3P)]$ profiles retrieved according to the cubic equations seem to represent two profiles of extreme values with respect to the *in-situ* $[O(^3P)]$ profile. Therefore, they were arithmetically averaged (see the violet crosses on the left in this figure), and seem to be in good agreement with the *in-situ* $[O(^3P)]$ profile values. This was done to estimate the efficiency of the known photochemical models, but we do not ascribe any deeper significance to this finding. Empirical coefficients were introduced in both cubic equations phenomenologically that stimulated to propose the MAC model. The MAC model involving $O_2(A)$ and $O_2(A')$, see Section 3.3, was applied at the retrieval steps provided in Table 8 and applied consequently to retrieve $[O(^3P)]$ profiles shown on the right by the solid colored lines similar to Fig. 3. Although the retrieval steps 2.1, 2.2, 2.3 and 3.2 applied on the basis of some ETON VER profiles result in lower $[O(^3P)]$ values compared to the *in-situ* ones, the retrieval step 4.1 applied on the basis of $VER\{O(^1S - ^1D)\}$ results in higher values. The last retrieval step 5.1 applied on the basis of concentrations of all chemical species retrieved at the previous steps results in $[O(^3P)]$ values being in good agreement with the *in-situ* values.

ETON $[O(^3P)]$ profile, but $[O(^3P)]$ profile values retrieved at the step 3.2 are in disagreement with all $[O(^3P)]$ profile values mentioned here. Llewellyn and Solheim (1978) analyzed emissions in the IRAtm and Meinel bands and proposed the rate of the reaction $OH(\nu' \geq 1) + O(^3P) \rightarrow H + O_2(a)$, which they suggested to implement in a photochemical model to retrieve $[O(^3P)]$. It should be mentioned that the vibrational population of $OH(\nu')$ has to be known in order to consider the reaction

5 $R_{h2.1}$ shown in Table 7 ($OH^* + O(^3P) \xrightarrow{\eta_{OH}^{3P}} H + O_2$, where OH^* describes the hydroxyl radical in all possible levels ν') in the MAC model. Wayne (1994) presented an excellent overview of reactions involving $O_2(a)$, and assumed that the reaction emphasized by Llewellyn and Solheim (1978) only produces about one-half of the $VER\{O_2(a - X)\}$ intensity needed. Wayne (1994) suggested that the reaction $OH(\nu' \geq 3) + O_2 \rightarrow OH + O_2(a)$ can be neglected due to its negligible contribution that was

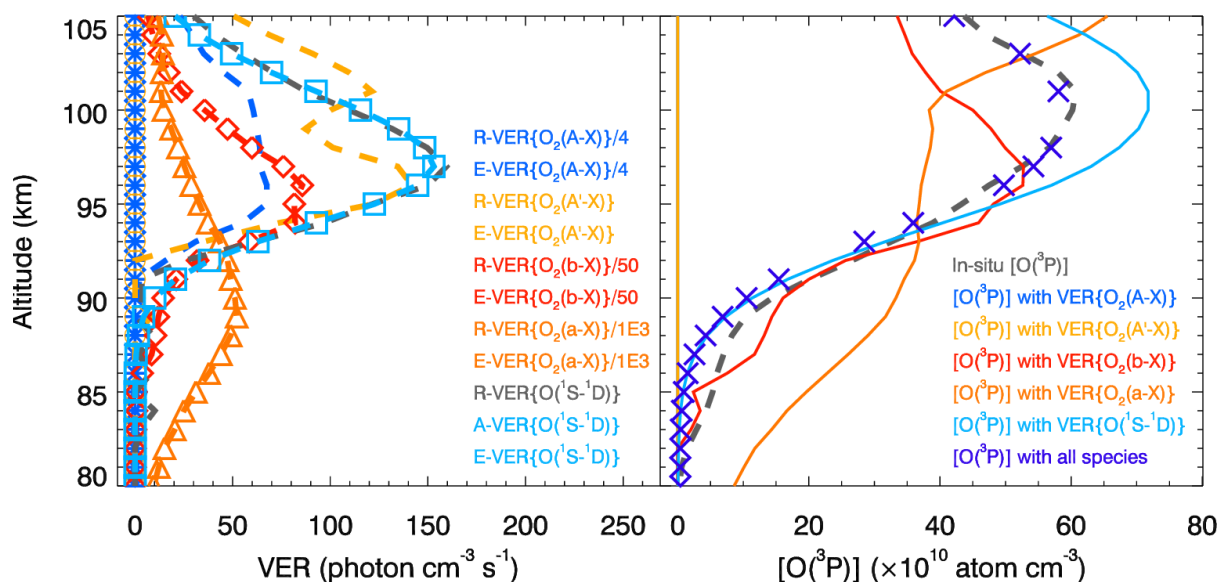


Figure 5. Similar to Figs. 3 and 4, but showing results obtained with the MAC model excluding $O_2(A)$ and $O_2(A')$. The first two retrievals steps 2.1 and 2.2 are not carried out, because now the $VER\{O_2(A-X)\}$ and $VER\{O_2(A'-X)\}$ profiles are not considered in the MAC calculations. The *in-situ* and retrieved VER and $[O(^3P)]$ profiles obtained at the retrieval steps 2.3, 3.2, 4.1 and 5.1 agree with each other by sight and with those shown in Fig. 4, and the MAC calculations are concluded to be verified and validated. The comparison of products related to $VER\{O(^1S-^1D)\}$ indicated by the cyan color and shown in this figure as well as in Fig. 3 enables concluding that the contribution of $O_2(A)$ and $O_2(A')$ to the $O(^1S)$ production is negligible. Therefore, $O_2(c)$ can be considered the major $O(^1S)$ precursor. It follows also that the triplet Herzberg states ($A^3\Sigma_u^+$, $A'^3\Delta_u$) are more strongly coupled with the triplet ground state ($X^3\Sigma_g^-$) than with the singlet states ($c^1\Sigma_u^-$, $b^1\Sigma_g^+$, $a^1\Delta_g$) because the $O_2(X)$ production is considered to be invariable.

experimentally confirmed. Hislop and Wayne (1977) emphasized two sources of the emission line at $\lambda_{1270}=1270$ nm. The first source is the $O_2(a-X)\{0-0\}$ transition at λ_{1270} that enables determining $VER\{O_2(a-X)\}$ profiles. The second source is the $HO_2\{^2A'(001)-^2A''(000)\}$ electronic transition at $\lambda_{HO_2}=1265\pm 10$ nm, which is very close to λ_{1270} . $^2A''$ denotes the ground state of HO_2 , $^2A'$ – its first excited state, and three numbers in parentheses – various levels of the vibrational excitation.

- 5 Additionally, Hislop and Wayne (1977) mentioned the reaction $HO_2\{^2A''(001)\} + O_2 \rightarrow HO_2 + O_2(a)$, which negligibly produces $O_2(a)$. It is possible to process OH^* emissions in future versions of the MAC model applied to measurements obtained during the ETON campaign, but emissions related to the excited HO_2 (HO_2^*) were measured neither during the ETON campaign nor other rocket campaigns known to the authors of this article. Unfortunately, it would be not enough to extend future versions of the MAC model with processes considering vibrational levels of OH^* because of the HO_2^* contribution. Sharma
- 10 et al. (2015) proposed a new mechanism responsible for the deactivation of OH^* as follows: $OH(\nu' \geq 5) + O(^3P) \rightarrow OH(0 \leq \nu'' \leq \nu' - 1) + O(^1D)$. Sharma et al. (2015) emphasized that this mechanism is represented by two reactions producing a transient HO_2^* complex at first, which is de-excited resulting in products shown in the proposed mechanism on the right. Contributions of processes involving both OH^* and HO_2 to the production of $O_2(a)$ need to be considered in order to retrieve



$[O(^3P)]$ using $VER\{O_2(a-X)\}$. This enables concluding that the disagreement of the reference $[O(^3P)]$ profiles with current $[O(^3P)]$ profiles retrieved at the step 3.2 using the MAC model will remain if the only currently known *in-situ* measurements are applied.

In summary, the MAC model was carefully applied to retrieve $[O(^3P)]$ on the basis of a limited number of VER profiles: (1) including or neglecting $VER\{O_2(A-X)\}$ and $VER\{O_2(A'-a)\}$ profiles and (2) using all VER profiles or a $VER\{O_2(b-X)\}$ profile only. This is possible because calculations carried out using the MAC model are separated by steps, and concentrations of various O_2 states are considered at each of the following retrieval steps provided in Table 8.

3.5 Influence of perturbations in model parameters on $[O(^3P)]$ retrieved using the MAC model

The results of the $[O(^3P)]$ retrievals carried out with the MAC model depend on values of the following MAC input parameters: temperature (T), $[N_2]$, $[O_2]$ and VER profiles. Therefore, the impact of perturbations in VER profiles by error values provided by Greer et al. (1986), see Section 2, and the impact of perturbations in profiles of T, $[N_2]$ and $[O_2]$ by 5% of their values on the retrieved $[O(^3P)]$ profiles is estimated and discussed in this section. Specifically, these retrieved (hereafter referred to as perturbed) $[O(^3P)]$ profiles are compared with the unperturbed (hereafter referred to as reference) $[O(^3P)]$ profiles estimating differences between them as follows:

$$\epsilon = [O^{\text{current}}] - [O^{\text{reference}}], \quad (5)$$

where the $[O^{\text{reference}}]$ profiles are shown in Fig. 4. To keep the results obtained according to Eq. (5) positive, perturbations in T were chosen to be introduced by 5% of T, but perturbations in $[N_2]$ and $[O_2]$ by -5% of the respective $([N_2] + [O_2])$ values. Perturbations in VER profiles were introduced by positive values of the respective error values. Specifically, the absolute accuracy of $VER\{O_2(a-X)\}$ (Infrared Atmospheric band, IRAtm) values was assumed to be $\pm 20\%$, and the absolute accuracy of the other VER values was assumed to be $\pm 10\%$ according to Greer et al. (1986), see Section 2 for details.

Both the perturbed and reference $[O(^3P)]$ profiles were retrieved using the MAC model with one MAC input parameter perturbed at a time according to the description provided in the beginning of this section. For instance, values of one VER profile only were perturbed at the particular retrieval step, see Table 8 for an overview of all steps of the consequent retrieval procedure. Figure 6 shows ϵ values in units of atoms cm^{-3} illustrating the influence of the perturbed input parameters on $[O(^3P)]$ profiles. Because the number of VER profiles used in the $[O(^3P)]$ retrieval increases with each step, the number of profiles of $[O(^3P)]$ differences also increases from the top left panel to the bottom middle panel of this figure. Note that a VER profile, which was considered to have a significant impact at one of the retrieval steps performed previously to calculate the corresponding concentration profile, was taken only implicitly into account at the current retrieval step, at which these concentrations are considered instead of the corresponding VER profile. A comparison of difference values shown in various panels indicates that perturbations in the VER and T profiles introduced simultaneously will cause the highest impact on $[O(^3P)]$ profiles.

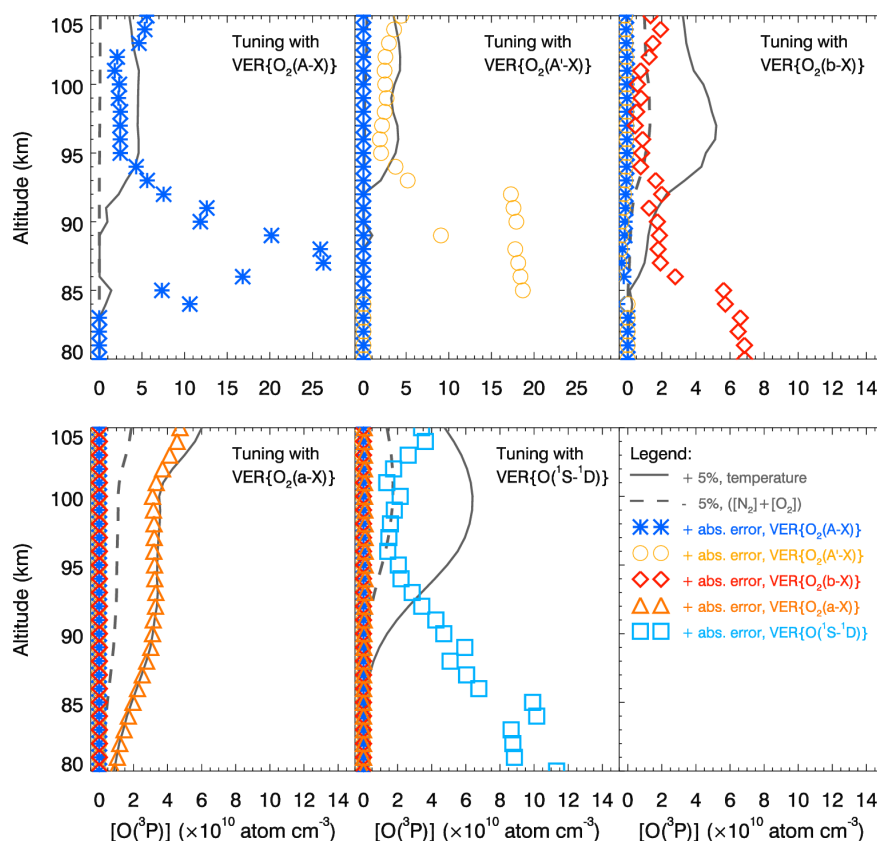


Figure 6. Effects of perturbations in the MAC input parameters on the retrieved $[O(^3P)]$ profiles. The retrievals were performed at the steps 2.1, 2.2, 2.3, 3.2 and 4.1 described in Table 8 on the basis of the following perturbed input parameters: Volume Emission Rates (VER), temperature (T), $[N_2]$ and $[O_2]$. Additionally, $[O(^3P)]$ profiles were retrieved on the basis of the not perturbed input parameters and denoted as reference $[O(^3P)]$ profiles shown in Fig. 4. Finally, differences between the reference and perturbed $[O(^3P)]$ profiles were estimated and shown in five panels using the colors of the perturbed input parameters shown in the legend, which is shown in the sixth panel (the last panel in the bottom row). The units of the differences shown in all panels of the top row are the same as those of the bottom row. VER values were perturbed by values of the absolute error: +20% for the $VER\{O_2(a-X)\}$ profile and +10% for the other VER profiles. Data sets of T, $[N_2]$ and $[O_2]$ were obtained using the NRLMSISE-00 model and perturbed by 5%: +5% for the T values and -5% for the sum of the $[N_2]$ and $[O_2]$ values. Profiles of $[O(^3P)]$ differences determined by perturbing VER profiles are shown by colored symbols, those determined by perturbing T profiles by solid gray lines, and those determined by perturbing $([N_2] + [O_2])$ profiles by dashed gray lines. Each retrieval step is indicated by the name of the corresponding *in-situ* ETON VER profile shown in the upper right corner of each panel.



4 Discussion of the obtained results

In-situ measurements obtained during the ETON campaign enable estimating the efficiency of $[O(^3P)]$ retrievals carried out using the well-known photochemical models and the proposed MAC model, see Section 3.4. For instance, Lednyts'kyy et al. (2015) considered O_2^* as the $O(^1S)$ precursor to retrieve the SCIAMACHY $[O(^3P)]$ time series, see Sections 3.1 and 3.4.

- 5 Further work discussed here and by Lednyts'kyy and von Savigny (2016) and Lednyts'kyy et al. (2018) validated suggestions and retrievals of Lednyts'kyy et al. (2015) carried out on the basis of various rocket campaigns that enabled proposing the MAC model. For instance, $O_2(cba, X)$ were adopted in the MAC model from the M- and H-models (see Sections 3.2.1 and 3.2.2, respectively) instead of O_2^* considered by Lednyts'kyy et al. (2015) in the G-model (see Section 3.1).

- Additionally to the excited singlet states $O_2(c, b, a)$, Huestis (2002) and Slanger et al. (2004b) considered $O_2(^5\Pi)$ and
 10 the triplet Herzberg states ($O_2(A)$ and $O_2(A')$) coupled with $O_2(c, b, a, X)$ which was also adopted in the MAC model. Specifically, processes coupling $O_2(^5\Pi, A, A', c, b, a, X)$ and $O(^1S, ^1D, ^3P)$ with each other were proposed as complementary processes in the MAC model. In fact, the removal of the $O_2(^5\Pi)-O_2(A, A')$ -group through collisions was suggested by Slanger et al. (2004b) and implemented in the MAC model implicitly by increasing the association rates of $O_2(b, a, X)$ in
 15 the three-body recombination reactions. This was done implicitly because reactions including $O_2(^5\Pi)$ are not well known, e.g., compare Krasnopolsky (2011) and Krasnopolsky (1986). It should be noted that $O_2(^5\Pi)$ has a shorter lifetime and a higher energy compared to the other states $O_2(A, A', c, b, a, X)$ as it was also mentioned by Huestis (2002) and Slanger et al. (2004b).

- The removal of the $O_2(^5\Pi)-O_2(A, A')$ -group and the weak coupling of the $O_2(A, A')$ triplet states with the $O_2(c, b, a)$ singlet states enabled omitting the $O_2(A, A')$ states in the MAC model. There are three reasons for the weak coupling of the
 20 $O_2(A, A')$ triplet states with the $O_2(c, b, a)$ singlet states. Firstly, the $O_2(A)$ and $O_2(A')$ states are strongly coupled with each other because vibrational states of these triplet states are energetically very close to each other. Vibrational states of these triplet states and the $O_2(c)$ singlet state are also very close to each other, but the spin flip energy is required for transitions from these triplet states to the $O_2(c)$ singlet state. Secondly, the probability of transitions from $O_2(A, A')$ to $O_2(b, a)$ is supposed to be negligibly higher than that of transitions to $O_2(X)$ because of Franck-Condon factors. Considering internuclear distances
 25 (INDs) of the corresponding Franck-Condon factors, it should be emphasized that the difference in INDs between the excited $O_2(A)$ state and the ground $O_2(X)$ state is approximately equal to the difference in INDs between the excited $O_2(A')$ state and the ground $O_2(X)$ state. Additionally, the difference in INDs between the excited $O_2(b)$ state and the ground $O_2(X)$ state is approximately equal to the difference in INDs between the excited $O_2(a)$ state and the ground $O_2(X)$ state. Thirdly, the probability of transitions from $O_2(A, A')$ to $O_2(X)$ is supposed to be significantly higher than that of transitions to $O_2(b, a)$
 30 because of a required spin flip. Note that data about INDs and Franck-Condon factors are used to calculate the transition intensities (Hollas, 2004). Therefore, we conclude that transitions from $O_2(A, A')$ to $O_2(X)$ are more probable than transitions from $O_2(A, A')$ to $O_2(c, b, a)$.

It should be kept in mind during the interpretation of the obtained results that the uncertainties of the ETON data sets are 10...20% in VER peak values, see Section 2). Varying the MAC input data within these uncertainty ranges significantly



influences the magnitude of products obtained with the MAC model. For example, the retrieved $[O(^3P)]$ peak values increase by up to 40% if VER values are increased by 10% due to the VER uncertainty, compare Figs. 6 and 3. Additionally, uncertainty in the *in-situ* $[O(^3P)]$ profile values of less than about 40% in $[O(^3P)]$ peak values is very high implying that novel *in-situ* data sets obtained with more accurate measurement techniques should be measured in the future. In fact, the ETON *in-situ* measurements were used to tune unknown or poorly constrained rate values of the complementary processes, and the importance of precise *in-situ* measurements is tremendous. Nevertheless, rate values of the processes implemented in the MAC model are considered to be validated through a comparison of the *in-situ* and retrieved $[O(^3P)]$ profiles. In the following three sections we discuss the tuning based on the ETON data set.

4.1 Discussion of tuned rate values of quenching processes implemented in the MAC model

All processes of the MAC model are provided in Section 3.3. These processes were separated into four groups: those considered in the G-, M- and H-models as well as those considered as complementary processes completing the MAC model and denoted as C-processes. Unknown or poorly constrained reaction rate values of the C-processes were tuned comparing (1) retrieved and evaluated concentrations of excited chemical species, (2) *in-situ* and evaluated VER profiles as well as (3) *in-situ* and retrieved $[O(^3P)]$ profiles. The validation procedure is related to the comparison of $[O(^3P)]$ profiles, and the verification procedure is related to the comparison of the other profiles, see Section 3.4. The verification and validation results support the use of the adjusted reaction rates provided in Tables 9 ... 12.

As it was mentioned in Section 2, unknown or poorly constrained reactions in the MAC model were tuned on the basis of the ETON *in-situ* measurements and applied to data sets measured during the WADIS-2, WAVE2000 and WAVE2004 campaigns, see the next article to be submitted. Dr. Fytterer and Dr. Sinnhuber from the Karlsruhe Institute of Technology suggested the rate values of the reactions $R_{b2.1}$, $R_{b4.1}$, $R_{b6.0}$, $R_{r1.2}$ and $R_{r2.3}$ for the data sets of the WAVE2004 campaign. The other reaction rates were adjusted on the basis of the described verification and validation procedures. Particularly, the $R_{a2.2}$ reaction rate was also adjusted within the range provided by Burkholder et al. (2015), who gave the upper limit of this reaction. Rate values of the reactions $R_{t10.1}$, $R_{d9.1}$ and $R_{c2.1}$ regarding the $O(^1S)$ production were adjusted taking studies of Krasnopolsky (2011), Huang and George (2014), Steadman and Thrush (1994) and Torr et al. (1985) into account. The adjustment of rate values of the three-body recombination reactions is described in Section 4.2.

The tuning of the rate coefficients was carried out by changing the values of dimensionless scaling factors (cTDu, cTCu, cTBu, cTAu, cDCu, cDBu, cDAu, cCBa, cCBm, cCAa, cCAm, cBAa, cBAm and cAXa shown in Tables 9 ... 12), which are multiplied with the corresponding rate coefficients and describe the strength of the coupling among O_2 states as follows:

1. cTDu is for coupling of $O_2(A)$ and $O_2(A')$, cTCu – $O_2(A)$ and $O_2(c)$, cTBu – $O_2(A)$ and $O_2(b)$, cTAu – $O_2(A)$ and $O_2(a)$.
2. cDCu is for coupling of $O_2(A')$ and $O_2(c)$, cDBu – $O_2(A')$ and $O_2(b)$, cDAu – $O_2(A')$ and $O_2(a)$.



3. cCBa is for coupling of $O_2(c)$ and $O_2(b)$ by quenching of $O_2(c)$ with $O(^3P)$, cCBm – $O_2(c)$ and $O_2(b)$ by quenching of $O_2(c)$ with $O_2(X)$, cCAa – $O_2(c)$ and $O_2(a)$ by quenching of $O_2(c)$ with $O(^3P)$, cCAm – $O_2(c)$ and $O_2(a)$ by quenching of $O_2(c)$ with $O_2(X)$.
4. cBAa is for coupling of $O_2(b)$ and $O_2(a)$ by quenching of $O_2(a)$ with $O(^3P)$, cBAm – $O_2(b)$ and $O_2(a)$ by quenching of $O_2(b)$ with $O_2(X)$.
5. cAXa is for coupling of $O_2(a)$ and $O_2(X)$ by quenching of $O_2(a)$ with $O(^3P)$.

Values of these scaling factors were altered to determine their influence on $[O^{\text{current}}]$ calculating differences with respect to $[O^{\text{reference}}]$ retrieved without adjusting these scaling factors. The differences were calculated according to Eq. (5) and used in the sensitivity analysis, the results of which are given by the interval of possible rate values shown in the third column of Tables 9 ... 12. For instance, perturbations in cTDu values do not cause changes in retrieved and evaluated MAC output parameters. Therefore, the tested interval is shown as $cTDu \in [1 \cdot 10^{-30}, 1 \cdot 10^{30}]$ in Table 9, and cTDu is set to an arbitrary value of $cTDu = 1 \cdot 10^{-2}$.

Additionally, the rate value of the $R_{a2.2}$ reaction was adjusted in the interval $cAXa \in [1 \cdot 10^{-30}, 1 \cdot 10^{-2}]$ of possible values multiplied by $2 \cdot 10^{-16} \text{ molec}^{-1} \text{ cm}^3 \text{ s}^{-1}$ and applied at the retrieval step 3.2 shown in Table 8. This adjustment of the scaling factor cAXa is allowed because $R_{a2.2} = 2 \cdot 10^{-16} \text{ molec}^{-1} \text{ cm}^3 \text{ s}^{-1}$ is given by Burkholder et al. (2015) as the upper interval value. A $R_{a2.2}$ reaction rate of higher than $R_{a2.2} = 2 \cdot 10^{-17} \text{ molec}^{-1} \text{ cm}^3 \text{ s}^{-1}$ seems by sight to cause higher $[O(^3P)]$ peak values than those obtained with $R_{a2.2} = 2 \cdot 10^{-18} \text{ molec}^{-1} \text{ cm}^3 \text{ s}^{-1}$. Therefore, $cAXa = 1 \cdot 10^{-2}$ is used so that the $R_{a2.2}$ reaction rate equal to $2 \cdot 10^{-18} \text{ molec}^{-1} \text{ cm}^3 \text{ s}^{-1}$ is employed in the MAC model.

4.2 Discussion of the obtained results regarding tuned rate values for implemented three-body recombination processes

This section continues reporting about adjusting unknown or poorly constrained reaction rate values.

The MAC model was proposed on the basis of the hypothesis of Huestis (2002) and Slanger et al. (2004b), who stressed that association rates of excited O_2 states in the three-body recombinations must be modified because O_2 molecules in various excited states collide with each other and other molecules so that an excitation transfer takes place. However, Huestis (2002) and Slanger et al. (2004b) did not provide modified association rates. This was also emphasized by Krasnopolsky (2011), who applied the two-step Barth excitation transfer scheme for each of the ETON VER profiles separately. Thus, Krasnopolsky (2011) substantially limited the number of the considered chemical reactions related to $O_2(^5II)$ comparing to Krasnopolsky (1986). Because the lifetime of $O_2(^5II)$ is less than $\sim 0.4 \mu\text{s}$ (Slanger and Copeland, 2003), it is impossible to determine a number of reaction rates involving $O_2(^5II)$ in the laboratory. For this reason reactions involving $O_2(^5II)$ cannot be adequately included in chemical-dynamic time-dependent atmospheric models. Nevertheless, the association rate values of O_2 states were tuned with the use of the hypothesis of Slanger et al. (2004b) to apply them in the MAC model as follows. Firstly, the theoretically known association rates (Bates, 1988a) were considered. Then, they were used to obtain the new association rate values of $O_2(b, a, X)$, see the respective yielding factors bY , aY and xY in Tables 10 and 11. Specifically, values of the known



association rates were increased using the association rate (pY) of $O_2(^5\Pi)$. For instance, the association rate of $O_2(b)$ was increased by an arbitrary value of 7% of the pY value to determine a new value of bY . In a similar way, the association rates of $O_2(a)$ and $O_2(X)$ were increased by arbitrary values of 68% and 25% of the pY value to determine new values of aY and xY , respectively.

- 5 It should be noted that Bates (1988a) provided the association rates for $O_2(^5\Pi, A, A', c, b, a, X)$ applying the concept of a hard-sphere to the reaction rates in the three-body recombinations ($O(^3P) + O(^3P) + \{N_2, O_2\}$) as it was done by Bates (1951), Wraight (1982) and Smith (1984). It is remarkable that N_2 was used as the third body in laboratory studies and that the reaction rate of the three-body recombination updated by Smith and Robertson (2008) is lower than that one provided by Campbell and Gray (1973) above 200 K and higher below 200 K. Nevertheless, Campbell and Gray (1973) and Smith and Robertson (2008)
- 10 assumed the obtained reaction rate ($\chi_{N_2}^{Px}$) to be equal to that one ($\chi_{O_2}^{Px}$) considering O_2 as the third body because of the used hard-sphere concept. Unfortunately, neither $\chi_{O_2}^{Px}$ nor $\chi_{N_2}^{Px}$ is provided in the established studies on chemical kinetics, e.g. the Jet Propulsion Laboratory databases (Burkholder et al., 2015). It is worth being mentioned that Bates (1979) interpreted the Chapman excitation process as follows: two colliding $O(^3P)$ atoms create an electronically excited O_2 molecule, which is presumably in the upper Herzberg state (Greer et al., 1987), see Section 1 for details. This altogether implies that an interaction
- 15 of O_2 in the ground or excited states with one or more $O(^3P)$ atoms is a complicated process worth of further investigation, and the hard-sphere concept should be used with caution.

There are two main adjustments done in the MAC model with respect to the three-body recombinations. The first one is related to the increased association rates of $O_2(b, a, X)$ taking collisions of higher excited O_2 molecules with $O_2(^5\Pi)$ into account and being implicitly considered in the MAC model. The second one is related to the increase of $\chi_{O_2}^{Px}$ compared

20 to $\chi_{N_2}^{Px}$ of the reactions $R_{x1.2}$ and $R_{x1.1}$, respectively. This adjustment was done because the used hard-sphere concept is probably misleading and because other $O(^3P)$ loss processes were required to be implemented in the MAC model implicitly according to the verification and validation procedures. The origin of the required $O(^3P)$ loss processes is currently not known definitely because both photochemical and dynamical phenomena might contribute to the total $O(^3P)$ loss. Note that the O_2 photodissociation into $O(^3P)$ atoms has its maximum at ~ 120 km according to Solomon and Qian (2005), and Colegrove et al.

25 (1965) invoked eddy diffusion to describe the $O(^3P)$ loss by transport from the lower thermosphere downwards.

Two cases are considered adjusting rate values of the $R_{x1.1-2}$ reactions considered in the MAC model. In the first case the $\chi_{O_2}^{Px}$ rate value is multiplied by $\sim 3.56 \cdot 10^4$, and the $\chi_{N_2}^{Px}$ rate value is left to be equal to that one given by Smith and Robertson (2008). The first case is used as the standard case of using the $R_{x1.1-2}$ reactions in the MAC model. In the second possible case used optionally both rate values ($\chi_{O_2}^{Px}$ and $\chi_{N_2}^{Px}$) are multiplied by $7.67 \cdot 10^3$. The $R_{x1.1-2}$ reactions are only involved in the last

30 $[O(^3P)]$ retrieval step considering all chemical species. The rate values of the $R_{x1.1-2}$ reactions were tuned and applied on the basis of the *in-situ* data sets obtained during the ETON and WAVE2004 campaigns described in Section 2. The dependence of $[O(^3P)]$ values on $O(^3P)$ loss processes is very high at the last retrieval step 5.1 because the $R_{x1.1-2}$ reactions are taken into account in the continuity equations at this step.

It should be noted that $[O(^3P)]$ values retrieved at the steps 2.1, 2.2, 2.3, 3.1, 3.2 and 4.1 significantly depend on perturbations

35 in VER values. As for the last retrieval step 5.1, concentrations of chemical species are retrieved at this step at first, and



$[O(^3P)]$ values are retrieved afterwards. It follows from the discussion of Fig. 6 that the dependence of $[O(^3P)]$ values on VER values used at the current step, e.g. the step 4.1, at which VER values belong to the MAC input parameters, is lower than the dependence of $[O(^3P)]$ values on VER values used at the previous steps.

In summary, the verification and validation procedures based on the comparison of the *in-situ* $O(^3P)$ profile with several $O(^3P)$ profiles retrieved at the steps 2.1, 2.2, 2.3, 3.1, 3.2, 4.1 and 5.1 support the complementary reactions considered in the continuity equations, see Appendix A. This implies that additional $O(^3P)$ loss processes considered by the $R_{x1.1-2}$ reactions implicitly are supported by calculations carried out with the MAC model, see also the next section.

4.3 Discussion of the causes responsible for additional $O(^3P)$ loss processes

This section deals with additional $O(^3P)$ loss processes implicitly considered in the MAC model by the $R_{x1.1-2}$ reactions according to the description provided in the previous section. Continuity equations implemented in the MAC model include the production and loss terms of various chemical species. The mentioned additional $O(^3P)$ loss processes concluded using results obtained at the last $[O(^3P)]$ retrieval step 5.1 were validated on the basis of all results obtained with the MAC model at each of the retrieval steps. Unfortunately, there are not enough data to quantify contributions of the diffusive velocities (molecular and turbulent ones) and the Eulerian mean velocity in the considered continuity equations to the transport of various chemical species. For instance, the molecular diffusive velocity may contribute to the additional $O(^3P)$ loss processes. Processes of atmospheric dynamics (damped atmospheric gravity waves, tides and advection) significantly contribute to the transport processes (Smith et al., 1987; Johnson and Gottlieb, 1973). Atmospheric dynamics responsible for the Eulerian mean velocity and the turbulent diffusive velocity would influence all chemical species considered in a continuity equation. As far as temperature, $[N_2]$ and $[O_2]$ are obtained with the NRLMSISE-00 model for the ETON campaign, these transport velocity components are not discussed in this article. Instead, they are discussed in our next article describing the WADIS-2, WAVE2000 and WAVE2004 campaigns.

The maximum of the O_2 photodissociation into $O(^3P)$ atoms is at ~ 120 km (Solomon and Qian, 2005). Shematovich et al. (2011) and Wei et al. (2014) discussed the ionized $O(^3P)$ drag to outer space. This drag might play a relatively negligible role at normal solar activity and atmospheric conditions due to a low-rate production of the ionized $O(^3P)$ from inelastic collisions involving $O(^3P)$ atoms. Colegrove et al. (1965) discussed the downward $O(^3P)$ transport from the lower thermosphere. The total downward $O(^3P)$ transport was explained by Colegrove et al. (1965) to occur due to high values of the diffusive transport velocity. Note that Grygalashvyly et al. (2012) and Qian et al. (2009) also derived relatively high values of the diffusive transport velocity in the MLT region comparing to those of Swenson et al. (2018).

The molecular diffusion velocity was emphasized in Brasseur and Solomon (2005) on page 138 to occur because of elastic collisions between particles and taking into account the effect of thermal diffusion, whereas reactive collisions were neglected. The issue regarding reactive collisions was discussed in Section 1 with respect to difficulties calculating the respective rate coefficients. In fact, it is even difficult to address the static and combined quenching processes in the laboratory, where dynamic quenching processes are often studied with the use of the Stern-Volmer method Lakowicz (2006). For instance, a tetraoxygen molecule, the chemistry of which is not well known because it had been detected by Cacace et al. (2001) recently, may be



produced from reactive collisions involving $O(^3P)$. It can be concluded that reactive collisions are not considered in the steady state continuity equations applied in the MAC model, but they should be taken into account. Therefore, a temporary solution was introduced to implement possible $O(^3P)$ loss processes discussed in the previous section implicitly, i.e. simply increasing the rate value of the three-body recombination reaction with O_2 as a third body.

5 4.4 Discussion of the obtained results regarding the $O(^1S)$ precursor

Preliminary conclusions about the origin of the $O(^1S-^1D)$ green line emission are drawn on the basis of the VER and $[O(^3P)]$ profiles shown on the left in Figs. 3, 4 and 5 compared with each other in Section 3.4. As far as the shown VER and $[O(^3P)]$ profiles retrieved via different pathways indicated in Figs. 1 and 2 seem to be in perfect agreement with each other, it was concluded that the contribution of processes involving $O_2(A)$ and $O_2(A')$ to the $O(^1S)$ production is negligible, and $O_2(c)$ was considered to be the major $O(^1S)$ precursor.

We start the discussion regarding the $O(^1S)$ precursor with two main findings and finish with considering arguments published previously.

Firstly, the MAC model is based mainly on the two-step Barth excitation transfer schemes which requires to consider the $O(^1S)$ precursor, see Sections 1 and A. The nature of the oxygen green line emission was investigated by many atmospheric scientists on the basis of *in-situ* airglow measurements by tuning the reaction rates including the $O(^1S)$ precursor as a not identified O_2^* state and the comparison of these rates with the ones measured in a ground-based laboratory. It can be assumed that the deduced O_2^* corresponds to an excited O_2 in a specific state or a group of O_2 states according to Huestis (2002). However, the hypothesis of Huestis (2002) was refuted by Slanger et al. (2004b).

Secondly, the Barth excitation transfer scheme was implemented in the MAC model sequentially considering $O_2(A)$, $O_2(A')$ and $O_2(c)$ as multiple $O(^1S)$ precursors according to Slanger et al. (2004b). It should be noted that $O_2(A)$, $O_2(A')$ and $O_2(X)$ are triplet states, and $O_2(c)$ is a singlet state. The verification and validation results shown in Section 3.4 enable separating MAC processes in two groups related to $O_2(^5\Pi, A, A', c, b, a, X)$ and $O(^1S, ^1D^3P)$ as well as related to $O_2(^5\Pi, c, b, a, X)$ and $O(^1S, ^1D^3P)$. This conclusion reflects the importance of the ETON rocket campaign (Greer et al., 1986) for identifying the $O(^1S)$ precursor.

$O_2(c)$ was proposed by Solheim and Llewellyn (1979), Llewellyn et al. (1980) and Krasnopolsky (1981) to be the $O(^1S)$ precursor on the basis of the electron-impact excitation spectrum of O_2 determined by Trajmar et al. (1972) and Stern-Volmer relations. As far as the results of Trajmar et al. (1972) are also valid for $O_2(^5\Pi)$, Krasnopolsky (1986) and Krasnopolsky (2011) proposed $O_2(^5\Pi)$ to be a possible $O(^1S)$ precursor. Nevertheless, $O_2(A)$ was concluded by Krasnopolsky (2011) to be the most probable $O(^1S)$ precursor according to experimental measurements of Stott and Thrush (1989) and Steadman and Thrush (1994).

Stott and Thrush (1989) excluded $O_2(^5\Pi)$, $O_2(A', \nu = 2-4)$ and $O_2(c, \nu = 0)$ from the list of possible $O(^1S)$ precursors and concluded that $O_2(A, \nu \geq 5)$ is the $O(^1S)$ precursor. Various arguments were provided Stott and Thrush (1989) on the basis of results obtained with the use of the Stern-Volmer relationship applied for each of the possible $O(^1S)$ precursors. Some of the arguments against $O_2(c)$ were based on the quenching of the triplet $O_2(A, A')$ states converting to the singlet $O_2(b, a)$



states. The validity of this argument was tested in the MAC model implementing the $O_2(A)$ quenching to $O_2(b)$ by using the $R_{t4.1-3}$ reactions, the $O_2(A)$ quenching to $O_2(c)$ by using the $R_{t3.1-3}$ reactions, and the $O_2(A)$ quenching to $O_2(a)$ by using the $R_{t6.1-3}$ reactions. The results of the sensitivity analysis discussed in Section 4.1 show that these reactions can be neglected in the MAC model, see Tables 5 and 9. Similarly, the $O_2(A')$ quenching to $O_2(c, b, a)$ implemented in the reactions $R_{d2.1-2}$, $R_{d3.1-2}$ and $R_{d4.1-2}$ can be also neglected in the MAC model. Quenching of the triplet $O_2(A, A')$ states to the singlet $O_2(b, a)$ states requires the spin flip that is energetically not favorable, and the arguments of Stott and Thrush (1989) can be considered as refuted. Therefore, $O_2(c, \nu \geq 2)$ can be considered the $O(^1S)$ precursor.

Steadman and Thrush (1994) excluded $O_2(A', c)$ from the list of possible $O(^1S)$ precursors and concluded that $O_2(A, \nu \geq 6)$ is the $O(^1S)$ precursor. As for the Franck-Condon factors in the $O_2(A-X)$ transitions, they were emphasized by Krasnopolsky (2011) to be low, so that $O_2(A, \nu \leq 5)$ in low vibrational levels does not seem to be an effective transition path of producing $O(^1S)$ from $O(^3P)$. The arguments provided by Steadman and Thrush (1994) against $O_2(A', c)$ as the $O(^1S)$ precursors were based on the general idea that the $O_2(A'^3\Delta_u)$ and $O_2(c^1\Sigma_u^-)$ quenching to $O_2(X^3\Sigma_g^-)$ is not symmetry allowed, but the $O_2(A^3\Sigma_u^+)$ quenching to $O_2(X^3\Sigma_g^-)$ is symmetry allowed. The validity of this argument was tested in the MAC model implementing the $O_2(A', c)$ quenching to $O_2(X)$ by using the reactions $R_{d9.1}$ and $R_{c2.1}$.

Steadman and Thrush (1994) suggested that if $O_2(c)$ is considered to be the $O(^1S)$ precursor, then it is probably at the vibrational state $\nu = 8$ because of the favorable Frank-Condon factors for transitions to vibrational states of the electronic O_2 ground state $O_2(X)$. Krasnopolsky (1981) also considered $O_2(c)$ as the $O(^1S)$ precursor on the basis of observations in the atmospheres of Venus and Mars, where $O_2(c)$ is in the vibrational ground state $\nu = 0$. Krasnopolsky (1981) concluded that the activation energy of $2.1 \text{ kcal mol}^{-1}$ is required for quenched $O_2(c, \nu = 0)$ molecules to produce $O(^1S)$. Altitude profiles of the fractional $O_2(c)$ vibrational populations with $\nu = 3 \dots 10$ are characterized by various peak altitude values in the altitude range $80 \dots 120 \text{ km}$, where they were derived by Llewellyn and McDade (1984) from a model by using reaction rate values given by Kenner and Ogryzlo (1983). The $[O_2(c, \nu = 6)]$ peak is at 94 km , and the $[O_2(c, \nu = 8)]$ peak is at 103 km according to the results of atmospheric modeling shown in Fig. 5 in Llewellyn and McDade (1984). These results enable determining the peak of $[O_2(c, \nu = 7)]$ at about 97 km , where the green line emission peak is, see Table 1. Additionally, the modeling results obtained by López-González et al. (1992a) and shown in their Fig. 6c indicate that the $[O_2(c, \nu = 6)]$ peak is at about 97 km . Stott and Thrush (1989) compared results obtained with laboratory experiments and atmospheric models (their Fig. 10) and found that the maximum of the relative vibrational $O_2(A)$ population is at $O_2(A, \nu = 2, 3)$ in laboratory experiments and at $O_2(A, \nu = 5)$ in model results. It follows that the maximum of the relative vibrational $O_2(c)$ population found in laboratory experiments might differ from the respective model results published in, e.g., Llewellyn and McDade (1984) and López-González et al. (1992a).

It is difficult to argue about the fractional $O_2(c)$ vibrational population of the $O(^1S)$ precursor because the $[O_2(c, \nu = 6, 7, 8)]$ peak might be at about 97 km altitude if the collisional activation energy mentioned by Krasnopolsky (1981) is neglected.



5 Conclusions

Photochemical processes in the altitude range 80...105 km were modeled considering seven states of molecular oxygen, $O_2(^5\Pi, A, A', c, b, a, X)$, and three states of atomic oxygen, $O(^1S, ^1D, ^3P)$. The Multiple Airglow Chemistry (MAC) model was proposed to explain the excitation mechanisms responsible for observed airglow. Processes of the photochemical models discussed in Sections 3.1, 3.2.1 and 3.2.2 were combined with complementary processes suggested to complete the list of processes implemented in the MAC model. Additional processes were proposed to couple the mentioned O_2 states and to implement the $O_2(^5\Pi)-O_2(A, A', c)$ -group in the MAC model according to the hypothesis of Slanger et al. (2004b). *In-situ* VER profiles obtained during the ETON campaign were applied to determine unknown or poorly constrained reaction rates and update known ones considered in the MAC model, see Sections 4.1, 4.2 and 4.3. Note that *in-situ* VER profiles obtained during the WADIS-2, WAVE2000 and WAVE2004 campaigns were applied to validate these reaction rates used in calculations carried out with the MAC model, see future publications. We would like to emphasize that the agreement between $[O(^3P)]$ profiles obtained at various retrieval steps and the corresponding *in-situ* $[O(^3P)]$ profiles for these three campaigns is perceived as significantly better than that for the ETON campaign. The proposed algorithm enabled calculating concentrations of such coupled minor species as $O_2(A, A', c, b, a)$ and $O(^1S, ^1D, ^3P)$ for the first time.

The integrity of the O_2 electronic states' identity formulated in the hypothesis of Huestis (2002) was refuted by Slanger et al. (2004b) which hinders representing the $O(^1S)$ precursor by O_2^* as it was done in Lednyts'kyy et al. (2015). Nevertheless, the $[O(^3P)]$ retrievals performed by Lednyts'kyy et al. (2015) according to the well-known and extended cubic equations were validated using the *in-situ* $[O(^3P)]$ measurements, see Sections 3.1 and 3.4. As for calculations with the MAC model, a consistent explanation of the origin of each of the considered airglow emissions, including the famous oxygen green line emission, was proposed. Specifically, the precursors of $O_2(b)$, $O_2(a)$ and $O(^1S)$ were identified and confirmed during the verification and validation procedures provided in Section 3.4. Firstly, $O_2(c)$ and states of the $O_2(^5\Pi)-O_2(A, A')$ -group were found to be the $O_2(b)$ precursors responsible for Atmospheric band emissions. Secondly, $O_2(c)$, $O_2(b)$ and states of the $O_2(^5\Pi)-O_2(A, A')$ -group were found to be the $O_2(a)$ precursors responsible for Infrared Atmospheric band emissions. Finally, $O_2(c)$ was found to be the major $O(^1S)$ precursor responsible for the oxygen green line emission, whereas the contribution of $O_2(A, A')$ was found to be negligible. Note that all states from the $O_2(^5\Pi)-O_2(A, A')$ -group can be considered to be the $O_2(b, a, X)$ precursors because $O_2(^5\Pi)$ was implicitly used to calculate new association rate values of $O_2(b, a, X)$.

Convincing verification and validation results should be accepted critically because the tuned rate values were obtained on the basis of the *in-situ* measurements with uncertainties provided by Greer et al. (1986) and discussed in Section 2. The influence of variability was studied in various MAC input parameters, see Section 3.5. In summary, perturbations in temperature of 5% cause variations in $[O(^3P)]$ of about 10%, but perturbations in atmospheric density of 5% cause about 3% $[O(^3P)]$ variations. Uncertainties in such VER values as $VER\{O_2(A-X)\}$ and $VER\{O_2(A'-a)\}$ at the retrieval steps 2.1 and 2.2 cause up to about 40% of $[O(^3P)]$ variations, uncertainties in such VER values as $VER\{O_2(b-X)\}$ and $VER\{O_2(a-X)\}$ at the retrieval steps 2.3 and 3.2 cause about 12% of $[O(^3P)]$ variations, but uncertainties in such VER values as $VER\{O(^1S-^1D)\}$ at the retrieval step 4.1 cause up to about 20% of $[O(^3P)]$ variations.



The following four key findings required to develop the MAC model were proposed for the first time to the best of our knowledge. Firstly, the algorithm was proposed without using *a priori* data applied to initiate calculations with the MAC model. Instead, sequent retrieval steps were applied to solve the system of continuity equations starting calculations from higher excited species, and providing concentrations of excited species at the following retrieval steps. Each polynomial equation was solved separately to obtain concentrations of chemical species required for the next polynomial equations, which were sequentially introduced and solved to retrieve $[O(^3P)]$ profiles, see Table 8 for retrieval steps applied using the MAC model. Secondly, participation of $O_2(^5\Pi)$ in chemical reactions was implemented implicitly adjusting the association rates of $O_2(b, a, X)$ (Bates, 1951) by using the value of the $O_2(^5\Pi)$ association rate. Thirdly, the singlet $O_2(c, b, a)$ excited states and the triplet $O_2(A, A', X)$ states as well as $O(^1S, ^1D, ^3P)$ states were identified and treated in the MAC model explicitly. Fourthly, calculations carried out using the MAC model were consistently verified for each considered ETON VER profile, and validated for each $[O(^3P)]$ retrieval step, see Section 3.4. The proposed algorithm also enables applying the MAC model on the basis of a $VER\{O_2(b - X)\}$ profile only, as the $[O(^3P)]$ retrieval results show in Fig. 5.

The proposed algorithm used to solve the system of continuity equations also enabled introducing perturbations in tuned rate values that was studied in their the impact on the MAC output parameters. The results of the sensitivity analysis enable neglecting not important processes coupling O_2 states, see the third column of Tables 9 ... 12 for interval values of the tuned reaction rates. For instance, transitions from the triplet $O_2(A, A')$ states to the singlet $O_2(c, b, a)$ states were found to be not intense and less probable than transitions from these excited triplet and singlet states to the triplet $O_2(X)$ ground state. This might be explained by the energy required for the spin flip during transitions between one triplet and one singlet states.

The following conclusions can be drawn from the results of the sensitivity analysis. Firstly, the triplet $O_2(A, A')$ states can be neglected in the MAC model because of their strong coupling with the ground triplet $O_2(X)$ state. Then, the following correspondences among the violated electric dipole selection rules and the transition intensity seem to be established. Collisional deactivation processes implemented in the MAC model involving $O_2(A)$ and $O_2(A')$ were found (1) strong between $O_2(c^1\Sigma_u^-)$ and $O_2(b^1\Sigma_g^+)$, (2) weak between $O_2(A'^3\Delta_u)$ and $O_2(c^1\Sigma_u^-)$, (3) almost absent between $O_2(A'^3\Sigma_u^+)$ and $O_2(A'^3\Delta_u)$ as well as $O_2(c^1\Sigma_u^-)$ and $O_2(a^1\Delta_g)$. These three findings are summarized with respect to the violation of the electric dipole selection rules as follows: $\Sigma^+ \leftrightarrow \Sigma^-$ and $\Delta\Lambda = 0, \pm 1$. In fact, the violation of the $\Sigma^+ \leftrightarrow \Sigma^-$ selection rule (1) describes the change of the wave function's sign by reflection in a plane containing the internuclear axis (Bates, 1962) and (2) seems to lead to relatively intense transitions in the O_2 band systems. The violation of the $\Delta\Lambda = 0, \pm 1$ selection rule (1) describes the orbital (or azimuthal) angular momentum Λ and (2) seems to lead to weak or no transitions in the O_2 band systems.

Two topics can be emphasized regarding open tasks of further research. Firstly, the MAC model should be extended to consider various vibrational O_2 and OH^* states because the MAC model was implemented with the use of the Local Thermodynamic Equilibrium (LTE) approximation and only a few O_2 and OH^* vibrational states were considered analyzing the ETON multiple emissions. This requires the use of the non-LTE approximation, see Sections 3.2.1 and 4.2 for details, but will possibly result in the $O(^3P)$ loss. Specifically, the MAC model will be extended to consider the $[O(^1D)]$ and $[O(^3P)]$ retrieval on the basis of measured $VER\{O(^1D - ^3P)\}$ profiles because of the role of the transient HO_2^* complex emphasized in the end of Section 3.4 and required to implement various OH^* vibrational states.



Code availability. The algorithm described in this study is available to the community and may be obtained by contacting the lead author of this article.

Appendix A: Algorithmic steps of the Multiple Airglow Chemistry model development

The retrieval steps of $[O(^3P)]$ are closely related to the development of the MAC model. For instance, the well-known photo-chemical model of McDade et al. (1986) is applied at the 1st substep of the 1st step (see Section A1.1) to retrieve $[O(^1S)]$ as a part of the prior retrieval procedure. Then simple continuity equations are applied in the prior retrieval procedure to retrieve $[O(^1D)]$ (see Section A1.2) as well as $[OH^*]$ and $[HO_2]$ (see Section A1.3). The next retrieval steps are provided with the results obtained from the prior retrieval procedure and described in the appendix starting from Section A2. An overview of these sequentially applied retrieval steps is provided in Section 3.4 in Table 8 for the MAC model.

Note that calculations of the prior retrieval procedure (see Section A1) are omitted in this study because neither the ETON campaign nor the NRLMSISE-00 model provide concentrations of chemical species required at this step. This implies that values of $[O_3]$, $[CO_2]$, $[O(^1D)]$, $[OH^*]$ and $[HO_2]$ included in calculations of the next retrieval steps (see Section A2 and the following sections) are equal to zero values.

Processes of the MAC model are described in the following sections according to the models, processes of which were adopted in the MAC model. For instance processes of the M-model (see Section 3.2.1) are marked with a character M, those of the H-model (see Section 3.2.2) are marked with a character H and the other (complementary) processes completing the development of the MAC model are marked with a character C. The complementary (or completing) processes are related to processes of the G-model, see Section 3.1, processes introduced to implement the hypothesis of Slanger et al. (2004b) and other processes coupling O_2 states with each other, see Section 3.3. For instance, $O_2(A)$ is only considered in complementary processes, and $[O_2(A)]$ are marked as $[O_2(A)-C]$. Production and loss terms of $O_2(A)$ are also marked with a character C as $P\{O_2(A)-C\}$ and $L\{O_2(A)-C\}$, respectively.

There are three kinds of the MAC products:

1. Retrieved concentrations of chemical species obtained using all relevant reactions. Retrieved concentration profiles are marked with a character R, e.g. $R-[O_2(A)]$.
2. Evaluated concentrations of chemical species obtained dividing the R-VER profiles, which correspond to the particular chemical species, by the respective transition probability. Evaluated concentration profiles are marked with a character E, e.g. $E-[O_2(A)]$.
3. Evaluated VER values obtained dividing the retrieved concentrations of the respective same chemical species by the respective transition probability. Evaluated VER profiles are marked with a character E, e.g. $E-VER\{O_2(A-X)\}$.



A1 The 1st retrieval step

The 1st retrieval step was performed at three substeps to calculate $[O(^1D)]$, $[OH^*]$ and $[HO_2]$ prior values. As for this study, this step was omitted for retrievals on the basis of measurements obtained *in-situ* during the ETON campaign, see Section 2, because profiles of temperature, $[N_2]$ and $[O_2]$ were obtained using the NRLMSISE-00 model. Nevertheless, measurements
 5 obtained remotely and *in-situ* during the WAVE2004 campaign described in the next publication provide data sets required in the prior retrieval to apply the MAC model.

The processes shown in Tables 2 (see Section 3.1) and A1 were used for retrievals at this step. Processes marked with a character P in these tables were not used as complementary processes proposing the MAC model. The resulting concentration values obtained at the prior retrieval step are also marked with the character P.

10 A1.1 Substep 1: prior retrieval of $[O(^1S)]$

The prior retrieval of $[O(^1S)]$ is performed according to the well-known cubic equation with empirical coefficients provided by McDade et al. (1986) on the basis of the *in-situ* $[O(^3P)]$ measurements.

A1.2 Substep 2: prior retrieval of $[O(^1D)]$

The prior retrieval of $[O(^1D)]$ is performed according to the corresponding continuity equation applied on the basis of $[O_3]$
 15 and $[CO_2]$ profiles.

The continuity equation for $[O(^1D)]$ includes the terms of the $[O(^1D)]$ production ($P\{O(^1D)\}$) and loss ($L\{O(^1D)\}$) as follows: $d[O(^1D)]/dt = P\{O(^1D)\} - L\{O(^1D)\} = 0$.

The production and loss terms were calculated according to the processes shown in Tables 2 and A1 as follows: $P\{O(^1D)\} = [O(^1S)](2R_{g1.1}[O(^3P)] + R_{g3.0}) + R_{s1.1-2}[O_2] + R_{s2.1}[O_3]$ and $L\{O(^1D)\} = [O(^1D)] \times D_r$, where the destruction term
 20 $D_r = R_{r1.1-3}\{[O(^3P)], [O_3], [O_3]\} + R_{r2.1-4}\{[N_2], [O_2], [O_2], [CO_2]\} + R_{r3.0}$.

The prior retrieval results in $[O(^1D)]$ profile values as follows:

$$P\text{-}[O(^1D)] = [O(^1D)] = ((2R_{g1.1}[O(^3P)] + R_{g3.0})[O(^1S)] + R_{s1.1-2}[O_2] + R_{s2.1}[O_3]) / D_r.$$

A1.3 Substep 3: prior retrieval of $[OH^*]$ and $[HO_2]$

25 The prior retrieval of $[OH^*]$ and $[HO_2]$ is performed according to the corresponding continuity equations applied on the basis of $[O_3]$, $[H]$ and $[O(^3P)]$ profiles.

The continuity equation for $[OH^*]$ including terms of the $[OH^*]$ production ($P\{OH^*\}$) and its loss ($L\{OH^*\}$) is as follows: $d[OH^*]/dt = P\{OH^*\} - L\{OH^*\} = 0$. The production and loss terms were calculated according to the processes shown in Tables 2 and A1 as follows: $P\{OH^*\} = [H]R_{h1.1}[O_3] + [H]2R_{h6.1}[HO_2] + [O(^3P)]R_{h4.1}[HO_2] = [OH^*] \times D_h$, where $D_h =$

30 $R_{h3.1}[O_3] + R_{h2.1}[O(^3P)]$.



The continuity equation for $[\text{HO}_2]$ including terms of the $[\text{HO}_2]$ production ($P\{\text{HO}_2\}$) and its loss ($L\{\text{HO}_2\}$) is as follows: $d[\text{HO}_2]/dt = P\{\text{HO}_2\} - L\{\text{HO}_2\} = 0$. The production and loss terms were calculated according to the processes shown in Tables 2 and A1 as follows: $P\{\text{HO}_2\} = [\text{OH}^*]R_{h3.1}[\text{O}_3] + [\text{H}][\text{O}_2]R_{h5.1-2}\{[\text{N}_2], [\text{O}_2]\} = [\text{HO}_2] \times D_2$, where $D_2 = R_{h6.1-3}[\text{H}] + R_{h4.1}[\text{O}(^3P)]$.

- 5 The system of continuity equations for $[\text{OH}^*]$ and $[\text{HO}_2]$ was transformed in the system of the two following equations: $P\cdot[\text{OH}^*] = [\text{OH}^*] = \frac{[\text{H}]R_{h1.1}[\text{O}_3] + 2[\text{H}]R_{h6.1}[\text{HO}_2] + [\text{O}(^3P)]R_{h4.1}[\text{HO}_2]}{D_h}$ and $[\text{HO}_2] = \frac{[\text{OH}^*]R_{h3.1}[\text{O}_3] + [\text{H}][\text{O}_2]R_{h5.1-2}\{[\text{N}_2], [\text{O}_2]\}}{D_2}$ and solved for the values of $[\text{HO}_2]$. The obtained values of $[\text{HO}_2]$ were calculated as follows: $P\cdot[\text{HO}_2] = [\text{HO}_2] = ([\text{H}]R_{h1.1}[\text{O}_3] \cdot R_{h3.1}[\text{O}_3] + [\text{H}][\text{O}_2]R_{h5.1-2}\{[\text{N}_2], [\text{O}_2]\} \cdot (R_{h3.1}[\text{O}_3] + R_{h2.1}[\text{O}(^3P)])) / (D_2 D_h)$, where $D_2 D_h = R_{h3.1}[\text{O}_3] \cdot R_{h6.1-3}[\text{H}] + R_{h2.1}[\text{O}(^3P)] \cdot (R_{h6.1-3}[\text{H}] + R_{h4.1}[\text{O}(^3P)])$.

10 A2 The 2nd retrieval step

The 2nd retrieval step was performed within four substeps to calculate $[\text{O}_2(b)]$ values.

A2.1 Substep 1: retrieval of $[\text{O}_2(A)]$

- Herzberg I band emission measured at 320nm was used to retrieve $\text{VER}\{\text{O}_2(A-X)\}$ values and then to retrieve $[\text{O}(^3P)]$ values according to the continuity equation for $[\text{O}_2(A)]$, i.e. the quadratic equation with respect to $[\text{O}(^3P)]$. Then, $[\text{O}_2(A)]$ values were retrieved ($R\cdot[\text{O}_2(A)]$) on the basis of $[\text{O}(^3P)]$ values by using the continuity equation considering all relevant processes of the MAC model. The continuity equation for $[\text{O}_2(A)]$ including terms of the $[\text{O}_2(A)]$ production ($P\{\text{O}_2(A)\}$) and its loss ($L\{\text{O}_2(A)\}$) is as follows: $d[\text{O}_2(A)]/dt = P\{\text{O}_2(A)\} - L\{\text{O}_2(A)\} = 0$. The production and loss terms were calculated considering the processes shown in Tables 6 ... 5 as follows: $P\{\text{O}_2(A)\} = P\{\text{O}_2(A)\text{-C}\} = [\text{O}(^3P)]^2 R_{t1.1-2}\{[\text{N}_2], [\text{O}_2]\}$ and $L\{\text{O}_2(A)\} = L\{\text{O}_2(A)\text{-C}\} = [\text{O}_2(A)] \times D_t$, where $D_t = (R_{t2.1-3} + R_{t3.1-3} + R_{t4.1-3} + R_{t6.1-3} + R_{t7.1-3})\{[\text{O}(^3P)], [\text{N}_2], [\text{O}_2]\} + R_{t10.1}[\text{O}(^3P)] + R_{t5.0} + R_{t9.0}$. Complementary processes were used in the production and loss terms that is denoted with a character C. Therefore, $R\cdot[\text{O}_2(A)]$ is also marked with the character C instead of the character R as follows: $R\cdot[\text{O}_2(A)] = [\text{O}_2(A)\text{-C}] = P\{\text{O}_2(A)\text{-C}\} / D_t$. In the case when Herzberg I band emissions are not given, $[\text{O}_2(A)]$ values can be retrieved on the basis of already known $[\text{O}(^3P)]$ values.

- $[\text{O}_2(A)]$ values were also evaluated ($E\cdot[\text{O}_2(A)]$) on the basis of retrieved $\text{VER}\{\text{O}_2(A-X)\}$ values ($R\cdot\text{VER}\{\text{O}_2(A-X)\}$), so that only the respective transition probability was used: $E\cdot[\text{O}_2(A)] = R\cdot\text{VER}\{\text{O}_2(A-X)\} / R_{t8.0}$.

Finally, $\text{VER}\{\text{O}_2(A-X)\}$ values were evaluated ($E\cdot\text{VER}\{\text{O}_2(A-X)\}$) on the basis of retrieved $[\text{O}_2(A)]$ values and the respective transition probability: $E\cdot\text{VER}\{\text{O}_2(A-X)\} = R\cdot[\text{O}_2(A)] \times R_{t8.0}$.

$[\text{O}_2(A)]$ values were retrieved and then evaluated to compare and verify these calculations. As for $\text{VER}\{\text{O}_2(A-X)\}$ values, they were also evaluated to compare them with retrieved values and so to verify calculations by using the MAC model, see

- 30 Section A2.4.



A2.2 Substep 2: retrieval of $[O_2(A')]$

Chamberlain band emission measured at 370 nm was used to retrieve $VER\{O_2(A' - a)\}$ values and then to retrieve $[O(^3P)]$ values according to the continuity equation for $[O_2(A')]$, i.e. the cubic equation with respect to $[O(^3P)]$. Note that $[O_2(A)]$ values retrieved at the previous step were used in the $[O(^3P)]$ retrieval at this step. Then, $[O_2(A')]$ values were retrieved (R- $[O_2(A')]$) on the basis of $[O(^3P)]$ values by using the continuity equation considering all relevant processes of the MAC model. The continuity equation for $[O_2(A')]$ including terms of the $[O_2(A')]$ production ($P\{O_2(A')\}$) and its loss ($L\{O_2(A')\}$) is as follows: $d[O_2(A')]/dt = P\{O_2(A')\} - L\{O_2(A')\} = 0$. The production and loss terms were calculated considering the processes shown in Tables 6 ... 5 as follows: $P\{O_2(A')\} = P\{O_2(A')-C\} = [O_2(A)]R_{t2.1-3}\{[O(^3P)], [N_2], [O_2]\} + [O(^3P)]^2 R_{d1.1-2}\{[N_2], [O_2]\}$ and $L\{O_2(A')\} = L\{O_2(A')-C\} = [O_2(A')] \times D_d$, where $D_d = (R_{d2.1-2} + R_{d3.1-2} + R_{d4.1-2} + R_{d7.1-2})\{[O(^3P)], [O_2]\} + R_{d9.1}[O(^3P)] + R_{d6.0} + R_{d8.0}$. $[O_2(A')]$ profile values were retrieved as follows: R- $[O_2(A')] = [O_2(A')-C] = P\{O_2(A')-C\}/D_d$. In the case when Chamberlain band emissions are not given, $[O_2(A')]$ values can be retrieved on the basis of already known $[O(^3P)]$ values.

$[O_2(A')]$ values were also evaluated (E- $[O_2(A')]$) on the basis of retrieved $VER\{O_2(A' - a)\}$ values (R- $VER\{O_2(A' - a)\}$), so that only the respective transition probability was used: E- $[O_2(A')] = R-VER\{O_2(A' - a)\}/R_{d5.0}$.

Finally, $VER\{O_2(A' - a)\}$ values were evaluated (E- $VER\{O_2(A' - a)\}$) on the basis of retrieved $[O_2(A')]$ values and the respective transition probability: E- $VER\{O_2(A' - a)\} = R-[O_2(A')] \times R_{d5.0}$.

$[O_2(A')]$ values were retrieved and then evaluated to compare and verify these calculations. As for $VER\{O_2(A' - a)\}$ values, they were also evaluated to compare them with retrieved given ones and so to verify calculations by using the MAC model, see Section A2.4.

A2.3 Substep 3: retrieval of $[O_2(b)]$

Atmospheric band emission measured at 761.9 nm was used to retrieve $VER\{O_2(b - X)\}$ values and then to retrieve $[O(^3P)]$ values according to the continuity equation for $[O_2(b)]$, i.e. the cubic equation with respect to $[O(^3P)]$. Note that $[O_2(A)]$ and $[O_2(A')]$ values retrieved at the previous steps were used in the $[O(^3P)]$ retrieval at this step. However, if the MAC model excluding $O_2(A)$ and $O_2(A')$ is used then $[O_2(A)]$ and $[O_2(A')]$ profile values are set to zero because these concentrations were not retrieved at the previous retrieval steps. This is justified because O_2 in these triplet excited states is decoupled from the singlet excited states according to the hypothesis of Slinger et al. (2004b) used to propose the MAC model, which were verified and validated, (see Section 3.4. Then, $[O_2(b)]$ values were retrieved (R- $[O_2(b)]$) on the basis of $[O(^3P)]$ values by using the continuity equation considering all relevant processes of the MAC model. The continuity equation for $[O_2(b)]$ including terms of the $[O_2(b)]$ production ($P\{O_2(b)\}$) and its loss ($L\{O_2(b)\}$) is as follows: $d[O_2(b)]/dt = P\{O_2(b)\} - L\{O_2(b)\} = 0$. The production and loss terms were calculated considering the processes shown in Tables 6 ... 5.

The production term was calculated as follows: $P\{O_2(b)\} = P\{O_2(b)-M\} + P\{O_2(b)-H\} + P\{O_2(b)-C\}$, where $P\{O_2(b)-M\} = [O(^1D)]R_{r2.3}[O_2] + R_{s3.0}[O_2]$, $P\{O_2(b)-H\} = [O(^3P)]^2 R_{b1.1-2}\{[N_2], [O_2]\} + [O_2(c)]R_{c3.1-2}\{[O(^3P)], [O_2]\}$, $P\{O_2(b)-C\} = [O_2(A)]R_{t4.1-3}\{[O(^3P)], [N_2], [O_2]\} + [O_2(A)]R_{t5.0} + [O_2(A')]R_{d3.1-2}\{[O(^3P)], [O_2]\} + [O_2(c)]R_{c4.0}$ so



$$P\{O_2(b)\} = [O_2(A)]R_{t4.1-3}\{[O(^3P)], [N_2], [O_2]\} + [O_2(A)]R_{t5.0} + [O_2(A')]R_{d3.1-2}\{[O(^3P)], [O_2]\} \\ + [O_2(c)]R_{c3.1-2}\{[O(^3P)], [O_2]\} + [O_2(c)]R_{c4.0} + [O(^3P)]^2R_{b1.1-2}\{[N_2], [O_2]\} + [O(^1D)]R_{r2.3}[O_2] + R_{s3.0}[O_2].$$

The loss term was calculated as follows: $L\{O_2(b)\} = L\{O_2(b)\text{-M}\} + L\{O_2(b)\text{-H}\} + L\{O_2(b)\text{-C}\} = [O_2(b)] \times D_b$, where $L\{O_2(b)\text{-M}\} = [O_2(b)] \times (R_{b2.2-5}\{[O(^3P)], [N_2], [O_2], [CO_2]\} + R_{b3.0})$ is related to the M-model discussed in Section 3.2.1, $L\{O_2(b)\text{-H}\} = [O_2(b)] \times (R_{b4.2-4}\{[O(^3P)], [N_2], [O_2]\} + R_{b6.0})$ is related to the H-model discussed in Section 3.2.2 and $L\{O_2(b)\text{-C}\} = [O_2(b)] \times (R_{b4.1,5-6}\{[CO_2], [O_3]\} + R_{b2.1}[O_3])$ corresponds to the complementary processes relevant here. Note that $D_b = (R_{b2.1-5} + R_{b4.1-6})\{[O_3], [O(^3P)], [N_2], [O_2], [CO_2], [O_3]\} + R_{b4.6}[O_3] + R_{b3.0} + R_{b6.0}$.

$[O_2(b)]$ values were retrieved taking M-, H- and C-processes into account as follows: $R\text{-}[O_2(b)] = [O_2(b)] = [O_2(b)\text{-M}] + [O_2(b)\text{-H}] + [O_2(b)\text{-C}]$, where $[O_2(b)\text{-M}] = P\{O_2(b)\text{-M}\}/(D_b D_c)$, $[O_2(b)\text{-H}] = P\{O_2(b)\text{-H}\}/(D_b D_c)$ and

10 $[O_2(b)\text{-C}] = P\{O_2(b)\text{-C}\}/(D_b D_c)$, so $R\text{-}[O_2(b)] = P\{O_2(b)\}/(D_b D_c)$. In the case when Atmospheric band emissions are not given, $[O_2(b)]$ values can be retrieved on the basis of already known $[O(^3P)]$ values.

$[O_2(b)]$ values were also evaluated (E- $[O_2(b)]$) on the basis of retrieved $VER\{O_2(b-X)\}$ values (R- $VER\{O_2(b-X)\}$), so that only the respective transition probability was used: $E\text{-}[O_2(b)] = R\text{-}VER\{O_2(b-X)\}/R_{b5.0}$.

Finally, $VER\{O_2(b-X)\}$ values were evaluated (E- $VER\{O_2(b-X)\}$) on the basis of retrieved $[O_2(b)]$ values and the
 15 respective transition probability: $E\text{-}VER\{O_2(b-X)\} = R\text{-}[O_2(b)] \times R_{b5.0}$.

$[O_2(b)]$ values were retrieved and then evaluated to compare and verify these calculations. As for $VER\{O_2(b-X)\}$ values, they were also evaluated to compare them with retrieved given ones and so to verify calculations performed with the MAC model, see Section A2.4.

A2.4 Substep 4: consistency tests in the retrieval of $[O_2(b)]$

20 The consistency tests in the retrievals performed with the MAC model are based on the comparison of the retrieved and evaluated values.

Calculations at the retrieval steps 2.1 and 2.2 are relevant for the MAC model involving $O_2(A)$ and $O_2(A')$, but calculations at the retrieval step 2.3 only are relevant for the MAC model excluding $O_2(A)$ and $O_2(A')$, see the following overview.

The retrieval step 2.1 described in Section A2.1 was carried out to retrieve $R\text{-}[O_2(A)]$ and $[O(^3P)]$ values on the basis of
 25 $R\text{-}VER\{O_2(A-X)\}$ values. $E\text{-}[O_2(A)]$ values were also evaluated to compare them with $R\text{-}[O_2(A)]$ values. Additionally, $E\text{-}VER\{O_2(A-X)\}$ values were also evaluated to compare them with $R\text{-}VER\{O_2(A-X)\}$ values.

The retrieval step 2.2 described in Section A2.2 was carried out to retrieve $R\text{-}[O_2(A')]$ and $[O(^3P)]$ values on the basis of $R\text{-}VER\{O_2(A'-a)\}$ and $R\text{-}[O_2(A)]$ values. $E\text{-}[O_2(A')]$ values were also evaluated to compare them with $R\text{-}[O_2(A')]$ values. Additionally, $E\text{-}VER\{O_2(A'-a)\}$ values were also evaluated to compare them with $R\text{-}VER\{O_2(A'-a)\}$ values.

30 The retrieval step 2.3 described in Section A2.3 was carried out with the MAC model to retrieve $R\text{-}[O_2(b)]$ and $[O(^3P)]$ values on the basis of $R\text{-}VER\{O_2(b-X)\}$ values. $E\text{-}[O_2(b)]$ values were also evaluated to compare them with $R\text{-}[O_2(b)]$ values. Additionally, $E\text{-}VER\{O_2(b-X)\}$ values were also evaluated to compare them with $R\text{-}VER\{O_2(b-X)\}$ values.



A3 The 3rd retrieval step

The 3rd retrieval step was performed at three substeps to calculate $[O_2(c)]$ and $[O_2(a)]$ values.

A3.1 Substep 1: retrieval of $[O_2(c)]$

$[O_2(c)]$ values were retrieved ($R-[O_2(c)]$) on the basis of $[O_2(A)]$, $[O_2(A')]$ and $[O_2(b)]$ values (obtained at the retrieval steps 2.1, 2.2 and 2.3, respectively) as well as $[O(^3P)]$ values (obtained at the retrieval step 2.3) according to the continuity equation for $[O_2(c)]$ considering all relevant processes of the MAC model.

The continuity equation for $[O_2(c)]$ including terms of the $[O_2(c)]$ production ($P\{O_2(c)\}$) and its loss ($L\{O_2(c)\}$) is as follows: $d[O_2(c)]/dt = P\{O_2(c)\} - L\{O_2(c)\} = 0$. The production and loss terms were calculated considering the processes shown in Tables 6 ... 5.

10 The production term was calculated as follows: $P\{O_2(c)\} = P\{O_2(c)-M\} + P\{O_2(c)-H\} + P\{O_2(c)-C\}$, where $P\{O_2(c)-M\} = 0$, $P\{O_2(c)-H\} = [O(^3P)]^2 R_{c1.1-2}\{[N_2], [O_2]\}$ and $P\{O_2(c)-C\} = [O_2(A)] R_{t3.1-3}\{[O(^3P)], [N_2], [O_2]\} + [O_2(A')] R_{d2.1-2}\{[O(^3P)], [O_2]\}$, so $P\{O_2(c)\} = [O_2(A)] R_{t3.1-3}\{[O(^3P)], [N_2], [O_2]\} + [O_2(A')] R_{d2.1-2}\{[O(^3P)], [O_2]\} + [O(^3P)]^2 R_{c1.1-2}\{[N_2], [O_2]\}$.

The loss term was calculated as follows: $L\{O_2(c)\} = L\{O_2(c)-M\} + L\{O_2(c)-H\} + L\{O_2(c)-C\} = [O_2(c)] \times D_c$, where
 15 $L\{O_2(c)-M\} = 0$, $L\{O_2(c)-H\} = [O_2(c)] \times (R_{c2.1}[O(^3P)] + R_{c3.1-2}\{[O(^3P)], [O_2]\} + R_{c7.1}[O(^3P)] + R_{c8.0})$ and $L\{O_2(c)-C\} = [O_2(c)] \times (R_{c5.1-2}\{[O(^3P)], [O_2]\} + R_{c4.0} + R_{c6.0} + R_{c7.2}[O_2])$,
 so $D_c = R_{c2.1}[O(^3P)] + (R_{c3.1-2} + R_{c5.1-2} + R_{c7.1-2})\{[O(^3P)], [O_2]\} + R_{c4.0} + R_{c6.0} + R_{c8.0}$.

$[O_2(c)]$ values were retrieved taking M-, H- and C-processes into account as follows: $R-[O_2(c)] = [O_2(c)] = [O_2(c)-M] + [O_2(c)-H] + [O_2(c)-C]$, where $[O_2(c)-M] = 0$, $[O_2(c)-H] = P\{O_2(c)-H\}/D_c$ and $[O_2(c)-C] = P\{O_2(c)-C\}/D_c$ so $R-[O_2(c)] =$
 20 $P\{O_2(c)\}/D_c$.

A3.2 Substep 2: retrieval of $[O_2(a)]$

Infrared Atmospheric band emission measured at $1.27 \mu m$ was used to retrieve $VER\{O_2(a-X)\}$ values and then to retrieve $[O(^3P)]$ values according to the continuity equation for $[O_2(a)]$, i.e. the cubic equation with respect to $[O(^3P)]$. Note that $[O_2(A)]$, $[O_2(A')]$, $[O_2(b)]$ and $[O_2(c)]$ values retrieved at the previous steps were used in the $[O(^3P)]$ retrieval at this step.
 25 Then, $[O_2(a)]$ values were retrieved ($R-[O_2(a)]$) on the basis of $[O(^3P)]$ values by using the continuity equation considering all relevant processes of the MAC model. on the basis of $VER\{O_2(a-X)\}$ values. The continuity equation for $[O_2(a)]$ including terms of the $[O_2(a)]$ production ($P\{O_2(a)\}$) and its loss ($L\{O_2(a)\}$) is as follows: $d[O_2(a)]/dt = P\{O_2(a)\} - L\{O_2(a)\} = 0$. The production and loss terms were calculated considering the processes shown in Tables 6 ... 5.

The production term is compounded of terms related to the M-model discussed in Section 3.2.1 ($P\{O_2(a)-M\}$), to the H-model discussed in Section 3.2.2 ($P\{O_2(a)-H\}$) and the complementary processes relevant here ($P\{O_2(a)-C\}$): $P\{O_2(a)\} =$
 30 $P\{O_2(a)-M\} + P\{O_2(a)-H\} + P\{O_2(a)-C\}$, where $P\{O_2(a)-M\} = [O_2(b)] R_{b2.1-5}\{[O_3], [O(^3P)], [N_2], [O_2], [CO_2]\} + [O_2(b)] R_{b3.0} + R_{s2.3}[O_3]$, $P\{O_2(a)-H\} = 0$ and $P\{O_2(a)-C\} = [O_2(A)] R_{t6.1-3}\{[O(^3P)], [N_2], [O_2]\}$



$$\begin{aligned}
 & + [\text{O}_2(A')](R_{d4.1-2}\{[\text{O}(^3P)], [\text{O}_2]\} + R_{d6.0}) + [\text{O}_2(c)](R_{c5.1-2}\{[\text{O}(^3P)], [\text{O}_2]\} + R_{c6.0}) \\
 & + [\text{O}(^3P)]^2 R_{a1.1-2}\{[\text{N}_2], [\text{O}_2]\} + [\text{O}(^1D)]R_{r2.2}[\text{O}_2] + R_{s2.1,5}[\text{O}_3]. \text{ The production term was calculated as follows: } P\{\text{O}_2(a)\} = \\
 & [\text{O}_2(A)]R_{t6.1-3}\{[\text{O}(^3P)], [\text{N}_2], [\text{O}_2]\} + [\text{O}_2(A')](R_{d4.1-2}\{[\text{O}(^3P)], [\text{O}_2]\} + R_{d6.0}) \\
 & + [\text{O}_2(c)](R_{c5.1-2}\{[\text{O}(^3P)], [\text{O}_2]\} + R_{c6.0}) + [\text{O}_2(b)]R_{b2.1-5}\{[\text{O}_3], [\text{O}(^3P)], [\text{N}_2], [\text{O}_2], [\text{CO}_2]\} + [\text{O}_2(b)]R_{b3.0} + R_{s2.1,3,5}[\text{O}_3] \\
 5 \quad & + [\text{O}(^3P)]^2 R_{a1.1-2}\{[\text{N}_2], [\text{O}_2]\} + [\text{O}(^1D)]R_{r2.2}[\text{O}_2].
 \end{aligned}$$

The loss term was calculated as follows: $L\{\text{O}_2(a)\} = L\{\text{O}_2(a)\text{-M}\} + L\{\text{O}_2(a)\text{-H}\} + L\{\text{O}_2(a)\text{-C}\} = [\text{O}_2(a)] \times D_a$, where $L\{\text{O}_2(a)\text{-M}\} = [\text{O}_2(a)] \times (R_{a2.2-4}\{[\text{O}(^3P)], [\text{N}_2], [\text{O}_2]\} + R_{a4.0})$, $L\{\text{O}_2(a)\text{-H}\} = 0$ and $L\{\text{O}_2(a)\text{-C}\} = [\text{O}_2(a)] \times (R_{a2.1}[\text{O}_3])$, so $D_a = R_{a2.1-4}\{[\text{O}_3], [\text{O}(^3P)], [\text{N}_2], [\text{O}_2]\} + R_{a4.0}$.

$[\text{O}_2(a)]$ values were retrieved taking M-, H- and C-processes into account as follows: $R\text{-}[\text{O}_2(a)] = [\text{O}_2(a)] = [\text{O}_2(a)\text{-M}] +$
 10 $[\text{O}_2(a)\text{-H}] + [\text{O}_2(a)\text{-C}]$, where $[\text{O}_2(a)\text{-M}] = P\{\text{O}_2(a)\text{-M}\}/(D_a D_c)$, $[\text{O}_2(a)\text{-H}] = P\{\text{O}_2(a)\text{-H}\}/(D_a D_c)$ and $[\text{O}_2(a)\text{-C}] = P\{\text{O}_2(a)\text{-C}\}/(D_a D_c)$, so $R\text{-}[\text{O}_2(a)] = P\{\text{O}_2(a)\}/(D_a D_c)$. In the case when Infrared Atmospheric band emissions are not given, $[\text{O}_2(a)]$ values can be retrieved on the basis of already known $[\text{O}(^3P)]$ values.

$[\text{O}_2(a)]$ values were also evaluated ($E\text{-}[\text{O}_2(a)]$) on the basis of retrieved $\text{VER}\{\text{O}_2(a-X)\}$ values ($R\text{-}\text{VER}\{\text{O}_2(a-X)\}$), so that only the respective transition probability was used: $E\text{-}[\text{O}_2(a)] = R\text{-}\text{VER}\{\text{O}_2(a-X)\}/R_{a3.0}$.

15 Finally, $\text{VER}\{\text{O}_2(a-X)\}$ values were evaluated ($E\text{-}\text{VER}\{\text{O}_2(a-X)\}$) on the basis of retrieved $[\text{O}_2(a)]$ values and the respective transition probability: $E\text{-}\text{VER}\{\text{O}_2(a-X)\} = R\text{-}[\text{O}_2(a)] \times R_{a3.0}$.

$[\text{O}_2(a)]$ values were retrieved and then evaluated to compare and verify these calculations. As for $\text{VER}\{\text{O}_2(a-X)\}$ values, they were also evaluated to compare them with retrieved given ones and so to verify calculations by using the MAC model, see Section A3.3.

20 A3.3 Substep 3: consistency tests in the retrieval of $[\text{O}_2(a)]$

The consistency tests in the retrievals performed with the MAC model are based on the comparison of the retrieved and evaluated values.

The retrieval step 3.1 described in Section A3.1 was carried out to retrieve $R\text{-}[\text{O}_2(c)]$ and $[\text{O}(^3P)]$ values. Calculations at the retrieval step 3.1 can not be tested for consistency because $[\text{O}_2(c)]$ was not retrieved on the basis of VER values, but con-
 25 centrations available from the previous retrieval steps. Indeed, emissions in the Herzberg II band were not measured, whereas emissions in the New system from Keck I/II and the Richards-Johnson system are of low signal to noise ratio. Therefore, calculations at the retrieval step 3.2 only can be tested for consistency.

The retrieval step 3.2 described in Section A3.2 was carried out to retrieve $R\text{-}[\text{O}_2(a)]$ and $[\text{O}(^3P)]$ values on the basis of $R\text{-}\text{VER}\{\text{O}_2(a-X)\}$ values and concentrations of available excited chemical species. $E\text{-}[\text{O}_2(a)]$ values were also evaluated
 30 to compare them with $R\text{-}[\text{O}_2(a)]$ values. Additionally, $E\text{-}\text{VER}\{\text{O}_2(a-X)\}$ values were also evaluated to compare them with $R\text{-}\text{VER}\{\text{O}_2(a-X)\}$ values.

A4 The 4th retrieval step

The 4th retrieval step was performed at two substeps to calculate $[\text{O}(^1S)]$ values.



A4.1 Substep 1: retrieval of $[O(^1S)]$

Oxygen green line emission measured at 557.7 nm was used to retrieve $VER\{O(^1S - ^1D)\}$ values and then to retrieve $[O(^3P)]$ values according to the continuity equation for $[O(^1S)]$, i.e. the cubic equation with respect to $[O(^3P)]$. Note that $[O_2(A)]$, $[O_2(A')]$, $[O_2(c)]$, $[O_2(b)]$ and $[O_2(a)]$ values retrieved at the previous steps were used in the $[O(^3P)]$ retrieval at this step.

- 5 Then, $[O(^1S)]$ values were retrieved ($R-[O(^1S)]$) on the basis of $[O(^3P)]$ values by using the continuity equation considering all relevant processes of the MAC model. The continuity equation for $[O(^1S)]$ including terms of the $[O(^1S)]$ production ($P\{O(^1S)\}$) and its loss ($L\{O(^1S)\}$) is as follows: $d[O(^1S)]/dt = P\{O(^1S)\} - L\{O(^1S)\} = 0$. The production and loss terms were calculated considering the processes shown in Tables 6 ... 5.

- The production term is compounded of terms related to the M-model discussed in Section 3.2.1 ($P\{O(^1S)-M\}$), to the H-
 10 model discussed in Section 3.2.2 ($P\{O(^1S)-H\}$) and the complementary processes relevant here ($P\{O(^1S)-C\}$): $P\{O(^1S)\} = P\{O(^1S)-M\} + P\{O(^1S)-H\} + P\{O(^1S)-C\}$, where $P\{O(^1S)-M\} = 0$, $P\{O(^1S)-H\} = [O(^3P)]R_{c2.1}[O_2(c)]$ and $P\{O(^1S)-C\} = [O(^3P)](R_{t10.1}[O_2(A)] + R_{d9.1}[O_2(A')])$. The production term was calculated as follows:
 $P\{O(^1S)\} = [O(^3P)](R_{t10.1}[O_2(A)] + R_{d9.1}[O_2(A')]) + [O(^3P)]R_{c2.1}[O_2(c)]$.

- The loss term was calculated as follows: $L\{O(^1S)\} = L\{O(^1S)-M\} + L\{O(^1S)-H\} + L\{O(^1S)-C\} = [O(^1S)] \times D_g$, where
 15 $L\{O(^1S)-M\} = 0$, $L\{O(^1S)-H\} = [O(^1S)] \times (R_{g1.2}[O_2] + R_{g3.0} + R_{g4.0})$ and $L\{O(^1S)-C\} = [O(^1S)] \times (R_{g1.1}[O(^3P)] + R_{g1.3}[O_3] + R_{g2.1-2}\{[N_2], [O_2(a)]\})$, so $D_g = R_{g1.1-3}\{[O(^3P)], [O_2], [O_3]\} + R_{g2.1-2}\{[N_2], [O_2(a)]\} + R_{g3.0} + R_{g4.0}$.

$[O(^1S)]$ values were retrieved taking M-, H- and C-processes into account as follows: $R-[O(^1S)] = [O(^1S)] = [O(^1S)-M] + [O(^1S)-H] + [O(^1S)-C]$, where $[O(^1S)-M] = 0$, $[O(^1S)-H] = P\{O(^1S)-H\}/(D_g D_c)$ and $[O(^1S)-C] = 0$. In the case when oxygen green line emissions are not given, $[O(^1S)]$ values can be retrieved on the basis of already known $[O(^3P)]$ values.

- 20 $[O(^1S)]$ values were also evaluated ($E-[O(^1S)]$) on the basis of retrieved $VER\{O(^1S - ^1D)\}$ values ($R-VER\{O(^1S - ^1D)\}$), so that only the respective transition probability was used: $E-[O(^1S)] = R-VER\{O(^1S - ^1D)\}/R_{g3.0}$.

Finally, $VER\{O(^1S - ^1D)\}$ values were evaluated ($E-VER\{O(^1S - ^1D)\}$) on the basis of retrieved $[O_2(a)]$ values and the respective transition probability: $E-VER\{O(^1S - ^1D)\} = R-[O_2(a)] \times R_{g3.0}$.

- $[O(^1S)]$ values were retrieved and then evaluated to compare and verify these calculations. As for $VER\{O(^1S - ^1D)\}$
 25 values, they were also evaluated to compare them with retrieved given ones and so to verify calculations by using the MAC model, see Section A4.2.

A4.2 Substep 2: consistency tests in the retrieval of $[O(^1S)]$

The consistency tests in the retrievals by using the MAC model is based on the comparison of the retrieved and evaluated values.

- 30 The retrieval step 4.1 described in Section A4.1 was carried out to retrieve $R-[O(^1S)]$ and $[O(^3P)]$ values on the basis of $R-VER\{O(^1S - ^1D)\}$ values and concentrations of available excited chemical species. $E-[O(^1S)]$ values were also evaluated to compare them with $R-[O(^1S)]$ values. Additionally, $E-VER\{O(^1S - ^1D)\}$ values were also evaluated to compare them with $R-VER\{O(^1S - ^1D)\}$ values.



A5 The 5th retrieval step

The 5th retrieval step was performed to calculate $[O_x]$ ($[O(^3P)]$, $[O(^1D)]$ and $[O_3]$) values on the basis of concentrations of all relevant chemical species.

A5.1 Substep 1: retrieval of $[O(^3P)]$ involving all relevant chemical species

- 5 $[O(^3P)]$ values were retrieved ($[O(^3P)-R]$) on the basis of concentrations of atmospheric minor species obtained at the previous retrieval steps according to the continuity equation for $[O(^3P)]$ considering all relevant processes of the MAC model. For instance, values of $[O_2(A)]$, $[O_2(A')]$, $[O_2(b)]$, $[O_2(c)]$, $[O_2(a)]$ and $[O(^1S)]$ were obtained at the retrieval steps 2.1, 2.2, 2.3, 3.1, 3.2 and 4.1, respectively.

The continuity equation for $[O(^3P)]$ including terms of the $[O(^3P)]$ production ($P\{O(^3P)\}$) and loss ($L\{O(^3P)\}$) is as follows: $d[O(^3P)]/dt = P\{O(^3P)\} - L\{O(^3P)\} = 0$. The production and loss terms were calculated considering the processes shown in Tables 6 ... 5.

The production term is compounded of terms related to the M-model discussed in Section 3.2.1 ($P\{O(^3P)-M\}$), to the H-model discussed in Section 3.2.2 ($P\{O(^3P)-H\}$) and the complementary processes relevant here ($P\{O(^3P)-C\}$):

15 $P\{O(^3P)\} = P\{O(^3P)-M\} + P\{O(^3P)-H\} + P\{O(^3P)-C\}$, where $P\{O(^3P)-M\} = [O(^1D)]R_{r2.1,3}\{[N_2], [O_2]\} + (R_{s1.1-2} + 2R_{s1.3-4})[O_2]$, $P\{O(^3P)-H\} = [O(^1S)](R_{g1.2}[O_2] + R_{g4.0})$ and $P\{O(^3P)-C\} = [O_2(b)]R_{b4.1}[O_3] + [O_2(a)]R_{a2.1}[O_3] + [O(^1S)]R_{g2.1-2}\{[N_2], [O_2(a)]\} + [O(^1D)](R_{r1.1}[O(^3P)] + R_{r2.2,4}\{[O_2], [CO_2]\} + R_{r3.0} + 2R_{r1.2}[O_3]) + 3R_{s2.2}[O_3] + R_{s2.5-6}[O_3] + [H]R_{h6.3}[HO_2]$. The production term was calculated as follows: $P\{O(^3P)\} = ([O_2(b)]R_{b4.1} + [O_2(a)]R_{a2.1})[O_3] + [O(^1S)](R_{g1.2}[O_2] + R_{g2.1-2}\{[N_2], [O_2(a)]\} + R_{g4.0}) + [O(^1D)](R_{r1.1}[O(^3P)] + 2R_{r1.2}[O_3] + R_{r2.1-4}\{[N_2], [O_2], [O_2], [CO_2]\} + R_{r3.0}) + (R_{s1.1-2} + 2R_{s1.3-4})[O_2] + 3R_{s2.2}[O_3] + R_{s2.5-6}[O_3] + [H]R_{h6.3}[HO_2]$.

20 The loss term was calculated as follows: $L\{O(^3P)\} = L\{O(^3P)-M\} + L\{O(^3P)-H\} + L\{O(^3P)-C\} = [O(^3P)] \times D_o$, where $L\{O(^3P)-M\} = [O(^3P)] \times ([O(^3P)]R_{a1.1-2}\{[N_2], [O_2]\})$, $L\{O(^3P)-H\} = [O(^3P)] \times ([O(^3P)](R_{x1.1-2} + R_{c1.1-2} + R_{b1.1-2})\{[N_2], [O_2]\} + R_{c2.1}[O_2(c)])$, $L\{O(^3P)-C\} = [O(^3P)] \times (R_{t10.1}[O_2(A)] + R_{d9.1}[O_2(A')] + [O(^3P)](R_{t1.1-2} + R_{d1.1-2})\{[N_2], [O_2]\} + R_{x2.1}[O_3] + [O_2]R_{x3.1-2}\{[N_2], [O_2]\} + R_{h2.1}[OH^*] + R_{h4.1}[HO_2])$, so $D_o = R_{t10.1}[O_2(A)] + R_{d9.1}[O_2(A')] + [O(^3P)](R_{x1.1-2} + R_{t1.1-2} + R_{d1.1-2} + R_{c1.1-2} + R_{b1.1-2} + R_{a1.1-2})\{[N_2], [O_2]\} + R_{x2.1}[O_3] + [O_2]R_{x3.1-2}\{[N_2], [O_2]\} + R_{h2.1}[OH^*] + R_{h4.1}[HO_2] + R_{c2.1}[O_2(c)]$.

25 $[O(^3P)]$ values were retrieved taking M-, H- and C-processes into account as follows: $[O(^3P)-R] = [O(^3P)-M] + [O(^3P)-H] + [O(^3P)-C]$, where $[O(^3P)-M] =$

30 $([O(^1D)]R_{r2.1,3}\{[N_2], [O_2]\} + (R_{s1.1-2} + 2R_{s1.3-4})[O_2]) / D_o$, $[O(^3P)-H] = ([O(^1S)](R_{g1.2}[O_2] + R_{g4.0})) / D_o$ and $[O(^3P)-C] = ([O_2(b)]R_{b4.1}[O_3] + [O_2(a)]R_{a2.1}[O_3] + [O(^1S)]R_{g2.1-2}\{[N_2], [O_2(a)]\} + 3R_{s2.2}[O_3] + R_{s2.5-6}[O_3]) / D_o + ([O(^1D)](R_{r1.1}[O(^3P)] + R_{r2.2,4}\{[O_2], [CO_2]\} + R_{r3.0} + 2R_{r1.2}[O_3]) + [H]R_{h6.3}[HO_2]) / D_o$.

The final equation for $[O(^3P)]$ is as follows: $[O(^3P)-R] = [O(^3P)] = ([O_2(a)]R_{a2.1}[O_3] + [O_2(b)]R_{b4.1}[O_3]) / D_o + ([O(^1S)](R_{g1.2}[O_2] + R_{g2.1-2}\{[N_2], [O_2(a)]\} + R_{g4.0})) / D_o$



$$+ ([O(^1D)](R_{r1.1}[O(^3P)] + R_{r2.1-4}\{[N_2], [O_2], [O_2], [CO_2]\} + R_{r3.0} + 2R_{r1.2}[O_3])) / D_o$$

$$+ ((R_{s1.1-2} + 2R_{s1.3-4})[O_2] + 3R_{s2.2}[O_3] + R_{s2.5-6}[O_3] + [H]R_{h6.3}[HO_2]) / D_o.$$

A5.2 Substep 2: retrieval of $[O(^1D)]$ involving all relevant chemical species

$[O(^1D)]$ values were retrieved ($[O(^1D)-R]$) on the basis of concentrations of atmospheric minor species obtained at the previous retrieval steps according to the continuity equation for $[O(^1D)]$ considering all relevant processes of the MAC model.

The continuity equation for $[O(^1D)]$ including terms of the $[O(^1D)]$ production ($P\{O(^1D)\}$) and loss ($L\{O(^1D)\}$) is as follows: $d[O(^1D)]/dt = P\{O(^1D)\} - L\{O(^1D)\} = 0$.

The production and loss terms were calculated considering the processes shown in Tables 5, 6 and 7.

The calculation of the production term was based on the considered M-, H- and C-processes as follows: $P\{O(^1D)\} = P\{O(^1D)-M\} + P\{O(^1D)-H\} + P\{O(^1D)-C\}$, where $P\{O(^1D)-M\} = R_{s1.1-2}[O_2] + R_{s2.3}[O_3]$, $P\{O_2(^1D)-H\} = R_{g3.0}[O(^1S)]$ and $P\{O_2(^1D)-C\} = [O(^1S)]2R_{g1.1}[O(^3P)] + R_{s2.4}[O_3]$, so $P\{O(^1D)\} = [O(^1S)](2R_{g1.1}[O(^3P)] + R_{g3.0}) + R_{s1.1-2}[O_2] + R_{s2.3-4}[O_3]$.

The calculation of the loss term was based on the considered M-, H- and C-processes as follows: $L\{O(^1D)\} = L\{O(^1D)-M\} + L\{O(^1D)-H\} + L\{O(^1D)-C\} = [O(^1D)] \times D_r$, where $L\{O(^1D)-M\} = R_{r2.1,3}\{[N_2], [O_2]\}$, $L\{O(^1D)-H\} = 0$ and $L\{O(^1D)-C\} = R_{r1.1-3}\{[O(^3P)], [O_3], [O_3]\} + R_{r2.2,4}\{[O_2], [CO_2]\} + R_{r3.0}$, so $D_r = R_{r1.1-3}\{[O(^3P)], [O_3], [O_3]\} + R_{r2.1-4}\{[N_2], [O_2], [O_2], [CO_2]\} + R_{r3.0}$.

$[O(^1D)]$ values were retrieved taking M-, H- and C-processes into account as follows: $[O(^1D)-R] = [O(^1D)] = [O(^1D)-M] + [O(^1D)-H] + [O(^1D)-C]$, where $[O(^1D)-M] = (R_{s1.1-2}[O_2] + R_{s2.3}[O_3]) / D_r$, $[O(^1D)-H] = (R_{g3.0}[O(^1S)]) / D_r$ and $[O(^1D)-C] = ([O(^1S)]2R_{g1.1}[O(^3P)]) / D_r$.

The final equation for $[O(^1D)]$ is as follows: $[O(^1D)-R] = ((2R_{g1.1}[O(^3P)] + R_{g3.0})[O(^1S)] + R_{s1.1-2}[O_2] + R_{s2.3-4}[O_3]) / D_r$.

A5.3 Substep 3: retrieval of $[O_3]$ involving all relevant chemical species

$[O_3]$ values were retrieved ($[O_3-R]$) on the basis of concentrations of atmospheric minor species obtained at the previous retrieval steps according to the continuity equation for $[O_3]$ considering all relevant processes of the MAC model.

The continuity equation for $[O_3]$ including terms of the $[O_3]$ production ($P\{O_3\}$) and loss ($L\{O_3\}$) is as follows: $d[O_3]/dt = P\{O_3\} - L\{O_3\} = 0$.

The production and loss terms were calculated considering the processes shown in Tables 5, 6 and 7.

The calculation of the production term was based on the considered M-, H- and C-processes as follows: $P\{O_3\} = P\{O_3-M\} + P\{O_3-H\} + P\{O_3-C\}$, where $P\{O_3-M\} = 0$, $P\{O_3-H\} = 0$ and $P\{O_3-C\} = P\{O_3\} = [O(^3P)][O_2]R_{x3.1-2}\{[N_2], [O_2]\}$.

The calculation of the loss term was based on the considered M-, H- and C-processes as follows: $L\{O_3\} = L\{O_3-M\} + L\{O_3-H\} + L\{O_3-C\} = [O_3] \times D_3$, where $L\{O_3-M\} = R_{s2.3}$, $L\{O_3-H\} = 0$, $L\{O_3-C\} = R_{x2.1}[O(^3P)] + R_{b4.1}[O_2(b)] + R_{a2.1}[O_2(a)] + R_{g1.3}[O(^1S)] + R_{r1.2-3}[O(^1D)] + R_{h1.1}[H] + R_{h3.1}[OH^*] + R_{s2.1-2,4-6}$, so $D_3 = R_{x2.1}[O(^3P)] + R_{b4.1}[O_2(b)] + R_{a2.1}[O_2(a)] + R_{g1.3}[O(^1S)] + R_{r1.2-3}[O(^1D)] + R_{s2.1-6} + R_{h1.1}[H] + R_{h3.1}[OH^*]$.



$[O_3]$ values were retrieved taking M-, H- and C-processes into account as follows: $[O_3-R] = [O_3-M] + [O_3-H] + [O_3-C]$, where $[O_3-M] = 0$, $[O_3-H] = 0$ and $[O_3-C] = ([O(^3P)][O_2]R_{x3.1-2}\{[N_2], [O_2]\}) / D_3$.

The final equation for $[O_3]$ is as follows: $[O_3-R] = [O_3] = ([O(^3P)][O_2]R_{x3.1-2}\{[N_2], [O_2]\}) / D_3$.

Author contributions. Olexandr Lednyts'kyy worked out the concept of the MAC approach proposed by Torr *et al.* (1985), developed corresponding software, performed needed computations and prepared the manuscript of the article. Christian von Savigny contributed to planning the work activities regarding the article, discussed the results, contributed to the manuscript of the article, corrected and edited it.

Competing interests. The authors declare that they have no conflict of interests.

Acknowledgements. The authors acknowledge the financial support provided by the German Research Foundation (German: DFG) through the grant SA 1351/6-1 and thank Dr. Sinnhuber and Dr. Fytterer for the corresponding helpful discussions. The authors acknowledge a positive stimulating influence of Edward Llewellyn on working out the doctoral thesis by Olexandr Lednyts'kyy under the supervision of Christian von Savigny. Olexandr Lednyts'kyy also acknowledges the financial support provided by the University of Greifswald and the International Helmholtz Graduate School for Plasma Physics.



References

- Ångström, J. A.: Spectrum des Nordlichts, *Annalen der Physik*, 213, 161–163, <https://doi.org/10.1002/andp.18692130510>, <http://dx.doi.org/10.1002/andp.18692130510>, 1869.
- Atkinson, R. and Welge, K. H.: Temperature Dependence of $O(^1S)$. Deactivation by CO_2 , O_2 , N_2 , and Ar, *The Journal of Chemical Physics*, 57, 3689–3693, <https://doi.org/10.1063/1.1678829>, <http://scitation.aip.org/content/aip/journal/jcp/57/9/10.1063/1.1678829>, 1972.
- Atkinson, R., Baulch, D. L., Cox, R. A., Hampson, R. F., Kerr, J. A., Rossi, M. J., and Troe, J.: Evaluated kinetic and photochemical data for atmospheric chemistry: Supplement VI. IUPAC subcommittee on gas kinetic data evaluation for atmospheric chemistry, *Journal of Physical and Chemical Reference Data*, 26, 1329–1499, 1997.
- Bates, D. R.: Rate of Formation of Molecules by Radiative Association, *Monthly Notices of the Royal Astronomical Society*, 111, 303, <https://doi.org/http://dx.doi.org/10.1093/mnras/111.3.303>, <http://dx.doi.org/10.1093/mnras/111.3.303>, 1951.
- Bates, D. R.: Atomic and Molecular Processes, pp. 1–46, Academic Press Inc., 1962.
- Bates, D. R.: On the proposals of Chapman and of Barth for $O(^1S)$ formation in the upper atmosphere, *Planetary and Space Science*, 27, 717–718, [https://doi.org/10.1016/0032-0633\(79\)90168-5](https://doi.org/10.1016/0032-0633(79)90168-5), <http://www.sciencedirect.com/science/article/pii/0032063379901685>, 1979.
- Bates, D. R.: The green light of the night sky, *Planetary and Space Science*, 29, 1061–1067, [https://doi.org/10.1016/0032-0633\(81\)90003-9](https://doi.org/10.1016/0032-0633(81)90003-9), <http://www.sciencedirect.com/science/article/pii/0032063381900039>, 1981.
- Bates, D. R.: Excitation and quenching of the oxygen bands in the nightglow, *Planetary and Space Science*, 36, 875–881, [https://doi.org/10.1016/0032-0633\(88\)90093-1](https://doi.org/10.1016/0032-0633(88)90093-1), <http://www.sciencedirect.com/science/article/pii/0032063388900931>, special Issue: Atomic Oxygen Abundance in Thermosphere, 1988a.
- Bates, D. R.: Special Issue: Atomic Oxygen Abundance in Thermosphere, Transition probabilities of the bands of the oxygen systems of the nightglow, *Planetary and Space Science*, 36, 869–873, [https://doi.org/10.1016/0032-0633\(88\)90092-X](https://doi.org/10.1016/0032-0633(88)90092-X), <http://www.sciencedirect.com/science/article/pii/003206338890092X>, 1988b.
- Bovensmann, H., Burrows, J. P., Buchwitz, M., Frerick, J., Noël, S., Rozanov, V. V., Chance, K. V., and Goede, A. P. H.: SCIAMACHY: Mission Objectives and Measurement Modes, *Journal of the Atmospheric Sciences*, 56, 127–150, [https://doi.org/10.1175/1520-0469\(1999\)056<0127:SMOAMM>2.0.CO;2](https://doi.org/10.1175/1520-0469(1999)056<0127:SMOAMM>2.0.CO;2), [https://doi.org/10.1175/1520-0469\(1999\)056<0127:SMOAMM>2.0.CO;2](https://doi.org/10.1175/1520-0469(1999)056<0127:SMOAMM>2.0.CO;2), 1999.
- Brasseur, G. and Solomon, S.: *Aeronomy of the middle atmosphere : chemistry and physics of the stratosphere and mesosphere*, Dordrecht: Springer, 2005.
- Burkholder, J. B., Sander, S. P., Abbatt, J., Barker, J. R., Huie, R. E., Kolb, C. E., Kurylo, M. J., Orkin, V. L., Wilmouth, D. M., and Wine, P. H.: Chemical Kinetics and Photochemical Data for Use in Atmospheric Studies. Evaluation No. 18. JPL Publication 15-10, Jet Propulsion Laboratory, Pasadena, http://jpldataeval.jpl.nasa.gov/pdf/JPL_Publication_15-10.pdf, 2015.
- Burrows, J. P., Hölzle, E., Goede, A. P. H., Visser, H., and Fricke, W.: SCIAMACHY – scanning imaging absorption spectrometer for atmospheric cartography, *Acta Astronautica*, 35, 445–451, [https://doi.org/10.1016/0094-5765\(94\)00278-T](https://doi.org/10.1016/0094-5765(94)00278-T), <http://www.sciencedirect.com/science/article/pii/009457659400278T>, earth Observation, 1995.
- Cacace, F., de Petris, G., and Troiani, A.: Experimental Detection of Tetraoxygen, *Angewandte Chemie International Edition*, 40, 4062–4065, [https://doi.org/10.1002/1521-3773\(20011105\)40:21<4062::AID-ANIE4062>3.0.CO;2-X](https://doi.org/10.1002/1521-3773(20011105)40:21<4062::AID-ANIE4062>3.0.CO;2-X), [http://dx.doi.org/10.1002/1521-3773\(20011105\)40:21<4062::AID-ANIE4062>3.0.CO;2-X](http://dx.doi.org/10.1002/1521-3773(20011105)40:21<4062::AID-ANIE4062>3.0.CO;2-X), 2001.
- Campbell, I. M. and Gray, C. N.: Rate constants for $O(^3P)$ recombination and association with $N(^4S)$, *Chemical Physics Letters*, 18, 607–609, [https://doi.org/10.1016/0009-2614\(73\)80479-8](https://doi.org/10.1016/0009-2614(73)80479-8), <http://www.sciencedirect.com/science/article/pii/0009261473804798>, 1973.



- Capetanakis, F. P., Sondermann, F., Höser, S., and Stuhl, F.: Temperature dependence of the quenching of $O(^1S)$ by simple inorganic molecules, *The Journal of Chemical Physics*, 98, 7883–7887, <https://doi.org/10.1063/1.464596>, <http://scitation.aip.org/content/aip/journal/jcp/98/10/10.1063/1.464596>, 1993.
- Chapman, S.: Bakerian Lecture. Some Phenomena of the Upper Atmosphere, *Proceedings of the Royal Society of London A: Mathematical, Physical and Engineering Sciences*, 132, 353–374, <https://doi.org/10.1098/rspa.1931.0105>, <http://rspa.royalsocietypublishing.org/content/132/820/353>, 1931.
- Chapman, S.: LXVI. On the production of auroral and night-sky light, *The London, Edinburgh, and Dublin Philosophical Magazine and Journal of Science*, 23, 657–665, <https://doi.org/10.1080/14786443708561840>, <http://dx.doi.org/10.1080/14786443708561840>, 1937.
- Colegrove, F. D., Hanson, W. B., and Johnson, F. S.: Eddy diffusion and oxygen transport in the lower thermosphere, *Journal of Geophysical Research*, 70, 4931–4941, <https://doi.org/10.1029/JZ070i019p04931>, <http://dx.doi.org/10.1029/JZ070i019p04931>, 1965.
- Dudok de Wit, T., Kretzschmar, M., Liliensten, J., and Woods, T.: Finding the best proxies for the solar UV irradiance, *Geophysical Research Letters*, 36, n/a–n/a, <https://doi.org/10.1029/2009GL037825>, <http://dx.doi.org/10.1029/2009GL037825>, 110107, 2009.
- Garcia, R. R. and Solomon, S.: The effect of breaking gravity waves on the dynamics and chemical composition of the mesosphere and lower thermosphere, *Journal of Geophysical Research: Atmospheres*, 90, 3850–3868, <https://doi.org/10.1029/JD090iD02p03850>, <http://dx.doi.org/10.1029/JD090iD02p03850>, 1985.
- García-Comas, M., López-Puertas, M., Marshall, B. T., Wintersteiner, P. P., Funke, B., Bermejo-Pantaleón, D., Mertens, C. J., Remsberg, E. E., Gordley, L. L., Mlynczak, M. G., and Russell, J. M.: Errors in Sounding of the Atmosphere using Broadband Emission Radiometry (SABER) kinetic temperature caused by non-local-thermodynamic-equilibrium model parameters, *Journal of Geophysical Research: Atmospheres*, 113, n/a–n/a, <https://doi.org/10.1029/2008JD010105>, <http://dx.doi.org/10.1029/2008JD010105>, d24106, 2008.
- Gobbi, D., Takahashi, H., Clemesha, B. R., and Batista, P. P.: Equatorial atomic oxygen profiles derived from rocket observations of OI 557.7 nm airglow emission, *Planetary and Space Science*, 40, 775–781, [https://doi.org/10.1016/0032-0633\(92\)90106-X](https://doi.org/10.1016/0032-0633(92)90106-X), <http://www.sciencedirect.com/science/article/pii/003206339290106X>, 1992.
- Gordiets, B. F., Ferreira, C. M., Guerra, V. L., Loureiro, J. M. A. H., Nahorny, J., Pagnon, D., Touzeau, M., and Vialle, M.: Kinetic model of a low-pressure N_2 - O_2 flowing glow discharge, *IEEE Transactions on Plasma Science*, 23, 750–768, <https://doi.org/10.1109/27.467998>, 1995.
- Greer, R. G. H., Llewellyn, E. J., Solheim, B. H., and Witt, G.: The excitation of $O_2(b^1\Sigma_g^+)$ in the nightglow, *Planetary and Space Science*, 29, 383–389, [https://doi.org/10.1016/0032-0633\(81\)90081-7](https://doi.org/10.1016/0032-0633(81)90081-7), <http://www.sciencedirect.com/science/article/pii/0032063381900817>, 1981.
- Greer, R. G. H., Murtagh, D. P., McDade, I. C., Dickinson, P. H. G., Thomas, L., Jenkins, D. B., Stegman, J., Llewellyn, E. J., Witt, G., Mackinnon, D. J., and Williams, E. R.: ETON 1: A data base pertinent to the study of energy transfer in the oxygen nightglow, *Planetary and Space Science*, 34, 771–788, [https://doi.org/10.1016/0032-0633\(86\)90074-7](https://doi.org/10.1016/0032-0633(86)90074-7), <http://www.sciencedirect.com/science/article/pii/0032063386900747>, 1986.
- Greer, R. G. H., Murtagh, D. P., McDade, I. C., Llewellyn, E. J., Witt, G., Thrush, B. A., Stott, I. P., and Bowhill, S. A.: Rocket Photometry and the Lower-Thermospheric Oxygen Nightglow [and Discussion], *Philosophical Transactions of the Royal Society of London A: Mathematical, Physical and Engineering Sciences*, 323, 579–595, <https://doi.org/10.1098/rsta.1987.0107>, <http://rsta.royalsocietypublishing.org/content/323/1575/579>, 1987.
- Grygalashvily, M., Becker, E., and Sonnemann, G. R.: Gravity Wave Mixing and Effective Diffusivity for Minor Chemical Constituents in the Mesosphere/Lower Thermosphere, *Space Science Reviews*, 168, 333–362, <https://doi.org/10.1007/s11214-011-9857-x>, <https://doi.org/10.1007/s11214-011-9857-x>, 2012.



- Grygalashvyly, M., Eberhart, M., Hedin, J., Strelnikov, B., Lübken, F.-J., Rapp, M., Löhle, S., Fasoulas, S., Khaplanov, M., Gumbel, J., and Vorobeve, E.: Atmospheric Band Fitting Coefficients Derived from Self-Consistent Rocket-Borne Experiment, *Atmospheric Chemistry and Physics Discussions*, 2018, 1–33, <https://doi.org/10.5194/acp-2018-696>, <https://www.atmos-chem-phys-discuss.net/acp-2018-696/>, 2018.
- 5 Hickey, M. P., Walterscheid, R. L., Taylor, M. J., Ward, W., Schubert, G., Zhou, Q., Garcia, F., Kelly, M. C., and Shepherd, G. G.: Numerical simulations of gravity waves imaged over Arecibo during the 10-day January 1993 campaign, *Journal of Geophysical Research: Space Physics*, 102, 11 475–11 489, <https://doi.org/10.1029/97JA00181>, <http://dx.doi.org/10.1029/97JA00181>, 1997.
- Hislop, R. J. and Wayne, R. P.: Production of $O_2(b^1\Sigma_g^+)$ in the $H+O_2$ system, *J. Chem. Soc., Faraday Trans. 2*, 73, 506–516, <https://doi.org/10.1039/F29777300506>, <http://dx.doi.org/10.1039/F29777300506>, 1977.
- 10 Hollas, J. M.: *Modern Spectroscopy*, John Wiley & Sons., <https://www.wiley.com/en-us/Modern+Spectroscopy%2C+4th+Edition-p-9780470844168>, 2004.
- Huang, T.-Y. and George, R.: Simulations of gravity wave-induced variations of the $OH(8,3)$, $O_2(0,1)$, and $O(^1S)$ airglow emissions in the MLT region, *Journal of Geophysical Research: Space Physics*, 119, 2149–2159, <https://doi.org/10.1002/2013JA019296>, <http://dx.doi.org/10.1002/2013JA019296>, 2014.
- 15 Huestis, D. L.: *Current Laboratory Experiments for Planetary Aeronomy*, pp. 245–258, American Geophysical Union, <https://doi.org/10.1029/130GM16>, <http://dx.doi.org/10.1029/130GM16>, 2002.
- Johnson, F. S. and Gottlieb, B.: Atomic oxygen transport in the thermosphere, *Planetary and Space Science*, 21, 1001 – 1009, [https://doi.org/10.1016/0032-0633\(73\)90146-3](https://doi.org/10.1016/0032-0633(73)90146-3), <http://www.sciencedirect.com/science/article/pii/0032063373901463>, 1973.
- Johnston, J. E. and Broadfoot, A. L.: Midlatitude observations of the night airglow: Implications to quenching near the mesopause, *Journal of Geophysical Research: Space Physics*, 98, 21 593–21 603, <https://doi.org/10.1029/93JA02318>, <http://dx.doi.org/10.1029/93JA02318>, 1993.
- 20 Jones, D. B., Campbell, L., Bottema, M. J., Teubner, P. J. O., Cartwright, D. C., Newell, W. R., and Brunger, M. J.: Electron-driven excitation of O_2 under night-time auroral conditions: Excited state densities and band emissions, *Planetary and Space Science*, 54, 45–59, <https://doi.org/10.1016/j.pss.2005.08.007>, <http://www.sciencedirect.com/science/article/pii/S003206330500190X>, 2006.
- 25 Kenner, R. D. and Ogryzlo, E. A.: A direct determination of the rate constant for the quenching of $O(^1S)$ by $O_2(a^1\Delta_g)$, *Journal of Photochemistry*, 18, 379–382, [https://doi.org/10.1016/0047-2670\(82\)87027-5](https://doi.org/10.1016/0047-2670(82)87027-5), <http://www.sciencedirect.com/science/article/pii/0047267082870275>, 1982.
- Kenner, R. D. and Ogryzlo, E. A.: Quenching of by $O(^3P)$, $O_2(a^1\Delta_g)$, and other gases, *Canadian Journal of Chemistry*, 61, 921–926, <https://doi.org/10.1139/v83-165>, <http://dx.doi.org/10.1139/v83-165>, 1983.
- 30 Kenner, R. D. and Ogryzlo, E. A.: Quenching of the $O_2(A_{\nu=2}-X_{\nu=5})$ Herzberg I band by $O_2(a)$ and O , *Canadian Journal of Physics*, 62, 1599–1602, <https://doi.org/10.1139/p84-204>, <https://doi.org/10.1139/p84-204>, 1984.
- Khomich, V. Y., Semenov, A. I., and Shefov, N. N.: *Airglow as an indicator of upper atmospheric structure and dynamics*, Springer, <http://www.springer.com/de/book/9783540758327>, 2008.
- Kramida, A., Ralchenko, Y., Reader, J., Sansonetti, J. E., and NIST, A. T.: *NIST Atomic Spectra Database (version 5.3)*, <http://physics.nist.gov/asd>, 2015.
- 35 Krasnopolsky, V. A.: Excitation of oxygen emissions in the night airglow of the terrestrial planets, *Planetary and Space Science*, 29, 925 – 929, [https://doi.org/10.1016/0032-0633\(81\)90053-2](https://doi.org/10.1016/0032-0633(81)90053-2), <http://www.sciencedirect.com/science/article/pii/0032063381900532>, 1981.



- Krasnopolsky, V. A.: Oxygen emissions in the night airglow of the Earth, Venus and Mars, *Planetary and Space Science*, 34, 511–518, [https://doi.org/10.1016/0032-0633\(86\)90089-9](https://doi.org/10.1016/0032-0633(86)90089-9), <http://www.sciencedirect.com/science/article/pii/0032063386900899>, 1986.
- Krasnopolsky, V. A.: Excitation of the oxygen nightglow on the terrestrial planets, *Planetary and Space Science*, 59, 754–766, <https://doi.org/10.1016/j.pss.2011.02.015>, <http://www.sciencedirect.com/science/article/pii/S0032063311000754>, 2011.
- 5 Krauss, M. and Neumann, D.: On the interaction of $O(^1S)$ with $O(^3P)$, *Chemical Physics Letters*, 36, 372–374, [https://doi.org/10.1016/0009-2614\(75\)80259-4](https://doi.org/10.1016/0009-2614(75)80259-4), <http://www.sciencedirect.com/science/article/pii/0009261475802594>, 1975.
- Lakowicz, J. R.: *Principles of Fluorescence Spectroscopy*, Springer US, <https://doi.org/10.1007/978-0-387-46312-4>, <https://link.springer.com/book/10.1007%2F978-0-387-46312-4>, 2006.
- Lednys'kyy, O. and von Savigny, C.: Development of a Multiple Airglow Chemistry model and validation with in-situ Airglow Measure-
10 ments, Midterm HEPP Meeting, Max Planck Society, 2016.
- Lednys'kyy, O., von Savigny, C., Eichmann, K.-U., and Mlynczak, M. G.: Atomic oxygen retrievals in the MLT region from SCIAMACHY nightglow limb measurements, *Atmospheric Measurement Techniques*, 8, 1021–1041, <https://doi.org/10.5194/amt-8-1021-2015>, <http://www.atmos-meas-tech.net/8/1021/2015/>, 2015.
- Lednys'kyy, O., von Savigny, C., and Weber, M.: Sensitivity of equatorial atomic oxygen in the MLT region to the 11-year and 27-day
15 solar cycles, *Journal of Atmospheric and Solar-Terrestrial Physics*, 162, 136–150, <https://doi.org/10.1016/j.jastp.2016.11.003>, <http://www.sciencedirect.com/science/article/pii/S1364682616303911>, layered Phenomena in the Mesopause Region, 2017.
- Lednys'kyy, O., von Savigny, C., and Llewellyn, E.: Validation of the extended Multiple Airglow Chemistry model with in-situ measurements of the Energy Transfer in the Oxygen Nightglow campaign, DPG Spring Meeting, 2018.
- Llewellyn, E. J. and McDade, I. C.: Singlet molecular oxygen in planetary atmospheres, *Journal of Photochemistry*, 25, 379 – 388,
20 [https://doi.org/10.1016/0047-2670\(84\)87039-2](https://doi.org/10.1016/0047-2670(84)87039-2), <http://www.sciencedirect.com/science/article/pii/0047267084870392>, 1984.
- Llewellyn, E. J. and Solheim, B. H.: The excitation of the infrared atmospheric oxygen bands in the nightglow, *Planetary and Space Science*, 26, 533–538, [https://doi.org/https://doi.org/10.1016/0032-0633\(78\)90044-2](https://doi.org/https://doi.org/10.1016/0032-0633(78)90044-2), <http://www.sciencedirect.com/science/article/pii/0032063378900442>, 1978.
- Llewellyn, E. J., Solheim, B. H., Witt, G., Stegman, J., and Greer, R. G. H.: On the excitation of oxygen emissions in the airglow of the
25 terrestrial planets, *Journal of Photochemistry*, 12, 179 – 183, [https://doi.org/10.1016/0047-2670\(80\)85041-6](https://doi.org/10.1016/0047-2670(80)85041-6), <http://www.sciencedirect.com/science/article/pii/0047267080850416>, 1980.
- López-González, M. J., López-Moreno, J. J., and Rodrigo, R.: Altitude and vibrational distribution of the O_2 ultraviolet nightglow emissions, *Planetary and Space Science*, 40, 913–928, [https://doi.org/10.1016/0032-0633\(92\)90132-8](https://doi.org/10.1016/0032-0633(92)90132-8), <http://www.sciencedirect.com/science/article/pii/0032063392901328>, 1992a.
- 30 López-González, M. J., López-Moreno, J. J., and Rodrigo, R.: Altitude profiles of the atmospheric system of O_2 and of the green line emission, *Planetary and Space Science*, 40, 783–795, [https://doi.org/10.1016/0032-0633\(92\)90107-Y](https://doi.org/10.1016/0032-0633(92)90107-Y), <http://www.sciencedirect.com/science/article/pii/003206339290107Y>, 1992b.
- Makhlouf, U. B., Picard, R. H., Winick, J. R., and F., T. T.: A model for the response of the atomic oxygen 557.7 nm and the OH Meinel airglow to atmospheric gravity waves in a realistic atmosphere, *Journal of Geophysical Research: Atmospheres*, 103, 6261–6269,
35 <https://doi.org/dx.doi.org/10.1029/97JD03082>, <https://agupubs.onlinelibrary.wiley.com/doi/abs/10.1029/97JD03082>, 1998.
- McConkey, J. W., Burns, D. J., Moran, K. A., and Emeleus, K. G.: Measurement of relative multipole transition probabilities in atomic oxygen, *Physics Letters*, 22, 416–417, [https://doi.org/10.1016/0031-9163\(66\)91206-6](https://doi.org/10.1016/0031-9163(66)91206-6), <http://www.sciencedirect.com/science/article/pii/0031916366912066>, 1966.



- McDade, I. C.: The photochemistry of the MLT oxygen airglow emissions and the expected influences of tidal perturbations, *Advances in Space Research*, 21, 787–794, [https://doi.org/10.1016/S0273-1177\(97\)00674-1](https://doi.org/10.1016/S0273-1177(97)00674-1), <http://www.sciencedirect.com/science/article/pii/S0273117797006741>, Proceedings of the C0.1 Symposium of COSPAR Scientific Commission C, 1998.
- McDade, I. C., Murtagh, D. P., Greer, R. G. H., Dickinson, P. H. G., Witt, G., Stegman, J., Llewellyn, E. J., Thomas, L., and Jenkins, D. B.:
5 ETON 2: Quenching parameters for the proposed precursors of $O_2(b^1\Sigma_g^+)$ and $O(^1S)$ in the terrestrial nightglow, *Planetary and Space Science*, 34, 789–800, [https://doi.org/10.1016/0032-0633\(86\)90075-9](https://doi.org/10.1016/0032-0633(86)90075-9), <http://www.sciencedirect.com/science/article/pii/0032063386900759>, 1986.
- Meier, R. R.: Ultraviolet spectroscopy and remote sensing of the upper atmosphere, *Space Science Reviews*, 58, 1–185, <https://doi.org/10.1007/BF01206000>, <http://dx.doi.org/10.1007/BF01206000>, 1991.
- 10 Meinel, A. B.: O_2 Emission Bands in the Infrared Spectrum of the Night Sky., *The Astrophysical Journal*, 112, 464–468, 1950.
- Minaev, B. F. and Ågren, H.: Collision-induced $b^1\Sigma^+-a^1\Delta_g$, $b^1\Sigma^+-X^3\Sigma^-$, $a^1\Delta_g-X^3\Sigma^-$ transition probabilities in molecular oxygen, *Journal of the Chemical Society, Faraday Transactions*, 93, 2231–2239, 1997.
- Mlynczak, M. G., Solomon, S., and Zaras, D. S.: An updated model for $O_2(a^1\Delta_g)$ concentrations in the mesosphere and lower thermosphere and implications for remote sensing of ozone at $1.27\ \mu\text{m}$, *Journal of Geophysical Research: Atmospheres*, 98, 18 639–18 648,
15 <https://doi.org/10.1029/93JD01478>, <http://dx.doi.org/10.1029/93JD01478>, 1993.
- Murtagh, D., Witt, G., Stegman, J., McDade, I., Llewellyn, E., Harris, F., and Greer, R.: An assessment of proposed $O(^1S)$ and $O_2(b^1\Sigma_g^+)$ nightglow excitation parameters, *Planetary and Space Science*, 38, 43–53, [https://doi.org/10.1016/0032-0633\(90\)90004-A](https://doi.org/10.1016/0032-0633(90)90004-A), <http://www.sciencedirect.com/science/article/pii/003206339090004A>, 1990.
- Nagy, A. F., Balogh, A., Cravens, T. E., Mendillo, M., and Müller-Wodarg, I.: *Comparative Aeronomy*, pp. 267–310, Springer-Verlag New
20 York, 2008.
- Nicolet, M.: Aeronomic reactions of hydrogen and ozone. In: *Mesospheric model and related experiments*, pp. 1–51, D. Reidel Publishing Company, Dordrecht-Holland, <https://doi.org/10.1007/978-94-010-3114-1>, 1971.
- Nicolet, M.: Aeronomic chemistry of ozone, *Planetary and Space Science*, 37, 1621–1652, [https://doi.org/10.1016/0032-0633\(89\)90150-5](https://doi.org/10.1016/0032-0633(89)90150-5), <http://www.sciencedirect.com/science/article/pii/0032063389901505>, 1989.
- 25 Nicolet, M. and Kennes, R.: Aeronomic problems of molecular oxygen photodissociation IV. The various parameters for the Herzberg continuum, *Planetary and Space Science*, 36, 1069–1076, [https://doi.org/10.1016/0032-0633\(88\)90044-X](https://doi.org/10.1016/0032-0633(88)90044-X), <http://www.sciencedirect.com/science/article/pii/003206338890044X>, 1988.
- Nicolet, M., Cleslik, S., and Kennes, R.: Aeronomic problems of molecular oxygen photodissociation V. Predissociation in the Schumann-Runge bands of oxygen, *Planetary and Space Science*, 37, 427–458, [https://doi.org/10.1016/0032-0633\(89\)90124-4](https://doi.org/10.1016/0032-0633(89)90124-4), <http://www.sciencedirect.com/science/article/pii/0032063389901244>, 1989.
30
- Pejaković, D. A., Copeland, R. A., Cosby, P. C., and Slinger, T. G.: Studies on the production of $O_2(a^1\Delta_g, \nu=0)$ and $O_2(b^1\Sigma_g^+, \nu=0)$ from collisional removal of $O_2(A^3\Sigma_u^+, \nu=6-10)$, *Journal of Geophysical Research: Space Physics*, 112, n/a–n/a, <https://doi.org/10.1029/2007JA012520>, <http://dx.doi.org/10.1029/2007JA012520>, a10307, 2007.
- Pendleton, W. R., Baker, D. J., Reese, R. J., and O’Neil, R. R.: Decay of $O_2(a^1\Delta_g)$ in the evening twilight airglow: Implications for the
35 radiative lifetime, *Geophysical Research Letters*, 23, 1013–1016, <https://doi.org/10.1029/96GL00946>, <https://agupubs.onlinelibrary.wiley.com/doi/abs/10.1029/96GL00946>, 1996.



- Pinheiro, M. J., Gousset, G., Granier, A., and Ferreira, C. M.: Modelling of low-pressure surface wave discharges in flowing oxygen: I. Electrical properties and species concentrations, *Plasma Sources Science and Technology*, 7, 524, <http://stacks.iop.org/0963-0252/7/i=4/a=010>, 1998.
- Predoi-Cross, A., Hambrook, K., Keller, R., Povey, C., Schofield, I., Hurtmans, D., Over, H., and Mellau, G. C.: Spectroscopic lineshape study of the self-perturbed oxygen A-band, *Journal of Molecular Spectroscopy*, 248, 85–110, <https://doi.org/10.1016/j.jms.2007.11.007>, <http://www.sciencedirect.com/science/article/pii/S0022285207003001>, 2008.
- Qian, L., Solomon, S. C., and Kane, T. J.: Seasonal variation of thermospheric density and composition, *Journal of Geophysical Research: Space Physics*, 114, <https://doi.org/10.1029/2008JA013643>, <https://agupubs.onlinelibrary.wiley.com/doi/abs/10.1029/2008JA013643>, 2009.
- 10 Remsberg, E. E., Marshall, B. T., García-Comas, M., Krueger, D., Lingenfelser, G. S., Martin-Torres, J., Mlynarczyk, M. G., Russell, J. M., Smith, A. K., Zhao, Y., Brown, C., Gordley, L. L., López-González, M. J., López-Puertas, M., She, C.-Y., Taylor, M. J., and Thompson, R. E.: Assessment of the quality of the Version 1.07 temperature-versus-pressure profiles of the middle atmosphere from TIMED/SABER, *Journal of Geophysical Research: Atmospheres*, 113, n/a–n/a, <https://doi.org/10.1029/2008JD010013>, <http://dx.doi.org/10.1029/2008JD010013>, d17101, 2008.
- 15 Rezac, L., Kutepov, A., Russell III, J. M., Feofilov, A. G., Yue, J., and Goldberg, R. A.: Simultaneous retrieval of T(p) and CO₂ VMR from two-channel non-LTE limb radiances and application to daytime SABER/TIMED measurements, *Journal of Atmospheric and Solar-Terrestrial Physics*, 130–131, 23–42, <https://doi.org/10.1016/j.jastp.2015.05.004>, <http://www.sciencedirect.com/science/article/pii/S1364682615000954>, 2015.
- Roble, R. G.: Energetics of the Mesosphere and Thermosphere, pp. 1–21, American Geophysical Union, <https://doi.org/10.1029/GM087p0001>, <http://dx.doi.org/10.1029/GM087p0001>, 2013.
- 20 Rodrigo, R., López-Moreno, J. J., López-Puertas, M., and Molina, A.: Progress in Atmospheric Physics, pp. 3–32, Springer Netherlands, 1988.
- Sakai, J., Hosokawa, K., Taguchi, S., and Ogawa, Y.: Storm time enhancements of 630.0 nm airglow associated with polar cap patches, *Journal of Geophysical Research: Space Physics*, 119, 2214–2228, <https://doi.org/10.1002/2013JA019197>, <http://dx.doi.org/10.1002/2013JA019197>, 2014.
- 25 Sandu, A. and Sander, R.: Technical note: Simulating chemical systems in Fortran90 and Matlab with the Kinetic PreProcessor KPP-2.1, *Atmospheric Chemistry and Physics*, 6, 187–195, <https://doi.org/10.5194/acp-6-187-2006>, <https://www.atmos-chem-phys.net/6/187/2006/>, 2006.
- Semenov, A. I.: Long-term changes in the height profiles of ozone and atomic oxygen in the lower thermosphere, *Geomagnetism and Aeronomy*, 37, 354–360, 1997.
- 30 Sharma, R. D., Wintersteiner, P. P., and Kalogerakis, K. S.: A new mechanism for OH vibrational relaxation leading to enhanced CO₂ emissions in the nocturnal mesosphere, *Geophysical Research Letters*, 42, 4639–4647, <https://doi.org/10.1002/2015GL063724>, <https://agupubs.onlinelibrary.wiley.com/doi/abs/10.1002/2015GL063724>, 2015.
- Sharp, W. E., Zaccheo, T. S., Browell, E. V., Ismail, S., Dobler, J. T., and Llewellyn, E. J.: Impact of ambient O₂(a¹Δ_g) on satellite-based laser remote sensing of O₂ columns using absorption lines in the 1.27 μm region, *Journal of Geophysical Research: Atmospheres*, 119, 7757–7772, <https://doi.org/10.1002/2013JD021324>, <http://dx.doi.org/10.1002/2013JD021324>, 2013JD021324, 2014.
- 35



- Shematovich, V. I., Bisikalo, D. V., Krauss, S., Hausleitner, W., and Lammer, H.: Influence of the hot oxygen corona on the satellite drag in the Earth's upper atmosphere, *Solar System Research*, 45, 231–239, <https://doi.org/10.1134/S003809461103004X>, <https://doi.org/10.1134/S003809461103004X>, 2011.
- Slanger, T. G.: Generation of $O_2(c^1\Sigma_u^-, C^3\Delta_u, A^3\Sigma_u^+)$ from oxygen atom recombination, *The Journal of Chemical Physics*, 69, 4779–4791, <https://doi.org/10.1063/1.436504>, <http://scitation.aip.org/content/aip/journal/jcp/69/11/10.1063/1.436504>, 1978.
- Slanger, T. G. and Copeland, R. A.: Energetic Oxygen in the Upper Atmosphere and the Laboratory, *Chemical Reviews*, 103, 4731–4766, <https://doi.org/10.1021/cr0205311>, <http://dx.doi.org/10.1021/cr0205311>, PMID: 14664631, 2003.
- Slanger, T. G., Cosby, P. C., and Huestis, D. L.: A new O_2 band system: The $c^1\Sigma_u^- - b^1\Sigma_g^+$ transition in the terrestrial nightglow, *Journal of Geophysical Research: Space Physics*, 108, n/a–n/a, <https://doi.org/10.1029/2002JA009677>, <http://dx.doi.org/10.1029/2002JA009677>, 1089, 2004a.
- Slanger, T. G., Cosby, P. C., and Huestis, D. L.: Co-variation of nightglow emission from the $O_2(A^3\Sigma_u^+)$ and $O_2(c^1\Sigma_u^-)$ states and the oxygen green line, observed with the Keck I/II telescopes, *Journal of Atmospheric and Solar-Terrestrial Physics*, 66, 617–622, <https://doi.org/10.1016/j.jastp.2004.01.013>, <http://www.sciencedirect.com/science/article/pii/S1364682604000252>, 2004b.
- Smith, G. P. and Robertson, R.: Temperature dependence of oxygen atom recombination in nitrogen after ozone photolysis, *Chemical Physics Letters*, 458, 6–10, <https://doi.org/10.1016/j.cplett.2008.04.074>, <http://www.sciencedirect.com/science/article/pii/S0009261408005691>, 2008.
- Smith, I. W. M.: The role of electronically excited states in recombination reactions, *International Journal of Chemical Kinetics*, 16, 423–443, <https://doi.org/10.1002/kin.550160411>, <http://dx.doi.org/10.1002/kin.550160411>, 1984.
- Smith, S. A., Fritts, D. C., and Vanzandt, T. E.: Evidence for a Saturated Spectrum of Atmospheric Gravity Waves, *Journal of the Atmospheric Sciences*, 44, 1404–1410, [https://doi.org/10.1175/1520-0469\(1987\)044<1404:EFASSO>2.0.CO;2](https://doi.org/10.1175/1520-0469(1987)044<1404:EFASSO>2.0.CO;2), [https://doi.org/10.1175/1520-0469\(1987\)044<1404:EFASSO>2.0.CO;2](https://doi.org/10.1175/1520-0469(1987)044<1404:EFASSO>2.0.CO;2), 1987.
- Solheim, B. H. and Llewellyn, E. J.: An indirect mechanism for the production of $O(^1S)$ in the aurora, *Planetary and Space Science*, 27, 473–479, [https://doi.org/10.1016/0032-0633\(79\)90124-7](https://doi.org/10.1016/0032-0633(79)90124-7), <http://www.sciencedirect.com/science/article/pii/0032063379901247>, 1979.
- Solomon, S. C. and Qian, L.: Solar extreme-ultraviolet irradiance for general circulation models, *Journal of Geophysical Research: Space Physics*, 110, <https://doi.org/10.1029/2005JA011160>, <https://agupubs.onlinelibrary.wiley.com/doi/abs/10.1029/2005JA011160>, 2005.
- Steadman, J. A. and Thrush, B. A.: A laboratory study of the mechanism of the oxygen airglow, *Journal of Atmospheric Chemistry*, 18, 301–317, <https://doi.org/10.1007/BF00712449>, <https://doi.org/10.1007/BF00712449>, 1994.
- Stegman, J. and Murtagh, D. P.: The molecular oxygen band systems in the U. V. nightglow: Measured and modelled, *Planetary and Space Science*, 39, 595–609, [https://doi.org/10.1016/0032-0633\(91\)90054-E](https://doi.org/10.1016/0032-0633(91)90054-E), <http://www.sciencedirect.com/science/article/pii/003206339190054E>, 1991.
- Stott, I. P. and Thrush, B. A.: Laboratory studies of the mechanism of the oxygen airglow, *Proceedings of the Royal Society of London A: Mathematical, Physical and Engineering Sciences*, 424, 1–17, <https://doi.org/10.1098/rspa.1989.0066>, <http://rspa.royalsocietypublishing.org/content/424/1866/1>, 1989.
- Swenson, G., Yee, Y., Vargas, F., and Liu, A.: Vertical diffusion transport of atomic oxygen in the mesopause region consistent with chemical losses and continuity: Global mean and inter-annual variability, *Journal of Atmospheric and Solar-Terrestrial Physics*, 178, 47 – 57, <https://doi.org/10.1016/j.jastp.2018.05.014>, <http://www.sciencedirect.com/science/article/pii/S1364682617305552>, 2018.



- Thomas, R. J.: Atomic hydrogen and atomic oxygen density in the mesopause region: Global and seasonal variations deduced from Solar Mesosphere Explorer near-infrared emissions, *Journal of Geophysical Research: Atmospheres*, 95, 16 457–16 476, <https://doi.org/10.1029/JD095iD10p16457>, <http://dx.doi.org/10.1029/JD095iD10p16457>, 1990.
- Torr, M. R., Torr, D. G., and Laher, R. R.: The O₂ atmospheric 0-0 band and related emissions at night from Spacelab 1, *Journal of Geophysical Research: Space Physics*, 90, 8525–8538, <https://doi.org/10.1029/JA090iA09p08525>, <http://dx.doi.org/10.1029/JA090iA09p08525>, 1985.
- Trajmar, S., Williams, W., and Kuppermann, A.: Angular Dependence of Electron Impact Excitation Cross Sections of O₂, *The Journal of Chemical Physics*, 56, 3759–3765, <https://doi.org/10.1063/1.1677774>, <https://doi.org/10.1063/1.1677774>, 1972.
- von Savigny, C. and Lednyts'kyi, O.: On the relationship between atomic oxygen and vertical shifts between OH Meinel bands originating from different vibrational levels, *Geophysical Research Letters*, 40, 5821–5825, <https://doi.org/10.1002/2013GL058017>, <http://dx.doi.org/10.1002/2013GL058017>, 2013.
- von Savigny, C., Lednyts'kyi, O., Forbes, J. M., and Zhang, X.: Lunar semidiurnal tide in the terrestrial airglow, *Geophysical Research Letters*, 42, 3553–3559, <https://doi.org/10.1002/2015GL063567>, <http://dx.doi.org/10.1002/2015GL063567>, 2015.
- Wayne, R. P.: Singlet oxygen in the environmental sciences, *Research on Chemical Intermediates*, 20, 395–422, <https://doi.org/10.1163/156856794X00397>, <https://doi.org/10.1163/156856794X00397>, 1994.
- Wei, Y., Pu, Z., Zong, Q., Wan, W., Ren, Z., Fraenz, M., Dubinin, E., Tian, F., Shi, Q., Fu, S., and Hong, M.: Oxygen escape from the Earth during geomagnetic reversals: Implications to mass extinction, *Earth and Planetary Science Letters*, 394, 94 – 98, <https://doi.org/10.1016/j.epsl.2014.03.018>, <http://www.sciencedirect.com/science/article/pii/S0012821X14001629>, 2014.
- Wright, P. C.: Association of atomic oxygen and airglow excitation mechanisms, *Planetary and Space Science*, 30, 251–259, [https://doi.org/10.1016/0032-0633\(82\)90003-4](https://doi.org/10.1016/0032-0633(82)90003-4), <http://www.sciencedirect.com/science/article/pii/0032063382900034>, 1982.
- Yankovsky, V. A., Kuleshova, V. A., Manuilova, R. O., and Semenov, A. O.: Retrieval of total ozone in the mesosphere with a new model of electronic-vibrational kinetics of O₃ and O₂ photolysis products, *Izvestiya, Atmospheric and Oceanic Physics*, 43, 514–525, <https://doi.org/10.1134/S0001433807040135>, <http://dx.doi.org/10.1134/S0001433807040135>, 2007.
- Yankovsky, V. A., Martysenko, K. V., Manuilova, R. O., and Feofilov, A. G.: Oxygen dayglow emissions as proxies for atomic oxygen and ozone in the mesosphere and lower thermosphere, *Journal of Molecular Spectroscopy*, 327, 209 – 231, <https://doi.org/10.1016/j.jms.2016.03.006>, <http://www.sciencedirect.com/science/article/pii/S0022285216300327>, new Visions of Spectroscopic Databases, Volume II, 2016.



Table 9. Rate values of processes considered in the MAC model involving $O_2(A)$ and $O_2(A')$. These reaction rates are followed by those shown in Tables 10, 11 and 12. Processes of the provided here rate values are shown in Table 5. References: r01 - Smith and Robertson (2008), r02 - Bates (1988a), r03 - Lednits'ky and von Savigny (2016), r04 - Rodrigo et al. (1988), r05 - Bates (1988b), r06 - Krasnopolsky (2011), r07 - Kenner and Ogryzlo (1984), r08 - Stegman and Murtagh (1991), r09 - López-González et al. (1992a).

R#	ΔH (eV)	Rate value	Rate unit	Ref.
$R_{t1.1}$		$\theta_{N_2}^{Pt} = tY \cdot 3 \cdot 10^{-33} (300/T)^{3.25}$	$\text{molec}^{-2} \text{cm}^6 \text{s}^{-1}$	r01
$R_{t1.2}$		$\theta_{O_2}^{Pt} = tY \cdot 3 \cdot 10^{-33} (300/T)^{3.25}$	$\text{molec}^{-2} \text{cm}^6 \text{s}^{-1}$	r01
		$tY = 0.06$	1	r02
$R_{t2.1-3}$		$\theta_{3P}^{td} = cTDu \cdot \theta_{3P}^{tx}, \theta_{N_2}^{td} = cTDu \cdot \theta_{N_2}^{tx}, \theta_{O_2}^{td} = cTDu \cdot \theta_{O_2}^{tx}$	$\text{molec}^{-1} \text{cm}^3 \text{s}^{-1}$	r03
		$cTDu = 1 \cdot 10^{-2}$ as $cTDu \in [1 \cdot 10^{-30}, 1 \cdot 10^{30}]$	1	r03
$R_{t3.1-3}$		$\theta_{3P}^{tc} = cTCu \cdot \theta_{3P}^{tx}, \theta_{N_2}^{tc} = cTCu \cdot \theta_{N_2}^{tx}, \theta_{O_2}^{tc} = cTCu \cdot \theta_{O_2}^{tx}$	$\text{molec}^{-1} \text{cm}^3 \text{s}^{-1}$	r03
		$cTCu = 1 \cdot 10^{-2}$ as $cTCu \in [1 \cdot 10^{-30}, 1 \cdot 10^{-2}]$	1	r03
$R_{t4.1-3}$		$\theta_{3P}^{tb} = cTBu \cdot \theta_{3P}^{tx}, \theta_{N_2}^{tb} = cTBu \cdot \theta_{N_2}^{tx}, \theta_{O_2}^{tb} = cTBu \cdot \theta_{O_2}^{tx}$	$\text{molec}^{-1} \text{cm}^3 \text{s}^{-1}$	r03
		$cTBu = 1 \cdot 10^{-2}$ as $cTBu \in [1 \cdot 10^{-30}, 1 \cdot 10^{-2}]$	1	r03
$R_{t5.0}$		$\theta_{BG}^A = 0.13$	s^{-1}	r04
$R_{t6.1-3}$		$\theta_{3P}^{ia} = cTAu \cdot \theta_{3P}^{tx}, \theta_{N_2}^{ia} = cTAu \cdot \theta_{N_2}^{tx}, \theta_{O_2}^{ia} = cTAu \cdot \theta_{O_2}^{tx}$	$\text{molec}^{-1} \text{cm}^3 \text{s}^{-1}$	r03
		$cTAu = 1 \cdot 10^{-2}$ as $cTAu \in [1 \cdot 10^{-30}, 1 \cdot 10^{-2}]$	1	r03
$R_{t7.1}$		$\theta_{3P}^{tx} = 1.3 \cdot 10^{-11}$	$\text{molec}^{-1} \text{cm}^3 \text{s}^{-1}$	r07
$R_{t7.2}$		$\theta_{N_2}^{tx} = 1.2 \cdot 10^{-11}$	$\text{molec}^{-1} \text{cm}^3 \text{s}^{-1}$	r03
$R_{t7.3}$		$\theta_{O_2}^{tx} = 1.3 \cdot 10^{-13}$	$\text{molec}^{-1} \text{cm}^3 \text{s}^{-1}$	r06
$R_{t8.0}$		$\theta_{320n}^A = 11$	s^{-1}	r08
$R_{t9.0}$		$\theta_{HI}^A = 11$	s^{-1}	r05
$R_{t10.1}$		$\theta_{IS}^{tx} = 1 \cdot 10^{-14}$ as $\theta_{IS}^{tx} \in [1 \cdot 10^{-30}, 1 \cdot 10^{-14}]$	$\text{molec}^{-1} \text{cm}^3 \text{s}^{-1}$	r03
$R_{d1.1}$		$\delta_{N_2}^{Pd} = dY \cdot 3 \cdot 10^{-33} (300/T)^{3.25}$	$\text{molec}^{-2} \text{cm}^6 \text{s}^{-1}$	r01
$R_{d1.2}$		$\delta_{O_2}^{Pd} = dY \cdot 3 \cdot 10^{-33} (300/T)^{3.25}$	$\text{molec}^{-2} \text{cm}^6 \text{s}^{-1}$	r01
		$dY = 0.18$	1	r02
$R_{d2.1-2}$		$\delta_{3P}^{dc} = cDCu \cdot \delta_{3P}^{tx}, \delta_{O_2}^{dc} = cDCu \cdot \delta_{O_2}^{tx}$	$\text{molec}^{-1} \text{cm}^3 \text{s}^{-1}$	r03
		$cDCu = 1 \cdot 10^{-2}$ close to $cDCu \in [1 \cdot 10^{-30}, 1 \cdot 10^{-3}]$	1	r03
$R_{d3.1-2}$		$\delta_{3P}^{db} = cDBu \cdot \delta_{3P}^{tx}, \delta_{O_2}^{db} = cDBu \cdot \delta_{O_2}^{tx}$	$\text{molec}^{-1} \text{cm}^3 \text{s}^{-1}$	r03
		$cDBu = 1 \cdot 10^{-2}$ as $cDBu \in [1 \cdot 10^{-30}, 1 \cdot 10^{-2}]$	1	r03
$R_{d4.1-2}$		$\delta_{3P}^{da} = cDAu \cdot \delta_{3P}^{dx}, \delta_{O_2}^{da} = cDAu \cdot \delta_{O_2}^{dx}$	$\text{molec}^{-1} \text{cm}^3 \text{s}^{-1}$	r03
		$cDAu = 1 \cdot 10^{-2}$ as $cDAu \in [1 \cdot 10^{-30}, 1 \cdot 10^{-2}]$	1	r03
$R_{d5.0}$		$\delta_{370n}^A = 0.85$	s^{-1}	r08
$R_{d6.0}$		$\delta_{Cha}^A = 0.85$	s^{-1}	r05
$R_{d7.1}$		$\delta_{3P}^{dx} = 1.3 \cdot 10^{-11}$	$\text{molec}^{-1} \text{cm}^3 \text{s}^{-1}$	r06
$R_{d7.2}$		$\delta_{O_2}^{dx} = 1.7 \cdot 10^{-11}$	$\text{molec}^{-1} \text{cm}^3 \text{s}^{-1}$	r09
$R_{d8.0}$		$\delta_{HIII}^A = 0.9$	s^{-1}	r05
$R_{d9.1}$		$\delta_{IS}^{dx} = 1 \cdot 10^{-14}$ as $\delta_{IS}^{dx} \in [1 \cdot 10^{-30}, 1 \cdot 10^{-14}]$	$\text{molec}^{-1} \text{cm}^3 \text{s}^{-1}$	r03



Table 10. Rate values of processes are related to those shown in Table 9 and followed by those shown in Tables 11 and 12. Processes of the provided here rate values are shown in Table 6. References: r10 - Predoi-Cross et al. (2008), r11 - Slanger (1978), r12 - Kenner and Ogryzlo (1983), r13 - Burkholder et al. (2015), r14 - Minaev and Ågren (1997). Labels r01, r02, r03, r06, r08 were used in Table 9. The enthalpy change (ΔH) was determined at standard temperature and pressure, see Table 12 for abbreviations.

R#	ΔH (eV)	Rate value	Rate unit	Ref.
$R_{c1.1-2}$		$\zeta_{N_2}^{Pc} = \zeta_{O_2}^{Pc} = cY \cdot 3 \cdot 10^{-33} (300/T)^{3.25}$	$\text{molec}^{-2} \text{cm}^6 \text{s}^{-1}$	r01
		$cY = 0.04$	1	r02
$R_{c2.1}$		$\zeta_{1S}^{cx} = 1.4 \cdot 10^{-8}$	$\text{molec}^{-1} \text{cm}^3 \text{s}^{-1}$	r03
$R_{c3.1}$		$\zeta_{3P}^{cb} = cCBa \cdot \zeta_{3P}^{cx}$	$\text{molec}^{-1} \text{cm}^3 \text{s}^{-1}$	r03
$R_{c3.2}$		$\zeta_{O_2}^{cb} = cCBm \cdot \zeta_{O_2}^{cx}$	$\text{molec}^{-1} \text{cm}^3 \text{s}^{-1}$	r03
		$cCBa = 5.8 \cdot 10^4$	1	r03
		$cCBm = 1 \cdot 10^{-1}$ as $cCBm \in [1 \cdot 10^{-30}, 1 \cdot 10^{-1}]$	1	r03
$R_{c4.0}$		$\zeta_{cbK}^A = \zeta_{RJ}^A/10$	s^{-1}	r03
$R_{c5.1}$		$\zeta_{3P}^{ca} = cCAa \cdot \zeta_{3P}^{cx}$	$\text{molec}^{-1} \text{cm}^3 \text{s}^{-1}$	r03
$R_{c5.2}$		$\zeta_{O_2}^{ca} = cCAm \cdot \zeta_{O_2}^{cx}$	$\text{molec}^{-1} \text{cm}^3 \text{s}^{-1}$	r03
		$cCAa = 1 \cdot 10^{-1}$ close to $cCAa \in [1 \cdot 10^{-30}, 1 \cdot 10^{+3}]$	1	r03
		$cCAm = 1 \cdot 10^{-1}$ close to $cCAm \in [1 \cdot 10^{-30}, 1]$	1	r03
$R_{c6.0}$		$\zeta_{RJ}^A = 0.073$	s^{-1}	r11
$R_{c7.1}$		$\zeta_{3P}^{cx} = 6 \cdot 10^{-12}$	$\text{molec}^{-1} \text{cm}^3 \text{s}^{-1}$	r12
$R_{c7.2}$		$\zeta_{O_2}^{cx} = 1.8 \cdot 10^{-11}$	$\text{molec}^{-1} \text{cm}^3 \text{s}^{-1}$	r06
$R_{c8.0}$		$\zeta_{HII}^A = 0.66$	s^{-1}	r08
$R_{b1.1-2}$	-3.49 ^E	$\beta_{N_2}^{Pb} = \beta_{O_2}^{Pb} = bY \cdot 3 \cdot 10^{-33} (300/T)^{3.25}$	$\text{molec}^{-2} \text{cm}^6 \text{s}^{-1}$	r01
		$bY = 0.03 + pY \cdot 0.07$	1	r03
		$pY = 0.5$ (for $O_2(^5\Pi)$)	1	r02
$R_{b2.1}$	-0.65 ^A	$\beta_{O_3}^{ba} = 0.15 \cdot 3.5 \cdot 10^{-11} \exp(-135/T)$	$\text{molec}^{-1} \text{cm}^3 \text{s}^{-1}$	r13
$R_{b2.2}$	-0.65 ^E	$\beta_{3P}^{ba} = cBAa \cdot \beta_{3P}^{bx}$	$\text{molec}^{-1} \text{cm}^3 \text{s}^{-1}$	r03
$R_{b2.3}$	-0.65 ^A	$\beta_{N_2}^{ba} = cBAm \cdot \beta_{N_2}^{bx}$	$\text{molec}^{-1} \text{cm}^3 \text{s}^{-1}$	r03
$R_{b2.4}$	-0.65 ^A	$\beta_{O_2}^{ba} = cBAm \cdot \beta_{O_2}^{bx}$	$\text{molec}^{-1} \text{cm}^3 \text{s}^{-1}$	r03
$R_{b2.5}$	-0.65 ^E	$\beta_{C_2}^{ba} = cBAm \cdot \beta_{C_2}^{bx}$	$\text{molec}^{-1} \text{cm}^3 \text{s}^{-1}$	r03
		$cBAa = cBAm = 1 \cdot 10^{-1}$ as $cBAa, cBAm \in [1 \cdot 10^{-30}, 1 \cdot 10^{-1}]$	1	r03
$R_{b3.0}$	0.65 ^E	$\beta_{NOx}^A = 0.0014$	s^{-1}	r14
$R_{b4.1}$	-1.63 ^A	$\beta_{O_3}^{bx} = 0.7 \cdot 3.5 \cdot 10^{-11} \exp(-135/T)$	$\text{molec}^{-1} \text{cm}^3 \text{s}^{-1}$	r13
$R_{b4.2}$	-1.63 ^E	$\beta_{3P}^{bx} = 8 \cdot 10^{-14}$	$\text{molec}^{-1} \text{cm}^3 \text{s}^{-1}$	r13
$R_{b4.3}$	-1.63 ^A	$\beta_{N_2}^{bx} = 1.8 \cdot 10^{-15} \exp(45/T)$	$\text{molec}^{-1} \text{cm}^3 \text{s}^{-1}$	r13
$R_{b4.4}$	-1.63 ^A	$\beta_{O_2}^{bx} = 3.9 \cdot 10^{-17}$	$\text{molec}^{-1} \text{cm}^3 \text{s}^{-1}$	r13
$R_{b4.5}$	-1.63 ^E	$\beta_{C_2}^{bx} = 4.2 \cdot 10^{-13}$	$\text{molec}^{-1} \text{cm}^3 \text{s}^{-1}$	r13
$R_{b4.6}$	-1.63 ^A	$\beta_{O_3}^{bx} = 0.15 \cdot 3.5 \cdot 10^{-11} \exp(-135/T)$	$\text{molec}^{-1} \text{cm}^3 \text{s}^{-1}$	r13
$R_{b5.0}$	1.63 ^E	$\beta_{762}^A = 0.079$	s^{-1}	r08
$R_{b6.0}$	1.63 ^E	$\beta_{Atm}^A = 0.083$	s^{-1}	r10



Table 11. Rate values of processes are related to those shown in Tables 9 and 10 and followed by those shown in Table 12. Processes of the provided here rate values are shown in Tables 6 and 7. References: r15 - Pendleton et al. (1996), r16 - Krauss and Neumann (1975), r17 - Capetanakis et al. (1993), r18 - Gordiets et al. (1995), r19 - Atkinson and Welge (1972), r20 - Kenner and Ogryzlo (1982), r21 - Kramida et al. (2015), r22 - Pinheiro et al. (1998), r23 - Sakai et al. (2014). Labels r01, r02, r03 were used in Table 9, and labels r13, r14 were used in Table 10. The enthalpy change (ΔH) was determined at standard temperature and pressure, see Table 12 for abbreviations.

R _#	ΔH (eV)	Rate value	Rate unit	Ref.
$R_{a1.1}$	-4.14 ^E	$\alpha_{N_2}^{Pa} = aY \cdot 3 \cdot 10^{-33} (300/T)^{3.25}$	$\text{molec}^{-2} \text{cm}^6 \text{s}^{-1}$	r01
$R_{a1.2}$	-4.14 ^E	$\alpha_{O_2}^{Pa} = aY \cdot 3 \cdot 10^{-33} (300/T)^{3.25}$	$\text{molec}^{-2} \text{cm}^6 \text{s}^{-1}$	r01
		$aY = 0.07 + pY \cdot 0.68$	1	r03
		$pY = 0.5$ (for $O_2(^5\Pi)$)	1	r02
$R_{a2.1}$	0.13 ^A	$\alpha_{O_3}^{ax} = 5.2 \cdot 10^{-11} \exp(-2840/T)$	$\text{molec}^{-1} \text{cm}^3 \text{s}^{-1}$	r13
$R_{a2.2}$	-0.98 ^E	$\alpha_{3P}^{ax} = cAXa \cdot 2 \cdot 10^{-16}$	$\text{molec}^{-1} \text{cm}^3 \text{s}^{-1}$	r13
		$cAXa = 1 \cdot 10^{-2}$ as $cAXa \in [1 \cdot 10^{-30}, 1 \cdot 10^{-2}]$	1	r03
$R_{a2.3}$	-0.98 ^A	$\alpha_{N_2}^{ax} = 1 \cdot 10^{-20}$	$\text{molec}^{-1} \text{cm}^3 \text{s}^{-1}$	r13
$R_{a2.4}$	-0.98 ^A	$\alpha_{O_2}^{ax} = 3.6 \cdot 10^{-18} \exp(-220/T)$	$\text{molec}^{-1} \text{cm}^3 \text{s}^{-1}$	r13
$R_{a3.0}$	0.98 ^E	$\alpha_{1u27}^A = 2.8 \cdot 10^{-4}$	$\text{molec}^{-1} \text{cm}^3 \text{s}^{-1}$	r15
$R_{a4.0}$	0.98 ^E	$\alpha_{1RA}^A = 1.9 \cdot 10^{-4}$	s^{-1}	r14
$R_{g1.1}$	-2.20 ^E	$\gamma_{1D}^{SP} = 2 \cdot 10^{-14}$	$\text{molec}^{-1} \text{cm}^3 \text{s}^{-1}$	r16, r20
$R_{g1.2}$	-4.17 ^E	$\gamma_{O_2}^{SP} = 2.32 \cdot 10^{-12} \exp(-811.88/T + 0.001816 \cdot T)$	$\text{molec}^{-1} \text{cm}^3 \text{s}^{-1}$	r17
$R_{g1.3}$	-6.26 ^E	$\gamma_{O_3}^{SP} = 6 \cdot 10^{-10}$	$\text{molec}^{-1} \text{cm}^3 \text{s}^{-1}$	r18
$R_{g2.1}$	-4.17 ^E	$\gamma_{N_2}^{SP} = 5 \cdot 10^{-17}$	$\text{molec}^{-1} \text{cm}^3 \text{s}^{-1}$	r19
$R_{g2.2}$	-4.17 ^E	$\gamma_{Oa}^{SP} = 2.6 \cdot 10^{-10}$	$\text{molec}^{-1} \text{cm}^3 \text{s}^{-1}$	r20
$R_{g3.0}$	2.20 ^E	$\gamma_{557n7}^A = 1.26$	s^{-1}	r21
$R_{g4.0}$	4.17 ^E	$\gamma_{1S3Pe}^A = A295n8 + A297n$	s^{-1}	r21
		$A295n8 = 2.42 \cdot 10^{-4}$	s^{-1}	r21
		$A297n2 = 7.54 \cdot 10^{-2}$	s^{-1}	r21
$R_{r1.1}$	-1.97 ^E	$\rho_{3P}^{DP} = 8 \cdot 10^{-12}$	$\text{molec}^{-1} \text{cm}^3 \text{s}^{-1}$	r22
$R_{r1.2}$	-0.86 ^A	$\chi_{2P}^{DP} = 1.2 \cdot 10^{-10}$	$\text{molec}^{-1} \text{cm}^3 \text{s}^{-1}$	r13
$R_{r1.3}$	-6.03 ^A	$\rho_{O_2}^{DP} = 1.2 \cdot 10^{-10}$	$\text{molec}^{-1} \text{cm}^3 \text{s}^{-1}$	r13
$R_{r2.1}$	-1.97 ^A	$\rho_{N_2}^{DP} = 2.15 \cdot 10^{-11} \exp(110/T)$	$\text{molec}^{-1} \text{cm}^3 \text{s}^{-1}$	r13
$R_{r2.2}$	-0.99 ^A	$\rho_{Oa}^{DP} = 0.2 \cdot 3.3 \cdot 10^{-11} \exp(55/T)$	$\text{molec}^{-1} \text{cm}^3 \text{s}^{-1}$	r13
$R_{r2.3}$	-0.34 ^A	$\rho_{Ob}^{DP} = 0.8 \cdot 3.3 \cdot 10^{-11} \exp(55/T)$	$\text{molec}^{-1} \text{cm}^3 \text{s}^{-1}$	r13
$R_{r2.4}$	-1.97 ^E	$\rho_{C2}^{DP} = 7.5 \cdot 10^{-11} \exp(115/T)$	$\text{molec}^{-1} \text{cm}^3 \text{s}^{-1}$	r13
$R_{r3.0}$	1.97 ^E	$\rho_{1D3Pe}^A = A630n0 + A636n4$	s^{-1}	r23
		$A630n0 = 5.63 \cdot 10^{-3}$	s^{-1}	r23
		$A636n4 = 1.82 \cdot 10^{-3}$	s^{-1}	r23



Table 12. Rate values of processes are related to those shown in Tables 9, 10 and 11. Processes of the provided here rate values are shown in Table 7. References: r24 - Nicolet (1971), r25 - Nicolet et al. (1989), r26 - Nicolet and Kennes (1988), r27 - Nicolet (1989), r28 - Mlynczak et al. (1993), r29 - Atkinson et al. (1997), r30 - Khomich et al. (2008).

Labels r01, r02, r03 were used in Table 9, and the label r13 was used in Table 10. The exothermic reaction energy content was determined for each reaction at standard temperature and pressure, see column “ ΔH ” for the enthalpy change. ΔH values were read out in the units of eV from Roble (2013), they are marked with a character R, and in the units of kJ mol^{-1} from Atkinson et al. (1997), they are marked with a character A. Additionally, ΔH values were evaluated, they are marked with a character E.

R#	ΔH (eV)	Rate value	Rate unit	Ref.
$R_{s1.1}$	8.98 ^A	$\sigma_{PS}^{UV} = 3 \cdot 10^{-9}$ (Day: $\lambda < 132$ nm)	s^{-1}	r03
$R_{s1.2}$	6.83 ^A	$\sigma_{PD}^{LA} = 3 \cdot 10^{-9}$ (Day: Lyman- α emission)	s^{-1}	r24
$R_{s1.3}$	6.83 ^A	$\sigma_{PD}^{Sc} = 3.7 \cdot 10^{-7}$ (Day: Schumann-Runge cont.)	s^{-1}	r24
$R_{s1.4}$	4.94 ^A	$\sigma_{PP}^{Sb} = 1.25 \cdot 10^{-7}$ (Day: Schumann-Runge B.)	s^{-1}	r25
$R_{s1.5}$	4.94 ^A	$\sigma_{PP}^{Hc} = 5.8 \cdot 10^{-10}$ (Day: Herzberg continuum)	s^{-1}	r26
$R_{s2.1}$		$\sigma_{aS}^{UV} = 2.5 \cdot 10^{-3}$ (Day: $\lambda = 193$ nm)	s^{-1}	r13
$R_{s2.2}$	5.95 ^A	$\sigma_{PP}^{Ha} = 1 \cdot 10^{-2}$ (Day: Hartley bands)	s^{-1}	r03
$R_{s2.3}$	3.86 ^A	$\sigma_{aD}^{Ha} = 1 \cdot 10^{-2}$ (Day: Hartley bands)	s^{-1}	r30
$R_{s2.4}$	2.91 ^A	$\sigma_{xD}^{Hu} = 1 \cdot 10^{-4}$ (Day: Huggins bands)	s^{-1}	r24
$R_{s2.5}$	1.96 ^A	$\sigma_{aP}^{Ch} = 3 \cdot 10^{-4}$ (Day: Chappuis band)	s^{-1}	r24
$R_{s2.6}$	1.01 ^A	$\sigma_{xP}^{Ch} = 3 \cdot 10^{-4}$ (Day: Chappuis band)	s^{-1}	r27
$R_{s3.1}$		$\sigma_{bl}^{O2} = 5.35 \cdot 10^{-9}$ (In sunlight conditions)	s^{-1}	r28
$R_{x1.1}$	-5.12 ^R	$\chi_{N2}^{Px} = cPXn \cdot xY \cdot 3 \cdot 10^{-33} (300/T)^{3.25}$	$\text{molec}^{-2} \text{cm}^6 \text{s}^{-1}$	r01
$R_{x1.2}$	-5.12 ^R	$\chi_{O2}^{Px} = cPXm \cdot xY \cdot 3 \cdot 10^{-33} (300/T)^{3.25}$	$\text{molec}^{-2} \text{cm}^6 \text{s}^{-1}$	r01
		$xY = 0.12 + pY \cdot 0.25$	1	r03
		$pY = 0.5$ (for $O_2(^5\Pi)$)	1	r02
		Optional: $cPXm = 7.67 \cdot 10^3$ for $cPXn = cPXm$	1	r03
		Current use: $cPXm \approx 3.56 \cdot 10^4$ for $cPXn = 1$	1	r03
$R_{x2.1}$	-4.06 ^A	$\chi_{O2}^{3P} = 8 \cdot 10^{-12} \exp(-2060/T)$	$\text{molec}^{-1} \text{cm}^3 \text{s}^{-1}$	r13
$R_{x3.1}$	-1.10 ^A	$\chi_{N2}^{P3} = 6 \cdot 10^{-34} (300/T)^{2.4}$	$\text{molec}^{-2} \text{cm}^6 \text{s}^{-1}$	r13
$R_{x3.2}$	-1.10 ^A	$\chi_{O2}^{P3} = 6 \cdot 10^{-34} (300/T)^{2.4}$	$\text{molec}^{-2} \text{cm}^6 \text{s}^{-1}$	r13
$R_{h1.1}$	-3.34 ^R	$\eta_{OH}^H = 1.4 \cdot 10^{-10} \exp(-470/T)$	$\text{molec}^{-1} \text{cm}^3 \text{s}^{-1}$	r13
$R_{h2.1}$	-0.73 ^A	$\eta_{OH}^{3P} = 1.8 \cdot 10^{-11} \exp(180/T)$	$\text{molec}^{-1} \text{cm}^3 \text{s}^{-1}$	r13
$R_{h3.1}$	-1.74 ^A	$\eta_{HO2}^{OH} = 1.7 \cdot 10^{-12} \exp(-940/T)$	$\text{molec}^{-1} \text{cm}^3 \text{s}^{-1}$	r13
$R_{h4.1}$	-2.33 ^A	$\eta_{HO2}^{3P} = 3.0 \cdot 10^{-11} \exp(200/T)$	$\text{molec}^{-1} \text{cm}^3 \text{s}^{-1}$	r13
$R_{h5.1}$	-2.11 ^A	$\eta_{N2}^H = 4.4 \cdot 10^{-32} (300/T)^{1.3}$	$\text{molec}^{-2} \text{cm}^6 \text{s}^{-1}$	r13
$R_{h5.2}$	-2.11 ^A	$\eta_{O2}^H = 4.4 \cdot 10^{-32} (300/T)^{1.3}$	$\text{molec}^{-2} \text{cm}^6 \text{s}^{-1}$	r13
$R_{h6.1}$	-1.60 ^A	$\eta_{OH}^{HO2} = 7.2 \cdot 10^{-11}$	$\text{molec}^{-1} \text{cm}^3 \text{s}^{-1}$	r13
$R_{h6.2}$	-2.41 ^A	$\eta_{H2}^{HO2} = 6.9 \cdot 10^{-12}$	$\text{molec}^{-1} \text{cm}^3 \text{s}^{-1}$	r13
$R_{h6.3}$	-2.33 ^A	$\eta_{H2O}^{HO2} = 1.6 \cdot 10^{-12}$	$\text{molec}^{-1} \text{cm}^3 \text{s}^{-1}$	r13



Table A1. Processes of the prior retrieval and continued to shown in Table 2.

R#	Odd oxygen processes related to $O(^1S)$
$R_{r1.1-3}$	$O(^1D) + \{O(^3P), O_3, O_3\} \xrightarrow{\rho_{3P}^{DP}, \rho_{2P}^{DP}, \rho_{O2}^{DP}} \{2O(^3P), 2O(^3P) + O_2, 2O_2\}$
$R_{r2.1-4}$	$O(^1D) + \{N_2, O_2, O_2, CO_2\} \xrightarrow{\rho_{N2}^{DP}, \rho_{Oa}^{DP}, \rho_{Ob}^{DP}, \rho_{C2}^{DP}} O(^3P) + \{N_2, O_2(a), O_2(b), CO_2\}$
$R_{r3.0}$	$O(^1D) \xrightarrow{\rho_{1D3Pe}^A} O(^3P) + h\nu$
R#	Odd oxygen processes related to absorption and the catalytic ozone destruction
$R_{s1.1-5}$	$O_2 + h\nu \xrightarrow{\sigma_{PS}^{UV}, \sigma_{PD}^{LA}, \sigma_{PD}^{Sc}, \sigma_{PP}^{Sb}, \sigma_{PP}^{Hc}} O(^3P) + \{O(^1S), O(^1D), O(^1D), O(^3P), O(^3P)\}$
$R_{s2.1-6}$	$O_3 + h\nu \xrightarrow{\sigma_{aS}^{UV}, \sigma_{PP}^{Ha}, \sigma_{aD}^{Hu}, \sigma_{xD}^{Hu}, \sigma_{aP}^{Ch}, \sigma_{xP}^{Ch}} \{O(^1S) + O_2(a), 3O, O(^1D) + O_2(a), O(^1D) + O_2, O + O_2(a), O + O_2\}$
$R_{s3.1}$	$O_2 + h\nu(\lambda = 762\text{nm}) \xrightarrow{\sigma_{b1}^{O2}} O_2(b)$
$R_{x1.1-2}$	$O(^3P) + O(^3P) + \{N_2, O_2\} \xrightarrow{\chi_{N2}^{Px}, \chi_{O2}^{Px}} O_2 + \{N_2, O_2\}$
$R_{x2.1}$	$O(^3P) + O_3 \xrightarrow{\chi_{O2}^{3P}} 2O_2$
$R_{x3.1-2}$	$O_2 + O(^3P) + \{N_2, O_2\} \xrightarrow{\chi_{N2}^{P3}, \chi_{O2}^{P3}} O_3 + \{N_2, O_2\}$
R#	Odd hydrogen processes
$R_{h1.1}$	$H + O_3 \xrightarrow{\eta_{OH}^H} OH(5 \leq \nu \leq 9) + O_2$
$R_{h2.1}$	$OH^* + O(^3P) \xrightarrow{\eta_{OH}^{3P}} H + O_2$
$R_{h3.1}$	$OH^* + O_3 \xrightarrow{\eta_{HO2}^{OH}} HO_2 + O_2$
$R_{h4.1}$	$HO_2 + O(^3P) \xrightarrow{\eta_{HO2}^{3P}} OH(\nu \leq 6) + O_2$
$R_{h5.1-2}$	$H + O_2 + \{N_2, O_2\} \xrightarrow{\eta_{N2}^H, \eta_{O2}^H} HO_2 + \{N_2, O_2\}$
$R_{h6.1-3}$	$H + HO_2 \xrightarrow{\eta_{OH}^{HO2}, \eta_{H2}^{HO2}, \eta_{H2O}^{HO2}} \{OH^* + OH^*, H_2 + O_2, O(^3P) + H_2O\}$

Article VI

Lednyts'kyi, O., von Savigny, C., Sinnhuber, M., Iwagami, N., and Mlynczak, M.: Multiple Airglow Chemistry approach for atomic oxygen retrievals on the basis of *in situ* nightglow emissions, *Journal of Atmospheric and Solar-Terrestrial Physics*, **194**, 105096, DOI: 10.1016/j.jastp.2019.105096, 2019.

The article VI is only available to subscribers of the journal.

B. Declaration of Originality (Eigenständigkeitserklärung)

Hiermit erkläre ich, dass diese Arbeit bisher von mir weder an der Mathematisch-Naturwissenschaftlichen Fakultät der Universität Greifswald noch einer anderen wissenschaftlichen Einrichtung zum Zwecke der Promotion eingereicht wurde.

Ferner erkläre ich, dass ich diese Arbeit selbstständig verfasst und keine anderen als die darin angegebenen Hilfsmittel und Hilfen benutzt und keine Textabschnitte eines Dritten ohne Kennzeichnung übernommen habe.

Ort und Datum: Greifswald, den 18. November 2019

Unterschrift
des Promovenden
Olexandr Lednyts'kyy:

Ort und Datum: Greifswald, den 18. November 2019

Unterschrift
des wissenschaftlichen Betreuers
Christian von Savigny:

C. Curriculum Vitae

D. Publications and contributions to conferences

Peer Reviewed Publications

Article I: von Savigny, C., and Lednyts'kyi, O.: On the relationship between atomic oxygen and vertical shifts between OH Meinel bands originating from different vibrational levels, *Geophysical Research Letters*, **40**, 21, 5821–5825, DOI: 10.1002/2013GL058017, 2013.

Article II: Lednyts'kyi, O., von Savigny, C., Eichmann, K.-U., and Mlynczak, M. G.: Atomic oxygen retrievals in the MLT region from SCIAMACHY nightglow limb measurements, *Atmospheric Measurement Techniques*, **8**, 3, 1021–1041, DOI: 10.5194/amt-8-1021-2015, 2015.

Article III: von Savigny, C., Lednyts'kyi, O., Forbes, J., and Zhang, X.: Lunar semidiurnal tide in the terrestrial airglow, *Geophysical Research Letters*, **42**, 9, 3553–3559, DOI: 10.1002/2015GL063567, 2015.

Article IV: Lednyts'kyi, O., von Savigny, C., and Weber, M.: Sensitivity of equatorial atomic oxygen in the MLT region to the 11-year and 27-day solar cycles, *Journal of Atmospheric and Solar-Terrestrial Physics*, **162**, 136–150, DOI: 10.1016/j.jastp.2016.11.003, 2017.

Article V: Lednyts'kyi, O., and von Savigny, C.: Photochemical modeling of molecular and atomic oxygen based on multiple *in-situ* emissions measured during the Energy Transfer in the Oxygen Nightglow rocket campaign, *Atmospheric Chemistry and Physics Discussions*, **2019**, 1–60, DOI: 10.5194/acp-2019-221, in review, 2019.

Article VI: Lednyts'kyi, O., von Savigny, C., Sinnhuber, M., Iwagami, N., and Mlynczak, M.: Multiple Airglow Chemistry approach for atomic oxygen retrievals on the basis of *in situ* nightglow emissions, *Journal of Atmospheric and Solar-Terrestrial Physics*, **194**, 105096, DOI: 10.1016/j.jastp.2019.105096, 2019.

Contributions of Olexandr Lednyts'kyi as the first author to conferences

Oral Presentations

Talk I: Lednyts'kyi, O., and von Savigny, C.: Atomic oxygen retrievals in the MLT region from SCIAMACHY nightglow observations, *DPG Spring Meeting*, 2014, Berlin (Germany).

Talk II: Lednyts'kyi, O., and von Savigny, C.: Quenching processes in terrestrial nightglow green line and Meinel band emissions in the MLT region, *DPG Spring Meeting*, 2015, Bochum (Germany).

Talk III: Lednyts'kyi, O., von Savigny, C., and Sinnhuber, M.: Variations of atomic oxygen in the MLT region retrieved from SCIAMACHY nightglow measurements, *12th Layered Phenomena in the Mesopause Region Workshop*, 2015, Boulder (United States of America).

Talk IV: Lednyts'kyi, O., and von Savigny, C.: $O(^1S)$ formation and loss processes in the terrestrial nightglow, *DPG Spring Meeting*, 2016, Hanover (Germany).

Talk V: Lednyts'kyi, O., and von Savigny, C.: Validation of the Multiple Airglow Chemistry model with *in situ* measurements, *DPG Spring Meeting*, 2017, Bremen (Germany).

Talk VI: Lednyts'kyi, O., and von Savigny, C.: Chemical heating rates derived with the developed Multiple Airglow Chemistry model, *6th Network for the Detection of Mesospheric Change Meeting*, 2017, Grainau (Germany).

Talk VII: Lednyts'kyi, O., and von Savigny, C.: Influence of temporal and spatial variability in observations used to develop Multiple Airglow Chemistry model on derived chemical heating rates, *13th International Workshop on Layered Phenomena in the Mesopause Region*, 2017, Kühlungsborn (Germany).

Talk VIII: Lednyts'kyi, O., von Savigny, C., and Llewellyn, E.: Validation of the extended Multiple Airglow Chemistry model with *in situ* measurements of the Energy Transfer in the Oxygen Nightglow campaign, *DPG Spring Meeting*, 2018, Erlangen (Germany).

Talk IX: Lednyts'kyi, O., Sinnhuber, M., and von Savigny, C.: Validation of the Multiple Airglow Chemistry model applied on the basis of data sets from various sources, *DPG Spring Meeting*, 2019, Munich (Germany).

Poster Presentations

Poster I: Lednyts'kyi, O., and von Savigny, C.: The retrieval of atomic oxygen profiles in the MLT region on the basis of SCIAMACHY airglow observations, *7th Atmospheric Limb Conference*, 2013, Bremen (Germany).

Poster II: Lednyts'kyi, O., and von Savigny, C.: Atomic oxygen retrievals in the MLT region from SCIAMACHY airglow observations, *11th Layered Phenomena in the Mesopause Region Workshop*, 2013, Leeds (United Kingdom).

Poster III: Lednyts'kyi, O., and von Savigny, C.: Optimization of atomic oxygen retrievals in the MLT region from oxygen greenline nightglow observations, *6th Network for the Detection of Mesospheric Change Symposium*, 2014, Grainau (Germany).

Poster IV: Lednyts'kyi, O., and von Savigny, C.: Atomic oxygen variations in MLT observed from SCIAMACHY sun-synchronous nightglow measurements, *40th COSPAR Scientific Assembly*, 2014, Moscow (Russian Federation).

Poster V: Lednyts'kyi, O., and von Savigny, C.: Sensitivity of equatorial atomic oxygen in the MLT to the 11-year and 27-day cycles of solar activity, *DPG Spring Meeting*, 2015, Heidelberg (Germany).

Poster VI: Lednyts'kyi, O., and von Savigny, C.: Sensitivity of equatorial atomic oxygen in the MLT region to the quasi-11-year and quasi-27-day solar cycles, *DPG Spring Meeting*, 2016, Regensburg (Germany).

Poster VII: Lednyts'kyi, O., and von Savigny, C.: Sensitivity analysis of equatorial atomic oxygen to solar forcing indicates a positive linear trend in the MLT region, *9th IAGA – ICMA/IAMAS – ROSMIC/VarSITI/SCOSTEP workshop on Long-Term Changes and Trends in the Atmosphere*, 2016, Kühlungsborn (Germany).

Poster VIII: Lednyts'kyi, O., and von Savigny, C.: Development of a Multiple Airglow Chemistry model and Validation with *in situ* Airglow Measurements, *Midterm HEPP Meeting at the Max Planck Society*, 2016, Berlin (Germany).

Poster IX: Lednyts'kyi, O., and von Savigny, C.: Estimation of heating rate values with the multiple airglow chemistry model, *DPG Spring Meeting*, 2017, Bremen (Germany).

Poster X: Lednyts'kyi, O., and von Savigny, C.: $O(^1S)$ quenching processes influence the sensitivity of equatorial MLT atomic oxygen to the ~ 11 -year and ~ 27 -day solar cycles positively, and not significantly, *7th Network for the Detection of Mesospheric Change Symposium*, 2017, Grainau (Germany).

Poster XI: Lednyts'kyi, O., Versick, S., Sinnhuber, M., and von Savigny, C.: Retrieval of atomic oxygen on the basis of simulated data sets and those obtained remotely from collocated measuring sites, *8th Network for the Detection of Mesospheric Change Symposium*, 2019, Oberpfaffenhofen (Germany).

Poster XII: Lednyts'kyi, O., and von Savigny, C.: Modeling of molecular and atomic oxygen photochemistry on the basis of multiple *in situ* and limb nightglow emissions, *10th Atmospheric Limb Conference*, 2019, Greifswald (Germany).

E. Acknowledgements

I sincerely thank my supervisor Christian von Savigny for believing in my capacity to meet the challenge, enabling me to work on the doctoral thesis and for making the last six years a positive graduate experience for me. Although I have written this doctoral thesis in my own words, I acknowledge pieces of advice made by Christian von Savigny on this doctoral thesis.

I acknowledge the financial support provided by the University of Greifswald for the time period from 2013 to 2016, the International Helmholtz Graduate School for Plasma Physics for the time period from 2014 to 2020, and the German Research Foundation (DFG) providing the grant SA 1351/6-1 for the time period from 2016 to 2020. I thank Prof. Christian von Savigny, Dr. Miriam Sinnhuber and Dr. Tilo Fytterer for helpful discussions during our work on the scientific project *Investigation of photochemistry of oxygen species in the mesopause region* financed by the DFG.

I am grateful to Prof. Solomon and Prof. Plane for the insightful and cheering up personal communication during small talks at the conferences. I am also grateful to Prof. Anatoly Semenov, Dr. Thomas von Clarmann, Prof. Naomoto Iwagami, Dr. Martin Mlynczak, Prof. Tai-Yin Huang and Prof. Valentine Yankovsky for giving me kind answers to my questions on clearing up my understanding of the retrieval models worked by them out. I thank Dr. Martin Kaufmann for critical comments stimulating my research. I also acknowledge a positive stimulating influence of Prof. Edward Llewellyn and Dr. Thomas von Clarmann on working out this doctoral thesis under the supervision of Prof. Christian von Savigny.

I thank anonymous reviewers for helpful discussions and insightful comments, helpful comments, recommendations and suggestions during the peer reviewing process to publish my articles.